Aston University

Some pages of this thesis may have been removed for copyright restrictions.

If you have discovered material in AURA which is unlawful e.g. breaches copyright, (either yours or that of a third party) or any other law, including but not limited to those relating to patent, trademark, confidentiality, data protection, obscenity, defamation, libel, then please read our Takedown Policy and contact the service immediately

COMPUTER SIMULATION OF MOIST AGGLOMERATE COLLISIONS

Guoping Lian, BSc, MSc

DOCTOR OF PHILOSOPHY

THE UNIVERSITY OF ASTON IN BIRMINGHAM

January 1994

This copy of the thesis has been supplied on condition that anyone who consults it is understood to recognise that its copyright rests with its author and that no quotation from the thesis and no information derived from it may be published without proper acknowledgement.

The University of Aston in Birmingham

COMPUTER SIMULATION OF MOIST AGGLOMERATE COLLISIONS

GUOPING LIAN, BSc, MSc

Thesis submitted for the degree of Doctor of Philosophy

1994

SUMMARY

In the process industries powders are frequently granulated in order to promote their handleability and flowability. During the operation of powder granulation, a liquid binder is usually mixed with the powders to increase their cohesiveness. For binder granulation processes, the coalescence and breakage behaviour of moist granules during collision is a major concern. This thesis considers the computer simulation of moist agglomerate collisions using the the discrete element method (DEM). The study is confined to pendular state moist agglomerates, at which liquid is presented as either adsorbed immobile films or pendular liquid bridges and the interparticle force is modelled as the adhesive contact force and interstitial liquid bridge force. Algorithms used to model the contact force due to surface adhesion, tangential friction and particle deformation have been derived by other researchers and are briefly described in the thesis.

A theoretical study of the pendular liquid bridge force between spherical particles has been made and the algorithms for the modelling of the pendular liquid bridge force between spherical particles have been developed and incorporated into the Aston version of the DEM program TRUBAL. It has been found that, for static liquid bridges, the more explicit criterion for specifying the stable solution and critical separation is provided by the total free energy. The critical separation is given by the cube root of the liquid bridge volume to a good approximation and the 'gorge method' of evaluation based on the toroidal approximation leads to errors in the calculated force of less than 10%.

Three dimensional computer simulations of an agglomerate impacting orthogonally with a wall are reported. The results demonstrate the effectiveness of adding viscous binder to prevent attrition, a common practice in process engineering. Results of simulated agglomerate-agglomerate collisions show that, for colinear agglomerate impacts, there is an optimum velocity which results in a near spherical shape of the coalesced agglomerate and, hence, minimises attrition due to subsequent collisions. The relationship between the optimum impact velocity and the liquid viscosity and surface tension is illustrated. The effect of varying the angle of impact on the coalescence/attrition behaviour is also reported.

Key words: Agglomeration
Coalescence and attrition of wet granules
Discrete element method
Impact
Liquid bridge forces and stability

To My Family

Acknowledgements

I sincerely thank my research supervisor Dr. Colin Thornton for his guidance, encouragement and support throughout the duration of the research programme. I sincerely appreciate his enthusiastic help in organising the project, his invaluable comments, advice and discussion provided at every crucial stage of the research and his diligent effort in checking the equations and correcting the script.

I would also wish to especially acknowledge Dr. Michael J. Adams of Unilever Research, Port Sunlight Laboratories for his enthusiasm in developing the project and his useful advice and discussion on the progress of the project.

My sincere appreciation is also extended to Unilever Research, Port Sunlight Laboratories and the CVCP for providing the financial support and an Overseas Research Studentship (ORS) that assured the smooth progress and success of the project, to Dr. David Kafui who provided technical assistance in the setting up of computer facilities and softwares and generously checking the final draft of the thesis, and to Cyril Hart for his help in correcting the draft and some other reports related to the project.

I also wish to acknowledge the understanding, support and encouragement of Zemin Ning, Teo Ciomocos, Leon Toland, Dr. Gexin Sun and Dr. David Kafui who all had their own challenges in applying TRUBAL to their specific problems.

Finally, special thanks to my dear wife Yanqing for her constant support while also working for her PhD degree, to my son Daniel for his understanding at his young age, and to my parents.

Contents

List of Figures

List of Tables

Chapter 1

Introduction

1.1 Background of the project

Most industrial materials or products such as food, detergents, agricultural chemicals and pharmaceuticals are either provided or processed in fine particulate or powder form. Unfortunately, these particulate materials are commonly manifested to be associated with the problems of dust, environmental pollution and hazard. They are also difficult to process and transport because of their poor flowability and handleability. Agglomeration of fine particulate materials is heavily utilized in the chemical processing industry. The benefit is that the agglomerated fine particles can be more easily conveyed and processed without imposing dust and other hazards on the environment. However, agglomeration can be also deleterious. One problem associated with agglomeration is the plug-blocking of fluidised beds. In ceramic processing, the overwhelming problem of defects or flaws in ceramic materials originates from agglomerates which are present in the ceramic powders.

With agglomeration as a heavily utilized beneficial operation to promote the flowability and handleability of fine powders, attrition of agglomerates during handling and

processing is, on the other hand, a commonly occurring nuisance. To prevent attrition, the agglomerates must be strong enough to resist breakage during flow, but must be easy to break down under intentional compression, grinding or shearing before moulding. The intentional breakage of agglomerates is referred to as comminution.

The particle enlargement process of agglomeration depends on the bonding forces between particles. It is a result of collisions between primary particles or granules caused by agitation. During the agglomeration process, primary feed particles collide with each other and coalesce into discrete granules. Binding liquid is often necessary to activate the coalescence of the particles. When the agglomerates grow in size to a certain stage, further collisions may result in the granulated agglomerates being abraded, comminuted or fractured. The degradation phenomena of agglomerate attrition, comminution and fragmentation are always found in competition with the agglomerate enlargement process during the agglomeration operation and the combination favours the production of agglomerates of specific size, strength, porosity and structure.

Both particle agglomeration and degradation depend on the cohesive force between particles. A wide range of mechanisms of adhesion contribute to the interparticle cohesive force. They are identified as the adhesive force of inter-molecular attraction between contacting surfaces, the binding force of liquid bridges and solid bridges and the attractive force of electrostatic and magnetic potentials (Rumpf 1977, Sherrington and Oliver 1981). The mechanics of single particle-pair interaction due to different bond forces is well-established. However, the bulk mechanical behaviour of particle systems in terms of the micro-level inter-particle forces is still a slowly unfolding mystery. In fact, there have been very few studies published to correlate agglomerate coalescence and degradation with packing geometry, interparticle bond forces and particle properties. Most previously reported studies of agglomeration and attrition are mainly descriptive. The theories are, in the main, concerned with simple

systems of mono-disperse and regular packings. Studies of poly-disperse and random packings are generally based on observations obtained from real experimentals. Real experiments are not only expensive, but are also restricted by the lack of adequate instruments and techniques for measuring internal quantities such as geometry, forces and velocities. As a result, the information obtained is often empirical, inaccurate, insufficient and incomplete; and lacks direct quantitative verification.

Computer simulated experimentation, using the Discrete Element Method (DEM) is a recent development which has been applied to the modelling of granular materials. By direct numerical simulation of the particle interactions the evolution of particle locations and interparticle forces may be examined. Consequently, computer simulation provides an opportunity to study the internal variables of particle assemblies and relate them to the macroscopic behaviour. However, the technique is a relatively recent development. Most current computer simulation programs only handle very simple spherical particles and use simple linear contact rules. Furthermore, most applications of computer simulation are only concerned with dry particle systems. It is desirable to extend the methodology to non-spherical particle systems and to incorporate different interactive laws between particles, in order to simulate the particle systems more realistically. Modifications and enhancement to the computer programs are also needed to apply the technique to agglomerate coalescence, attrition and other problems in process engineering.

This research project is concerned with the application of the Discrete Element Method (DEM) to the modelling of moist particle systems. In this project, the effect of pendular liquid bridges between spherical particles is examined. Algorithms to model interparticle liquid bridge forces have been developed and incorporated into the Aston version of the DEM computer program TRUBAL (Thornton and Kafui 1992).

The modified 3D computer program has been used to simulate the collision of a

moist agglomerate with a wall and with another moist agglomerate. The underlying objective of the project is to investigate moist agglomerate coalescence and degradation in more detail by examining their correlation with the internal geometrical structure and contact bond strength so as to establish the criteria for assessing the attrition resistance and coalescence propensity of wet agglomerates in terms of the bulk properties of the constituent particles, the bond strength between the contiguous particles and the physical properties of the liquid binder.

1.2 Presentation order

Chapter 2 presents a review of the previous research work on agglomeration, attrition, comminution and agglomerate strength. Particle agglomeration and attrition are closely related problems in process engineering industries and both depend on the strength of the agglomerates. The application of computer simulations to agglomerate impact, using the Discrete Element Method (DEM), is also discussed.

Chapter 3 briefly introduces the contact mechanics of single pairs of spherical particles. The theories of Hertz (see Johnson 1985) and Mindlin and Deresiewicz (1953) for the elastic deformation of spheres and the theories of Johnson et al (1971), Savkoor and Briggs (1977) and Thornton (1991) for the additional effects of surface energy are presented. These theories have been implemented in the Aston version of TRUBAL for the modelling of dry particle systems (Thornton and Randall 1988, Thornton and Yin 1991, Thornton and Kafui 1992).

Chapter 4 is concerned with pendular liquid bridge forces between spheres under conditions when the effect of gravity is negligible. The condition for stable liquid bridges has been examined by a minimum free energy formulation. The criterion for specifying the stable liquid bridges and the relationship for the critical separation distance of rupture have been established. For the static force of liquid bridges,

algorithms according to the 'gorge method' (Hotta et al 1974) of evaluation based on Fisher's toroidal approximation (Fisher 1926) have been developed by comparing them with the numerical solutions to the Laplace-Young equation. The theory of Adams and Perchard (1985) is applied to the calculation of the viscous force of liquid bridges.

Chapter 5 considers the incorporation of the liquid bridge algorithms into the Aston version of TRUBAL. The methodology of the Distinct Element Method (DEM) developed by Cundall (1971) is described. Modifications and enhancement to adapt TRUBAL to simulate and to view agglomerate collisions are also discussed.

Chapter 6 and Chapter 7 present the results of computer simulated moist agglomerate collisions. Chapter 6 is concerned with the collision of an agglomerate of body-centred cubic packing consisting of 4062 primary particles with a wall. Chapter 7 is concerned with the collision of two randomly packed agglomerates each consisting of 1000 primary particles. The transition from coalescence to attrition is examined and the influence of the physical properties of the liquid binder is investigated.

Finally, Chapter 8 provides some concluding remarks concerned with the criteria for assessing the attrition resistance and coalescence propensity of moist agglomerates based on the results of the computer simulations. The general application of the DEM technique to the computer modelling of moist particle systems is also discussed.

Chapter 2

Literature Review

This chapter presents a review of the previous research work on agglomeration, attrition, comminution and agglomerate strength. No attempt is made to cover all of the relevant literature and the emphasis is placed on the studies of microlevel interparticle forces and their effects on the bulk behaviour of granules. The application of computer simulations to agglomerate collisions, using the Discrete Element Method, is also discussed.

2.1 Agglomeration

Agglomeration or granulation of fine particles of micron size is frequently used in the chemical engineering industries to promote the containment and flowability of chemical products and hence to reduce the potential pollution hazard that the chemical dust imposes on the environment. The mechanism of particle size enlargement by agglomeration is very often viewed as a sequence of collisions and coalescence of primary particles into discrete granules and successive granule growth (Sherrington and Oliver 1981). In the first stage of agglomeration, the nucleation of the primary feed particles takes place initially by rapid random coalescence of primary particles. At the second stage of granule growth, collisions of primary feed particles with the granules or one granule with another can both occur. Many studies have been made highlighting the granule growth by collision and coalescence of primary feed particles. There are very few studies that have been made of the mechanism of granule growth by collision and coalescence of small granules.

2.1.1 Interparticle bond forces

A considerable number of previous investigations have been made, at the microscopic level, about the relevance of interparticle bonding forces to the cohesiveness of agglomerates (Rumpf 1962, 1977; Sherrington and Oliver 1981; Hartley and Parfitt 1985a, 1985b; and Ayala et al 1986). Various interparticle attractive forces have been identified as the contributing mechanisms for the adhesion and coalescence of particles and granules. Rumpf (1962, 1977) first studied the various interparticle bonding forces at the microscopic level. The contributing interparticle bonding forces that affect the adhesion and cohesiveness of agglomerates were identified as intermolecular van der Waals's adhesive forces, electrostatic and magnetic attractive forces, liquid bridges forces, solid sintering and crystallisation forces.

In most cases, the van der Waals adhesion forces and liquid binding forces between particles are considered to be the most important forces that hold fine particles together. For the intermolecular van der Waals's adhesion forces between spherical particles, the theory of Hamaker (1937) is often quoted. For two small spherical particles of radii R_1 and R_2 with separation distance S, the Hamaker equation estimates the interparticle attraction force as,

$$P_c = \frac{AR^*}{6S^2} \tag{2.1}$$

where A is the Hamaker constant and R^* is defined as,

$$R^* = \frac{R_1 R_2}{R_1 + R_2} \tag{2.2}$$

The expression for the Hamaker attractive forces has been used to estimate the cohesive strength of agglomerates by Rumpf (1962), Cheng (1968) and Hartley and Parfitt (1985a).

Applying the Hamaker equation requires finite arbitrary values to be assumed for the separation of surfaces because it predicts infinity for intimate contact. More recent models for the adhesion forces between spheres were presented by Johnson et al (1971) and Derjaguin et al (1975). The model of Johnson et al, the so-called JKR model, predicts the pull-off force for the detachment of two particles as,

$$P_c = \frac{3}{2}\pi\Gamma R^* \tag{2.3}$$

where Γ is the mutual interfacial surface energy of adhesion between two surfaces. The model of Derjaguin et al, the so-called DMT model, predicts the pull-off force as,

$$P_c = 2\pi\Gamma R^* \tag{2.4}$$

It is believed that the JKR model is applicable to larger soft particles such as rubber and the DMT model is most appropriate for small hard spheres (Tabor 1977, 1978).

For most industrial agglomeration processes, particles are usually granulated in the presence of a liquid. According to the degree of saturation of liquid, i.e. the ratio of the amount of pore volume occupied by liquid to the total pore volume, the liquid state in moist particle systems may be described as a pendular state, funicular state or capillary state (Schubert et al 1975, Sherrington and Oliver 1981). In the pendular state, only a small quantity of liquid is held at the contacts between particles in the form of bridges. Each liquid bridge is isolated from the others. By increasing the degree of liquid saturation, some liquid bridges will become inter-connected. The state is considered as the funicular state because both liquid bridges and pores partially filled with liquid are present. A further increase in liquid saturation to the state where all pores are completely filled with liquid is regarded as the capillary state.

When fine particles are wetted by liquid, the cohesiveness between particles increases. In the case of pendular liquid bridges, the attractive force between particles is due to the effect of the surface tension, fluid pressure deficiency and viscous resistance of the liquid. The static liquid bridge force which arises from the pressure deficiency and surface tension of pendular liquid bridges may be calculated from the Laplace-Young equation which relates the mean curvature of the bridge to the bulk pressure deficiency. The total static force is expressed as,

$$Fs = 2\pi\gamma_{lv}y_0 + \pi\Delta p y_0^2 \tag{2.5}$$

where γ_{lv} is the liquid-vapor interfacial surface energy and is usually called the surface tension of the liquid, y_0 is the radius of the bridge neck and Δp is the hydrostatic pressure deficiency of the liquid bridge.

In practice, however, the toroidal approximation proposed by Fisher (1926) has

been frequently used because the Laplace-Young ordinary differential equation can not be solved analytically except for a few special cases. Based on Fisher's toroidal approximation, some analyses on the effect of liquid bonding forces in agglomeration were made by Rumpf (1962, 1977) and others (Sherrington and Oliver 1981, Hartley and Parfitt 1985b, Ayala et al 1986).

The presence of a thin liquid film between two approaching particles can significantly increase the cohesiveness of particles due the viscosity of the liquid. Adams and Perchard (1985) derived an expression for the viscous force of pendular liquid bridges between identical spherical particles based on the classical theory of lubrication between two surfaces. The viscous resistance force is given as,

$$F_v = \frac{6\pi\eta(R^*)^2 v_n}{S} \tag{2.6}$$

where η is the viscosity of the fluid and v_n is the relative approaching velocity of the two spheres. The same expression was also derived later by Matthewson (1988) and Ennis et al (1990) for the viscous force between spheres coated by thin liquid layers. An experimental investigation of the viscous force of dynamic liquid bridges between two moving spheres was presented by Mazzone et al (1987). It was found that the viscous force could be orders of magnitude larger than the meniscus force of static liquid bridges for very viscous liquid. The shape and the rupture distance of dynamic liquid bridges were also found to be quite different from the static case.

2.1.2 Primary particle coalescence

Although interparticle attraction forces are necessary for fine particles to be held together, energy dissipation is also essential for the successful coalescence of colliding particles and granules. At the microscopic level, some studies of the dynamic collision and coalescence of two small particles were made by Davis and his co-workers (Davis

et al 1986; Serayssol and Davis 1986; Davis 1987; and Barnocky and Davis 1988a, 1988b). Their elasto-hydrodynamic approach considers the viscous liquid, the attractive and repulsive surface forces, and elastic deformation of the particles in order to determine whether the particles will stick together or bounce apart subsequent to collision. Davis et al (1986) first presented a theory which only considered an elastic solid sphere colliding with another elastic solid sphere, or plane, covered by a thin viscous fluid layer. By determining the elastic deformation of the particle surface and hydrodynamic pressure profile in the fluid layer via asymptotic and numerical techniques, their theory established the criterion for predicting whether a colliding particle sticks or rebounds in terms of the Stokes number S_t of the liquid and Young's Modulus E of the particles.

Davis (1987) and Serayssol and Davis (1986) included the influence of London-van der Waals adhesion forces and double layer repulsive forces into the elasto-hydrodynamic model. In order to account for the interparticle surface forces, they used the Hamaker equation (Hamaker 1937) for the London-van der Waals's adhesion forces and the Derjaguin equation (1940) for the electrical double layer repulsive forces. The total surface stress which causes the particles to deform was considered as the sum of the interparticle surface forces and the hydrodynamic pressure forces. Through numerical solutions, they found that the interparticle surface forces are typically weak compared to the viscous forces if the elastic deformation of the solid is significant. In this case, the viscous forces damp out most of the particle inertia before the interparticle forces come into play. A criterion to predict the conditions under which particles rebound or separate was established for different ratios of the repulsive force to the attractive force. For relatively strong London-van der Waals's forces, a critical dimensionless Hamaker constant was identified. Above the critical Hamaker constant, the attractive forces pull the surfaces of particles together and prevent rebound.

In principle, the elasto-hydrodynamic approach assumes no-slip fluid boundary conditions. Barnocky and Davis (1988a) employed the Maxwell slip-flow approximation for the hydrodynamic pressure of the liquid layer and found that the effect of the slip flow is to reduce the viscous force and permit colliding particles to make intimate contact with sufficient inertia. A critical Stokes number, S_t^*, a function of slip parameter, β, was determined in order to determine if the colliding spheres stick or rebound. The critical Stokes' number was seen to decrease when the slip parameter increases. Experiments with small metal and plastic spheres dropped upon smooth and artificially rough quartz surfaces were made by Barnocky and Davis (1988b) to delineate the conditions under which the particles rebound, as opposed to sticking. The minimum drop height that allowed the tested particles to rebound from smooth surfaces were found to be in good agreement with the theory of Davis et al (1986). For the experiments with rough surfaces, the viscous resistance to rebound was significantly reduced.

Assuming that only the static and viscous liquid bridge forces are the dominant operative parameters for particle granulation, Ennis et al (1991) presented a microscale model for the granulation of granules. Considering the colliding granules as rigid spheres, Ennis et al (1991) derived the critical Stokes number for two colliding granules in terms of the radius of the granules and the thickness of the binder layer. Successful coalescence of granules could occur if the granules collide with initial Stokes numbers less than the critical one. Ennis et al (1991) also linked the micro-level based critical Stokes number to the engineering granulation process by considering the different regimes of a granulation bed. Within the granulation bed, there is a spatial variation of the Stokes number. For non-inertial granulation, the entire distribution of Stokes numbers within the granulation bed is well below the critical Stokes number and hence all granule collisions cause coalescence. When the agglomerates within the granulation bed grow in size, so does the spatial distribution of Stokes numbers. In the regime of inertial granulation, the Stokes numbers of some

large agglomerates reach the critical value. Coalescence may be expected only for those collisions of smaller agglomerates with lower than critical values of Stokes numbers. As the agglomerates further grow in size, to a point where the average Stokes number equals to the critical one, the successful coalescence by the collisions of small agglomerates will be balanced by the degradation of large agglomerates colliding with others. This regime of agglomeration is referred to as coating granulation with which agglomerate growth by collisional coalescence may not be achieved.

It should be noted that the microlevel granulation mechanism presented by Ennis et al (1991) is based on the collisional energy dissipation of rigid spheres by viscous liquid binder only. However, as pointed out earlier, the interstitial liquid binder is only a part of the functioning mechanisms of granulation. During the process of agglomerate growth by collision, van der Waals' forces are always present. Apart from ignoring the surface adhesion between particles, a major problem of the theory of Ennis et al (1991) is the assumption that the granules may be represented by rigid spheres. In reality, granules are themselves clusters of primary particles held together by interparticle bonding forces. The granules do not behave like rigid or even elastic spheres any more. Plastic deformation may be dominant and hence will contribute to energy dissipation during the collisional event. Given the fact that different mechanisms of particle sticking and energy dissipation may operate for particle granulation, the deterministic approach of two granule coalescence model given by Ennis et al (1991) must be considered as a gross oversimplification.

Apart from the interparticle cohesive forces that hold particles together and the energy that has to be dissipated for successful coalescence, there are other additional factors that may influence particle agglomeration. They have been identified, mainly from experimental observations, as the particle bulk properties such as size, shape, surface area and wettability. Investigations by Holm et al (1985) and Kristensen et al (1985b) showed that the particle size, distribution and shape affected the porosity of

the powder bed, and also the degree of liquid saturation necessary for agglomeration to occur. Other studies (Hunter and Ganderton 1972, Bier et al 1979, and Jaiyeoba and Spring 1979) indicated that the granule porosity was inversely proportional to the particle size. Kristensen and Schaefer (1987) suggested that the influence of bulk particle properties could be explained in terms of the effective surface area of the materials. For granule growth by agglomerate coalescence, Kapur (1978) and Kristensen et al (1985a, 1985b) stated that the ability of the agglomerate to withstand strain without degradation was essential.

2.1.3 Agglomerate growth

At the macroscopic operational level, agglomerate size, porosity, morphology, strength and growth rate are of primary interest. Investigations of these final product properties of agglomerates in relation to the operational parameters such as the spray drop size, atomizer type and location, liquid viscosity, primary feed particle size and properties and flow rate were made by several disjointed bits of experimental measurements. An investigation of the fluidised-bed granulation of pharmaceuticals was made by Schaefer and Worts (1977). They observed a linear relationship between the granule size and the spray drop size. Some studies on high speed mixer granulation were made by Lindberg (1977) and Holm et al (1985a, 1985b). They showed that the power consumption and granule growth rate were correlated with the liquid saturation of moist granules, i.e. in the range of liquid saturation where the deformation behaviour of granules changes from brittleness into plastic, both the power consumption and granule growth increase rapidly for a slight increase in saturation. Kristensen et al (1985a, 1985b) suggested that the correlation of power consumption and granule growth with liquid saturation could be explained in terms of their dependence on the strain behaviour of moist agglomerates exposed to external stresses due to agitation, tumbling and rolling etc. They demonstrated by experiments that the

plastic deformation of the moist agglomerates is the principal parameter that affects granule growth. When the liquid content increases, the strength of moist granules decreases and the deformability is improved. This gives rise to increased granule growth and power consumption.

According to the suggested effect of deformability on granule growth by coalescence, it is to be expected that the reduction in granule strength also improves the granule growth rate. However, the effect of a reduced granule strength means a reduction of the interparticle bonding force and the work required to separate particles. As a result, successful coalescence of granules by collision may be reduced due to possible attrition. Studies (Nienow and Rowe 1985; Kristensen et al 1985b; and Parker and Rowe 1991) on the effect of particle size and morphology upon granule growth suggest there exists a critical limit for the granule strength below which the agglomerate strength is insufficient to ensure survival of the agglomerates.

2.1.4 Discussion

It is seen that the first step in the process of granulation is the wetting of the powder mixture with the binding liquid. Nucleation of primary particles is the dominating granule growth mechanism at this stage. The wettability and solubility of the powder in association with the uniformity of the moisture distribution are the principle factors which affect the granule growth rate and energy requirement (Ayala and Parfitt 1984, and Ayala et al 1986). In the second stage, granule growth by mutual collisions and successful coalescence becomes the dominating mechanism. Liquid saturation is essential to regulate the strength and deformability of the agglomerates and hence the granule growth rate. The assessment of the liquid requirement for the nucleation and granule growth process is therefore essential to control the operation of granulation processes and the quality of the final agglomerate product. Most previous

studies have been mainly concerned with micro-level interparticle bond forces and the conditions for the successful coalescence of primary particles. At the operational level of agglomeration processes, very few studies have been made on the assessment of agglomerate size, porosity and strength in terms of operational parameters, micro-level particle properties and interparticle bonding forces. Investigations of particle agglomeration have been generally carried out by experiments and scale-up procedures. Any changes in the material properties such as particle type, size, morphology and binding liquid require new experiments. The problem of predicting the effect on energy dissipation and the final product properties as a result of changing primary feed particles, operation parameters and wetting liquid remains unsolved.

2.2 Attrition and comminution

Although particle breakdown is generally an unwanted nuisance associated with environmental and hazard problems, it can also be beneficial, such as in grinding mills. Terminologically, the intentional size reduction of materials is described as comminution and attrition is normally defined as the unwanted breakdown of materials. Collectively, both comminution and attrition may be referred to as degradation which, however, also includes fragmentation, abrasion, wear and erosion.

Like the agglomeration process, most processes of attrition and comminution of particulate materials are also caused by the collision between the materials with a vessel wall or with themselves during the handling and processing. The difference is that with agglomeration, the collision is to enhance the coalescence of particles and granules, but with attrition and comminution, the collision is to produce fine particles and daughter clusters that breakdown from the parent particles or agglomerates. In some cases, agglomeration and fragmentation may occur in the same process. One example is suspensions of solid particles in liquid (Ray and Hogg 1987). Gentle

agitation of the suspension increases the frequency of particle-particle collisions and can enhance the rates of agglomeration. More intense agitation, however, causes breakage and, ultimately, the complete destruction of the agglomerates.

2.2.1 Attrition mechanisms of solid particles

Attrition and comminution may occur to both solid particles and porous agglomerates. The degradation of agglomerates during their handling and processing is more common. Unfortunately, most previous studies have been mostly concerned with the attrition and comminution of solid particles. The attrition and comminution of solid particles have been believed to be due to the particle fracture by crack initiation and propagation. Particle properties of shape, size, surface and hardness in association with the handling and processing conditions such as shearing stress and relative velocity have been identified as the most important factors that affect the particle fracture process upon attrition and comminution (British Materials Handling Board 1987).

It is believed that the fragmentation of solid particles also strongly depends on the strength of the material. Paramanathan and Bridgwater (1983a, 1983b) studied the attrition mechanisms of solids by using an annular attrition cell which they developed. Their investigation indicated that the particle attrition in the annular cell could occur by both fracture and/or surface abrasion, depending on the material property. The attrition of soda ash and laboratory salt was seen to be caused by surface abrasion with edges and corners being most obviously lost. The attrition of Pure Dried Vacuum (PDV) salt, however, was mainly caused by bodily fractures that form cubic materials. It was also observed that granular salt was fractured radially to form hemispheres and other fragments. It was also found that strain rate had little effect on the amount of attrition produced.

The attrition mechanisms of NaCl salt were investigated in more detail by Yuregir

et al (1987) through single particle impact tests. It was shown that, for sodium chloride crystal particles produced by cleaving melt-grown ingots to about 1mm in size, low velocity impact causes extensive plastic deformation on the impacting corner and removal of thin platelets from the faces adjacent to it. The breakdown process by impaction were compared with the fracture of single particles under quasi-static indentation presented earlier by Badrick and Puttick (1986) and Ghadiri and Yuregir (1987). It was suggested that the localised loading on the corner caused plastic deformation and produced a rigid wedge acting as an indenter which initiates and propagates cracks within the crystal. The formation of platelets was attributed to sub-surface lateral cracks. It was also shown that impact loading leads to the removal of thin platelets from the faces adjacent to the impact corner. Unfortunately, this feature is not observed under quasi-static indentation. Ghadiri et al (1991) also examined the attrition propensity of NaCl crystals and suggested it could be related to the micro-hardness of the material. They also observed that the removal of thin platelets was due to the sub-surface lateral cracks. However, the mechanism of the sub-surface lateral cracks is not well-understood.

Knight and Bridgwater (1985) made a comparison of different methods used for assessing solid attrition. They tested the attrition of spray-dried detergent powders by using an annular shear cell test, single particle compression and spiral air classifier respectively. It was shown that the single particle compression test did not provide a reliable assessment of particle attrition, but the annular shear cell and spiral classifier showed reasonable agreement.

2.2.2 Mass balance for particle fragmentation

For solid particle degradation, there has also been considerable interest in predicting the evolution of daughter particle-size distributions during the fragmentation of par-

ent particles. Theoretically, according to the mass balance principle, the evolution of the particle size distribution for a continuous system undergoing fragmentation may be described by (Ziff and McGrady 1985, McGrady and Ziff 1987),

$$\frac{\partial w(x,t)}{\partial t} = -B(x)w(x,t) + \int_x^\infty B(y)b(x|y)w(y,t)dy \tag{2.7}$$

where $w(x,t)$ is the concentration of particles of size x, $B(x)$ is the rate at which particles of size x breakdown and $b(x|y)$ is the distribution of the products from the breakdown of particles of size y.

Physically, the first term of the right hand side of equation 2.7 represents the loss of particles of size x due to their breaking up and the second term represents the increase of particles of size x produced from the larger particles of size y. Obviously, the distribution rate of production of particles must be normalized so that the mass is conserved, i.e.,

$$\int_0^y b(x|y)xdx = y \tag{2.8}$$

For a discrete system, the size distribution $w_i(t)$ is represented by the discrete kinetic equation,

$$\frac{dw_i(t)}{dt} = -B_i w_i(t) + \sum_{j=i+1}^{\infty} b_{ij}B_j w_j(t) \tag{2.9}$$

where B_i is the specific rate of breakage for particles of size i and b_{ij} is the daughter fragment distribution or primary breakage distribution which represents the fraction of particles of size i that breakdown from the particles of size j.

Applying the particle size distribution evolution theory requires the determination of breakage parameters B_i, b_{ij}. Methods for determining the specific rates of breakage B_i and primary breakage distributions b_{ij} have received considerable attention in

comminution literature. Numerous papers on the breakage parameters of grinding fracture were presented by Austin and his co-workers (Austin, Jindal and Gotsis 1979; Shoji, Lohrasb and Austin 1980; Austin and Brame 1983; Klimpel and Austin 1983; Austin, Barahona and Menacho 1986; Austin 1987; Austin and Klimpel 1989; and Vervoorn and Austin 1990). Assuming that the grinding kinetics follows first-order breakage law, their investigations cover a wide range of laboratory grinding mills including hammer mills, dry ball mills and sizing wet tumbling ball mills. For their laboratory mills, the specific rates of breakage were evaluated from batch feeding of single sized particles. At steady-state conditions, the size of the feeding particle is the maximum and equation 2.9 is reduced to,

$$\frac{dw_1(t)}{dt} = -B_1 w_1(t) \tag{2.10}$$

Since a first-order breakage law is assumed, the solution for the fraction of feed particles is $w_1(t) = exp(-k_1 t)$ with which k_1 can be readily determined from the slope of a semi-logarithmic plot. The complete set of k_i can be obtained from a series of experiments of feed particles with different sizes. The underlying assumption is that the breakage rates are independent of the presence of other sized particles. But, in real attrition and comminution, particles break up through mutual interactions or with the vessel, fluid and others, the specific rates of breakage of certain size also depends on the presence of the other sizes.

Experimental determination of the primary breakage distribution is more difficult. The direct measurement is based on the grinding of a single sized fraction of particles over very short times. A correction procedure has to be used to account for the secondary breakage. Another method is the back-calculation by nonlinear regression of the product size distribution. The back-calculation is more frequently used in practice. Unfortunately, the calculated values of b_{ij} are extremely sensitive to errors in the size distributions. Using specific functional forms for the primary breakage

distributions is also essential.

Koka and Trass (1987), using the mass-balance method to study the breakup of Pittsburgh coal in a laboratory Szego mill, determined the breakage parameters. However, when the experimentally determined breakage parameters are introduced in the modelling of multi-pass grinding, it was found that the predicted size distributions only fit the experimental data well at low rotational speed, and there is some deviation at higher rotational speeds.

2.2.3 Attrition of agglomerates

Although the attrition and comminution of particulate materials in chemical engineering are mostly associated with porous agglomerates, there is correspondingly little information published to deal with the degradation of agglomerates. An early investigation of the free-fall impact of sand-cement and spherical glass agglomerates was reported by Arbiter et al (1969). In their free-fall impact tests, they observed that the breakage started from the region of contact between the sphere and the loading platen. Meridian fracture planes were seen to start from the periphery of the contact circle (between the sphere and the platen) and believed to be developed by the wedging action of the cone formed in the contact region. They also found the size distribution curves of the fractured daughter fragments could be approximated by two straight lines on a log-log plot. They ascribed this to two different operative breakage mechanisms, the exoclastic coarse fragments with a small difference in size and the endoclastic fine particles. The fines were mainly produced from the region around the cones of impact and from the fracture surfaces.

Mullier et al (1991) investigated the agglomerate attrition of sand particles bound with polyvinylpyrrolidone through both fluidised bed measurement and oblique impact of single agglomerates. Their study showed that the agglomerate attrition during

fluidisation occurs mainly by oblique impaction. The breakdown of agglomerates is also seen to be quite different from that of solid particles. The debris produced by the oblique impact of a single agglomerate with a rough wall was seen to consist of very small particles resulting from the removal of single particles from the agglomerate surface. The shape of the agglomerates after impact was largely unchanged. It was suggested that the attrition process of agglomerates was analogous to abrasive wear and the rate of material removal was found to be proportional to the reciprocal of the critical stress intensity factor K_c of the material, where K_c is the material strength parameter introduced from fracture mechanics.

A study of the agglomerate breakage in polymer-flocculated suspensions was carried out on kaolin particles by Ray and Hogg (1987). Flocculated with a non-ionic polyacrylamide, their experimental measurements of floc size distributions in agitated suspensions showed that floc breakage was consistent with the simple first-order size reduction model. They also investigated the effects of system variables. It was found that the specific rate of breakage decreases rapidly with increasing polymer dosage, indicating that the floc strength is improved substantially by the addition of flocculant. It was also found that the specific rate of breakage generally increased with agitation speed. However, because of the sensitivity of the back calculation approach used to evaluate the breakage rates and primary breakage distributions, the confidence intervals of the estimated parameters were rather broad.

2.2.4 Discussion

Generally speaking, little progress has been made in understanding the controlling physical and chemical mechanisms involved in the attrition and comminution of either porous agglomerates or solid particles. Consequently, the characterization of material degradation, friability, prediction of breakage rates and determination of

daughter particle/cluster size distributions and fractal dimensions rely largely on practical experience gained from experiments rather than basic principles. Studies of single particle/agglomerate breakdown have been mainly based on the continuum mechanics approach which only allows for the prediction of the critical stress at which the material fails and does not permit the characterization of the fractal geometry of the daughter particles/clusters. Besides, it seems that under different controlled conditions, the assessments of the degradation are not quite in agreement with each other (Knight and Bridgwater 1985). The mass-balance model used extensively in the laboratory grinding mill is in fact a scale-up black-box approach in which the mechanisms of particle/agglomerate break-up in a grinding mill are not directly taken into consideration. Apart from the sensitivity of the breakage parameters to measurement errors, predicting the effects on the breakage parameters and energy requirements of changes in the feeding particles/agglomerates, operating system, control velocities and additive liquids still remains a problem.

2.3 Agglomerate strength

Agglomerate strength is of concern in a number of industries. In the processing industry, for example, where agglomeration is required to promote containment and flowability of fine particles and powders, agglomerate strength serves as a direct assessment of the attrition resistance and coalescence propensity of the agglomerates. In some other industries such as ceramics, however, because agglomerates inhibit sintering and act as defects and flaws, understanding and controlling the agglomerate strength is crucial to obtain the required breakdown and dispersion of agglomerates.

2.3.1 Rumpf's model

The strength of agglomerates mainly depends on the strength of the bond force between particles. Early studies on agglomerate strength are based on the analysis of fairly simple particle assemblies of mono-disperse and regular packings. Rumpf (1962) studied agglomerate strength and derived an expression for the tensile strength of agglomerates with regular packing structures. Assuming that (a) all particle bonds are due to van der Waals' attractive forces, (b) the bonds along the fracture plane are ruptured simultaneously upon tensile failure, and (c) the strength of all these bonds are the same for each contact, Rumpf obtained the tensile strength σ for a mono-disperse system as,

$$\sigma = \frac{1.1\phi P_c}{4(1-\phi)R^2} \tag{2.11}$$

where ϕ is the volume fraction of the assembly, R is the radius of the constituent primary particles and P_c is the van der Waals' attractive force between the constituent particles, which, in terms of the Hamaker constant A (Hamaker 1937), is given by equation 2.1,

Rumpf's model of agglomerate strength was also extended to moist agglomerates by Schubert (Schubert 1975, 1977; and Schubert et al 1975). The tensile strength of wet agglomerates in the capillary state where all pores are filled with liquid was assumed to be given by,

$$\sigma = p\theta_l \tag{2.12}$$

where θ_l is the degree of liquid saturation and p is the capillary pressure.

In the pendular state where only a small quantity of liquid is held between contiguous particles, the bonding forces between particles is considered as mainly due

to the meniscus attractive force of liquid bridges. The tensile strength of the moist agglomerate in the pendular state is then given by substituting the van der Waals' force in equation 2.11 with the pendular liquid bridge force given by Fisher's toroidal approximation.

In the funicular state which is between the pendular state and capillary state, both liquid bridges and pores filled with liquid are present in the moist agglomerates. As a result, both the bridge bond force and the capillary pressure may contribute to the strength of the moist agglomerate. Schubert et al (1975) assumed that the agglomerate strength is the superimposition of the bonding mechanisms of the pendular liquid bridge forces and the capillary pressure of the pore liquid.

2.3.2 Cheng's model

Cheng (1968) proposed a different model relating the tensile strength of an agglomerate to its packing density and interparticle forces. Assuming the contact area per unit fracture area as A_c and the bonding force per unit contact area as $f(S)$, the tensile strength was expressed as,

$$\sigma = A_c f(S) \tag{2.13}$$

The overall contact area of fractured bonds per unit area was related to the packing structure and density by,

$$A_c = \frac{1}{2} f_n f_a Z \frac{A_p \rho}{V_p \rho_p} \tag{2.14}$$

where the $\frac{1}{2}$ is introduced to allow for the random directions of each contact bond, f_n is the ratio of the number of particle contact pairs per unit area to the number of pairs per unit volume, f_a is the ratio of the real contact area per particle pair to the

surface area per particle, Z is the coordination number, A_p is the mean surface area per particle and $V_p(S)$ is the mean volume per particle.

The separation distance of the bonds between the contiguous particles was also related to the packing density,

$$S = S_0 - \frac{2R}{3}(\frac{\rho}{\rho_0} - 1) \tag{2.15}$$

where S_0 is the effective range over which the interparticle attractive forces act and ρ_0 is the corresponding density of the packing at the relative separation of S_0 when the attractive force vanishes.

Recently, Hartley and Parfitt (1985a, 1985b) developed another model which formulated the overall contact area per unit fracture area in equation 2.13 differently. Assuming that in a unit fracture area there are n_f contact bonds between particles with the attractive forces randomly directed between $\pm\frac{\pi}{2}$ and the contact area of each contact bond is A_{cp}, the overall contact area per unit fracture area was given as,

$$A_c = \frac{1}{2} n_f A_{cp} \tag{2.16}$$

Using an empirical relationship between the coordination number Z and the packing density given as,

$$Z \approx \frac{3}{1 - \rho/\rho_s} \tag{2.17}$$

they obtained the following expression for the number of contact bonds in a unit fracture area as,

$$n_f = \frac{9(2R + S)\rho/\rho_s}{8\pi R^3(1 - \rho/\rho_s)} \tag{2.18}$$

where ρ is the density of the packing and ρ_s is the density of the constituent particles.

Arguing that with fine particles, the distance of contact bonds between contiguous particles will vary from a state where asperities are in contact to a state where not all particles make actual physical contact but interparticle forces act, Hartley and Parfitt proposed a simple geometric relationship for the contact area of each bond,

$$A_{cp} = \pi R(S_0 - S) \tag{2.19}$$

where S_0 is the effective separation distance between particles when the bond force reduces to zero.

Substituting equations 2.18 and 2.19 into equation 2.16, Hartley and Parfitt (1985a) derived the tensile strength as,

$$\sigma = \frac{9(2R + S)(S_0 - S)(\rho/\rho_s)}{16R^2(1 - \rho/\rho_s)} f(S) \tag{2.20}$$

for which the separation distance between adjacent particles is also related to the packing density in a different empirical equation,

$$S = 2R[(\frac{0.74\rho_s}{\rho})^{1/3} - 1] \tag{2.21}$$

Both of the models developed by Cheng (1968) and Hartley and Parfitt (1985a) require a knowledge of S_0 and ρ_0 which, as defined above, are obtained from experimental data by extrapolation. As a result, the models are in fact semi-empirical. Based on Cheng's theory of equation 2.13, Chan et al (1983) also derived an expression for the tensile strength of binary powder packings. However, instead of requiring a knowledge of S_0, the model used the 'reduced tensile strength', which also needs to be determined experimentally.

2.3.3 Fracture mechanics approach

A common assumption in all the above agglomerate strength theories is that all inter-particle bonds in the fracture plane are ruptured simultaneously upon failure. It is also implicitly assumed that values of the separation distance between contiguous particles and the attractive forces of all contact bonds are uniformly distributed. This is only theoretically possible for mono-disperse regular packings. For random packings, however, both photoelastic experiments (De Josselin de Jong and Verruijt 1969, and Drescher and De Josselin de Jong 1972) and computer simulated experiments (Cundall and Strack 1979b, and Thornton and Barnes 1986) have showed that the distribution of contact forces is random. There are chains of large contact forces formed by a very small number of contact bonds; other contact forces are relatively small. Apparently, not only the simultaneous failure assumption does not apply, but also the bond forces are not uniformly distributed. Horwatt et al (1989) measured the tensile strength of carbon-black agglomerates in diametrical compression experiments. They used the experimental data to calculate the effective Hamaker constant according to the model of Hartley and Parfitt (1985a) and predicted an order of magnitude decrease.

Considering that particulate materials do not fail by instantaneous formation of new surfaces but by fracture through a process of crack propagation, Adams (1985) applied theoretical fracture mechanics to predict the strength of agglomerates and showed that the tensile strength of perfectly elastic material, given as,

$$\sigma = \frac{K_c}{c^{1/2} Z} \tag{2.22}$$

can be modified to give the tensile strength of particulate solids by the following equation,

$$\sigma = \frac{K_c}{(c + c_Z)^{1/2} Z} \tag{2.23}$$

where K_c is the so-called stress intensity factor which has been tabulated for various initial crack geometries and can be fitted by experimental tests, c is the geometrical size of the initial crack length, cz is the corrected nominal crack length accounting for the inherent flaw size of agglomerates and Z is a dimensionless parameter which depends on the geometry of the specimen and the crack.

For particulate materials, the critical stress intensity factor K_c is an intrinsic material property related to the inter-particle bond forces (Mullier et al 1987, 1991; Adams et al 1989; and Adams, Williams and Williams 1989). Some experimental measurements of the stress intensity factor for agglomerates made of sand, polyvinylpyrrolidone (PVP) and glass ballotini were made by Adams (1985) and Mullier et al (1987). It was found that the stress intensity factor of these materials increases with increase in the inter-particle bond strength.

The shortcoming of the fracture mechanics model for the strength of agglomerate is that the strength parameter is not directly related to the interparticle bonding forces. Instead, it needs to be determined experimentally using, for example, three-point bend tests. As Adams (1985) pointed out, a fracture mechanics description for the strength of agglomerates depends on the development of suitable equations relating the stress intensity factor to the inter-particle bond forces and energy losses due to the bond breakage and local plastic deformations.

An alternative approach, also based on the fracture mechanics, was developed by Kendall (1988) which assumed that at the macroscopic level, an agglomerate was a continuous block of material which behaves like a perfect elastic, brittle solid but contains a flaw of length c. In this case, the agglomerate strength is given by equation 2.22 and the stress intensity factor is given as,

$$K_c^2 = \frac{G_a E_a}{1 - \nu_a^2} \tag{2.24}$$

where G_a is the critical strain energy release rate for crack propagation to occur and E_a and ν_a are the ensemble Young's modulus and Poisson's ratio of the agglomerate. Kendall (1988) then attempted to relate the effective Young's modulus and Poisson's ratio to the interface energy by assuming that the agglomerate assembly of spherical particles of radius R deforms elastically under stress because of the compliance of the contact bonds. For dry powders (without binder) of titanium dioxide, alumina, silica, and zirconia, Kendall (Kendall 1987, Kendall et al 1987) derived the following relationship for the effective Young's modulus of the assembly in terms of the primary particle properties,

$$E_a = 17.1\phi^4(\frac{E^2\gamma}{2R})^{1/3} \tag{2.25}$$

where E is the Young's modulus of the constituent particles, γ is the interfacial energy of the contact bonds. ϕ and R are volume fraction and particle radius as defined before.

The critical strain energy release rate was also derived as,

$$G_a = 56\phi^4(\frac{\gamma_c^5}{4E^2R^2})^{1/3} \tag{2.26}$$

where γ_c was derived from measurements to be higher than γ and was defined as the fracture energy.

In principle, the fracture energy γ_c can be directly related to the interfacial energy γ although the plastic deformation near the fracture crack also contributes to the fracture energy losses. However, Kendall (1988) was not able to formulate an expression for the fracture energy γ_c in terms of the interfacial energy γ. Instead, he presented some experimental data for several materials (titanium dioxide and alumina). It is seen again, apart from the questionable assumption that agglomerates are, at the macroscopic level, continuous elastic and brittle materials, Kendall's model

still depends on the development of suitable equations for the stress intensity factor in relation to the interfacial energy of the individual particle bonding forces and geometric factors associated with particle packing.

2.3.4 Discussion

For granular systems like agglomerates, inter-particle forces are significant in determining their properties and behaviour. Traditional theoretical analyses of agglomerate strength are based on the assumption of fairly simple regular packings of mono-disperse systems. For real agglomerates, however, very little is known about the quantitative inter-particle forces and the packing geometries. The fracture mechanics approach, on the other hand, considers agglomerates, at the macro-level, as continuous media containing flaws. Knowledge about the effect of interparticle bond strength and packing geometry, as well as particle properties, on the macro-agglomerate fracture strength is lacking. Especially when one considers the wide range of different properties of agglomerates from mono-disperse to poly-disperse and from dry systems to moist systems, the traditional theoretical analyses and the fracture mechanics approaches to the strength of agglomerates seem to be over idealized. Determination of the agglomerate properties of strength and deformability still relies mainly on real experimental measurements.

2.4 Computer simulation

2.4.1 Discrete element method

Agglomerates are examples of complex and redundant particulate assemblies. It has been shown that most traditional experimental and analytical studies on agglomer-

ation, degradation and strength of agglomerates either ignore the internal contact bonds and geometrical structures or consider only very simple systems of monodisperse and regular packings. Because of the difficulty of measuring the internal quantities such as porosity, stress, and velocity, little information is known about what actually happens internally and how the internal quantities affect the handling and processing behaviour of particle materials. Current understanding of the processes of agglomeration, attrition and comminution of particulate assemblies is mainly obtained from empirical and statistical interpretations. The theories are always inaccurate, insufficient, incomplete and lack direct quantitative verifications.

In the case when the traditional approach of experimental and analytical investigations is restricted by the complexity and redundancy of particle systems, computer simulation offers the unique opportunity to obtain a better understanding of the microscopic mechanisms of particulate materials. With the computer simulation approach, each constituent particle of the granular assembly is monitored through the computation of its trajectories and interactions with others. The macroscopic behaviour of the simulated particle system is directly related to the internal microscopic interaction mechanism of individual particles.

Computer simulation of particulate materials is a fairly recent development which started in the 1970s. There have been several computer programs reported in the literature, e.g. by Cundall (1971, 1978), Cundall and Strack (1979a, 1979b), Walton (1983), and Campbell and Brennen (1985a, 1985b). According to the different ways in which the interparticle interactions are handled, the computer models are classified as rigid (hard) and soft particle models (Walton 1984). For rigid particle models, the collision between constituent particles is modelled as instantaneous. The application of the rigid sphere models has been mainly concerned with the modelling of rapid flows of granular materials such as Couette flow, inclined chute flow and shear flow (Campbell and Brennen 1985a, 1985b; and Campbell and Gong 1986).

The soft particle model differs from the rigid particle model in that it simulates the interparticle collision as a process taking place in a finite time duration. By employing appropriate interaction laws, the interparticle contact and bond forces are computed according to the distance of relative approach between the contiguous particles. Cundall (1971, 1978) pioneered the soft particle approach to computer simulation. A numerical technique, known as as the Distinct Element Method (DEM) was developed to simulate soils composed of discrete discs (Cundall 1978, Cundall and Strack 1979b).

Originally, the DEM program was designed to study the micromechanics of quasi-static granular systems and to aid in the development of constitutive relationships for soils, e.g. Cundall and Strack (1979a), Cundall (1988), Cundall et al (1989), Thornton (1987a, 1987b, 1989) and others (Bathurst and Rothenburg 1988; Jenkins et al 1989; Thornton and Barnes 1986; and Ting et al 1989). However, it has also been applied to the simulation of both quasi-static and dynamic particle systems. Walton (1983) applied the soft particle model to simulate the inclined chute flow of particulate materials. An application of modelling hopper flow was also presented by Thornton (1992).

2.4.2 Computer simulated agglomerate collisions

In principle, the methodology used by the soft particle model of DEM may be applied to the simulation of many problems related to particle systems in process engineering. Technologically, however, applying the DEM technique to this area requires appropriate interaction laws to be incorporated to account for the various bonding and adhesion mechanisms that play a dominant role in holding micron and/or submicron sized particles together. When the DEM computer program BALL (2D) and TRUBAL (3D) were first developed by Cundall and Strack (Cundall 1978; Cundall

and Strack 1979a, 1979b), only very simple models for the normal and tangential elastic deformation forces of the contacting spheres was considered. They used linear springs to model the contact stiffnesses of the elastic deformation. Dashpots were introduced to damp out the kinetic energy of the system in order to simulate the quasi-static particulate systems. Although the theories of Hertz and Mindlin and Deresiewicz (1953) were also implemented into the DEM program to simulate the elastic contact deformation forces more realistically (Thornton and Randall 1988, Randall 1989, Walton and Braun 1985), little effort has been made to implement various bond forces between particles into the DEM program until recently.

The DEM program of Cundall was recently modified and enhanced by Yin (1992) and Thornton and Yin (1991) to perform computer simulated experiments of agglomerate collisions. New algorithms were developed and implemented in the Aston versions of BALL and TRUBAL to model the surface adhesion forces and elastic deformation forces of particles. BALL and TRUBAL are two dimensional (2D)and three dimensional (3D) DEM computer programs originally developed by Cundall and Strack (Cundall 1978, Cundall and Strack 1979a). For the interaction force between two contiguous spheres, the theory of JKR, Johnson et al (1971), was used to compute the normal component and the theory of Thornton (1991) was applied to calculate the tangential component. The JKR theory was extended from the Hertz theory by including the surface adhesion force into the normal elastic deformation force. The theory of Thornton combines the previous work of Savkoor and Briggs (1977) and Mindlin and Deresiewicz (1953) in order to model the tangential compliance force in the presence of adhesion.

Computer simulated two dimensional agglomerate impact with a wall was performed by Yin (1992) and others (Thornton, Kafui and Yin 1993). The simulated 2D agglomerates consisted of 1000 monodisperse primary particles. Three types of behaviour were observed. At high impact velocities, the agglomerate was shattered

with most of the bonded contacts between particles broken. At moderate impact velocities, the agglomerate was fractured in a semi-brittle manner. At low impact velocities, it was observed that the agglomerate bounces off the wall with very few single particles or small clusters broken off; no significant fracture or crack damage occurred to the agglomerate. The threshold velocity below which no significant damage occurred was shown to be exponentially dependent on the surface energy γ, a measure of the interparticle bond strength of the primary particles due to surface adhesion. The impact velocity at which the transition from shattering breakup to semi-brittle fracture occurred was also found to be related to the interfacial surface energy by an exponential relationship.

From the computer simulated impacts of 2D monodisperse agglomerates, it was observed that crack initiation and propagation was preceded by local plastic deformation as a consequence of contact sliding between contiguous particles. At high impact velocities, because the plastic deformation zone is extensive, there is no clear crack formation. Instead, the agglomerate was shattered mostly into singlets and small clusters. At moderate impact velocities, however, the plastic deformation zone was confined to a small zone near the contact between agglomerate and the platen. Crack initiation was observed to take place in the plastic deformation zone. It was difficult to predict the direction of the cracks because of the random force transmission within the agglomerate.

Yin (1992) also performed computer simulated diametrical compression tests on the same 2D agglomerate by crushing it between two parallel platens. The results showed that at high platen velocities, extensive plastic deformation and crushing were produced in the agglomerate. At low platen velocities, however, semi-brittle failure was observed in which cracks were initiated in the agglomerate near to the platens and propagated inwards towards the centre. The maximum force the agglomerate could sustain was shown to be dependent on the nominal strain-rate. Higher strain-

rates generated higher platen forces and the relationship was linear. The diametrical compression tests were compared with the impact tests and reasonable agreement was obtained for the damage ratio in terms of applied velocity or input energy.

Some results of a computer simulated 3D agglomerate impacting orthogonally with a wall were presented by Thornton and Kafui (Thornton and Kafui 1992; Thornton, Kafui and Yin 1993; Kafui and Thornton 1993). The agglomerate consisted of 7912 mono-disperse particles arranged in a face-centred cubic packing. The computer graphics visualisation of the fracture/fragmentation of the agglomerate showed good qualitative agreement with the real experimental results reported by Arbiter et al (1969). They identified a threshold velocity below which no significant damage occurred to the agglomerate. The threshold velocity was found to be dependent on the contact bond strength, packing geometry, agglomerate size and impact angle. The particle size distributions of the fragmentation clusters produced by the simulated impacts were compared with published data and showed good general agreement.

At the micro-level, Thornton and Kafui (1992) examined the damage that occurred to the agglomerate due to the collisions. It was found that during a simulated impact, the number of broken contacts initially increases rapidly until a constant value is reached. The damage ratio of the agglomerate was shown to be logarithmically related to the impact velocity. However, in order to establish the relationship between the macro agglomerate fracture/fragmentation behaviour and the micro packing geometry as well as the interparticle bond strength, more work is necessary to examine the effect of primary particle properties, packing structures and many other factors.

It has been demonstrated that the computer program TRUBAL can be used to simulate a wide range of problems relating to particle systems, including agglomerate collisions. Further work is desirable to modify and enhance the computer program by incorporating various interparticle bonding forces such as liquid bridge forces in order to model particle systems more realistically. Computer programs that model

different shaped particles are also needed.

2.5 Summary

Agglomeration and attrition/comminution are closely related problems in process engineering during the handling and processing of fine particulate materials. They both depend on the strength of agglomerates. Most previous studies have been concerned either with very simple systems of mono-disperse regular packings or carried out in very complex experimental conditions. The mechanisms of agglomerate coalescence, attrition, comminution and their dependence on agglomerate strength have not been correlated with the micro-level packing geometry, interparticle bond forces and particle properties. The application of computer simulation, using the the DEM technique, to the modelling of particle systems in process engineering is a very recent development and hence is still at the rudimentary stage. Most current DEM computer programs only handle assemblies of spherical particles. For the interaction force between particles, only the elastic deformation force, surface adhesion force and tangential friction force have been accounted for. The need is apparent to develop computer programs that handle different particle shapes and incorporate different interparticle interaction forces, such as the liquid bridge attraction forces, crystal sintering forces and plastic deformation forces. These forces may greatly affect agglomerate strength and hence the coalescence and fragmentation behaviour.

Chapter 3

Interparticle force of adhesive spheres

In this chapter we discuss the theory of contact forces interacting between two adhesive spherical particles, that is, the van der Waals' intermolecular adhesive force which acts along the line of centres of the particles and the reactive contact force due to the elastic deformation of the solid particles under load. For the condition of normal loading, the Hamaker (1937) theory for rigid spheres is presented and is followed by the theories of Johnson et al (1971) (JKR) and Derjaguin et al (1975) (DMT). For the oblique loading of elastic spheres, the theories of Savkoor and Briggs (1977) and Thornton (1991) are discussed.

3.1 Adhesion force between rigid spheres

Adhesive forces exist between micron or sub-micron sized particles and are mainly attributed to the London-van der Waals's attractive potential between individual atoms or molecules in contiguous bodies. At the micro-level, the intermolecular interactive energy between two molecules may be given as,

$$U_p = -\frac{\lambda}{r^6} \tag{3.1}$$

where λ is the London-van der Waals' constant and r denotes the distance between the two atoms or molecules.

For macroscopic particles, the adhesive force between them is explained by pairwise addition of the intermolecular interactive energy between individual atoms. This adhesive force may be significant if the particles are of micron or submicron size. Hamaker (1937) first applied the London-van der Waals' theory to compute the overall adhesive force between spherical particles. In his calculation, the intermolecular interactive energy between two similar particles was expressed as,

$$U = -\int_{V_{p1}} \int_{V_{p2}} \frac{q^2 \lambda}{r^6} dV_{p1} dV_{p2} \tag{3.2}$$

where V_{p1} and V_{p2} are the total volumes of the two particles and q is the number of atoms or molecules contained in a unit volume of the particles.

By integration, Hamaker (1937) obtained the intermolecular interactive energy between two spheres at small separation distance S as,

$$U = -\frac{AR^*}{6S} \tag{3.3}$$

from which the overall adhesion force was obtained as,

$$P_a = \frac{\partial U}{\partial S} = \frac{AR^*}{6S^2} \tag{3.4}$$

where the two spheres are assumed to be rigid and $A = \pi^2 q^2 \lambda$ is the Hamaker constant and its numerical value has been quoted in the range of $0.01 - 200 \times 10^{-19} J$. The parameter R^* is the relative radius of the two spheres which, for two spheres of radii R_1 and R_2, is defined by the following expression,

$$\frac{1}{R^*} = \frac{1}{R_1} + \frac{1}{R_2} \tag{3.5}$$

Tabor and Winterton (1969) and Israelachvili and Tabor (1972) performed direct experimental measurements of the forces between solid surfaces of cylindrical sheets of mica at separations below $10^3 \mathring{A}$. They found that the unretarded van der Waals attractive forces could be expressed as,

$$F_u = \frac{AR^*}{6S^2} \tag{3.6}$$

which is obviously of the same form as equation 3.4.

For retarded van der Waals attractive forces, the expression was, however, given in the following different form,

$$F_r = \frac{2\pi A_r R^*}{3S^3} \tag{3.7}$$

where A_r is the retarded Hamaker constant.

Generally speaking, the attractive force between micron or submicron particles becomes relevant if the separation distance is $\sim 10^3 \mathring{A}$. One problem with the Hamaker equation 3.4 is that the attractive force tends to infinity when the separation distance approaches zero. In practice, however, when the relative separation between particles

reduces below a certain value, the roughness of the surfaces becomes significant. Besides, the repulsive force between particles may also become significant to balance the attractive adhesion force.

On the other hand, other researchers describe the interactive adhesion force between solids in a different way. Johnson (1976) argued that arising from the competing forces of attraction and repulsion between the individual atoms or molecules in both bodies, the variation of force per unit surface area as a function of separation is represented by a law of the form

$$p = -A_a S^{-n} + B_r S^{-m} \qquad (m > n) \tag{3.8}$$

where A_a and B_r are two constants of attraction and repulsion respectively. When the two ideally flat solid surfaces come into atomic contact, they will have an equilibrium separation S_0. At separations less than S_0 the surfaces will repel each other and at separations greater than S_0 they will attract. On this basis, a tensile force—which equals the adhesion force in magnitude—has to be exerted to separate the surfaces and the work done in separating the surfaces is defined as the surface energy that each surface possesses, thus the interface energy, Γ, is defined as,

$$\Gamma = \gamma_1 + \gamma_2 - \gamma_{12} = \int_{S_0}^{\infty} p dS = \frac{(m-n)A_a}{(n-1)(m-1)S_0^{n-1}} \tag{3.9}$$

where γ_1 and γ_2 are the surface energies of the two surfaces and γ_{12} is the energy of interface. In the case of like solids, γ_{12} is conventionally zero.

Since $m > n$, the short-range repulsive forces do not appreciably affect the overall force when it is attractive. If the repulsive force is ignored then, as shown in figure 3.1, the attractive force (dashed line) is essentially the same as the solid line, which represents the overall attractive force, at most separations. Consequently, integration of equation 3.9 can be further simplified. Such a formulation was given by Tabor

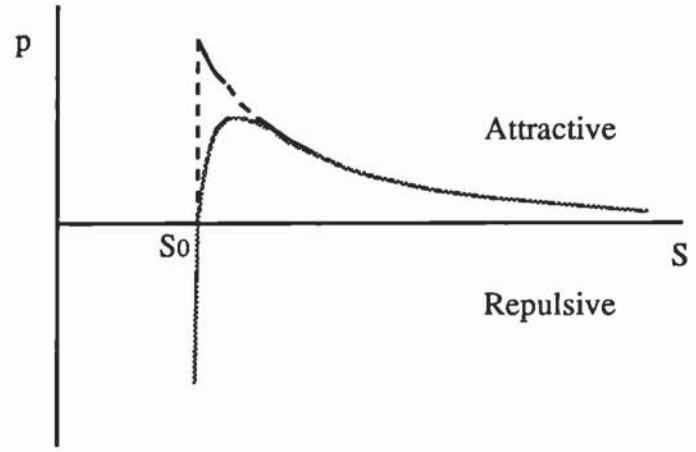

Figure 3.1: Pure attractive (dashed line) and overall (solid line) interactive surface forces as a function of separation between ideal surfaces.

(1977) who assumed the attractive force per unit area between two parallel flat plates to be,

$$p = \frac{A}{6\pi S^3} \tag{3.10}$$

and obtained

$$\Gamma = \gamma_1 + \gamma_2 - \gamma_{12} = \frac{A}{12\pi S_0^2} \tag{3.11}$$

Substituting equation 3.11 into 3.4, we obtain another expression for the adhesion force between two spheres at equilibrium separation, given as,

$$P_c = 2\pi R^* \Gamma = 2\pi R^* (\gamma_1 + \gamma_2 - \gamma_{12}) \tag{3.12}$$

or, if both spheres are of the same material, $\gamma_1 = \gamma_2 = \gamma$ and $\gamma_{12} = 0$,

$$P_c = 4\pi\gamma R^* \tag{3.13}$$

This was first derived by Bradley (1932).

3.2 Normal loading of adhesive elastic spheres

More realistically, for solid particles in contiguous contact, both elastic and plastic deformations will take place around the contact region of the particles due to the attractive and repulsive forces between the atoms in the solids. The elastic and plastic deformation, on the other hand, will in turn affect the adhesive forces. Therefore, the reciprocal influence of the contact deformation and intermolecular interactive force between particles should be considered.

Some theoretical studies about the reciprocal influence between the contact deformation and surface adhesion of elastic spheres were represented by Johnson et al (1971) (JKR theory) and Derjaguin et al (1975) (DMT theory). The JKR model considers not only the effect of particle elastic deformation on the adhesion force but also the influence of the adhesion force on the elastic deformation. The model assumes that the surface adhesion acts only over the deformed contact area which is larger than the Hertzian area. It also assumes an equivalent elastic load which would create that same contact area. Based on the two assumptions, the surface adhesion force was included in the extended Hertzian theory which is in line with the theory of contact mechanics. Alternatively, the DMT model, as suggested by Derjaguin et al (1975), considers the intermolecular adhesive force both inside and outside the deformed contact area. However, the theory assumes that the van der Waals's adhesive force does not affect the deformation of the spheres, and only takes into account the effect of elastic deformation on the adhesion force. As a result, the reciprocal influence of the particle deformation and intermolecular adhesion is decoupled. Therefore, both the

JKR and DMT models are approximations. The two theoretical models are discussed below.

3.2.1 JKR theory

The JKR (Johnson et al 1971) theory is extended from the Hertzian model to adhering elastic spheres. For two elastic spheres with no surface adhesion, the classical Hertzian theory shows that, under a normal load P, the contact radius a between the two spheres is related to the normal load by the following relationship,

$$a^3 = \frac{3PR^*}{4E^*} \tag{3.14}$$

and the corresponding relative approach of the two spheres, α, is given as,

$$\alpha = \frac{a^2}{R^*} \tag{3.15}$$

where R^* is the relative radius as already defined by equation 3.5 and E^* is the relative Young's modulus related to the elastic properties, E_1, E_2 and ν_1, ν_2, of the two spheres by the following expression,

$$\frac{1}{E^*} = \frac{1-\nu_1^2}{E_1} + \frac{1-\nu_2^2}{E_2} \tag{3.16}$$

Now if the two spheres are adhesive, an additional attractive force will apparently act between the two contact spheres. Johnson et al (1971) argued that because of the additional attractive adhesion force, the equilibrium contact area between the two spheres would increase and it could be regarded as corresponding to an equivalent Hertzian force P_1,

$$a^3 = \frac{3P_1R^*}{4E^*} \tag{3.17}$$

However, as it will be shown later, this equivalent Hertzian force P_1 is not simply the sum of the applied load and the adhesion force. Johnson et al (1971) derived an expression for the out-of balance applied load in relation to the adhesion force through an energy balance approach. It is argued that because of the additional attractive force of adhesion, the total energy of the system U_t is increased which Johnson et al (1971) assumed as being made up of three components: the increment of the stored elastic energy U_e due to the increased elastic deformation, the released surface energy U_s due to adhesion over the contact area and the increment of the mechanical energy U_m due to the applied load. The three components were formulated as,

$$U_e = (\frac{3}{4E^*})^{2/3}\frac{1}{3(R^*)^{1/3}}[\frac{1}{5}P_1^{5/3} + P^2P_1^{-1/3}] \tag{3.18}$$

$$U_s = -2\pi\gamma(\frac{3R^*P_1}{4E^*})^{2/3} \tag{3.19}$$

$$U_m = -(\frac{3}{4E^*})^{2/3}\frac{P^2}{3(R^*)^{1/3}}[P_1^{-1/3} + 2P_1^{-1/3}] \tag{3.20}$$

where γ is the surface energy of the spheres.

The equilibrium condition requires that the first derivative of the total energy $U_t(= U_e + U_s + U_m)$ with respect to the equivalent Hertzian load P_1 becomes zero. This leads to the following expression for the equivalent Hertzian load,

$$P_1 = P + 6\pi\gamma R^* \pm \sqrt{(P + 6\pi\gamma R^*)^2 - P^2} \tag{3.21}$$

It can be shown that for stable equilibrium it is necessary to take the positive sign so that

$$P_1 = P + 6\pi\gamma R^* + \sqrt{(P + 6\pi\gamma R^*)^2 - P^2} \tag{3.22}$$

The corresponding radius of the contact area is

$$a^3 = \frac{3R^* P_1}{4E^*} = \frac{3R^*}{4E^*}[P + 6\pi\gamma R^* + \sqrt{(P + 6\pi\gamma R^*)^2 - P^2}] \tag{3.23}$$

Rearranging equation 3.23, we obtain the expression for the applied load of adhering spheres in terms of the contact radius as

$$P = \frac{4E^* a^3}{3R^*} - \sqrt{16\pi\gamma E^* a^3} \tag{3.24}$$

Thus equation 3.24 provides an explicit expression for the applied out-of-balance force for the adhering spheres in terms of the radius of the contact area and the surface energy. It is, however, still incomplete without knowing the pressure distribution over the contact area. Johnson (1976) argued that this problem could be solved theoretically by combining the adhesion force with the principles of contact mechanics. He provided a distribution of normal traction over the contact area that is described by the following equation,

$$p(r) = \frac{3P_1}{2\pi a^2}(1 - \frac{r^2}{a^2})^{1/2} - \frac{P_1 - P}{2\pi a^2}(1 - \frac{r^2}{a^2})^{-1/2} \tag{3.25}$$

According to the classical elasticity theory (see Johnson 1985), the first term of equation 3.25 leads to a normal displacement over the contact area as,

$$u_i^{(1)} = \frac{3(1 - \nu_i^2)P_1}{8E_i a^3}(2a^2 - r^2) \tag{3.26}$$

and the second term of equation 3.25 leads to a uniform normal displacement over the contact area,

$$u_i^{(2)} = -\frac{(1 - \nu_i^2)(P_1 - P)}{2E_i a} \tag{3.27}$$

where $i = 1$, or 2.

Here, the underlying assumption is that, in line with contact mechanics, the profiles of the two surfaces in the contact region can be adequately described by the Hertzian approximation and the surface displacement is the combination of the Hertzian solution that corresponds to the first term of equation 3.25 and the uniform displacement that corresponds to the second term of equation 3.25. Thus, the relative approach of the two sphere may be derived as,

$$\alpha = u_1^{(1)} + u_2^{(1)} + u_1^{(2)} + u_2^{(2)} + \frac{r^2}{2R^*} = \frac{3P_1(2a^2 - r^2)}{8E^*a^3} - \frac{P_1 - P}{2E^*a} + \frac{r^2}{2R^*} \tag{3.28}$$

Substituting P_1 (equation 3.23) and P (equation 3.24) into equation 3.28, we derive the relative approach as a function of the radius of the contact area as follows,

$$\alpha = \frac{a^2}{2R^*} - \sqrt{\frac{4\pi\gamma a}{E^*}} \tag{3.29}$$

Equation 3.24 indicates that, when the applied force $P = 0$, the radius of the contact area decreases to a finite value given by,

$$a^3{}_{(P=0)} = \frac{9\pi\gamma(R^*)^2}{E^*} \tag{3.30}$$

In order to further decrease the contact area, the applied force needs to be made negative. However, a real solution may ensue only if the negative load (i.e. the applied load is a pulling force) is in the critical limit of,

$$P \geq -3\pi\gamma R^* \tag{3.31}$$

Johnson et al (1971) assumed that separation of the two spheres takes place when the applied negative force reaches the critical value,

$$P = -P_c = -3\pi\gamma R^* \tag{3.32}$$

where P_c is termed as the pull-off force. At the critical load $P = -P_c$, the corresponding radius of the contact area is further decreased to the following finite value,

$$a_c^3 = \frac{3R^* P_c}{4E^*} \tag{3.33}$$

and the relative approach between the two spheres is given as,

$$\alpha_c = -\left[\frac{4P_c^2}{3(E^*)^2 R^*}\right]^{1/3} + \left[\frac{9P_c^2}{16(E^*)^2 R^*}\right]^{1/3} \tag{3.34}$$

which is obviously negative.

After the applied force reaches the critical value $P = -P_c$, further decrease of the contact area is still possible. This happens when the two spheres are further pulled apart and corresponds to the non-equilibrium state at which the negative sign of equation 3.21 is taken. At the non-equilibrium state, the applied force slightly increases but is still negative. Separation of the two spheres is assumed to have taken place when $\partial\alpha/\partial a = 0$, i.e.

$$\frac{a}{R^*} - \left(\frac{\pi\gamma}{E^* a}\right)^{1/2} = 0 \tag{3.35}$$

from which the radius of the contact area at separation is derived as,

$$a_s^3 = \frac{P_c R^*}{12E^*} \tag{3.36}$$

Substituting a_s into equations 3.21 and 3.29, we derive the corresponding applied force and relative approach as follows,

$$P_s = -\frac{5}{9}P_c \tag{3.37}$$

$$\alpha_s^3 = -\frac{3P_c^2}{16(E^*)^2 R^*} \tag{3.38}$$

Finally, with the JKR model, the force-displacement relationship is implicitly expressed by equations 3.29 and 3.24. Differentiating both equations with respect to the radius of the contact area a, we obtain,

$$\frac{d\alpha}{da} = \frac{a}{R^*} - \sqrt{\frac{\pi\gamma}{E^* a}} \tag{3.39}$$

$$\frac{dP}{da} = \frac{4E^* a^2}{R^*} - 6\sqrt{\pi\gamma E^* a} \tag{3.40}$$

Thus, by using the chain law, the normal stiffness of two contact spheres with adhesion can be expressed as,

$$k_n = \frac{dP}{d\alpha} = 2E^* a \frac{3 - 3\sqrt{P_c/P_1}}{3 - \sqrt{P_c/P_1}} \tag{3.41}$$

which degenerates to the Hertzian form in the case of no surface adhesion ($P_c = 0$).

3.2.2 DMT model

Derjaguin et al (1975) made an alternative attempt to take into account the effect of contact deformation (due to the Hertzian load) on the adhesion force of spherical particles. They, however, assumed that the intermolecular attractive force between the two solid spheres did not appreciably change the deformation of the particles. Consider two elastic spheres of radii R_i and properties E_i, ν_i ($i = 1, 2$) under a normal load P. According to the theory of Hertz, the distribution of the normal pressure over the contact area, when no surface adhesion force acts, is described as,

$$p_H = \frac{3P_H}{2\pi a^2}\sqrt{1 - r^2/a^2} \qquad 0 < r < a \tag{3.42}$$

where a is the radius of the contact area which is related the applied Hertzian load,

$$a^3 = \frac{3P_H R^*}{4E^*} \tag{3.43}$$

The relative approach of the two spheres $\alpha = \alpha_1 + \alpha_2$ is given as,

$$\alpha_i = \frac{a^2}{R_i} \tag{3.44}$$

In accordance with the Hertzian distribution p_H, the deformation (the displacement of the surfaces) inside and outside the contact area of the two spheres is given as,

$$w_i(r) = \frac{3(1-\nu_i^2)P_H}{8E_i a^3}(2a^2 - r^2) \qquad r \leq a \tag{3.45}$$

$$w_i(r) = \frac{3(1-\nu_i^2)P_H}{4\pi E_i a^3}[2a\sqrt{r^2 - a^2} + (2a^2 - r^2)\arccos(1 - \frac{2a^2}{r^2})] \quad r > a \tag{3.46}$$

where $i = 1$ or 2.

According to equation 3.45, it appears that at the coordinate origin $r = 0$, the deformation is,

$$w_i(r = 0) = \alpha_i = \frac{3(1-\nu_i^2)P_H}{4E_i a} \tag{3.47}$$

Comparing equation 3.44 and 3.47 we obtain,

$$\frac{1}{R_i} = \frac{3(1-\nu_i^2)P_H}{4E_i a^3} \tag{3.48}$$

When this relationship is substituted into expression 3.45 and 3.46, it follows that,

$$w_i(r) = \frac{1}{2R_i}(2a^2 - r^2) \qquad r \leq a \tag{3.49}$$

ASTON UNIVERSITY
LIBRARY AND
INFORMATION SERVICES

$$w_i(r) = \frac{1}{\pi R_i}[2a\sqrt{r^2 - a^2} + (2a^2 - r^2)\arccos(1 - \frac{2a^2}{r^2})] \quad r > a \tag{3.50}$$

where $i = 1$ or 2.

Derjaguin et al (1975) argued that at the microlevel, the distance between the two contact surfaces is not equal to zero, but a value of ε which depends on the roughness of the material. Therefore, the separation distance between the two deformed surfaces is given as,

$$z = \frac{r^2}{2R^*} + w_1 + w_2 - \alpha + \varepsilon \tag{3.51}$$

Substituting equation 3.49 into 3.51 we obtain the separation distance over the contact area as,

$$z = \varepsilon \qquad r \leq a \tag{3.52}$$

Outside the contact area of Hertzian load the separation distance between the two surfaces is,

$$z = \frac{1}{\pi R^*}[a\sqrt{r^2 - a^2} - (2a^2 - r^2)\arccos\frac{a}{r}] + \varepsilon \qquad r > a \tag{3.53}$$

The interactive surface energy may be expressed as,

$$U_s = \int_0^\infty 4\pi\gamma(z)rdr \tag{3.54}$$

Over the contact surface $z = \varepsilon$, the corresponding part of the free surface energy is given as,

$$U_{si} = 2\pi a^2\gamma(\varepsilon) = 2\pi\alpha R^*\gamma \tag{3.55}$$

Outside the contact area, the integral 3.54 has been shown to equal,

$$U_{so} = 4\pi \int_a^\infty \gamma(z) r dr \tag{3.56}$$

which, by substituting $\bar{r}^2 = r^2 - a^2$, may be rearranged as

$$U_{so} = 4\pi \int_0^\infty \gamma[z(\bar{r}, a)] \bar{r} d\bar{r} \tag{3.57}$$

where

$$z(\bar{r}, a) = \frac{1}{\pi R^*}[a\bar{r} + (\bar{r}^2 - a^2) \arctan \frac{\bar{r}}{a}] + \epsilon \tag{3.58}$$

To obtain the adhesion force, Derjaguin et al (1975) expressed the adhesion force between the two elastic spheres as the derivative of the interactive surface energy with respect to the relative approach α,

$$P_a = \frac{dU_s}{d\alpha} = \frac{dU_{si}}{d\alpha} + \frac{dU_{so}}{d\alpha}$$

$$= 2\pi\gamma R^* + 4\pi \int_0^\infty \frac{\partial \gamma(z)}{\partial z} \frac{\partial z}{\partial \alpha} \bar{r} d\bar{r} \tag{3.59}$$

The second term of the equation cannot be expressed analytically.

The applied out-of-balance force due to adhesion and Hertzian elastic deformation is thus expressed as,

$$P = P_H - P_a = \frac{4E^* a^3}{3R^*} - 2\pi\gamma R^* - 4\pi \int_0^\infty \frac{\partial \gamma(z)}{\partial z} \frac{\partial z}{\partial \alpha} \bar{r} d\bar{r} \tag{3.60}$$

For the case when the two spheres are just touching, i.e. $\alpha \rightarrow 0^+$, it follows from equation 3.58 that

$$z\Big|_{\alpha\to 0} = \frac{\bar{r}^2}{2R^*} + \varepsilon \tag{3.61}$$

$$\frac{\partial z}{\partial \alpha}\Big|_{\alpha\to 0} = -\frac{1}{2} \tag{3.62}$$

Substituting equations 3.61, 3.62 into equation 3.59 we obtain the pull-off force as,

$$P_c = P_a\,|_{\alpha=0} = 2\pi\gamma R^* + 2\pi\gamma R^* = 4\pi\gamma R^* \tag{3.63}$$

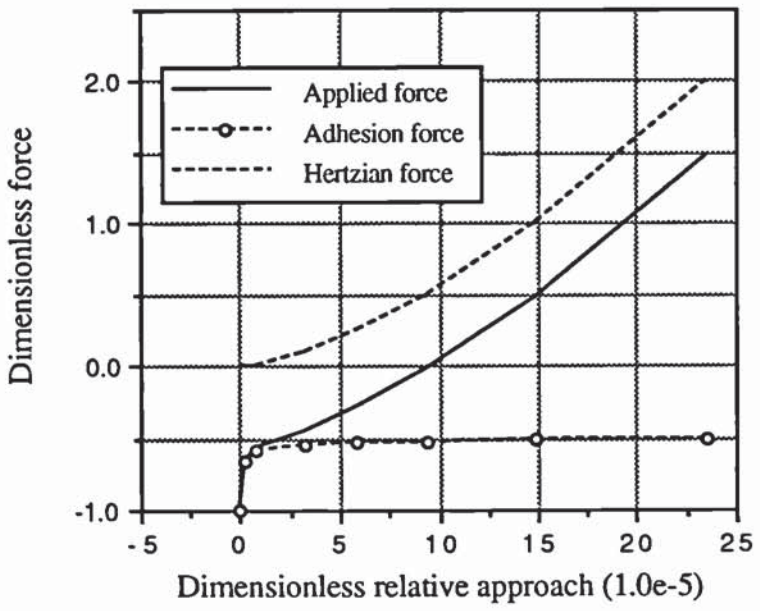

Figure 3.2: Force-displacement relationships of DMT model in comparison with the Hertzian theory. The forces are made dimensionless to $P_c = 4\pi\gamma R^*$ and the displacement is made dimensionless to R^*

For a finite approach α between two spheres, the adhesion force has to be obtained numerically. Figure 3.2 shows the dependence of the numerically obtained adhesion force (made dimensionless to $4\pi\gamma R^*$) on the relative approach (made dimensionless to R^*. Together with the adhesion force is shown the applied out-of-balance force

(also made dimensionless to $4\pi\gamma R^*$) and the Hertzian force. As shown by figure 3.2, it is surprising to see that the DMT model predicts an adhesion force which first decreases dramatically and then converges to a constant value, which is half of the pull-off force, as the flattening at the contact of the two spheres increases. This trend of the adhesion force is contrary to the normal expectation that an increase in the relative approach will result in an increase of the adhesion force because the contact area increases.

3.2.3 Discussion

As far as the JKR and DMT models are concerned, they are both approximations. The JKR model considers the adhesive forces between spheres as pure surfaces forces which stitch the two surfaces together if they are in close proximity contact but snaps when they are separated. Consequentially, the adhesive force is assumed to act only on the contact area. In order to conform with the principles of contact mechanics, the adhesive traction distribution was conceived in the form of

$$p_a = p_0'(1 - \frac{r^2}{a^2})^{-1/2} \tag{3.64}$$

where p_0' was given by Johnson (1976) as,

$$p_0' = \frac{P_1 - P}{2\pi a^2} \tag{3.65}$$

Figure 3.3a illustrates pressure distributions of the attractive force, the equivalent Hertzian force and overall contact force according to the JKR model. This distribution of the contact traction has two main problems. The first problem is the sharp discontinuity at the edge of the contact area. Consequently, the outer annulus at the perimeter of the contact area involves large strains and classical elasticity cannot be

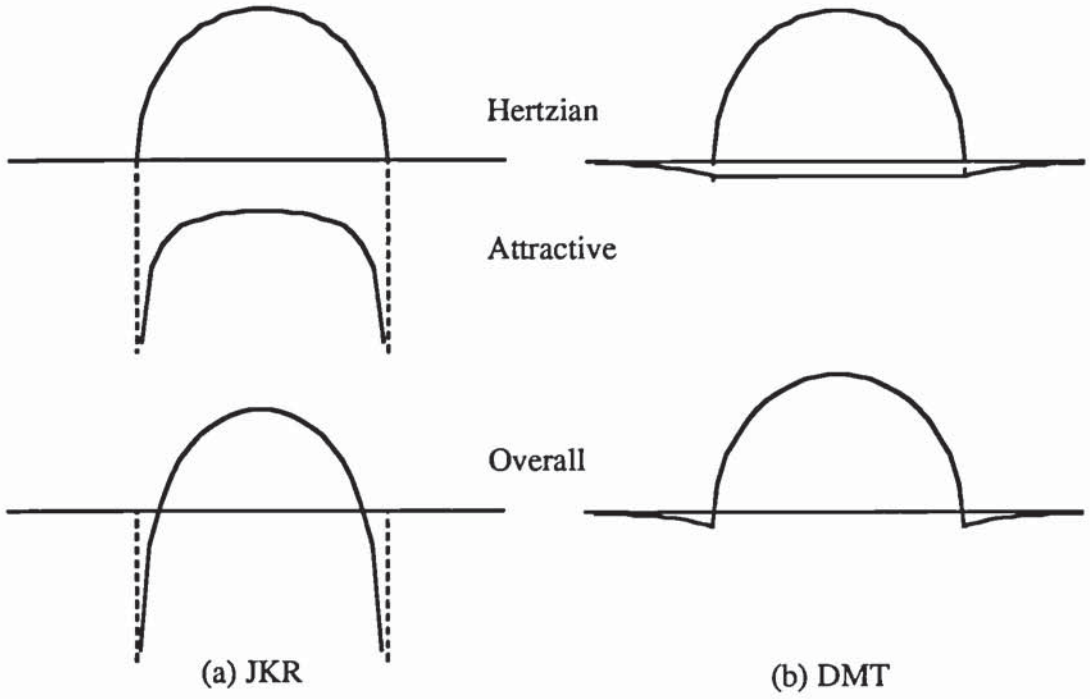

Figure 3.3: The normal traction distribution assumed by (a) the JKR theory and (b) the DMT theory

strictly applied. Tabor (1977) argued that in practice there would be some rounding off at the sharp discontinuity region because the stress at the region could not exceed the limiting attractive forces that the interface can withstand. The second problem is the inconsistency between the proposed attractive force distribution and the classical assumption of interactive surface adhesions. In order to keep the adhesion mechanism in line with the principles of contact mechanics, the JKR model assumed that the intermolecular attractive force could be approximated by a pure surface force that operates in an infinitely short range of separations and is important within the immediate contact area. On this basis, one would normally expect a constant attractive force distribution over the contact area since the separation is constant and the surface property of the material is also uniformly distributed. However, the JKR model assumed a non-uniform pressure distribution of the attraction force given in the form

of equation 3.64.

It has been indicated earlier that for two undeformable flat half-spaces of two parallel solid bodies that come into atomic contact, the variation of the force arising from the competing forces of attraction and repulsion is usually represented by a law of the form as given by equation 3.8. This form of surface interaction law should still hold for elastic deformable solids if the intermolecular interactive forces can be envisaged as pure surface forces. In these circumstances, it is clear that for two elastic spheres, the adhesion force inside the contact area has to be uniformly distributed and outside the contact area the adhesion force must be also significant over a finite range. On this basis, it seems that the approach of the DMT model should be more appropriate. The pressure distribution of the adhesion of the DMT model was considered in the form as shown by figure 3.3b. However, with the DMT model the quantitative expression of the adhesive force distribution is still not available. Apart from that, the most serious problem is that the DMT model predicts an adhesion force that first drops dramatically when the relative approach slightly increases from the point contact.

Some critical discussions about the JKR and DMT models were given by Tabor (1977, 1978) and Derjaguin et al (1978). Tabor (1977) showed that according to the experimental results of mica glued surfaces of glass cylinders, the shape of the deformed interface and the way in which the surfaces separate were more consistent with the analysis of the JKR model rather than the DMT theory. Abandoning the hypothesis that adhesion forces do not change the Herzian profile, Muller et al (1980, 1983) made a modification to the DMT model by considering the pressure distribution being in the following special form of equation 3.8,

$$p(r) = \frac{A}{6\pi S_0^3}\left[(\frac{S_0}{z(r)})^9 - (\frac{S_0}{z(r)})^3\right] \tag{3.66}$$

where A is the Hamaker constant, S_0 is the equilibrium separation distance between surfaces and $z(r)$ is the local separation distance between the two profiles of the two spheres. According to equation 3.9, the interfacial surface energy corresponding to equation 3.66 may be obtained as

$$\Gamma = \frac{A}{16\pi S_o^2} \tag{3.67}$$

A general analysis of the contact of two elastic spheres subjected to the Lennard-Jones pressure given by equation 3.66 has been carried out numerically by Muller et al (1980). It has been shown that, as far as the pull-off force is concerned, the more general solution is a continuous transition from the DMT to JKR theory and is determined by the parameter μ which is defined as,

$$\mu = \frac{8}{3\pi^2}\left[\frac{A^2R^*}{4S_0^7(E^*)^2}\right]^{1/3} = \frac{32}{3\pi}\left[\frac{\Gamma^2R^*}{\pi S_0^3(E^*)^2}\right]^{1/3} \tag{3.68}$$

For $\mu \ll 1$ (hard solids of small radius and low surface energy) the solution corresponds to the DMT theory. For $\mu \gg 1$ (soft solids, large radius and high surface energy) the JKR theory is valid.

Horn et al (1987) pointed out that the exact solution to the contact problem of two adhering elastic spheres is very difficult because the deformation of the spheres that determines the interactive surface depends also on the pressure distribution of the adhesion force. Maugis (1992) has more recently studied the adhesion interaction between a sphere and a planar substrate using a fracture mechanics approach. He demonstrated that the JKR theory corresponds to the formulae of a spherical punch in linear fracture mechanics. For the case of two spheres in contact, the pressure distribution is,

$$p' = \frac{2E^*a}{\pi R^*}\left(1-\frac{r^2}{a^2}\right)^{1/2} - \frac{K_I}{\sqrt{\pi a}}\left(1-\frac{r^2}{a^2}\right)^{-1/2} \tag{3.69}$$

where K_I is the stress intensity factor defined as,

$$K_I = -\frac{E^*}{\sqrt{\pi a}}\left(\alpha' - \frac{a^2}{2R^*}\right) = \sqrt{2\Gamma E^*} \tag{3.70}$$

and α' is the relative approach due to p'.

For the JKR pressure distribution, singularity appears when $r \rightarrow a$. In order to cancel the stress singularity at the tip of the crack, Maugis (1992) assumed that the intermolecular Lennard-Jones potential outside the contact area as a constant pressure p'' (attractive) applied on a length $d = c - a$. This constant pressure is then considered to be equivalent to an external axisymmetric crack of neck radius a in an infinite solid, for which the stress distribution over the neck (i.e. the contact area) is derived as,

$$\sigma = \frac{p''}{\pi a}\left(\sqrt{c^2 - a^2} + \frac{c^2}{a}\arccos\frac{a}{c}\right)\left(1 - \frac{r^2}{a^2}\right)^{-1/2} - \frac{2p''}{\pi}\arctan\sqrt{\frac{c^2 - a^2}{a^2 - r^2}} \tag{3.71}$$

Introducing a stress intensity factor K_m defined as,

$$K_m = \frac{p''}{\sqrt{\pi a}}\left(\sqrt{c^2 - a^2} + \frac{c^2}{a}\arccos\frac{a}{c}\right) \tag{3.72}$$

the stress distribution of equation 3.71 can be also written as,

$$\sigma = \frac{K_m}{\sqrt{\pi a}}\left(1 - \frac{r^2}{a^2}\right)^{-1/2} - \frac{2p''}{\pi}\arctan\sqrt{\frac{c^2 - a^2}{a^2 - r^2}} \tag{3.73}$$

for which a singularity also appears if $r \rightarrow a$.

Adding equations 3.69 and 3.73 we see that the stress singularity at the edge of the contact area disappears if,

$$K_I = K_m = \frac{p''}{\sqrt{\pi a}}\left(\sqrt{c^2 - a^2} + \frac{c^2}{a}\arccos\frac{a}{c}\right) = \sqrt{2\Gamma E^*} \tag{3.74}$$

This equation relates the length $d = c - a$ of the constant attractive force to the material property of spheres.

Using the Dugdale (1960) model, Maugis (1992) formulated the energy release rate equation by the J-integral method and derived that, at equilibrium, the interfacial energy Γ is related to the constant pressure p'' by the following equation,

$$G = \Gamma = \frac{p''a^2}{\pi R^*}[\sqrt{m^2-1} + (m^2-2)\arctan\sqrt{m^2-1}]$$

$$+\frac{4(p'')^2 a}{\pi E^*}[\sqrt{m^2-1}\arctan\sqrt{m^2-1} - m + 1] \tag{3.75}$$

where $m = c/a$.

Letting,

$$\lambda_p = 2p''\left[\frac{9R^*}{16\pi\Gamma(E^*)^2}\right]^{1/3} \tag{3.76}$$

we may rewrite equation 3.75 as,

$$1 = \frac{\lambda_p a^2}{2}\left[\frac{4E^*}{3\pi\Gamma(R^*)^2}\right]^{2/3}[\sqrt{m^2-1} + (m^2-2)\arctan\sqrt{m^2-1}]$$

$$+\frac{4\lambda_p^2 a}{3}\left[\frac{4E^*}{3\pi\Gamma(R^*)^2}\right]^{1/3}[\sqrt{m^2-1}\arctan\sqrt{m^2-1} - m + 1] \tag{3.77}$$

This relation plus equation 3.74 fixes the values of $m = c/a$, p'' and λ^p as functions of the material properties of E^*, R^* and Γ.

Due to the cancellation of the stress intensity factor K_m with K_I, the overall pressure distribution of the attractive and repulsive force over the contact area is $p = p' + \sigma$, which, according to equations 3.69 and 3.73, may be given as,

$$p = \frac{2E^* a}{\pi R^*}\left(1 - \frac{r^2}{a^2}\right)^{1/2} - \frac{2p''}{\pi}\arctan\sqrt{\frac{c^2 - a^2}{a^2 - r^2}} \qquad r \leq a \tag{3.78}$$

Outside the contact area there is a constant attractive pressure p'',

$$p = -p'' \qquad a < r \leq c \tag{3.79}$$

From the overall pressure distribution the applied load and relative approach can be further derived as follows,

$$P = \frac{4E^*}{3R^*}a^3 - \lambda_p a^2\left[\frac{16\pi\Gamma(E^*)^2}{9R^*}\right]^{1/3}(\sqrt{m^2-1} + m^2\arctan\sqrt{m^2-1}) \tag{3.80}$$

$$\alpha = \frac{a^2}{2R^*} - \frac{4\lambda_p a}{3}\left(\frac{3\pi\Gamma}{4E^*R^*}\right)^{1/3}\sqrt{m^2-1} \tag{3.81}$$

When $\lambda_p \to 0$, $m = c/a \to \infty$ and it can be derived from equation 3.77 that,

$$\lambda_p m \to 0 \tag{3.82}$$

$$\lambda_p m^2 = \frac{4}{\pi a^2}\left[\frac{3\pi\Gamma(R^*)^2}{4E^*}\right]^{2/3} \tag{3.83}$$

Thus equations 3.80 and 3.81 may be simplified as,

$$P = \frac{4E^*}{3R^*}a^3 - 2\pi\Gamma R^* \tag{3.84}$$

$$\alpha = \frac{a^2}{2R^*} \tag{3.85}$$

This is simply the Hertz curve shifted by $2\pi\Gamma R^*$. When the radius of the contact area approaches zero ($a \to 0$), we get the DMT result.

On the other hand, when $\lambda_p \to \infty$, we get $m = c/a \to 1$ and the following relationships (from equation 3.77),

$$\sqrt{m^2-1}+m^2\arctan\sqrt{m^2-1}=2\arctan\sqrt{m^2-1}\simeq 2\sqrt{2(m-1)} \tag{3.86}$$

$$\lambda_p^2(m-1)=\frac{3}{4a}\left[\frac{3\pi\Gamma(R^*)^2}{4E^*}\right]^{1/3} \tag{3.87}$$

Substituting equations 3.86 and 3.87 into 3.80 and 3.81, we get,

$$P=\frac{4E^*a^3}{3R*}-\sqrt{8\pi\Gamma E^*a^3} \tag{3.88}$$

$$\alpha=\frac{a^2}{2R^*}-\sqrt{\frac{2\pi\Gamma a}{E^*}} \tag{3.89}$$

which are the JKR equations.

Maugis (1992) pointed out that the parameter λ_p is similar to the parameter μ (equation 3.68) as introduced by Muller at al (1980). If we assume that the attraction pressure is a function of the Lennard-Jones potential,

$$p''=1.03\frac{\Gamma}{S_o} \tag{3.90}$$

we see that,

$$\lambda_p=0.4\mu \tag{3.91}$$

Thus, the analytical solution of Maugis (1992) represents more general conditions and depends on the parameter λ_p. When $\lambda_p \rightarrow 0$ (hard solids of small radius and low surface energy), the solution degenerates to the Hertz curve but shifted by $2\pi\Gamma R^*$. When $\lambda_p \rightarrow \infty$ (soft spheres of large radius and high surface energy), the solution reduces to the JKR theory.

3.3 Oblique loading of adhesive elastic spheres

3.3.1 The theory of Savkoor and Briggs

The oblique loading of two elastic spheres in the presence of adhesion is an even more complicated problem. A rigorous analysis accounting for both the non-linear response of the tangential force and the coupled effect of the surface interaction and deformation is almost intractable. An approximate analysis, however, was first given by Savkoor and Briggs (1977). They extended the JKR model to account for the effect of oblique loading by arguing that with adhesion the tangential shear traction distribution over the contact area could be prescribed by the 'no-slip' solution of Mindlin (1949),

$$q(r) = \frac{T}{2\pi a}(a^2 - r^2)^{-1/2} \qquad r \leq a \tag{3.92}$$

The corresponding tangential force T in relation to the tangential displacement δ is given by,

$$T = 8G^* a\delta \tag{3.93}$$

and the stiffness is,

$$k^t = 8G^* a \tag{3.94}$$

where G^* is related to the elastic properties of the two spheres G_1, G_2 and ν_1, ν_2 by the following expression,

$$\frac{1}{G^*} = \frac{2-\nu_1}{G_1} + \frac{2-\nu_2}{G_2} \tag{3.95}$$

Savkoor and Briggs (1977) assumed that due to the application of the tangential force T, the mechanical potential energy is $-T\delta$ and the elastic energy is $T\delta/2$. Consequently, the addition of the tangential force reduces the potential energy of the system by an amount of

$$U_T = -\frac{1}{2}T\delta = -\frac{T^2}{16G^*a} \tag{3.96}$$

Recalling equations 3.18–3.20, we obtain the total potential energy of the system as,

$$U = U_e + U_s + U_m + U_T$$

$$= \frac{1}{15}\left[\frac{9}{16(E^*)^2R^*P_1}\right]^{1/3}(P_1^2 - 5PP_1 - 5P^2 - 30\pi\gamma R^*P_1 - \frac{5E^*}{4G*}T^2) \tag{3.97}$$

Thus, equilibrium of the system ensues when $\partial U/\partial P_1 = 0$ which leads to the following expression for the equivalent Hertzian force,

$$P_1 = P + 6\pi\gamma R^* \pm \sqrt{(P + 6\pi\gamma R^*)^2 - P^2 - \frac{E^*}{4G^*}T^2} \tag{3.98}$$

The stable solution requires the positive sign. If $P_c = 3\pi\gamma R^*$, it follows that,

$$P_1 = P + 2P_c + (4PP_c + 4P_c^2 - \frac{E^*}{4G^*}T^2)^{1/2} \tag{3.99}$$

for which the radius of the contact area is expressed as,

$$a^3 = \frac{3R^*}{4E^*}[P + 2P_c + (4PP_c + 4P_c^2 - \frac{E^*}{4G^*}T^2)^{1/2}] \tag{3.100}$$

Equation 3.100 indicates that as the tangential force T increases, the contact area is reduced in a stable manner. This was suggested by Savkoor and Briggs (1977) as a

'peeling' mechanism which they claimed was verified by experimental data. Savkoor and Briggs also suggested that the 'peeling' process continues until the tangential force T reaches a critical value, given by the equation

$$T_p = 4\sqrt{\frac{G^*}{E^*}(PP_c + P_c^2)} \tag{3.101}$$

and the corresponding radius of the contact area is reduced to,

$$a_p^3 = \frac{3R^*}{4E^*}(P + 2P_c) \tag{3.102}$$

If T exceeds T_p, there is no real solution to both the equations 3.99 and 3.100. Savkoor and Briggs (1977) argued that at this stage the rate of elastic energy release is more rapid than the rate at which the work of adhesion can absorb the energy and hence the quasi-static approach is no longer adequate.

3.3.2 The theory of Thornton

One question about the model of Savkoor and Briggs (1977) is what happens next? Besides, another very important fact that Savkoor and Briggs ignored is the interparticle sliding. Since the critical 'peeling' force is not related to the friction coefficient, it is possible that long before the 'peeling' process is completed, the tangential force T may exceed the limiting value given by the sliding criterion. For adhesive elastic spheres, Thornton (1991) suggested that the sliding criterion could be given as,

$$T \leq \mu(P + 2P_c) \tag{3.103}$$

where μ is the friction coefficient of the material.

By quoting the experimental data reported by Briscoe and Kremnitzer (1979), Thornton (1991) indicated that the sliding rule is comparable with the other two

criteria proposed by Kendall (1986) and Barquins et el (1977) respectively. The sliding criterion of Kendall (1986) reads as,

$$T \leq \mu P_1 = \mu(P + 2P_c + \sqrt{4PP_c + 4P_c^2}) \tag{3.104}$$

Thornton (1991) also suggested an alternative criterion in the following form,

$$T \leq \mu P_1 (1 - \frac{P_1 - P}{3P_1})^{3/2} \tag{3.105}$$

Figure 3.4 shows the sliding criterion using equation 3.103 in comparison with the critical 'peeling' failure criterion of equation 3.101, where the normal and tangential forces are both made dimensionless to the pull-off force $P_c = 3\pi\gamma R^*$. The two curves intersect when the normal load reaches,

$$P_2 = 2P_c \left[(\frac{4G^*}{\mu^2 E^*} - 1) \pm \sqrt{\frac{4G^*}{\mu^2 E^*}(\frac{4G^*}{\mu^2 E^*} - 1)} \right] \tag{3.106}$$

As is shown by figure 3.4, in the region $P < P_2$ the tangential force at the end of peeling is greater than that necessary for sliding. Consequently, the other question to be answered is whether the tangential force is allowed to violate the sliding rule before it reaches the 'peeling' failure criterion.

Thornton (1991) re-examined the oblique loading problem of two adhesive elastic spheres. He suggested if $P < P_2$ the tangential force at the end of 'peeling' falls to the value of the sliding force. For $P > P_2$, it is suggested that there is a smooth transition from peeling to sliding. This implies that when $T = T_p$, the contact area given by equation 3.102 is subject to an equivalent Hertzian normal traction corresponding to an effective normal force $P_e = (P + 2P_c)$ or $P_e = P_1(1 - \frac{P_1 - P}{3P_1})^{3/2}$. It then follows that the situation of the tangential force is well disposed to the micro-slip proposition of Mindlin and Deresiewicz (1953). In other words, it is assumed that the peeling is

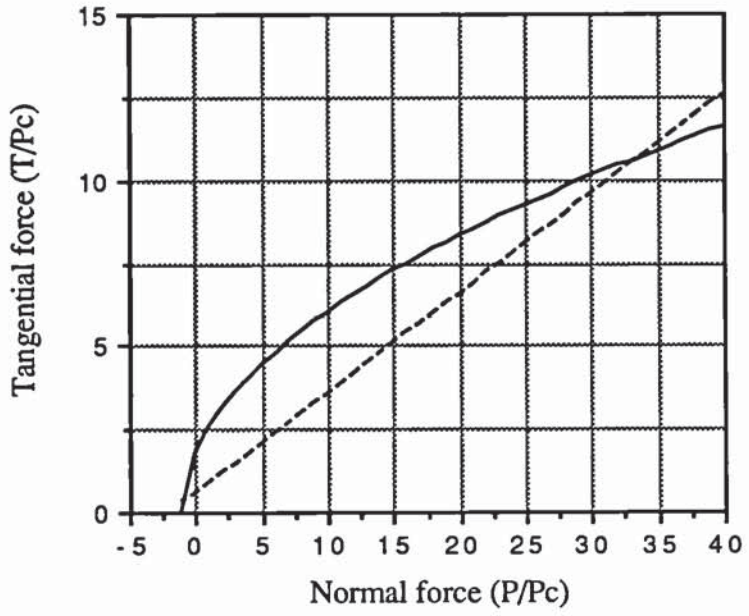

Figure 3.4: Comparison of the peeling failure criterion (solid line) defined by equation 3.99 and sliding criterion (broken line) defined by equation 3.101

followed by the development of a slip annulus which spreads radially inwards until the tangential force reaches the sliding criterion. Therefore, for monotonic loading of the tangential force with $T > T_p$, the equation of the partial solution of Mindlin and Deresiewicz (1953) can be written as,

$$T = \mu(P_e)\left[1 - (1 - \frac{16G^*a}{3\mu(P_e)}\delta)^{3/2}\right] \tag{3.107}$$

and the corresponding radius of the slip annulus is,

$$c_0 = a\sqrt[3]{1 - \frac{T}{\mu(P_e)}} \tag{3.108}$$

where δ represents the relative tangential displacement at the contact between the two spheres.

If the tangential force is unloading-reloading and/or the normal force is changing, the analysis of the history dependent tangential force loading-unloading-reloading is

much more complicated. Based on the theory of Mindlin and Deresiewicz (1953), the tangential stiffness after 'peeling' was obtained by Thornton and Randall (1988) and Randall (1989) as,

$$k_t = 8G^* c_j + (-1)^j \mu (1 - \frac{c_j}{a}) \frac{\Delta P_e}{\Delta \delta} \qquad j = 0, 1, 2 \tag{3.109}$$

where if $\Delta T / \Delta P_e < \mu$,

$$c_j = a \qquad j = 0, 1, 2 \tag{3.110}$$

Otherwise,

$$c_j = \begin{cases} a\sqrt[3]{1 - \frac{T + \mu \Delta P_e}{\mu P_e}} & j = 0 \\ \\ a\sqrt[3]{1 - \frac{(-1)^j (T - T_j) + 2\mu \Delta P_e}{2\mu P_e)}} & j = 1, 2 \end{cases} \tag{3.111}$$

where j = 0, 1, 2 denotes the path of loading, unloading and reloading respectively. The effect due to the variation of the normal force ΔP_e is taken into account by updating the T_j,

$$T_j = T_j - (-1)^j \mu \Delta P \tag{3.112}$$

Before the 'peeling' process is complete, the tangential force is given by Mindlin's 'no-slip' solution of equation 3.93 from which we can derive the stiffness as,

$$k_t = 8G^* a \tag{3.113}$$

Again, if there is no surface adhesion ($\gamma = 0$), the pull-off force P_c and the critical peeling force T_p both become zero and the expressions for the tangential stiffness and forces degenerates to the partial-slip solution of non-adhesive spheres provided by Mindlin and Deresiewicz (1953).

3.4 Energy dissipation

When two elastic spheres with adhesion collide with each other, they may bounce off or stick together, depending on whether the kinetic energy of the two collided spheres is greater than the energy required to break the contact. The energy required to break the contact of two adhesive spheres is regulated by the energy dissipation due to adhesive peeling, tangential slip and sliding.

The energy dissipation of adhesive peeling refers to the work required to pull two adhered spheres apart to create new surfaces. An expression was given by Yin (1992) where the energy dissipation was considered as the work done to pull the two spheres apart from the point that the two spheres come into contact. In the case of the JKR theory, this leads to the following expression for the energy dissipation of adhesive peeling,

$$W_p = \int_0^{\alpha_s} P d\alpha \tag{3.114}$$

where α_s is the critical relative approach where separation of the two adhered surfaces takes place. It is given by,

$$\alpha_s = -\sqrt[3]{\frac{27\pi^2\gamma^2 R^*}{16(E^*)^2}} = -\sqrt[3]{\frac{3P_c^2}{16(E^*)^2 R^*}} \tag{3.115}$$

Substituting equations 3.24 and 3.39 into 3.114, it follows that

$$W_p = \int_{a_0}^{a_s} \left(\frac{4E^* a^3}{3R^*} - 4\sqrt{\pi\gamma E^* a^3}\right)\left(\frac{a}{R^*} - \sqrt{\frac{\pi\gamma}{E^* a}}\right) da \tag{3.116}$$

where the contact area a_s at separation and a_0 when $\alpha = 0$ are given by,

$$a_s = \sqrt[3]{\frac{\pi\gamma(R^*)^2}{4E^*}} \tag{3.117}$$

$$a_0 = \sqrt[3]{\frac{4\pi\gamma(R^*)^2}{E^*}} \tag{3.118}$$

Thus, the energy dissipation due to adhesive peeling is obtained as,

$$W_p = \frac{2}{5}(12 + \sqrt[3]{2})\sqrt[3]{\frac{\pi^5\gamma^5(R^*)^4}{4(E^*)^2}}$$

$$= -\frac{4}{45}(1 + 6\sqrt[3]{4})P_c\alpha_s \simeq -0.9355P_c\alpha_s \tag{3.119}$$

For adhesive elastic spheres, energy dissipation may be also caused by the frictional slip and sliding after peeling due to the effect of tangential loading. In the context of the Thornton (1991) theory, if the applied tangential force is less than that required to cause rigid body sliding, it is to generate relative microslip. As demonstrated by Mindlin (1949), the microslip is initiated at the edge of the contact area and progresses inward until the tangential force reaches the sliding criterion. Consequently, energy is continuously dissipated as a result of this microslip.

Complete derivations of the frictional energy dissipation due to tangential slip and sliding are provided in appendix A. It has been shown that, if $(-1)^j\Delta T/\Delta P_e < \mu$, the energy dissipation due to partial slip is

$$\Delta W_{slip} = 0 \tag{3.120}$$

Otherwise, if $(-1)^j\Delta T/\Delta P_e > \mu$, the energy dissipation may be expressed as,

$$\Delta W_{slip} = \frac{\mu(P_e + \Delta P_e)[(-1)^j\Delta T - \mu\Delta P_e]}{16G^*c_j}[2 - \frac{3c_j}{a} + \frac{c_j^3}{a^3}] \tag{3.121}$$

where $j = 0, 1, 2$ refers to the path of loading, unloading and reloading, and c_j is again given by 3.110 or 3.111.

During sliding, the stored elastic energy is defined by,

$$\Delta W_e = \frac{3\mu^2 P_e \Delta P_e}{20 G^* a} \tag{3.122}$$

and hence, the frictional energy dissipation during sliding can be derived as,

$$\Delta W_{slide} = T\Delta\delta - \Delta A_e = \mu P_e(\Delta\delta - \frac{3\mu\Delta P_e}{20 G^* a}) \tag{3.123}$$

Chapter 4

Interparticle forces of moist spheres

This chapter is concerned with the cohesive forces exerted on particles by liquid bridges. The first part discusses the effect of a liquid on the cohesiveness of fine particles and the second part deals with the force and stability of a static liquid bridge held between two rigid spheres. In order to resolve the uncertainties in the rupture criterion of stable liquid bridges and the accuracy of the toroidal approximation, a simple numerical scheme for solving the Laplace-Young equation is described. For the viscous force of liquid bridges, the classical theory of lubrication flow is presented and is followed by the semi-infinite theory. Most of the work presented in this chapter has been reported by Lian, Thornton and Adams (1993b).

4.1 Cohesiveness of moist particles

For the particle size enlargement process of granulation, a binder liquid is usually mixed with the powders to increase their cohesiveness. When a liquid is mixed with micron and submicron sized particles, it may be present as either a mobile phase or an immobile adsorbed layer. The mobile liquid may exist in different forms described as pendular, funicular and capillary state respectively (shown by figure 4.1), depending on the degree of saturation of the system.

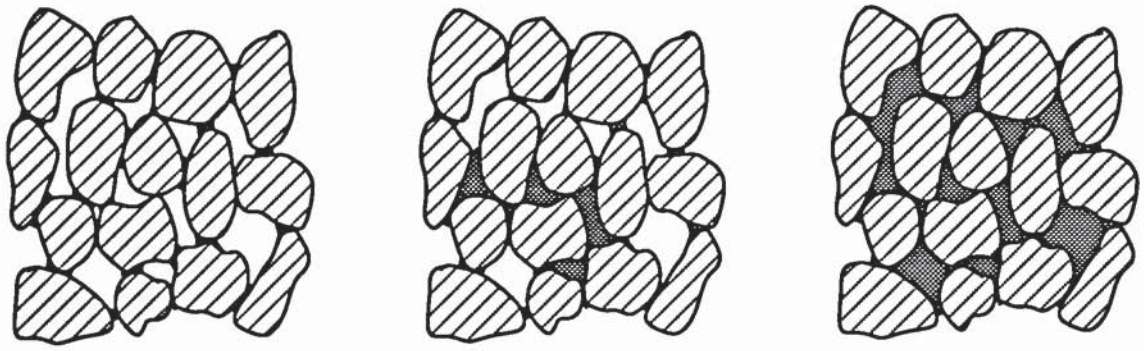

(a) Pendular state (b) Funicular state (c) Capillary state

Increasing liquid saturation

Figure 4.1: States of liquid presented in particle systems as the degree of saturation increases: (a) pendular state, (b) funicular state and (c) capillary state

For a small quantity of liquid that is uniformly dispersed in particle systems, the liquid is either adsorbed by the particle surfaces as immobile films or held between particles as pendular liquid bridges. This state is defined as the pendular state. By increasing the amount of liquid, we get the funicular state where in addition to the adsorbed liquid and pendular liquid bridges, some pores are also filled with the

excessive liquid. Further increase in the amount of liquid leads to the capillary state where all pores are completely filled with liquid.

Different states of the liquid phase in particle systems influence the cohesiveness of particles in different ways. Due to the adsorbed layer of liquid, the surface adhesion of the particles changes. For two solids 1 and 2 in the case of liquid immersion, the Dupré work of surface adhesion is given as (Adams and Edmondson 1987),

$$\Gamma = \gamma_{sl}^{(1)} + \gamma_{sl}^{(2)} - \gamma_{12} \tag{4.1}$$

where γ_{12} is the interfacial free surface energy which in the case of like solids is theoretically zero. The solid-liquid interfacial energy $\gamma_{sl}^{(i)}$ $(i = 1, 2)$ is related to the solid-liquid contact angle θ, liquid-vapour interfacial energy γ_{lv} and solid-vapour interfacial energy $\gamma_{sv}^{(i)} = \gamma_i$ by the Young's equation,

$$\gamma_{sl}^{(i)} = \gamma_i - \gamma_{lv} \cos\theta \tag{4.2}$$

where $i = 1, 2$. Substituting equation 4.2 into 4.1, we obtain the surface adhesion between two wetted solid surfaces as,

$$\Gamma = \gamma_1 + \gamma_2 - 2\gamma_{lv} \cos\theta - \gamma_{12} \tag{4.3}$$

Apparently, the surface adhesion force between wetted solids decreases due to the presence of the adsorbed liquid. In the case of like solids with perfect wetting (i.e. $\theta = 0$), there is no adhesion between the solids and hence Γ equals zero. The other case for spontaneous separation to occur is when

$$2\gamma_{lv} \cos\theta + \gamma_{12} > \gamma_1 + \gamma_2 \tag{4.4}$$

In the pendular state, liquid is mainly held between particles in the form of bridge necks, which produce resultant forces between particles. These forces arise from the capillary pressure deficiency of the liquid bridges, the surface tension and the viscous resistance of the liquid respectively. Since the pressure deficiency and surface tension only depend on the geometry of the liquid bridge, the combination of the two terms is quoted as the static liquid bridge force. The viscous resistance is however produced by the dynamic liquid bridge between relatively moving spheres. In the following sections, the static and dynamic liquid bridge forces are discussed.

4.2 Static liquid bridge forces and stability

4.2.1 Brief literature review

When a quantity of liquid is introduced at the contact point between two contiguous rigid solid spheres, a stable liquid bridge is formed which produces a resultant attractive force between the two spheres. This arises from a combination of two contributions, the effect of surface tension and the pressure deficiency generated by the curvature of the bridge, both dependent on the geometry of the liquid bridge. The geometry of a liquid bridge is dependent on the separation distance between the spheres and a liquid bridge will be stable when stretched up to some critical separation distance which will correspond to rupture. For relatively large liquid bridges, the geometry is influenced by the gravitational distortion. The effect of the gravity distortion has been addressed by Princen (1968) and recently investigated by Mazzone et al (1986), Bayramli et al (1987) and Bayramli and van de Ven (1987). Here we will be only concerned with small liquid bridges when the gravity effects and also the buoyancy force are negligible.

For a liquid bridge between two rigid solid spheres, when the effect of gravity is

negligible, the geometry is governed by the Laplace-Young equation which relates the mean curvature of the geometry to the pressure deficiency of the liquid. However, the Laplace-Young equation cannot be solved analytically except for a few special cases, Orr et al (1975). Numerical evaluation procedures have been developed by a number of workers, most notably by Erle et al (1971) and DeBisschop and Rigole (1982). They found that there were two solutions which converged to a single solution at a critical separation distance. For separation distances that exceeded this critical value, no solutions existed. It was conjectured that of the two solutions, the one with the minimum Gibbs' free surface energy was stable. It was also conjectured that the critical separation distance where the two solutions converged corresponded to the liquid bridge rupture. Erle et al (1971) suggested that if the two solutions were expressed in terms of the liquid bridge diameter, the critical separation distance corresponded to the point of rupture. DeBisschop and Rigole (1982) proposed an alternative criterion based on the minimum half-filling angle of the liquid bridge. The corresponding separation distance is less than the critical value at which the two solutions converge. More recently, Mazzone et al (1986) argued that it was the critical separation distance which was the correct rupture criterion.

The established approach for prescribing a stable solution to the Laplace-Young equation, if one exists, is to apply the calculus of variations to the Gibbs' free energy. The first variational problem, the necessary condition for a minimum surface free energy was formulated in different ways by Erle et al (1971) and DeBisschop and Rigole (1982). Both solutions are of the same form as the Laplace-Young equation. It is not clear which formulation is the correct one, because the second variation, the sufficient condition for a minimum surface free energy, which should provide the criterion for liquid bridge stability, has not been solved analytically.

It is now common practice to compare numerical solutions with the comprehensive set of experimental data obtained for a small liquid-solid contact angle by Mason and

Clark (1965). Erle et al (1971) and Mazzone et al (1986) obtained comparable force-separation results with constant liquid volumes which were consistent with Mason and Clark's data except at very small separation distances. Erle et al (1971) pointed out that there was some uncertainty in the experimental data in this region and that they obtained good agreement with other data measured by Cross and Picknett (1963) for spheres in contact. Mazzone et al (1986) made a detailed comparison of their calculated rupture distances with the experimental data of Mason and Clark (1965) and found that there was good agreement, while the rupture criterion due to DeBisschop and Rigole (1982) resulted in 25-30% underestimation.

Fisher (1926) proposed a much simpler approach for estimating the liquid bridge forces. It was based on a toroidal approximation which involved treating the meridional profile of the liquid-air interface as an arc of a circle. This leads to a simple closed-form solution which has been widely applied for the estimation of the forces between spherical bodies (eg. Mehrotra and Sastry 1980, Sherrington and Oliver 1981, Adams and Perchard 1985). The toroidal approximation has been shown to give good agreement with experimentally measured forces between two spheres and between a sphere and a plane in contact (Clark et al 1968). However, it has been claimed recently that there is an increasingly large underestimation as the separation distance increases (Mazzone et al 1986).

An important factor in the uncertainty of the accuracy of the toroidal approximation is the confusion regarding the way that the forces should be calculated. Previous workers have chosen to employ the liquid bridge geometry at either the neck or at the liquid bridge solid contact region (Hotta et al 1974). The now established 'correct' method has been stated by Princen (1968). However, since the toroidal approximation leads to a liquid bridge surface of non-constant mean curvature which is inconsistent with the Laplace-Young equation, there is no physically correct solution, only one that leads to an optimal simple procedure in terms of the accuracy of calculating the

forces.

In order to resolve the uncertainties in the accuracy of the toroidal approximation and the stability of liquid bridges, we describe a simple numerical scheme for solving the Laplace-Young equation of liquid bridges between two spheres. The more fundamental criterion for specifying the stable solutions of Laplace-Young equation and the critical separation distance of rupture is also examined.

4.2.2 Theory and computational procedures

Consider a liquid bridge between two equal sized rigid solid spheres of radius R as shown by figure 4.2. In the absence of gravitational effects, the pressure deficiency across the air-liquid interface of the liquid bridge is given by the Laplace-Young equation which may be expressed in the following dimensionless form,

$$2H^* = \frac{\ddot{Y}}{(1+\dot{Y}^2)^{3/2}} - \frac{1}{Y(1+\dot{Y}^2)^{1/2}} \tag{4.5}$$

where X and Y are dimensionless coordinates with respect to the sphere radius, R, and H^* is the dimensionless mean curvature defined as,

$$H^* = \frac{\Delta p\, R}{2\gamma_{lv}} \tag{4.6}$$

where Δp is the pressure deficiency across the air-liquid interface, γ_{lv} is the surface tension of the liquid (i.e. the liquid-vapor interfacial surface energy).

The total force, F, acting between the two spheres is the combination of two components: (a) the axial component of the surface tension acting at the three-phase contact line and (b) the hydrostatic pressure acting on the axially projected area of the liquid contact on either sphere. This leads to the following expression for the force,

$$F = 2\pi\gamma_{lv}R\sin\phi\sin(\phi+\theta) + \pi R^2\Delta p\sin^2\phi \tag{4.7}$$

where ϕ is the half-filling angle as shown by figure 4.2 and Y_0 is the dimensionless neck radius of the liquid bridge.

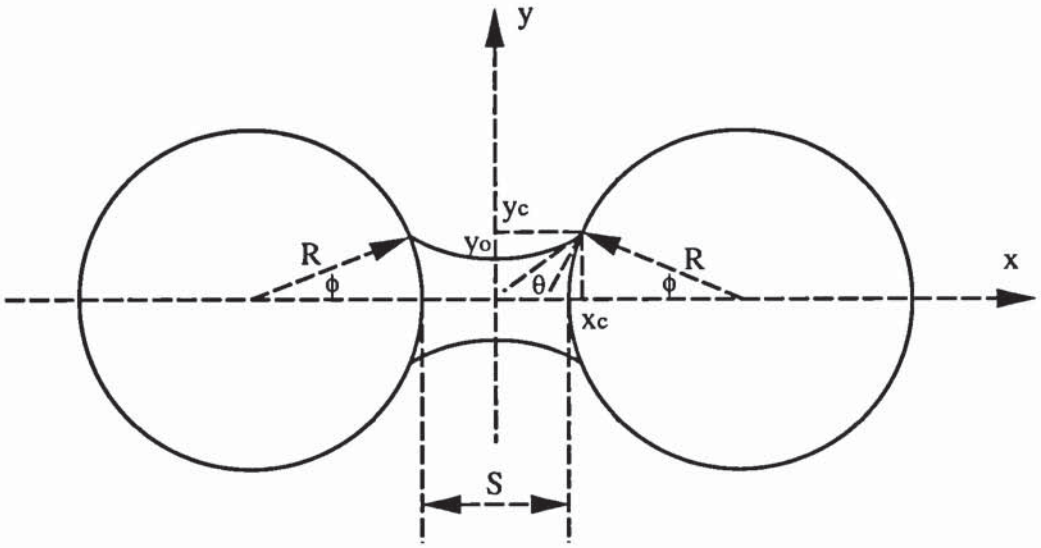

Figure 4.2: A symmetric liquid bridge between two equal sized rigid spheres

The solution of equation 4.5, $Y(X)$, represents the meridian profile of the liquid bridge and it cannot be solved analytically. The numerical solution of equation 4.5 may be approximated by a truncated Taylor series to obtain the following recurrence equation,

$$Y_{i+1} \simeq Y_i + (X_{i+1} - X_i)\dot{Y}_i + \frac{1}{2}(X_{i+1} - X_i)^2\ddot{Y}_i \quad i = 0, 1, 2, ... \tag{4.8}$$

This is the modified Euler method for the numerical solution of ordinary differential equations. In order to evaluate equation 4.8, it is necessary to obtain the expressions for $\dot{Y}_i$, $\ddot{Y}_i$ and the initial value $Y_{i=0}$ which is the neck radius, Y_0 of the liquid bridge. Substituting $Q = \dot{Y}^2 + 1$ into equation 4.5 yields

$$\frac{dQ}{dY} - \frac{2Q}{Y} = 4H^*Q^{3/2} \tag{4.9}$$

This is in the form of a Bernoulli equation which may be integrated to give

$$\frac{Y}{(1+\dot{Y}^2)^{1/2}} + H^*Y^2 = C \tag{4.10}$$

where C is an integration constant for which an expression may be found from the following boundary conditions at $X = X_c$,

$$Y = \sin\phi \tag{4.11}$$

$$\dot{Y} = \cot(\phi + \theta) \tag{4.12}$$

which yield

$$C = \sin\phi\sin(\phi+\theta) + H^*\sin^2\phi \tag{4.13}$$

Since the liquid bridge is symmetrical about the Y axis, it follows that $\dot{Y} = 0$ at $X = 0$ which allows for the following expression for Y_0 to be obtained from equation 4.10,

$$Y_0 = \begin{cases} C & \text{if } H^* = 0 \\ \frac{-1+\sqrt{1+4H^*C}}{2H^*} & \text{if } H^* \neq 0 \end{cases} \tag{4.14}$$

Expressions for $\dot{Y}_i$ and $\ddot{Y}_i$ may be found by rearranging equation 4.5 and 4.10 as follows,

$$\dot{Y}_i = \sqrt{(\frac{Y_i}{C - H^*Y_i^2})^2 - 1} \tag{4.15}$$

$$\ddot{Y}_i = \frac{1+\dot{Y}_i^2}{Y_i} + 2H^*(1+\dot{Y}_i^2)^{3/2} \tag{4.16}$$

In summary, the numerical solution to the Laplace-Young equation was obtained from the recurrence equation 4.8 evaluated using the expressions 4.14, 4.15 and 4.16 in the interval $X = 0$ and $X = X_c$, see figure 4.2. The final limit at X_c was determined by the boundary condition 4.11 and the other boundary condition 4.12 was employed to ensure that the interval $\Delta X = X_{i+1} - X_i$ was sufficiently small such that the error in $\dot{Y}$ at $X = X_c$ was less than 10^{-6}. This ensures that further reduction in the interval ΔX did not lead to changes in $Y(X)$ greater than 10^{-6}. In order to evaluate Y_0 and $\dot{Y}$, $\ddot{Y}$ at different X_i locations using equations 4.14, 4.15 and 4.16, values of the dimensionless mean curvature, H^*, the half-filling angle, ϕ, and the solid-liquid contact angle, θ, were specified. This is equivalent to specifying the dimensionless liquid bridge force, F^*, which, from equations 4.7 and 4.14, may be written as,

$$F^* = \frac{F}{\gamma_{lv}R} = 2\pi Y_0(1 + H^*Y_0) \tag{4.17}$$

The dimensionless liquid volume, $V^* = V/R^3$, was obtained directly from $Y(X)$ as follows,

$$\begin{aligned} V^* &= \int_0^{X_c} 2\pi Y^2 dX - \frac{2\pi}{3}(1-\cos\phi)^2(2+\cos\phi) \\ &\simeq \sum_{X_i=0}^{X_i=X_c} 2\pi Y_i^2 \Delta X - \frac{2\pi}{3}(1-\cos\phi)^2(2+\cos\phi) \end{aligned} \tag{4.18}$$

To maintain a constant volume of liquid for a given set of calculations, at a given dimensionless mean curvature and a given solid-liquid contact angle, an interval-halving iteration method was adopted to obtain the corresponding value of the half-filling angle. The recurrence and iteration scheme were repeated for different values of the dimensionless mean curvature to obtain a corresponding set of half-filling angles, dimensionless liquid bridge forces and dimensionless separation distances (made

dimensionless to the sphere radius, $S^* = S/R$), for a constant volume of liquid. This scheme results in high accuracies and computational efficiency.

4.2.3 Rupture criterion and stability of liquid bridges

For the first part of this work, numerical solutions to the Laplace-Young equation were evaluated for the dimensionless liquid bridge between two spheres with different solid-liquid contact angles (from 0^0 to 40^0) and different dimensionless liquid volumes (from 0.001 to 0.03). Some results of the numerically evaluated solutions to the Laplace-Young equation are shown in figure 4.3 (a to d), where the variation of the dimensionless neck radius, Y_0, the half-filling angle, ϕ, the dimensionless mean curvature, H^*, and the dimensionless force, F^*, are plotted as a function of the dimensionless separation distance, S^*, for different constant liquid volumes and a zero contact angle. It confirms that for the Laplace-Young equation there are two possible solutions. The two solutions converge at the maximum separation of the constant liquid volume curves. Since for separations which exceeds this maximum, no solution exists, it is natural to choose this as the critical rupture distance of stable liquid bridges.

It was pointed out earlier that previous workers have selected the neck diameter (Erle et al 1971) and the half-filling angle (DeBisschop and Rigole 1982, Mazzone et al 1986) as arbitrary criteria for determining the critical rupture separation distance. The mean curvature and total force would be equally valid criteria on this basis since these parameters are also obtained from the numerical evaluation of the Laplace-Young equation. Figure 4.3 shows the plots of the numerically evaluated quantities of neck radius, half-filling angle, mean curvature and force in dimensionless forms as a function of the dimensionless separation distance. For all the cases, there are two possible solutions and the upper limit value of the separation distance corresponds to

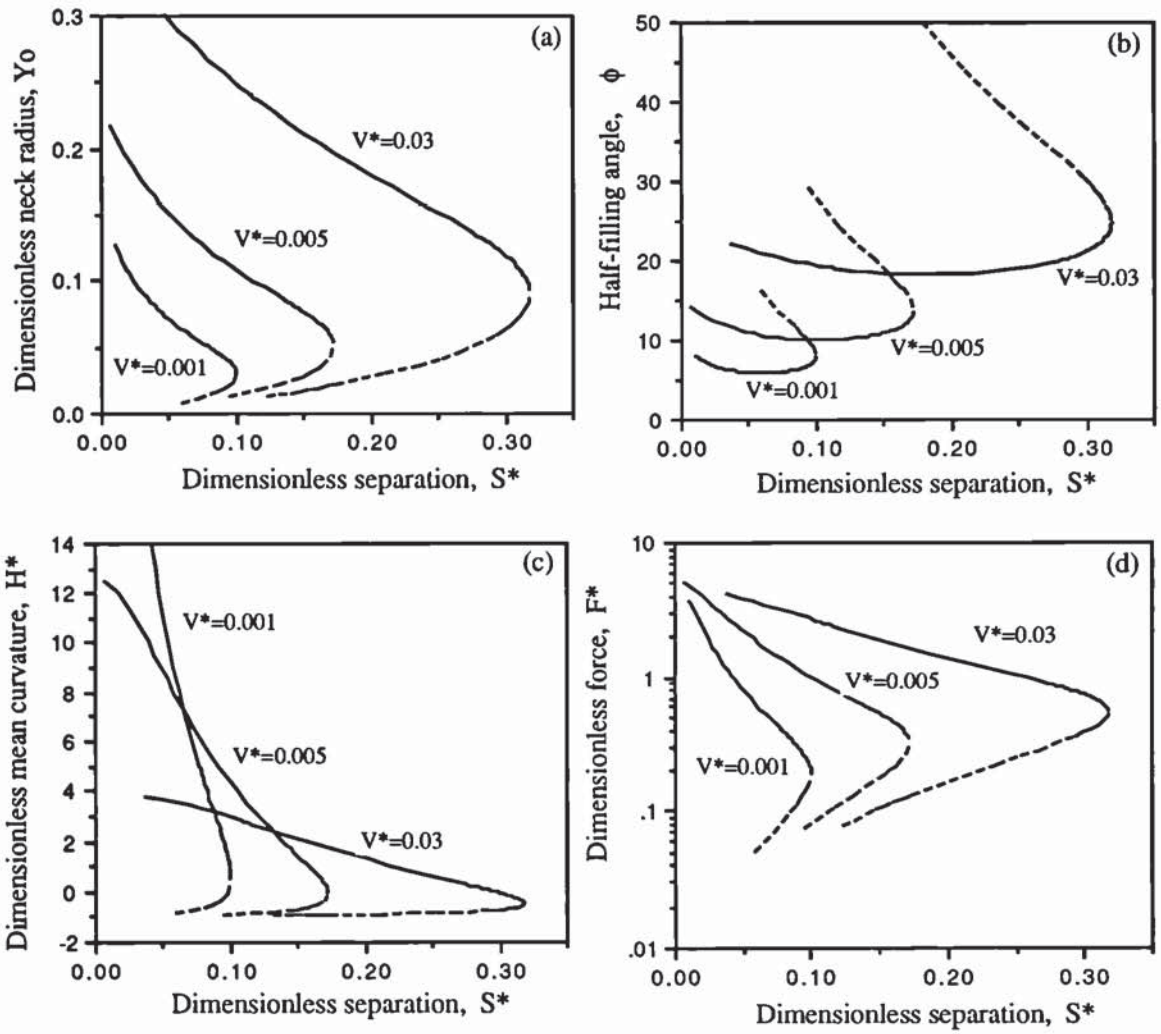

Figure 4.3: Stable (solid lines) and unstable (dashed lines) numerical solutions of the Laplace-Young equation versus dimensionless separation with different dimensionless liquid volumes and a zero contact angle expressed in terms of dimensionless quantities of (a) neck radius, (b) half-filling angle, (c) mean curvature and (d) total force.

the point where the two solutions converge.

The values of the critical dimensionless separation distance, S_c^*, shown in this figure, corresponding to the convergence of the two solutions, are all identical in terms of each criterion and are consistent with the values obtained by Erle et al (1971) and Mazzone et al (1986) and are in excellent agreement with the experimental data of Mason and Clark (1965). This comparison is shown in figure 4.4 for three liquid-solid contact angles of 0^0, 5^0 and 10^0. The optimal 'fit' corresponds to a contact angle of about 7^0 which is consistent with the comments made by Mason and Clark (1965) that the contact angle for their experimental systems was slightly greater than zero.

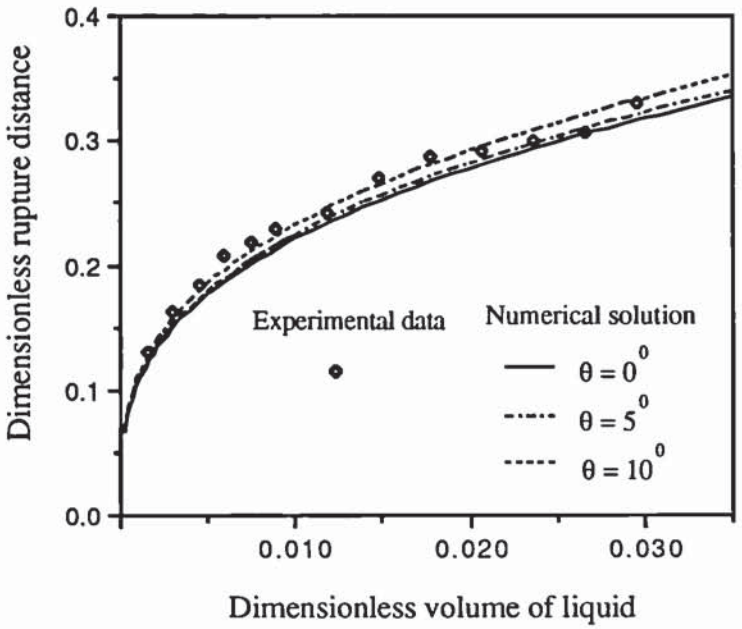

Figure 4.4: The dimensionless critical rupture distances of stable liquid bridges as a function of the dimensionless liquid bridge volume–A comparison of Mason and Clark's (1965) measured data with the numerically computed values at contact angles of 0^0, 5^0 and 10^0.

While the above criteria do produce good agreement with experimental data, it is necessary to obtain the numerical solution for both branches and to identify the stable one. Figure 4.3b shows that there is a minimum in the half-filling angle at separation distances less than the maximum critical values. As correctly pointed out by Mazzone et al (1986), this local minima of the half-filling angle was previously employed by DeBisschop and Rigole (1982) as a rupture criterion which leads to a large underestimation of the rupture distances determined by Mason and Clark (1965).

A more fundamental approach to specifying stable solutions of the Laplace-Young equation is to examine the minimum condition for the Gibbs' free energy of the liquid bridge system. The minimum Gibbs' free energy formulation of liquid bridges was previously obtained by Erle et al (1971) and DeBisschop and Rigole (1982) in different ways. Since the first variational problem, the necessary condition of minimum Gibbs' free energy, using either formulation, leads to the Laplace-Young equation, it is not clear which is correct. This will be examined here by considering the previous work involving the calculus of variations undertaken by Erle et al (1971) and DeBisschop and Rigole (1982).

Assuming that the surfaces of the spheres which were not nominally in contact with the liquid bridge were also wetted by a thin layer of liquid, Erle et al (1971) derived the following expression for the surface free energy of the system, E_E, as

$$E_E = 4\pi\gamma_{lv}\left[\int_0^{x_c} y\sqrt{1+(\frac{dy}{dx})^2}\,dx + \int_{x_c}^{S/2+2R} u\sqrt{1+(\frac{du}{dx})^2}\,dx\right] \tag{4.19}$$

where x, y are dimensional coordinates, S is the dimensional separation distance and $u = u(x)$ represents the circular profile of the spheres which is defined as follows,

$$u(x) = \sqrt{R^2-(x-x_a)^2} \tag{4.20}$$

where $(x_a, 0)$ is the centre of the right hand sphere. Equation 4.19 may expressed in the following form by substitution of equation 4.20,

$$E_E = \int_0^{x_c} G_E(x, y, \frac{dy}{dx})\, dx + 2\pi\gamma_{lv} R(S + 2R) \tag{4.21}$$

where

$$G_E(x, y, \frac{dy}{dx}) = 4\pi\gamma_{lv} \left[y\sqrt{1 + (\frac{dy}{dx})^2} - R \right] \tag{4.22}$$

DeBisschop and Rigole (1982) considered that the total Gibbs' free energy of a liquid bridge comprised the sum of the energy involved in displacing the air phase volume and the surface free energy associated with the liquid-air interface of the bridge and also the liquid-solid interface where the bridge makes contact with the spheres. This leads to the following expression for the total Gibbs' free energy of the system, E_D, given as,

$$E_D = 4\pi\gamma_{lv} \int_0^{x_c} y\sqrt{1 + (\frac{dy}{dx})^2}\, dx + 4\pi(\gamma_{sl} - \gamma_{sv}) \int_{S/2}^{x_c} u\sqrt{1 + (\frac{du}{dx})^2}\, dx + p_a V \tag{4.23}$$

where p_a is the pressure in the vapour phase and γ_{sl}, γ_{sv} are the surface tensions of the solid-liquid and solid-vapour interfaces respectively. Because of the well-known Young's formula of equation 4.2, it follows that equation 4.23 may be written as follows by substitution of $(\gamma_{sl} - \gamma_{sv})$,

$$E_D = \int_0^{x_c} G_D(x, y, \frac{dy}{dx})\, dx + 2\pi\gamma_{lv} RS\cos\theta + p_a V \tag{4.24}$$

where

$$G_D(x, y, \frac{dy}{dx}) = 4\pi\gamma_{lv} \left[y\sqrt{1 + (\frac{dy}{dx})^2} - R\cos\theta \right] \tag{4.25}$$

The constraint which was placed on both formulations of the free energy was the condition of a constant volume for the liquid bridge. This volume, V, as given by equation 4.18 in the dimensionless form, may be also written in the following dimensional form,

$$V = 2\pi \int_0^{x_c} y^2\, dx - 2\pi \int_{S/2}^{x_c} u^2\, dx$$

$$= 2\pi \int_0^{x_c} [y^2 - R^2 + (x - R - S/2)^2]\, dx + \frac{2\pi}{3}(2R^3 + \frac{3}{4}RS^2 - \frac{1}{8}S^3) \qquad (4.26)$$

The minimisation of the Gibbs' free energy subject to the constant volume constraint is equivalent to the minimisation of the following integral function,

$$E' = E + \Lambda V = \int_0^{x_c} G'(x, y, \frac{dy}{dx}) + E_0 \qquad (4.27)$$

where E is given by E_E or E_D, the parameter Λ is the Lagrange multiplier and E_0 is an arbitrary constant. The function $G'(x, y, dy/dx)$ is given by the following expression

$$G'(x, y, \frac{dy}{dx}) = G(x, y, \frac{dy}{dx}) + 2\pi\Lambda[y^2 - R^2 + (x - R - \frac{S}{2})^2] \qquad (4.28)$$

where G is given by G_E or G_D corresponding to E_E or E_D respectively. The necessary condition for the liquid bridge to have a minimum Gibbs' free energy requires that the following equation be satisfied,

$$\frac{\partial G'}{\partial y} - \frac{d}{dx}(\frac{\partial G'}{\partial \dot{y}}) = 0 \qquad (4.29)$$

Substitution of either equation 4.22 or 4.25 into 4.29 both lead to the same expression as follows,

$$\Lambda = -\gamma_{lv}\left\{\frac{\ddot{y}}{(1 + \dot{y}^2)^{3/2}} - \frac{1}{y(1 + \dot{y}^2)^{1/2}}\right\} \qquad (4.30)$$

which is the other form of the Laplace-Young equation 4.5 with $\Lambda = -\Delta p$.

Strictly, it is necessary to introduce a supplementary condition for a minimum in the Gibbs' free energy since the integrals in equation 4.19 to 4.27 must be evaluated between 0 and x_c where the upper limit x_c is not uniquely defined for a given volume of liquid but is given by a function $\psi(x, y)$ as follows,

$$\psi(x, y) = (x - R - S/2)^2 + y^2 - R^2 = 0 \tag{4.31}$$

The previous work of Erle et al (1971) and DeBisschop and Rigole (1982) ignored the fact that a minimum Gibbs' free energy also requires that the following supplementary condition be satisfied,

$$\left.\frac{\partial \psi}{\partial y}\left(G' - \dot{y}\frac{\partial G'}{\partial \dot{y}}\right)\right|_{x=x_c} = \left.\frac{\partial \psi}{\partial x}\frac{\partial G'}{\partial \dot{y}}\right|_{x=x_c} \tag{4.32}$$

When this equation is evaluated by employing equation 4.22 of Erle et al (1971) substituted into 4.28, the equation 4.32 reduces to,

$$R\cos\theta = R \tag{4.33}$$

This implies that the formulation of Erle et al (1971) is only applicable for a zero contact angle. However, in the case of DeBisschop and Rigole's (1982) formulation of Gibbs' free energy, i.e. by employing equation 4.25 for the substitution, both the left and right hand sides of equation 4.32 reduce to the expression $R\cos\theta$, showing that it applies to a more general situation of finite solid-liquid contact angles.

Mathematically, for a stable liquid bridge with a minimum Gibbs's free energy, not only should the necessary condition, the first variation equals zero, be satisfied, but also the sufficient condition, the second variation being positive, must hold. Unfortunately, the second variation problem of the Gibbs' free energy has not yet been

solved analytically. However, since for the Laplace-Young equation, which satisfies the necessary condition of a minimum Gibbs' free energy, there are two possible solutions, we can alternatively identify the stable branch by comparing the Gibbs's free energy of the two solutions. For the more general formulation of the Gibbs' free energy given by DeBisschop and Rigole (1982), the term $p_a V$ in equation 4.23 is in fact a constant and, consequently, is not relevant to liquid bridge stability. Therefore, it is only necessary to consider the case when $p_a = 0$ and define the Gibbs's free surface energy of a liquid bridge system as follows,

$$E = 4\pi\gamma_{lv}\left[\int_0^{x_c} y\sqrt{1+\dot{y}^2}\,dx - \cos\theta\int_{S/2}^{x_c} u\sqrt{1+\dot{u}^2}\,dx\right] \tag{4.34}$$

or, in dimensionless form,

$$E^* = 4\pi\int_0^{X_c} Y\sqrt{1+\dot{Y}^2}\,dX - 4\pi(X_c - S^*/2)\cos\theta \tag{4.35}$$

In accordance with the numerical solution, we further derive the expression for the free energy as follows,

$$E^* \simeq 4\pi\sum_0^{X_c} Y_i\sqrt{1+\dot{Y}_i^2}\,\Delta X - 4\pi(X_c - S^*/2)\cos\theta \tag{4.36}$$

Equation 4.35 or 4.36 now arguably provides a fundamental way of expressing the stability of liquid bridges since it is written directly in terms of the Gibbs' free surface energy.

For the same numerical solutions to the Laplace-Young equation, as shown by figure 4.3, the corresponding dimensionless free surface energy curves are shown in figure 4.5 for different dimensionless liquid volumes. Here it is obvious that, of the two numerical solutions to the Laplace-Young equation, the stable branches correspond to the lower free energy.

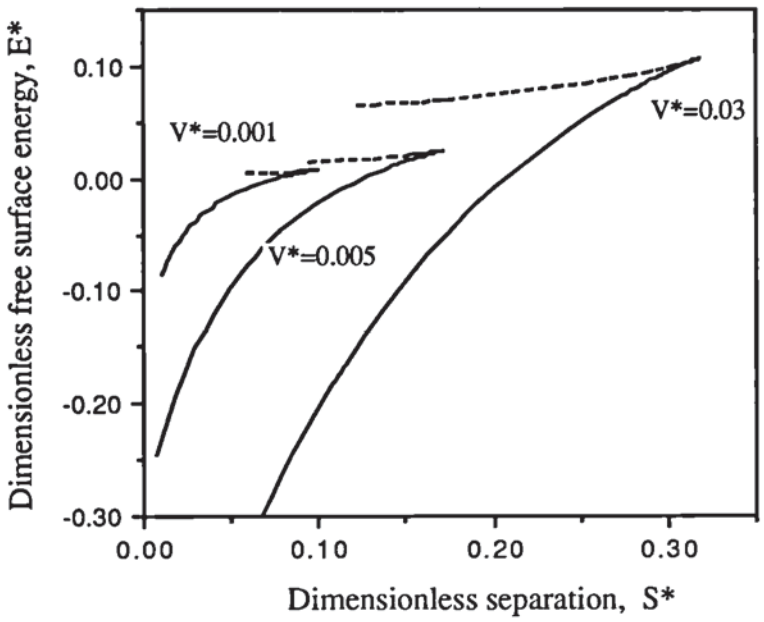

Figure 4.5: The dimensionless Gibbs' free surface energy as a function of the dimensionless separation distance for a range of dimensionless liquid bridge volumes and a zero contact angle corresponding to the stable (solid lines) and unstable (broken lines) numerical solutions of the Laplace-Young equation

A comparison of figure 4.5 with figure 4.3 shows that the variation with the liquid volume of the critical rupture distance at which the solutions converge is identical to that found previously using the other criteria. This is the expected result since a liquid bridge is uniquely specified by its volume, the separation distance between the spheres and one of these five criteria. Finally in this section, an interesting observation was made that there is a simple relationship between the calculated dimensionless rupture distance, S_c^* and the dimensionless liquid volume, V^*. These quantities are plotted on logarithmic scales in figure 4.6 for a number of solid-liquid contact angles.

It may be seen that each set produces a straight line of slope 1/3 and can be represented by the following fitting equation,

$$S_c^* \simeq (1 + 0.5\theta)\sqrt[3]{V^*} \tag{4.37}$$

where the solid-liquid contact angle is expressed in radians. To a good approximation, the dimensionless rupture distance is equal to the cube root of the dimensionless volume for small contact angles.

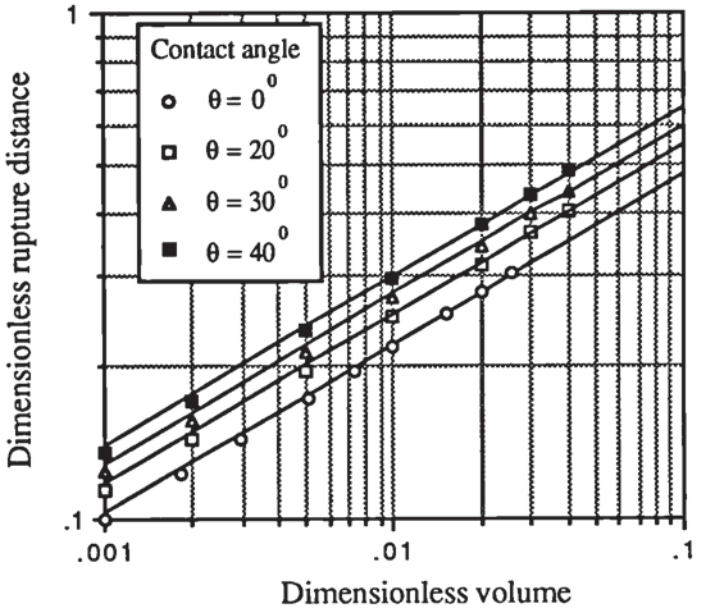

Figure 4.6: A double logarithmic plot of the numerically computed dimensionless rupture distance as a function of the dimensionless liquid bridge volume at a number of contact angles.

4.2.4 Liquid bridge forces

One of the intentions of this work was to compare the numerically calculated liquid bridge forces with the experimental data of Mason and Clark (1965) and with the various methods of applying the toroidal approximation (Fisher 1926). The experimental data of Mason and Clark (1965) have become a recognised standard of comparison. They measured the forces for two $15mm$ radius spheres with liquid

bridges comprising di-n-butyl phthalate/liquid paraffin mixture which had a surface tension of $2.45 \times 10^{-3}\, Nm^{-1}$. The liquid bridges were suspended in water to eliminate gravitational distortion. Consequently, these values of sphere radius and liquid surface tension were employed in the work described here. Mason and Clark (1965) did not specify the contact angle for their system but indicated that it was small. In the current work, a range of solid-liquid contact angles was examined from 0^0 to 40^0.

In the case of the much simpler toroidal approximation proposed by Fisher (1926), the meridional profile of the liquid-air interface $Y_F(X)$ is an arc of a circle (see figure 4.7) which may be expressed as,

$$Y_F = \rho_1^* + \rho_2^* - \sqrt{(\rho_1^*)^2 - X^2} \tag{4.38}$$

where ρ_1^* and ρ_2^* are the dimensionless principal radii of curvature with respect to the radius of the spheres, R, such that ρ_1 corresponds to the radius of the meridian profile and ρ_2 is the radius at the neck (refer to figure 4.7).

From the geometry of figure 4.7 the dimensionless principal radii can be derived as,

$$\rho_1^* = \frac{S^*/2 + 1 - \cos\phi}{\cos(\phi + \theta)} \tag{4.39}$$

$$\rho_2^* = \sin\phi - \frac{[1 - \sin(\phi + \theta)][S^*/2 + 1 - \cos\phi]}{\cos(\phi + \theta)} \tag{4.40}$$

Substitution of equation 4.38 into equation 4.5 leads to the dimensionless local mean curvature, H_F^*, and the dimensionless volume of liquid, V_F^* defined as follows,

$$H_F^* = \frac{2Y - \rho_1^* - \rho_2^*}{2Y\rho_1^*} \tag{4.41}$$

$$V_F^* = 2\pi \left[(\rho_1^* + \rho_2^*)^2 X_c + (\rho_1^*)^2 X_c - \frac{X_c^3}{3} \right.$$

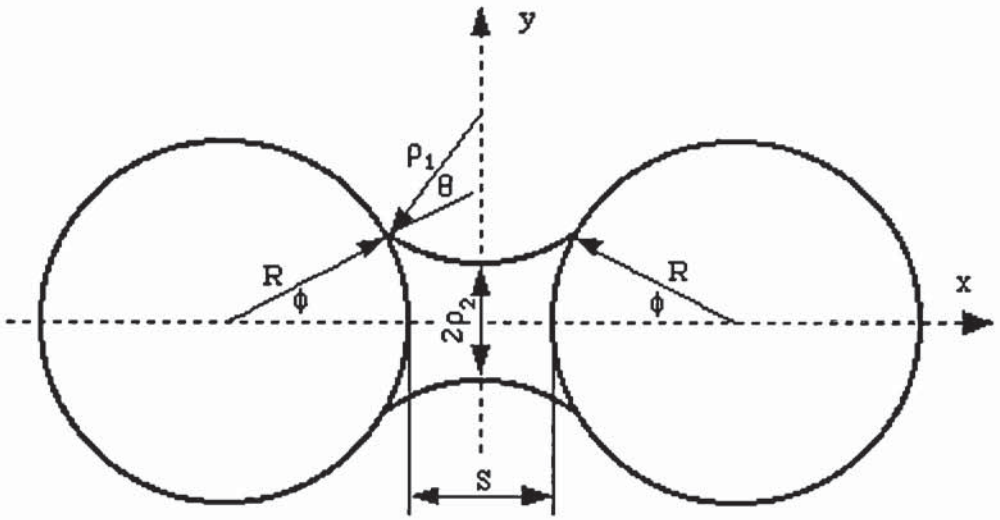

Figure 4.7: Toroidal approximation of a liquid bridge between two equal sized spheres

$$- (\rho_1^* + \rho_2^*)(X_c\sqrt{(\rho_1^*)^2 - X_c^2} + (\rho_1^*)^2 \arcsin\frac{X_c}{\rho_1^*})\Big]$$

$$-\frac{2\pi}{3}(1-\cos\phi)^2(2+\cos\phi) \tag{4.42}$$

The minimum value of H_F^* is at the bridge neck and is given by,

$$(H_F^*)_{min} = \frac{\rho_2^* - \rho_1^*}{2\rho_1^*\rho_2^*} \tag{4.43}$$

The maximum value corresponds to that at the solid-liquid-vapour contact line, thus,

$$(H_F^*)_{max} = \frac{2\sin\phi - \rho_1^* - \rho_2^*}{2\rho_1^*\sin\phi} \tag{4.44}$$

When using the toroidal approximation to calculate the force, various methods are possible, depending on the location along the liquid bridge used to compute the two components of the total force. The physically most 'correct' formulation of the total force is that obtained from equation 4.7,

$$F^*_{F1} = 2\pi\{\sin\phi\sin(\phi+\theta) + (H^*_F)\sin^2\phi\} \tag{4.45}$$

where H^*_F is the maximum value specified by equation 4.44. One alternative is to use the minimum value of H^*_F given by equation 4.43, which in this work is referred to as the 'mixed method'. Another quite different formulation is based on what has been termed the 'gorge method' (Hotta et al 1974). This involves using the area at the neck to obtain the force arising from the hydrostatic pressure deficiency and the tangent at the neck to obtain the surface tension component of the force, leading to the following expression for the total liquid bridge force,

$$F^*_{F2} = 2\pi\rho^*_2\{1 + (H^*_F)_{min}\rho^*_2\} \tag{4.46}$$

That this expression is of the same form as equation 4.17 with $Y_0 = \rho^*_2$ is fortuitous.

Calculations based on the toroidal approximation were also carried out for the liquid bridges with the same ranges of liquid volume, solid-liquid contact angle and separation distance as those used for the numerical computations. The forces calculated using either the numerical scheme described in this paper or the toroidal approximation were both consistent with the values published by others (Erle et al 1971, DeBisschop and Rigole 1982, and Mazzone et al 1986). A comparison was made of the numerically evaluated liquid bridge forces with those calculated using the different procedures for the toroidal approximation. It was not possible to reproduce the large differences reported by Mazzone et al (1986). Figure 4.8 shows some results of the comparison where, for the toroidal approximation, both the physically most 'correct' formulation (equations 4.44 and 4.45) and the 'mixed method' (equations 4.43 and 4.45) were used. The dimensionless liquid bridge force is plotted as a function of the relative separation distance, (S/S_c), where S_c is the critical separation distance corresponding to rupture. It is shown by figure 4.8 that there is a significant overestimation of the force by using the physically 'correct' formulation. Using the

'mixed method', there is only a small overestimation at small separation distances. At large separations, however, the 'mixed method' severely underestimates the liquid bridge force. The difference increases for large liquid volumes and large separation distances.

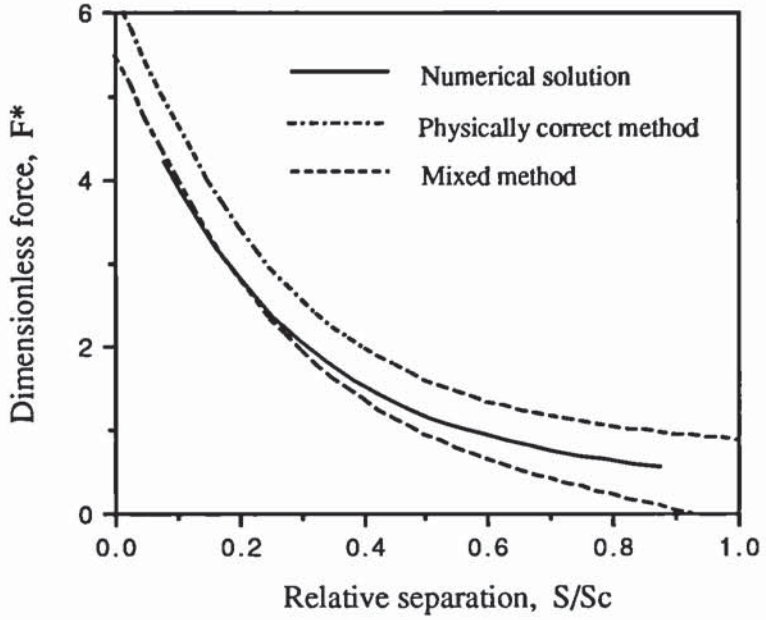

Figure 4.8: A comparison of the dimensionless liquid bridge force as a function of the relative separation distance for a constant dimensionless liquid bridge volume (0.005) and a zero contact angle, calculated using the numerical method, the physically 'correct' method and the 'mixed' method of the toroidal approximation

For the toroidal approximation, the best estimate of the total liquid bridge force was obtained using the gorge method, equation 4.46. Figure 4.9a shows some results of such calculations for a zero solid-liquid contact angle and different liquid volumes. The dimensionless liquid bridge force is again plotted as a function of the relative separation. It can be seen that when the gorge method is used, the toroidal approximation also underestimates the numerical values but the maximum difference is less than 10% corresponding to the greatest volume considered. The accuracy does not even change much when the separation distance increases.

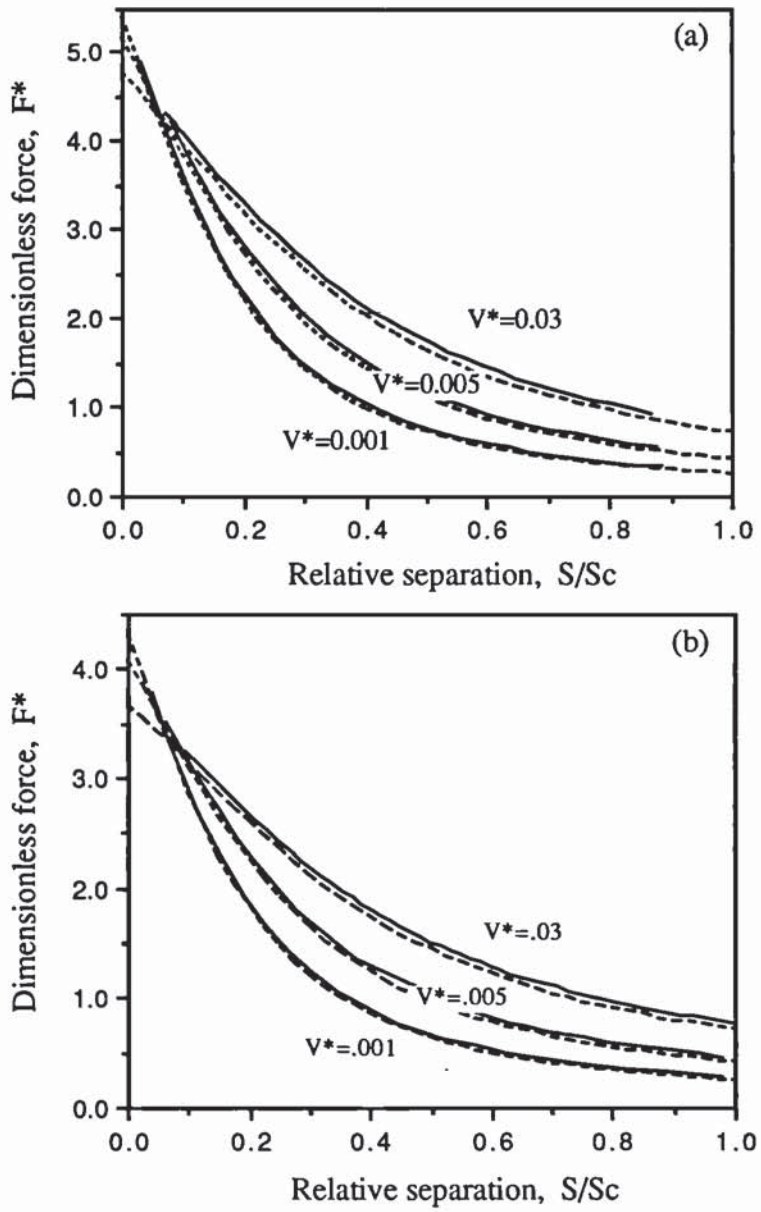

Figure 4.9: A comparison of the dimensionless liquid bridge force as a function of the relative separation distance for a range of dimensionless liquid bridge volumes calculated using the numerical method (solid lines) and the gorge method (broken lines) of the toroidal approximation for contact angle of (a) 0^0 and (b) 40^0

Figure 4.9b shows a comparable set of data but for a contact angle of 40^0. It can be seen that when the gorge method is used there is virtually no change in the accuracy of the toroidal approximation. This may be expected because of the self-similarity of liquid bridges between two spheres as exemplified by figure 4.10.

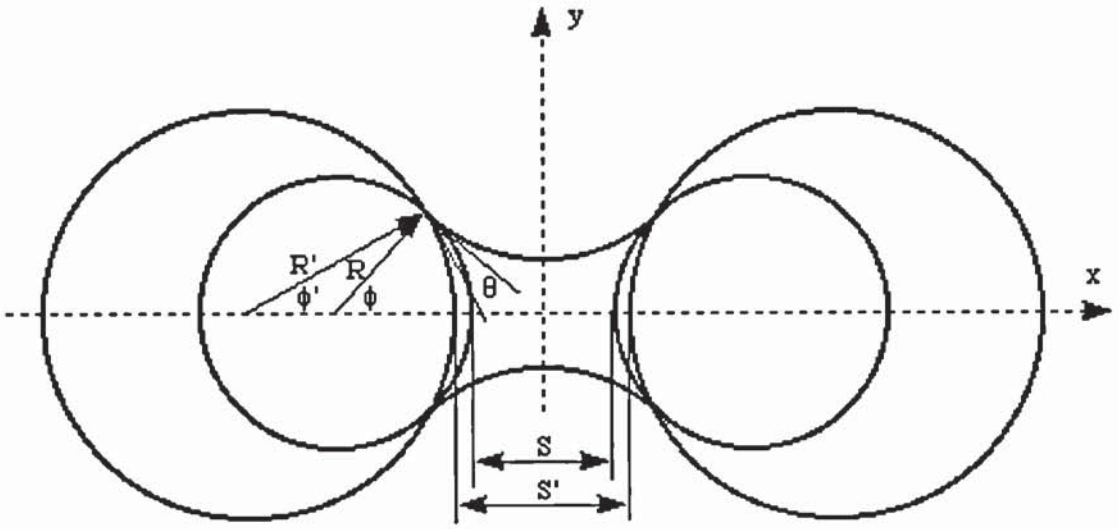

Figure 4.10: A liquid bridge between two pairs of solid spheres of different radii and with different half-filling angle and different separation distances

It is shown that a liquid bridge between two solid spheres of radius, R, with a contact angle, 0^0, half-filling angle, ϕ, and separation distance, S, is identical to a liquid bridge with a finite contact angle, θ, and the following transformed quantities denoted by a prime,

$$\phi' = \phi - \theta \tag{4.47}$$

$$R' = R\frac{\sin\phi}{\sin(\phi-\theta)} \tag{4.48}$$

$$S' = S + 2R\frac{\sin\theta - \sin\phi + \sin(\phi-\theta)}{\sin(\phi-\theta)} \tag{4.49}$$

To underline the accuracy of the gorge method using the toroidal approximation, a comparison was also made with the experimental data of Mason and Clark (1965) as shown in figure 4.11. These calculations were performed for a solid-liquid contact angle of 7^0. It may be seen that the agreement with the experimental data is comparable for the exact and the toroidal gorge approximation. The discrepancies produced by both methods at large volumes and small separations were discussed previously.

An alternative approach to estimating the forces using the toroidal approximation is to scale the dimensionless mean curvature and neck radius in equation 4.17 by expressions calculated from the toroidal approximation. For the scaling coefficient for the neck radius, $k_Y = Y_0/\rho_2^*$, a plot of the coefficient as a function of the relative separation distance for a range of liquid bridge volumes is shown in figure 4.12a. It can be seen that large deviations from unity are only apparent at large relative separations. Furthermore, this scaling coefficient is independent of the bridge volume. Consequently, it may be expressed as a function of the relative separation only. By employing an exponential form function, the scaling coefficient may be best fitted by,

$$k_Y = 1.0 - 0.00032 \exp(6.8S/S_c) \tag{4.50}$$

The scaling coefficient employed for the dimensionless mean curvature was k_H defined as $(H^* + 1)/[(H_F^*)_{max} + 1]$ where $(H_F^*)_{max}$ is the dimensionless mean curvature evaluated at the solid-liquid contact from equation 4.44 using the toroidal approximation. This coefficient is plotted in figure 4.12b as a function of the relative separation for a range of liquid volumes. In this case, deviations from unity start at low separation distances but again the coefficient is relatively insensitive to the bridge volume. The coefficient may be expressed in terms of the relative separation by the following second order polynomial,

$$k_H = 0.91 - 0.10\frac{S}{S_c} - 0.61(\frac{S}{S_c})^2 \tag{4.51}$$

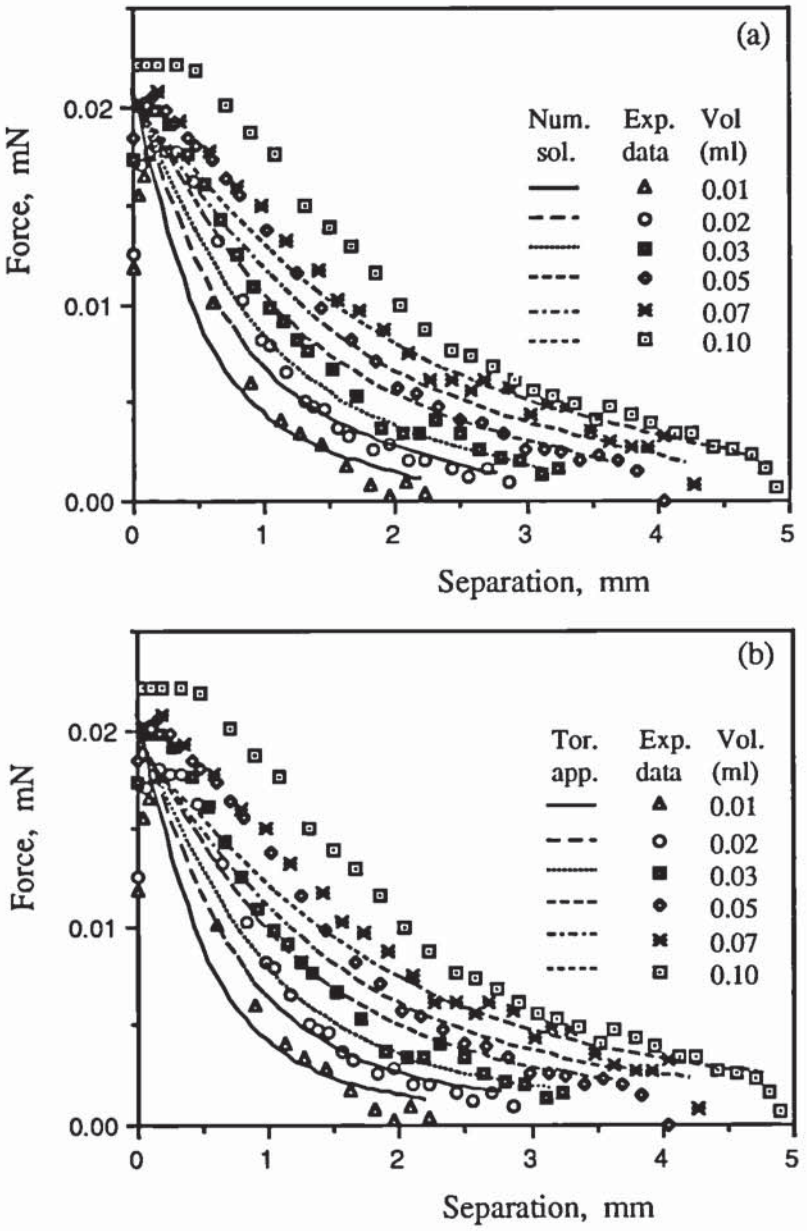

Figure 4.11: A comparison of Mason and Clark's (1965) data for the liquid bridge force between two $30mm$ diameter spheres with the results obtained using (a) the numerical computation and (b) the toroidal approximation.

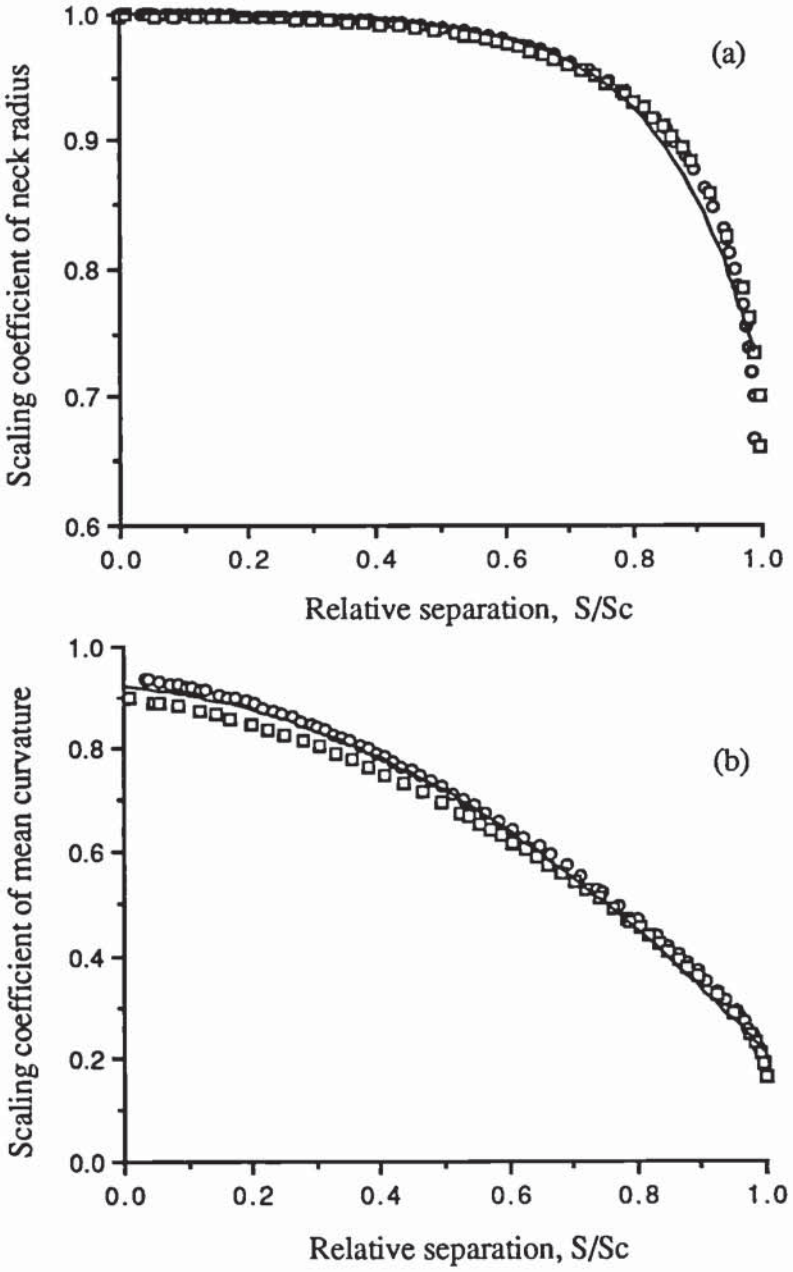

Figure 4.12: The scaling coefficients for (a) the neck radius and (b) the maximum mean curvature from the toroidal approximation as a function of the relative separation for dimensionless liquid bridge volumes of 0.001 (o) and 0.01 (□)

Thus a reasonably exact closed-form approximation to the total dimensionless liquid bridge force may be derived using equation 4.17 with the modified dimensionless mean curvature and liquid bridge neck radius obtained from the toroidal approximation. It is written as,

$$F^* = 2\pi k_Y \rho_2^* \{1 + [k_H (H_F^*)_{max} + k_H - 1] k_y \rho_2^*\} \tag{4.52}$$

This expression is applicable for separation distances up to critical rupture value and for any liquid bridge volume and contact angle. However, it does assume that the gravitational effect is negligible.

4.2.5 Liquid bridge between unequal sized spheres

For a liquid bridge between two unequal sized spheres, the toroidal approximation can be modified. This is achieved by choosing the origin of the coordinate system at the neck of the bridge as shown by figure 4.13 where the sphere radii are denoted as R_1, R_2. From geometric considerations, the two principal radii, ρ_1, ρ_2, that characterize the toroidal bridge may be expressed as,

$$\rho_1 = \frac{S_i + R_i(1 - \cos\phi_i)}{\cos(\phi_i + \theta)} \tag{4.53}$$

$$\rho_2 = R_i \sin\phi_i - \frac{[1 - \sin(\phi_i + \theta)][S_i + R_i(1 - \cos\phi_i)]}{\cos(\phi_i + \theta)} \tag{4.54}$$

where $i = 1$ or 2.

For a given separation distance, $S = S_1 + S_2$, between the two spheres the toroidal approximation provides the following expression for the total volume of liquid $V = V_1 + V_2$

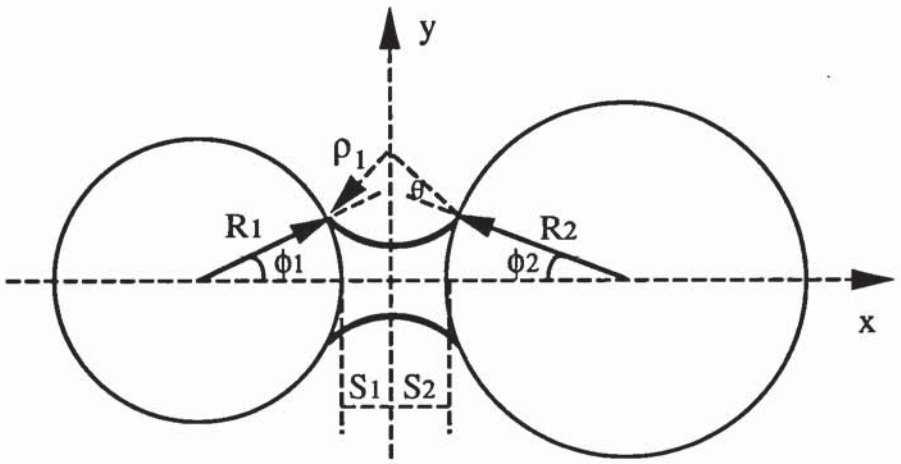

Figure 4.13: Toroidal approximation of a liquid bridge between two unequal sized spheres

$$V_i = \pi[(\rho_1+\rho_2)^2 x_{ci} + \rho_1^2 x_{ci} - \frac{x_{ci}^3}{3} - (\rho_1+\rho_2)(x_{ci}\sqrt{\rho_1^2 - x_{ci}^2} + \rho_1^2 \arcsin\frac{x_{ci}}{\rho_1})]$$

$$-\frac{\pi R_i^3}{3}(1-\cos\phi_i)^2(2+\cos\phi_i) \tag{4.55}$$

where $i = 1, 2$ and

$$x_{ci} = S_i + R_i(1-\cos\phi_i) \tag{4.56}$$

From equation 4.53 and the relation $S = S_1 + S_2$, it follows that the half-separation distances, S_1, S_2, can be expressed as,

$$S_1 = S + R_2(1-\cos\phi_2) - \frac{S + R_1 + R_2 - R_1\cos\phi_1 - R_2\cos\phi_2}{\cos(\phi_1+\theta)+\cos(\phi_2+\theta)}\cos(\phi_2+\theta) \tag{4.57}$$

$$S_2 = S + R_1(1-\cos\phi_1) - \frac{S + R_1 + R_2 - R_1\cos\phi_1 - R_2\cos\phi_2}{\cos(\phi_1+\theta)+\cos(\phi_2+\theta)}\cos(\phi_1+\theta) \tag{4.58}$$

Substituting the expressions of S_1 and S_2 into equation 4.54, we obtain the following equation by rearrangement,

$$\frac{R_1 \sin\phi_1 - R_2 \sin\phi_2}{[S + R_1(1-\cos\phi_1) + R_2(1-\cos\phi_2)]} = \frac{\sin(\phi_2+\theta) - \sin(\phi_1+\theta)}{\cos(\phi_1+\theta) + \cos(\phi_2+\theta)} \tag{4.59}$$

which can be further rewritten as,

$$(R_1 - R_2)\sin\phi_1\cos(\phi_2+\theta) + [(R_1-R_2)\cos\phi_1 - (S+R_1+R_2)]\sin(\phi_2+\theta)$$

$$+ (S+R_1+R_2)\sin(\phi_1+\theta) - (R_1-R_2)\sin\theta = 0 \tag{4.60}$$

From this expression, it is further derived that the half-filling angle ϕ_2 may be expressed in terms of ϕ_1 as follows,

$$\sin(\phi_2+\theta) = \frac{S_R^2\sin(\phi_1+\theta) - (R_1-R_2)^2\sin(\phi_1-\theta) - 2S_R(R_1-R_2)\sin\theta}{S_R^2 + (R_1-R_2)^2 - 2S_R(R_1-R_2)\cos\phi_1} \tag{4.61}$$

where we denote $S_R = S + R_1 + R_2$. Thus a liquid bridge between two unequal sized spheres is uniquely determined for a given set of parameters of sphere radii, R_1, R_2, separation distance, S, and half-filling angle, ϕ_1. This is equivalent to specifying the volume of liquid, as given by equation 4.56, and the force, as approximated by equation 4.46, of the liquid bridge.

4.3 Viscous force of dynamic liquid bridges

4.3.1 Governing equations

For a dynamic liquid bridge between two spheres, a continuous deformation of the liquid bridge takes place due to the relative movement of the spheres and hence the

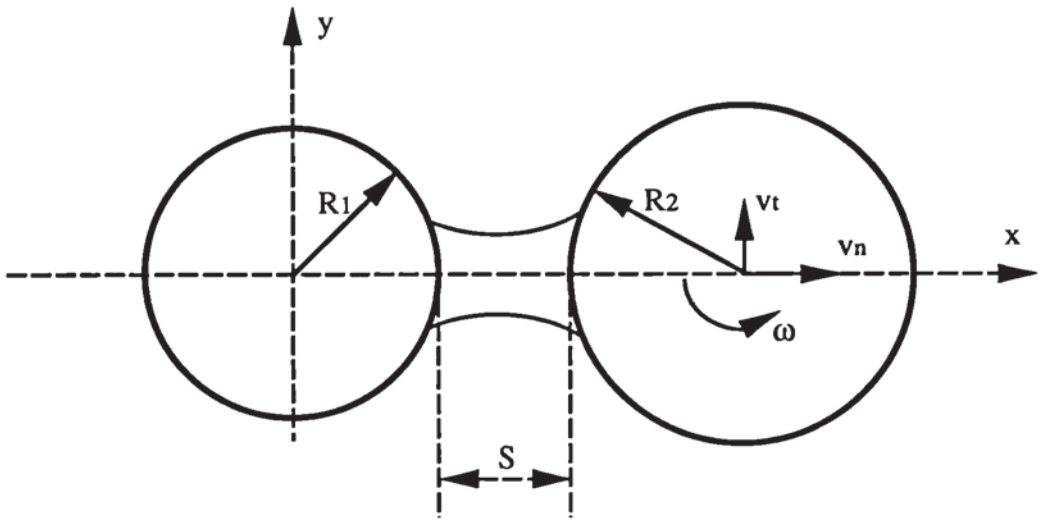

Figure 4.14: Schematic representation of a dynamic liquid bridge between two equal sized spheres with three different relative movements

strength of the bridge depends not only on the shape-dependent meniscus force of the bridge but also on the rate-dependent viscous resistance of the fluid. In certain chemical processing engineering problems such as fluidized beds, dryers, agglomerators and powder flows, the viscous force is very significant for highly viscous liquids. The viscous term can be also dominant for moderatly viscous fluid at high shear rates. An understanding of the viscous effects is therefore important when considering the high-strain-rate properties of moist agglomerates.

In general, for a dynamic liquid bridge between two equal sized spheres, if the coordinate system is chosen such that the origin is fixed on the centre of one sphere and the $x-$axis points to the centre of the other sphere, as shown by figure 4.14, the relative movement between the two spheres can be resolved in terms of (a) the normal translation v_n, (b) the tangential translation v_t and (c) the rotation ω. For all the cases the following Stokes-Navier equation should be satisfied if the inertia effect of

the liquid bridge fluid is negligible. The Stokes-Navier equations are,

$$\left.\begin{aligned} \nabla p &= \eta \nabla^2 \vec{v} \\ \nabla \vec{v} &= 0 \end{aligned}\right\} \tag{4.62}$$

where p is the fluid pressure, $\vec{v} = (v_x, v_y, v_z)$ is the velocity field and η is the fluid viscosity. ∇ and ∇^2 are the Hamilton and Laplace operators which are defined as follows,

$$\nabla = \vec{i}\frac{\partial}{\partial x} + \vec{j}\frac{\partial}{\partial y} + \vec{k}\frac{\partial}{\partial z} \tag{4.63}$$

$$\nabla^2 = \frac{\partial^2}{\partial x^2} + \frac{\partial^2}{\partial y^2} + \frac{\partial^2}{\partial z^2} \tag{4.64}$$

where $\vec{i}$, $\vec{j}$, $\vec{k}$ are the unit vectors in the $x-$, $y-$, $z-$ axial directions.

For the three different relative motions, solutions to the Stokes-Navier equations should be evaluated separately in association with the corresponding boundary conditions. However, exact solutions are very difficult.

For a dynamic liquid bridge when the spheres are subjected to relative movement in the normal direction, McFarlane and Tabor (1950) observed experimentally that the viscous force was significant for more viscous liquids (viscosity $\sim 1 Pa\,s$). Recently, studies have been made by Adams and Perchard (1985), Mazzone et al (1987), Matthewson (1988) and Ennis et al (1990). They considered the Reynolds' lubrication equation for the case of a sphere moving normal to a flat surface or another sphere at a small separation distance. The solution obtained however is asymptotic which is very similar to the asymptotic solution of a sphere moving through a semi-infinite fluid. Here, both the Reynolds' lubrication theory and the semi-infinite theory are discussed.

4.3.2 Reynolds' lubrication approximation

Assuming that locally and instantaneously the flow is taken to be steady, Hocking (1973) showed that the Reynolds's lubrication equation that describes the pressure distribution, $p(r)$, in the squeezed fluid between two close surfaces reduced to the following equation (refer to figure 4.15 for the notation),

$$12\eta v_n = \frac{1}{r}\frac{\partial}{\partial r}\left[rz^3(r)\frac{\partial p(r)}{\partial r}\right] \tag{4.65}$$

where $p(r)$ is the pressure distribution, $z(r)$ is the local separation distance between the two surfaces and r is the radial distance from the centre.

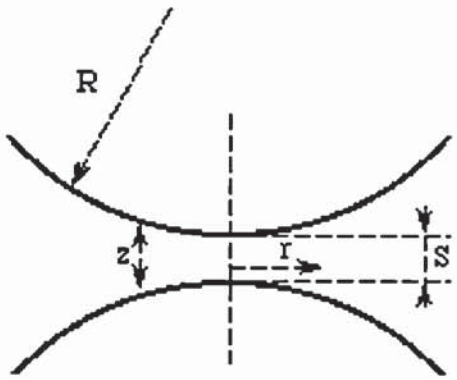

Figure 4.15: Schematic representation of the squeezing flow between two colliding spheres.

For a power law liquid film between two axisymmetric surfaces, a solution for equation 4.65 was obtained by Adams and Edmondson (1987) which leads to an expression for the viscous force as follows,

$$F_v = 2^{m+1}\pi k_\eta \left(\frac{2m+1}{2m}\right)^m v_n^m \int_0^{R\sin\phi} \frac{r^{m+2}}{z^{2m+1}(r)}\,dr \tag{4.66}$$

where m is the power law index (i.e. $\eta = k_\eta v^m$).

In the case of two spheres with a separation distance S, Adams and Perchard (1985) assumed that the liquid bridge is only around the small area of the contact and thus the local separation distance between the two profiles $z(r)$ can be approximated by,

$$z = S + \frac{r^2}{R} \tag{4.67}$$

For a Newtonian liquid of $m = 0$ and $k_\eta = \eta$, substitution of equation 4.67 into 4.66 leads to the following expression for the viscous force of the dynamic liquid bridge,

$$F_v = \frac{3\pi\eta R^2 v_n}{2S} \tag{4.68}$$

A similar expression for the viscous force of the liquid film between a sphere and a flat surface was obtained by Chan and Horn (1985)

$$F_v = 6\pi\eta R^2 v_n / S \tag{4.69}$$

For a liquid bridge between a sphere and a plane with a finite half-filling angle ϕ, Matthewson (1988) modified this equation to give the viscous force as follows,

$$F_v = 6\pi\eta R^2 [1 - \frac{S}{S + R(1 - \cos\phi)}]^2 \frac{v_n}{S} \tag{4.70}$$

For a liquid film between two unequal sized spheres of radii R_1, R_2 at a separation distance, S, we can similarly approximate the local separation distance between the two surfaces as,

$$z(r) = S + \frac{r^2}{2R_1} + \frac{r^2}{2R_2} = S + \frac{r^2}{2R^*} \tag{4.71}$$

where R^* is as defined by equation 3.5. With the substitution of equation 4.71 into 4.65, it follows that the pressure distribution over the spherical surfaces can be obtained as,

$$p(r) = 3\eta R^* v_n \frac{1}{(S + r^2/2R^*)^2} \tag{4.72}$$

which can be integrated to derive the viscous force as,

$$F_v = 6\pi\eta (R^*)^2 v_n / S \tag{4.73}$$

It is obvious that both equations 4.68 and 4.69 are two special cases of equation 4.73.

The above analysis only considers the relative movement of rigid solid spheres. The more general case is the viscous resistance of an elastic sphere moving towards a second elastic sphere or a plane surface, under the condition that the two solid surfaces are separated by a thin infinite fluid layer or a finite liquid bridge. The problem of elastohydrodynamic collisions of particles has been studied by Davis (1987) and others (Davis et al 1986; Serayssol and Davis 86; Barnocky and Davis 1988a, 1988b). In their studies, the pressure profile of the Reynolds' lubrication equation 4.65 was obtained numerically by considering the dynamic deformation of the solid spheres. However, this is a more complicated case for which analytical expressions are not possible. For most cases, we may assume that the spheres are rigid enough that the deformations of the surfaces are small and hence negligible in relation to the sphere displacement.

4.3.3 Semi-infinite theory

For the viscous force of a dynamic liquid bridge due to either the tangential or rotational relative movements of the spheres, there are no direct experimental nor theoretical studies published in the literature. The more relevant semi-infinite theory,

however, may approximately apply. In fact, the Reynolds' lubrication equation can be also regarded as a special case of the semi-infinite problem. The semi-infinite theory considers a rigid solid sphere (or two spheres) moving through a semi-infinite fluid bounded by a plane. There are several different cases. The typical cases which are relevant to the liquid bridge problems include (a) a sphere translating towards or away from a plane wall, (b) a sphere translating parallel to a plane wall and (c) the rotation of a sphere parallel to a plane wall. The three cases and their relevance to the dynamic liquid bridges are discussed below.

Translation of a sphere normal to a plane

The case of a sphere translating towards or away from a plane which bounds a semi-infinite viscous fluid was studied by Brenner (1961). He showed that for a sphere of radius R at a separation distance, S, and velocity, v_n, the viscous force exerted on the sphere due to the translatory motion can be expressed as follows,

$$F_v = 6\pi\eta R v_n \lambda_n(S/R) \tag{4.74}$$

where $\lambda_n(S/R)$ is a correction factor to the Stokes force arising from the presence of the plane. If the plane is a rigid plane wall, Cox and Brenner (1967), by employing singular perturbation theory, obtained an approximate expression for $\lambda_n(S/R)$ which applies to small gaps of $S/R \to 0$ and may be expressed as,

$$\lambda_n(S/R) = \frac{R}{S}\left(1 + \frac{S}{R}\ln\frac{R}{S} + 0.9713\frac{S}{R}\right) \tag{4.75}$$

Substituting this expression into 4.74 and comparing with 4.69, we recognize that the solution to the Reynolds' lubrication equation can be also regarded as a special case of the semi-infinite solution with the last two terms of equation 4.75 being truncated, which for small separation distances, only account for a very small part of the

total viscous force. Therefore, the viscous force for a dynamic liquid bridge at small separation distances can be reasonably approximated by the semi-infinite solutions.

Translation of a sphere parallel to a plane

For the translatory motion of a rigid solid sphere in a semi-infinite viscous fluid and parallel to a nearby rigid plane wall with a velocity, v_t, and at a separation distance, S, Goldman et al (1967a, 1967b) solved the Stokes equation and presented an analytical expression for the viscous force exerted on the sphere. For a small gap of $S/R \rightarrow 0$, asymptotic, lubrication-theory-like expressions for the viscous forces were derived as follows,

$$T_v = (\frac{8}{15} \ln \frac{R}{S} + 0.9588) 6\pi\eta R v_t \tag{4.76}$$

$$M_v = (\frac{2}{15} \ln \frac{R}{S} - 0.2527) 6\pi\eta R^2 v_t \tag{4.77}$$

where T_v is the viscous force and M_v is the viscous torque. Goldman et al (1967a) also carried out numerical calculations and indicated that the asymptotic solutions are in good agreement with the exact solutions for a ratio of the separation to the sphere radius S/R smaller than 0.3.

The parallel translation of a sphere in a semi-infinite viscous fluid resembles the tangential relative translation of the dynamic liquid bridge spheres if the rigid wall bounding the semi-infinite fluid is treated as a sphere with an infinite radius. On this basis, the semi-infinite solutions of equations 4.76 and 4.77 may be extended to approximate the viscous force due to the tangential translation of liquid bridge spheres.

Rotation of a sphere parallel to a plane

The relative rotation of spheres connected by a dynamic liquid bridge is very similar to the rotation of a sphere in a semi-infinite viscous fluid bounded by a rigid plane wall and about an axis parallel to the wall. This semi-infinite problem was also studied by Goldman et al (1967a). For a sphere of radius, R, at separation distance, S, from the wall and rotating with a velocity, ω, Goldman et al derived the approximate asymptotic expressions for the viscous force at small gaps as follows.

$$F_\omega = (\frac{1}{10}\ln\frac{R}{S} - 0.1895)8\pi\eta R^2\omega \tag{4.78}$$

$$M_\omega = (\frac{2}{5}\ln\frac{R}{S} - 0.3817)8\pi\eta R^3\omega \tag{4.79}$$

where F_ω is the viscous force and M_ω is the viscous torque.

As an approximation, equations 4.78 and 4.79 may be applied to evaluate the viscous resistance of a dynamic liquid bridge due to the relative rotation of the spheres by replacing R with R^*.

Chapter 5

DEM computer program TRUBAL

This chapter is primarily concerned with the application of the Distinct Element Method (DEM) to the simulation of dry and moist particle systems. The implementation of the contact force and liquid bridge force in the DEM simulation of particle systems using Cundall's (1988) computer program TRUBAL is discussed. At Aston, there are two new versions of TRUBAL. One version is the basic version which is used for the modelling of dry particle systems and the other is developed from the basic version to simulate moist particle systems with pendular liquid bridges. In this chapter, the latest developments and enhancements of the two versions of TRUBAL are also explained.

5.1 Introduction

TRUBAL is a computer program for the modelling of three-dimensional particle systems of elastic spheres by using the Distinct Element Method (DEM). It was originally written in FORTRAN by Cundall in 1979 and modified from time to time. In 1989, Cundall's latest version of TRUBAL was introduced to Aston. This version of TRUBAL is capable of modelling cuboidal assemblies of dry particles under different loading and unloading conditions. During a simulation, particles are randomly generated in a specified cubic space (unit cell or work-space). Periodic boundaries are introduced for the unit cell. The progressive movement of each constituent particle is calculated according to Newton's second law of motion using a time-dependent finite difference scheme. At the contacts between particles, the normal force-displacement is modelled according to the Hertzian theory and the tangential force-displacement is modelled as a linear spring. Extra facilities including servo-control, two dimensional mode option and rudimentary 2D plots were included. The earlier applications of TRUBAL have been mainly concerned with the simulation of quasi-static shear tests on dense sphere assemblies (Zhang and Cundall 1986, Cundall 1988, and Cundall et al 1989). The focus of their work was to establish micromechanically based constitutive laws for granular materials.

At Aston, extensive modifications and enhancements have been made to the computer program TRUBAL. One major modification is that more realistic interaction laws are now implemented. For particles without surface adhesion, the version of TRUBAL at Aston models the normal and tangential contact forces according to the theories of Hertz (see Johnson 1985) and Mindlin and Deresiewicz (1953) respectively. In the presence of adhesion, the theories of Johnson, Kendall and Roberts (1971) and Thornton (1991) are used for the normal and tangential contact forces between particles. Modelling of the liquid bridge forces for the simulation of moist particle systems has also been incorporated. The static forces of the liquid bridges

are modelled according to the toroidal approximation (Fisher 1926). The viscous forces are modelled according to the theory of Adams and Perchard (1985). Other modifications and enhancements made to TRUBAL at Aston include,

- Options to generate particles randomly or automatically. The former is used to generate random packings and the latter to generate regular packings.
- Options to generate particles in the unit cell or in a specified spherical region in the unit cell.
- Options to define smooth plane walls or spherical containers. A servo control mechanism is also available for walls.
- Options of a number of three-dimensional graphics output to view particles, velocities, displacements, contact forces, contact connection diagram and clusters etc.
- Options of screen graphics monitoring of energy partition, stress tensor, contact number and other general information.

At Aston, recent applications of TRUBAL have focussed on the simulation of agglomerate impact with a wall and collisions of two agglomerates (Yin 1992, Thornton and Kafui 1992, Kafui and Thornton 1993, Lian et al 1993a). The underlying objective is to establish the criteria for assessing the fracture, fragmentation and other degradation processes in terms of the physical and mechanical properties of the constituent particles and binding materials. Computer simulated compression and shearing tests of particulate assemblies have also been performed (Thornton and Sun 1993). At present, there are two versions of TRUBAL at Aston. They are capable of modelling a wide range of problems related to particle systems such as hopper flow, shear tests, diametrical compression tests and agglomerate collisions. One version is

the basic version of TRUBAL which is used for the simulation of dry particle assemblies and the other has been developed from the basic version in order to model the liquid bridge forces in moist particle systems. In the following, the development and enhancement of the latest versions of TRUBAL at Aston is discussed.

5.2 General structure of TRUBAL

5.2.1 Program structure

TRUBAL simulates the mechanical behaviour of granular assemblies consisting of spherical particles. To simulate a particulate assembly, the Distinct Element Method–a time-dependent finite difference scheme developed by Cundall (1971)–is applied to the cyclic calculation of the incremental contact forces and progressive movements of the spheres. For each calculation cycle, the translational and rotational accelerations of each of the constituent particles are given by Newton's second law of motion. Numerical integration is then performed over a small time-step to give updated velocities and displacements for each sphere. The velocities of each particle are used to find the relative approach between contacting particles which is in turn used to calculate the incremental contact forces (normal and tangential) according to contact force-displacement laws. The contact forces are resolved to obtain the out-of-balance forces on each particle, from which new accelerations of each particle are then calculated at the next time-step.

The basic structure of TRUBAL (as shown in figure 5.1) consists of four parts. The first part is the assembly generation module which is used to generate assemblies of particles and to define particle properties. The main part of TRUBAL is the cyclic simulation module, with which the evolution of contact forces and particle movements is simulated using the Distinct Element Method. In order to perform a wide

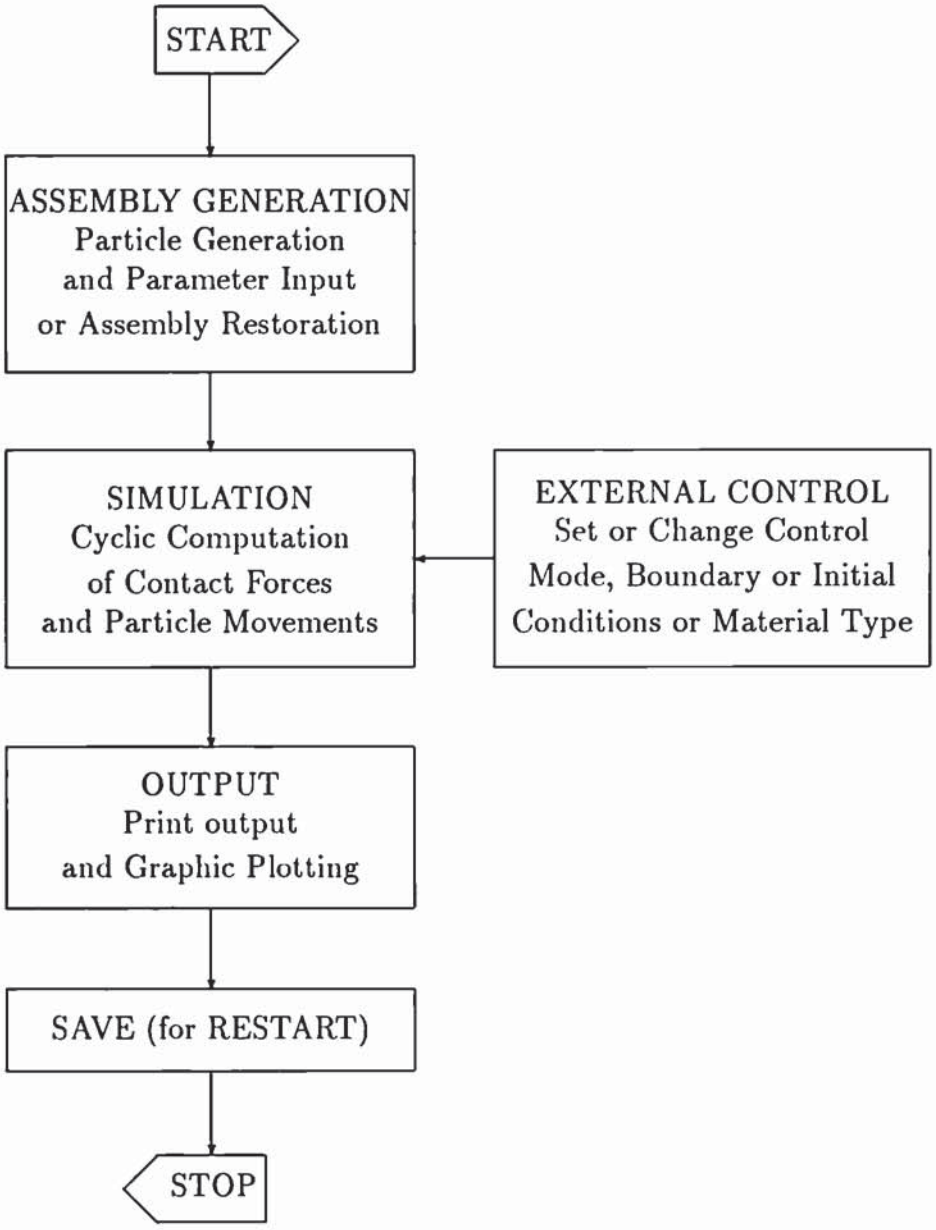

Figure 5.1: The program structure of TRUBAL

range of computer simulated experiments, the external control module is included in TRUBAL. Interactive laws and physical properties can also be changed. External control options can be set or changed at any time during the simulation. The fourth part of TRUBAL is the output module which provides a large selection of graphic and print out options to facilitate the interpretation of the simulated experimental results.

The basic structure of TRUBAL has not been changed since the program was first written by Cundall in 1979 (Cundall and Strack 1979b). However, many modifications have been made and many extensions provided in the present version of TRUBAL to permit a wide range of problems related to particle systems to be simulated.

TRUBAL uses operative commands. Each operative command is associated with the computation of one or a few basic steps related to the modelling of particle systems. The operative commands can be regarded as modules with different algorithmic capabilities. The advantage of introducing operative commands is that one can apply TRUBAL to different simulation problems of particle systems without changing the program code of TRUBAL. If necessary, modules of the operative commands can be enhanced and new ones can be added without interrupting other user's capabilities.

When executing TRUBAL, the user only needs to learn the mnemonic language of the operative commands and to form a specific operative command list for the given problem. The simulation procedure for the given problem is then controlled by the operative command list. A full list of the operative commands and their usage provided by the present versions of TRUBAL is given in appendix B.

5.2.2 Main memory map

The running of TRUBAL is initiated by the command **'START'** or **'RESTART'**. If the first command is **'RESTART'**, a previously-saved problem is restored. When

the '**START**' command is given on the first line of the command list, a new problem is initiated, for which the scale of the particle assembly to be generated is specified by the following parameters,

$$l_x, l_y, l_z, Mbox, Msphere, Mwall$$

where l_x, l_y and l_z specify the size of the rectangular parallelepiped that defines the workspace. $Msphere$ and $Mwall$ are the maximum number of spheres and walls that may be required to be generated and $Mbox$ is the number of boxes that the workspace is sub-divided into. TRUBAL divides the workspace into small boxes in such a way that both the number of boxes and the size of a box in each axial direction are the same. Hence the actual number of boxes that the workspace is divided into is given as $Nbox = (int\sqrt[3]{Mbox})^3$.

TRUBAL uses a main memory A which is partitioned to store all the arrays of sphere data, wall data, box data, link lists and contact data. Each array is dynamically dimensioned according to the number of boxes and the maximum number of spheres and walls requested by the '**START**' command for a given problem. The main memory map is shown by figure 5.2. $M5$ is the upper limit address of the main memory and is declared in the program. If the capacity of the main memory is exceeded, an error message is printed and the program stops. The main memory limit needs to be changed to a higher value if overflow occurs.

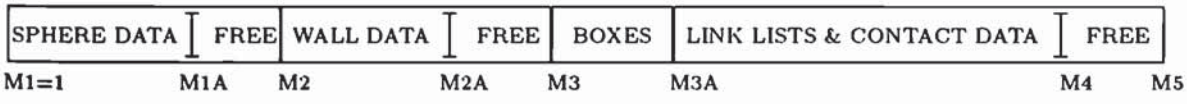

Figure 5.2: The memory map of the main array

$M2, M3$ and $M3A$ are dynamic addresses pointing to the upper limit of the arrays of sphere data, wall data and box data respectively. They are determined according to the following equations,

$$M2 = M1 + Msphere * Nvarb \tag{5.1}$$

$$M3 = M2 + Mwall * Nvarw \tag{5.2}$$

$$M3A = M3 + 2 * Nbox \tag{5.3}$$

where $Nvarb$ is the number of variables stored in each sphere data array and $Nvarw$ is the number of variables stored in each wall data array.

The memory for sphere data is allocated between $M1$ and $M2$ with the lowest address at $M1$, and the wall data between $M2$ and $M3$ with the lowest address at $M2$. The actual storage taken by the sphere data and wall data, however, is dynamically located depending on the actual number of spheres generated and walls defined. The upper addresses of their actual storage are adjusted according to,

$$M1A = Nball * Nvarb \tag{5.4}$$

$$M2A = M2 + Nwall * Nvarw \tag{5.5}$$

where $M1A$ and $M2A$ are the actual highest addresses of sphere data and wall data respectively, $Nball < Msphere$ and $Nwall < Mwall$ are the actual number of particles and walls generated.

The storage for link lists and contact data is allocated between $M3A$ and $M5$. The lower address is at $M3A$ and the higher address, $M4$, moves up according to the number of links and contacts detected and is given by the following equation,

$$M4 = M3A + 2 * Nlink + Ncont * Nvarc \tag{5.6}$$

where $Nvarc$ is the number of variables stored in each contact data array, $Nlink$ is the number of links detected and $Ncont$ the number of contacts detected ($Ncont$ includes near-contacts which are not currently transferring load, see section 5.5).

5.2.3 Arrays of sphere data, wall data and contacts

In the current version of TRUBAL, the dimension size of one sphere data array is set to $Nvarb = 30$. The information stored in the 30 elements of a sphere data array $B(Nvarb)$ are as follows,

B(1) to B(3):	Coordinates of the sphere x_i
B(4) to B(6):	Accumulated displacement increments Δx_i
B(7) to B(9):	Components of translation velocity v_i
B(10) to B(12):	Angular displacement Φ_i
B(13) to B(15):	Accumulated angular displacement increment $\Delta\Phi_i$
B(16) to B(18):	Components of rotational velocity ω_i
B(19) to B(21):	Components of out-of-balance force F_i
B(22) to B(24):	Components of out-of-balance moment M_i
B(25):	Code indicating material and size type $ITYPM, ITYPS$
B(26) to B(30):	Free.

The dimension of one wall data array $W(Nvarw)$ is set to $Nvarw = 41$. Since both platen wall and spherical container (wall) can be handled in the current version of TRUBAL (see section 5.4), the information contained in a wall data array is correspondingly different. If it is a platen wall, the data stored in the array are, the following,

W(1) to W(4):	Parameters d, a, b, c which define a plane wall as $d = ax + by + cz$
W(5):	Normal force F_s (set by servo)
W(6):	Maximum normal velocity of the wall v_m (set by servo)
W(7) to W(9):	Components of wall translation velocity v_i
W(11):	Measured normal force on the wall F_n
W(12):	code indicating the wall type (= 1)
W(14):	Gain parameter used by servo control
W(15) to W(17):	Accumulated displacement increment of the wall Δx_i
W(19) to W(21):	Components of out-of-balance force F_i
W(25):	Code indicating material type $ITYPM$
Others:	Free.

If it is a spherical container (wall), the information contained is the following,

W(1) to W(4):	Parameters d, a, b, c which define a spherical container as $d^2 = (x-a)^2 + (y-b)^2 + (z-c)^2$
W(5):	Total radial force F_s set by servo
W(6):	Maximum radial velocity v_m (set by servo)
W(7) to W(9):	Components of wall translation velocity v_i
W(10):	Radial velocity of the spherical wall v_r
W(11):	Measured radial force on the wall F_n
W(12):	code indicating the wall type (= 2)
W(14):	Gain parameter used by servo control
W(15) to W(17):	Accumulated wall displacement increment Δx_i
W(18):	Accumulated radial displacement increment of the wall Δd
W(19) to W(21):	Components of out-of-balance force F_i
W(25):	Code indicating material type $ITYPM$
Others:	Free.

There are two versions of TRUBAL at Aston. For the version that simulates dry particle systems, there are 23 elements for a contact data array $C(Nvarc)$ (i.e. $Nvarc = 23$) and the data stored in the contact array are,

C(1) to C(3):	Components of the tangential force at the contact T_i
C(4):	Normal contact force (Hertz or JKR) P
C(5) to C(6):	Links pointing to the ball or wall addresses
C(7) to C(9):	Components of the relative tangential displacement δ_i
C(10):	Relative tangential displacement δ
C(11):	Tangential force at the contact T
C(12):	Tangential force from which unloading commenced, T_1
C(13):	Tangential force from which reloading commenced, T_2
C(14):	Accumulated distance that the tangential force falls short of its equivalent curve of constant normal force, see Thornton and Randall (1988)
C(15):	Tangential peeling force in the presence of adhesion, T_p
C(16):	Interfacial surface energy γ
C(17):	Radius of the contact area, a
C(18):	Code indicating the direction of the tangential force,CDF
C(19) to C(20):	Free
C(21):	Normal stiffness of the contact
C(22):	Tangential stiffness of the contact
C(23):	Link pointing to the address of next contact.

For the version of TRUBAL that simulates moist particle systems, each contact array is expanded to 31 elements (i.e. $Nvarc = 31$) in order to model the liquid bridge forces. $C(19)$ and $C(23)$ are also changed. The data stored in the expanded and modified elements are,

C(19): Volume of liquid held at the contact, V_l

C(23): Rupture distance of the liquid bridge, S_c

C(24): Static force of the liquid bridge, F_c

C(25): Normal component of viscous force of the liquid bridge, F_v^n

C(26): Tangential component of viscous force of the liquid bridge, F_v^t

C(27): Half filling angle of the liquid bridge with the sphere C(5), ϕ_1

C(28): Free

C(29): Energy required to break the static liquid bridge bond

C(30): Gap or overlap between the two spheres α

C(31): Link pointing to the address of next contact.

5.3 Assembly generation

In Cundall's 1988 version of TRUBAL, the particles of a simulated assembly were generated randomly over the whole region of the working space of which the boundaries were periodic. To generate a particle randomly, three random numbers are selected in the closed intervals of $[0, l_x]$, $[0, l_y]$ and $[0, l_z]$ and are assigned as the coordinates of the centre of the particle. If the newly generated particle overlaps with previously-generated particles, it is rejected. Otherwise, it is added to the assembly. The process is repeated until the desired number of particles are generated or the limit set to the number of tries is exceeded.

The current version of TRUBAL generates the particles in two different ways. In addition to the random generation method, an option for automatic generation of regular packings is now provided. The automatic generation of a regular packing is achieved by a scheme as follows. One specifies the coordinates of the centre of a particle with given size-type and material-type. The particle is located at the lower back left of the unit cell. The remaining particles of the same size-type and

material-type are automatically generated by placing them at given increments in x-, y- and z-directions. Overlap checks are also carried out during the auto-generation of a regular packing. The basic auto-generated structure is orthorhombic. To generate body-centred orthorhombic packings, one should use the auto generation command repeatedly by specifying the location of the lower back left particle at different positions. The following example shows how to generate a regular packing of body-centred cubic by using the automatic generation command twice,

start *0.1 0.1 0.1 1000 2000 2 log*

rad *0.004330127 1*

agen *1 1 1 0 0 0 0.01 0.01 0.01*

agen *1 1 1 0.005 0.005 0.005 0.01 0.01 0.01*

where the size of the unit cell is $0.1 \times 0.1 \times 0.1$, '**rad**' is the command that specifies the radius of a size-type particles (where the radius of size-type 1 particles is set to be equal to 0.004330127), '**agen**' is the command for automatic generation of regular packings (refer to Appendix B Command List).

Another option provided in the present version of TRUBAL for assembly generation is to generate particles in a specified spherical region within the working space (unit cell). Using the agglomerate command, the current version of TRUBAL allows one to define up to two spherical regions within which particles may be generated to form agglomerates. The agglomerate command must be given before the particle generation commands and the agglomerate-type (i.e. which spherical region) must be specified. During particle generation, a location check is carried out before the overlap check. If the newly generated particle resides outside the spherical region corresponding to the specified agglomerate-type, it is rejected. Otherwise, overlap check is performed and the particle is accepted if it does not overlap with existing particles.

If the agglomerate command for defining the spherical region(s) is ignored before specifying the particle generation command particles will be generated in the whole region of the working space (unit cell). However, the agglomerate-type in the particle generation command still needs to be specified as 1. During particle generation, because the spherical region corresponding to the agglomerate is not defined, the location check is not used.

It is also possible to create an individual particle at a specified position using the **'CREATE'** command available in the original version of TRUBAL. This command has now been modified to incorporate an overlap check.

5.4 Introducing walls

In Cundall's version of TRUBAL, rough 'walls' are provided by two layers of 'fixed' particles that are intersected by two specified planes. During calculations, particles 'fixed' by the two upper and lower planes perpendicular to the y-axis are only allowed to move according to a specified velocity. The mechanical and physical properties of the rough wall are difficult to characterize and vary greatly at different positions.

The present version of TRUBAL defines walls in a totally different way. Instead of having rough walls, two types of smooth and continuous 'massive' elastic walls are introduced. One can define either smooth plane walls perpendicular to one of the x-, y- and z- axes defined as,

$$x_i = d \tag{5.7}$$

or smooth hollow spherical walls (containers) defined as,

$$(x-a)^2 + (y-b)^2 + (z-c)^2 = d^2 \tag{5.8}$$

where the centre of the hollow sphere wall is located at (a, b, c) and the radius of the hollow sphere is d.

Translational movement of both types of walls is achieved by specifying the appropriate velocities. The hollow spherical wall is also allowed to have a radial velocity so that the wall can shrink or enlarge by changing its radius. A servo control mechanism is also introduced for walls with which the velocity is continuously adjusted so that the difference between the calculated normal (platen wall) or radial (spherical container) force acting on the wall and the required force is minimized.

A wall is generated by the wall definition command **'DWALL'**. During cyclic calculations one can also change some parameters of a previously defined wall with the wall alteration command **'AWALL'**.

5.5 Contact searching in the DEM

The simulation of particle systems requires cyclic calculations of particle displacement increments and contact force increments. For the calculation of contact forces between particles, an efficient searching scheme is needed to detect the contacts between particles. Because a particle cannot make contact with particles which are far away from it, the principle is to search for contacts with only those particles lying in the local vicinity. The contact detection scheme is described below.

5.5.1 Initial particle generation

In the Distinct Element Method, the workspace or periodic cell is divided into $Nbox$ boxes or sub-cells where $Nbox$ is specified by the **'START'** command and is so chosen that the size of the boxes should be larger than the diameter of the largest sphere.

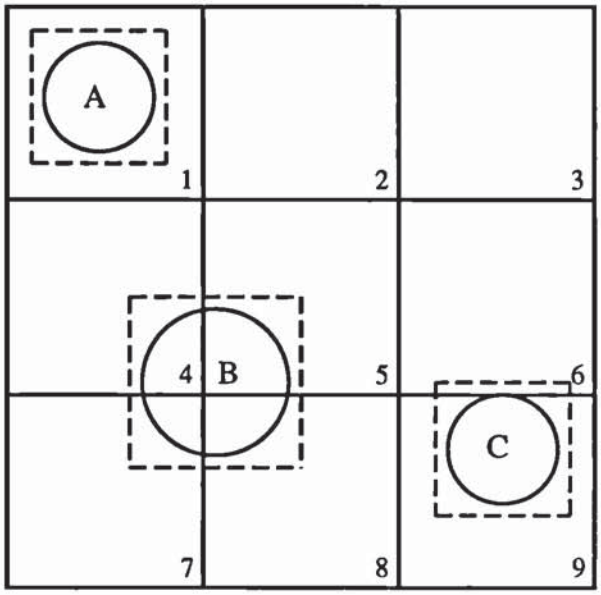

Spheres	Box entries
A	1
B	4, 5, 7, 8
C	6, 9

Figure 5.3: The mapping scheme for spheres

However, in order for the Distinct Element Method to search the contacts efficiently, the box size should normally be less than twice the largest sphere diameter.

The first step in the contact detection scheme is to form link lists for each box by mapping all constituent particles into the appropriate boxes. A spherical particle is said to be mapped into a box if one or more corners of the circumscribing cube of dimension $2(R + TOL)$ falls into the box. Because the maximum radius of the constituent particles is restricted such that $R_{max} < (DEL/2 + TOL)$, where DEL is the dimension of the boxes, the maximum number of boxes in which a particle has entries is eight. The mapping scheme for spheres is shown in figure 5.3 for the 2-D case.

In fact, each particle is mapped twice. The first mapping uses the circumscribing cube as the same dimension of the sphere diameter $2R$ and the second one uses that of a dimension of $2(R + TOL)$. Through the first mapping scheme, link lists are

formed for each box to locate the addresses of all spheres that are mapped into it. For the box data allocated in the main memory from $M3$ to $M3A$, each box has two addresses. The lower address stores the start of a particle link list. The upper address stores the start of a contact link list. The link list for a box is formed in the following way. When particles are first generated (or created), the address of a sphere that first maps into a box is stored in the lower address of that box. When another sphere is mapped into the same box, two links are allocated from $M4$ to $M4+1$ and $M4$ (the end pointer of the link lists and contact arrays which is initially set to $M3A$) is updated to $M4+2$. The higher link stores the address of the first sphere. The lower link stores the address of the second sphere. The content of the lower box address is then updated by the address of the lower link (i.e. $M4-2$). For the third sphere that maps into the box, another two links are allocated from the updated address of $M4$ and $M4+1$ and $M4$ is updated again by moving up another two elements. The higher link stores the address of the second sphere and the lower link holds the address of the third sphere. The lower memory of the two previously created links is updated to store the lower address of the newly created links. The procedure is continued until the link list for all spheres that map into the box has been created. At the end of the link list, both the last lower and higher links store the addresses of the two spheres that last mapped into the box. In this way, the link lists identify those spheres in near proximity to each other.

The second step is the contact searching. Since possible contacts exist only between those particles which are mapped into the same box, contact searching needs only to be performed between those spheres that are held in the link lists of each box. With the Distinct Element Method, the contact search is in fact performed in the same process during the mapping for link list forming. Each time when a sphere is mapped into a box, the spheres that previously mapped into the same box are searched and their distances to the newly mapped sphere are calculated. Any sphere in the link list lying within a specified gap distance TOL of the newly mapped sphere

is regarded as a potential contact. The gap centre between the two spheres is defined as the contact point which is also mapped into the boxes. A contact array is allocated for the contact from the address $M4$ to $M4 + Nvarc$. $M4$ is updated by moving up $Nvarc + 1$ elements. For a contact that first maps into a box, the address of the contact array is stored in the higher box memory. The address of the second contact that maps into the same box is stored in the last memory of the first contact array. The procedure is continued until the contact arrays for each box are established. For the last contact array of each box, a '0' is stored in the last memory.

If the currently mapped sphere is very close to the border of the mapped boxes, it may also have potential contacts with the spheres that are mapped into other boxes in close proximity with the sphere. For instance, the sphere C in figure 5.3 may have potential contacts with the spheres that reside in box 6. In order to detect the possible contacts of a sphere with those spheres that reside in neighbouring boxes, the second mapping uses the circumscribing cube with the dimension of $2(R+TOL)$. This enables the mapping of a sphere into its neighbouring boxes and the detection of the spheres (held in the link list of the neighbouring box) that may be in close contact with the currently mapped sphere. The second mapping is also useful to retrieve the old links of a remapped sphere and delete them when the box entries of the remapped sphere are changed. Remapping is only necessary when the maximum component of the accumulated displacement increment of a sphere exceeds $XRES$ ($XRES < TOL/2\sqrt{3}$), see section 5.5.2.

The whole scheme for the storage of box data, link lists and contact arrays is illustrated by figure 5.4.

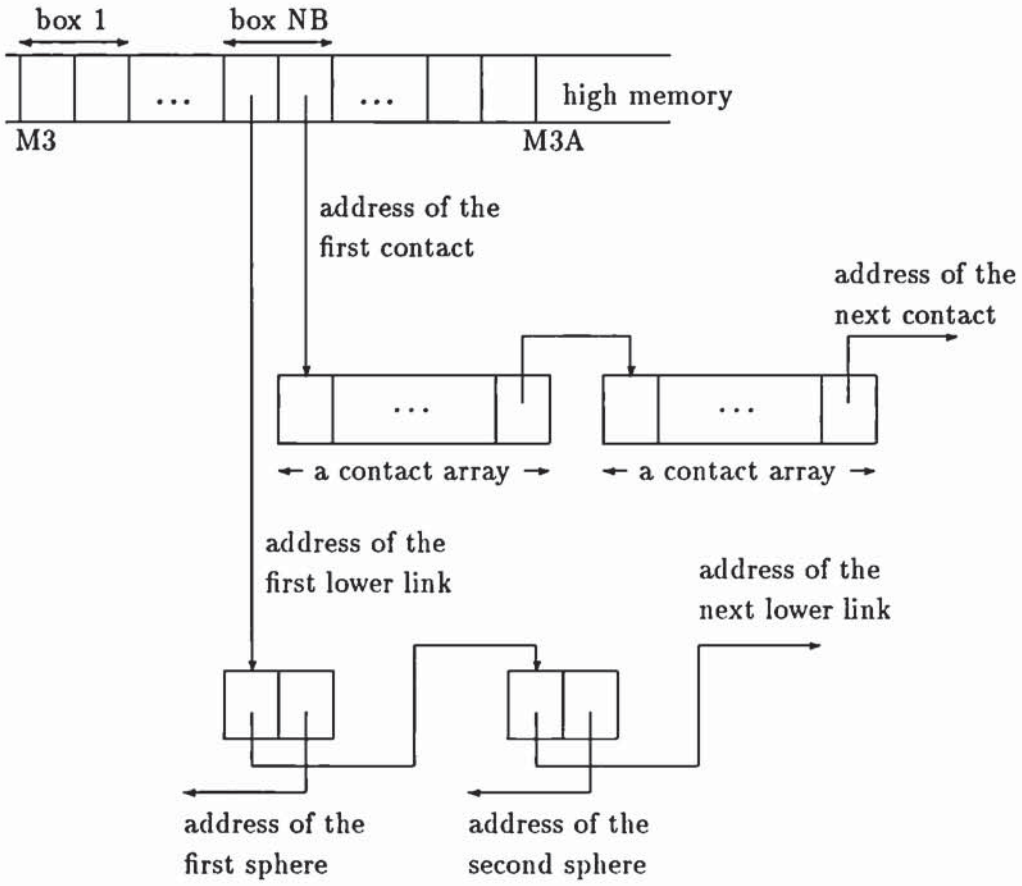

Figure 5.4: The storage scheme for link lists and contact arrays.

5.5.2 Remapping

Once the link lists and contact arrays are established and allocated, the next particle remapping and search for new contacts is only necessary after several time steps when the maximum accumulated component of the translational displacement increment of any constituent particles exceeds $XRES$ ($XRES < TOL/2\sqrt{3}$), where TOL is a tolerance set for the sphere mapping. If this condition is false then the maximum relative movement between any pair of spheres is less than TOL. During the previous contact search, if those spheres were not detected as potential contacts, the gaps between them must have been larger than TOL at that time. Consequently, they will still not be in contact and will not contribute any forces until the next contact search

is triggered. Before the the next sphere mapping and contact searching is necessary, the cyclic calculation of contact force increments needs to be only performed for the contact arrays that were established and allocated previously. By avoiding sphere mapping and contact searching at every timestep a lot of computer time is saved.

Whenever the maximum component of the accumulated translational displacement increment of a sphere exceeds $XRES$, the sphere is remapped twice again. During the first mapping, the circumscribing cube of the same dimension as the sphere diameter $2R$ is used. The link lists of the boxes that the sphere mapped into are checked and if any of the link list does not contain the address of the remapped sphere, it is added. Contact searching is then performed by mapping the sphere again but using the circumscribing cube of dimension $2(R+TOL)$. Any contact of the remapped sphere with other spheres that is not contained in the corresponding contact arrays is added. For the remapped sphere, however, there may be a need to delete its old links or contact arrays. The problem arises when the remapped sphere and its contact points moves from one box to another. Since for the box that the sphere previously mapped, the sphere is not mapped into again during the remapping, the two links contained in the box should be deleted and so should the contact arrays. The deletion of old links and contact arrays are described below.

Since the maximum component of the accumulated displacement increment of the remapped sphere is $XRES < TOL/2\sqrt{3}$, the second mapping using the circumscribing cube of dimension $2(R+TOL)$ not only identifies the boxes the remapped sphere resides, but also retrieves the boxes that the sphere previously mapped into. But with the first mapping, the remapped sphere is only mapped into the boxes the sphere currently resides. For any corner of the circumscribing cubes, if the box entry of the first mapping $NBSAV$ is different from that of the second mapping $NBNEW$ (see figure 5.5), then $NBNEW$ indicates the boxes that the sphere had previously been mapped into. As a result, the two links contained in the link list of box $NBNEW$ should be

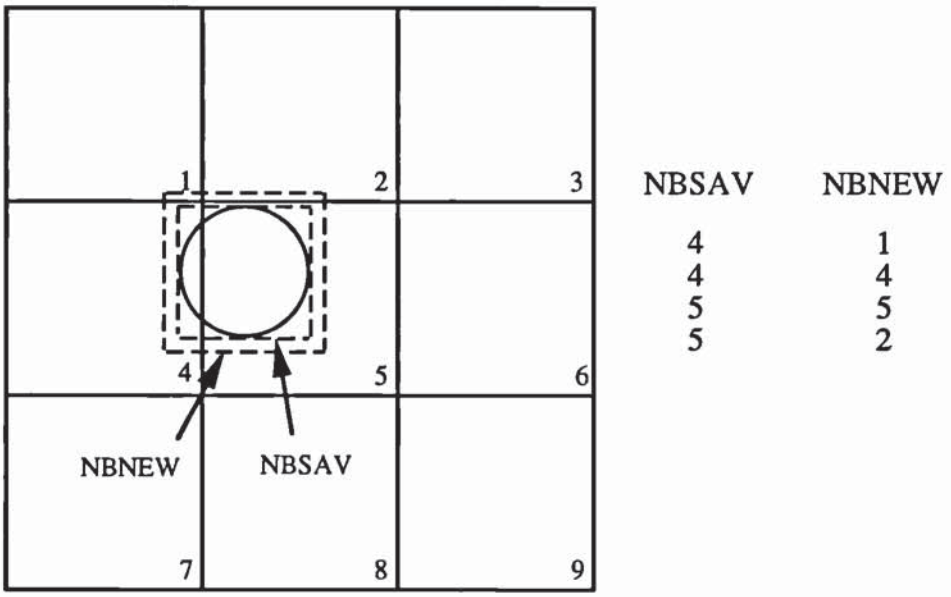

Figure 5.5: New and old box entries of a remapped sphere

deleted. The two links are deleted by setting the higher link to '0' and the lower link to $NEML$. $NEML$ is updated by the lower address of the deleted two links, where $NEML$ is the indicator pointing to the beginning address of the deleted link list and is initially set to '0'. The content of the deleted lower link is now stored in the lower link of the two links preceding the deleted ones. For the deletion of contact arrays, a similar procedure is used. The address of the currently deleted contact array is indicated by $NEMC$ which is also initially set to '0'. The address of the previously deleted contact array is stored in the last element of the currently deleted contact array.

Every time a sphere is reboxed, any memory space available due to deleted links or contact arrays is first used if new links and contacts are detected. Free links and contact arrays due to deleted links and contact arrays are available when the indicators $NEML$ and $NEMC$ are non-zero. If there are no free links and contact arrays, however, the free space between $M4$ and $M5$ will be used in the normal way.

5.5.3 Contacts with walls

In the new versions of TRUBAL at Aston, because continuous 'massive' walls are incorporated, contacts between particles and walls need to be considered. In order to deal with walls in a manner consistent with the handling of particles, a similar scheme for the mapping of walls is used. The mapping scheme for walls is shown by figure 5.6.

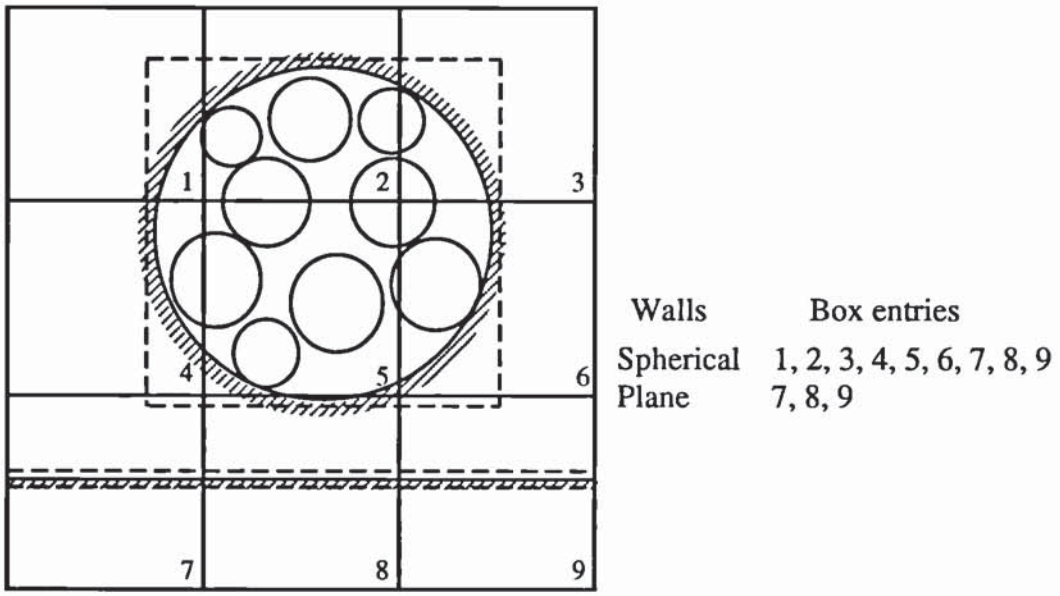

Figure 5.6: Mapping scheme for walls

A plane wall is mapped into a box if any part of the wall (with the given tolerance TOL) falls into the box. A hollow spherical container wall is said to be mapped into a box if any part of the circumscribing cube of dimension $2(d + TOL)$ falls into the box, where the tolerance TOL is only used for the second mapping. A separate subroutine in the program was written to handle the mapping of walls. When a wall is mapped into a box, the address of the wall is inserted into the link list of the box by allocating another two links. During the second mapping for contact searching,

the distances between the wall and the neighbouring spheres held in the link list are also calculated to detect possible contacts. All the other procedures for allocating or deleting links and contact arrays are the same as for contacts between particles.

5.6 System evolution

5.6.1 Particle displacements

TRUBAL uses the finite difference method to simulate the evolution of contact forces and particle movements. The progressive movement of each constituent particle is modelled by Newton's second law of motion. For a particle over an interval of time step Δt, the out-of-balance forces and hence the accelerations are assumed to be constant. Consequently, Newton's equations of motion for the particle with global damping are given as follows,

$$F_i + mg_i - \beta_g \frac{v_i^{new} + v_i^{old}}{2} = m \frac{v_i^{new} - v_i^{old}}{\Delta t} \tag{5.9}$$

$$M_i - \beta_g \frac{\omega_i^{new} + \omega_i^{old}}{2} = I \frac{\omega_i^{new} - \omega_i^{old}}{\Delta t} \tag{5.10}$$

from which the updated velocity components are given as,

$$v_i^{new} = \frac{m/\Delta t - \beta_g/2}{m/\Delta t + \beta_g/2} v_i^{old} + \frac{F_i + mg_i}{m/\Delta t + \beta_g/2} \tag{5.11}$$

$$\omega_i^{new} = \frac{I/\Delta t - \beta_g/2}{I/\Delta t + \beta_g/2} \omega_i^{old} + \frac{M_i}{I/\Delta t + \beta g/2} \tag{5.12}$$

where $i = 1, 2, 3$ indicates the three components in $x-, y-$ and $z-$ coordinate directions, β_g is the global damping coefficient, Δt is the time-step, F_i are the components of the out-of-balance force, M_i are the components of the out-of-balance momentum,

g_i are the components of gravity, m is the mass of the sphere, I is the rotational inertia of the sphere, v_i^{new} and ω_i^{new} are the updated components of the linear and rotational velocities and v_i^{old} and ω_i^{old} are the previous ones.

Using the updated velocity components of each sphere, the components of the linear and rotational displacement increments of each particle in the time-step are accordingly obtained from,

$$\Delta x_i = v_i^{new} \Delta t \tag{5.13}$$

$$\Delta \Phi_i = \omega_i^{new} \Delta t \tag{5.14}$$

which are then added to update the coordinates and rotational displacements of each sphere. For the linear translation, the coordinates of a sphere are determined by two parts. The first part is the original coordinates of the sphere at the previous mapping and the other part is the accumulated displacement since the last mapping. When the newly obtained linear displacement increment is added to the accumulated displacement, a check is also made about the maximum component of the accumulated displacement. If it exceeds $XRES(< TOL/2\sqrt{3})$, the sphere is reboxed. The accumulated displacements are set to '0' after they have been added to the original coordinates of the sphere.

5.6.2 Solid contact forces

The interaction force between each pair of contacting spheres is computed in an incremental way. In the case of two spheres contacting one another, the relative movement at the contact has three components, the relative normal approach along the centre line of the two spheres, the relative tangential displacement between the two particle centroids and the relative rotation of the two spheres. Because the area

of the contact is very small, the twisting resistance at the contact due to the relative spin about the line joining the centroids of the two spheres is ignored and hence only the normal and tangential contact forces are considered in the current version of TRUBAL.

For a pair of spheres in contact, if the linear and rotational velocities are denoted as v_i^A, ω_i^A and v_i^B, ω_i^B respectively, the relative normal displacement increment at the contact in a time step can be given as,

$$\Delta\alpha = (v_i^B - v_i^A)n_i\Delta t \tag{5.15}$$

where $i = 1, 2, 3$ indicates the three coordinate directions and n_i is the component of the unit vector normal to the contact plane and directed from sphere A to sphere B.

In a time-step, the component of the relative tangential displacement increment at the contact between the two sphere is,

$$\Delta\delta_i = (v_i^B - v_i^A)\Delta t - \Delta\alpha n_i$$

$$-(\omega_{i+1}^A n_{i+2} - \omega_{i+2}^A n_{i+1})R_A\Delta t - (\omega_{i+1}^B n_{i+2} - \omega_{i+2}^B n_{i+1})R_B\Delta t \tag{5.16}$$

where R_A and R_B are the radii of the two spheres and all the subscripts $i, i+1, i+2$ should be rotated from 1 to 3.

The updated normal force at the contact is given as,

$$N^{new} = N^{old} + \Delta N \tag{5.17}$$

where ΔN is the normal force increment which is obtained from (3.41) which applies to both adhesive and non-adhesive spheres.

The computation of tangential force increment due to the tangential displacement increment differs according to the interaction laws used. If Mindlin's no-slip solution is used, the tangential force-displacement relationship is linear elastic. As a result, the resultant tangential force increment can be calculated from its components by substituting $\Delta\delta_i$ into equation 3.112, viz.

$$\Delta T_i = 8G^* a \Delta\delta_i \tag{5.18}$$

However, adding the tangential force increment to the previous tangential force is complicated due to the fact that the contact plane may be rotating. Over a time-step, the rotation of the contact plane can be derived as,

$$\Omega_i = [(v^B_{i+2} - v^A_{i+2})\Delta t - \Delta\alpha n_{i+2}]\frac{n_{i+1}}{Z_m} - [(v^B_{i+1} - v^A_{i+1})\Delta t - \Delta\alpha n_{i+1}]\frac{n_{i+2}}{Z_m} \tag{5.19}$$

where Z_m is the distance between the centroids of the two spheres and the subscripts $i, i+1, i+2$ should also be rotated from 1 to 3.

Hence, the components of the previous tangential force and displacement are re-calculated using

$$T_i = \Omega_{i+1} T^{old}_{i+2} - \Omega_{i+2} T^{old}_{i+1} \tag{5.20}$$

$$\delta_i = \Omega_{i+1} \delta^{old}_{i+2} - \Omega_{i+2} \delta^{old}_{i+1} \tag{5.21}$$

where T^{old}_i and δ^{old}_i are the components of the previous tangential force and displacement prior to rotation.

If the partial-slip solution of Mindlin and Deresiewicz is used for the tangential force, the calculation becomes much more complicated because the force-displacement law is history dependent. As a result of the nonlinear hysteretic interaction rule, the

loading history of each component is different and the loading history of the resultant tangential force differs from its components. Consequently, the partial-slip solution cannot be applied to each component independently. The resultant tangential force increment has to be calculated directly.

In three dimensions, the resultant tangential displacement can have any orientation in the contact plane. In order to identify the loading path of the resultant tangential force, the direction of the resultant tangential displacement has to be identified. In the current version of TRUBAL, the direction of the resultant tangential displacement at the first time step of each contact is regarded as positive. For any subsequent time step, suppose the previous resultant tangential displacement is δ and its orientation, after correction for the rotation of the contact plane, is defined by the components δ_i. It follows that the updated tangential displacement components due to the incremental displacement should be given as,

$$\delta_i^{new} = \delta_i + \Delta\delta_i \tag{5.22}$$

The updated resultant tangential displacement is given by the following equation,

$$\delta^{new} = sign(\delta) sign(\delta_i \Delta\delta_i) \sqrt{\delta_i^{new} \delta_i^{new}} \tag{5.23}$$

The sign of the updated resultant tangential displacement is determined as shown by figure 5.7, where the previous tangential displacement is taken as positive and the updated tangential displacement is negative. Suppose the contact plane is divided into two regions by the line normal to the previous tangential displacement. If the updated tangential displacement lies on the same side of the previous one, the sign of the updated resultant tangential displacement is the same as that of the previous one and $sign(\delta_i \Delta\delta_i)$ in equation 5.23 is positive. Otherwise, $sign(\delta_i \Delta\delta_i)$ is negative and the sign of the updated resultant tangential displacement changes to the opposite sign to that of the previous one.

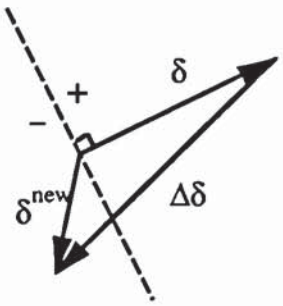

Figure 5.7: The sign of the updated resultant tangential displacement

From the updated resultant tangential displacement, one obtains the magnitude of the resultant tangential displacement increment as,

$$\Delta\delta = \delta^{new} - \delta \tag{5.24}$$

which is used to obtain the resultant tangential force increment ΔT by using equations 3.109–3.111. The resultant tangential force is now updated as,

$$T^{new} = T + \Delta T \tag{5.25}$$

The updated resultant tangential force is compared with the sliding criterion. If the sliding criterion is exceeded then the tangential force is reset to the limiting value. The direction of the resultant tangential force is assumed to be in the same direction as the tangential displacement and its components are given as,

$$T_i^{new} = T^{new} \frac{\delta_i^{new}}{|\delta^{new}|} \tag{5.26}$$

From the updated normal and tangential contact forces, the contribution to the out-of-balance force of each sphere is obtained as,

Sphere A $$F_i^A = -N^{new} n_i - T_i^{new} \tag{5.27}$$

$$M_i^A = R_A(n_{i+1}T_{i+2}^{new} - n_{i+2}T_{i+1}^{new}) \tag{5.28}$$

Sphere B $$F_i^B = N^{new} n_i + T_i^{new} \tag{5.29}$$

$$M_i^B = -R_B(n_{i+1}T_{i+2}^{new} - n_{i+2}T_{i+1}^{new}) \tag{5.30}$$

5.6.3 Liquid bridge forces

The binding forces of liquid bridges are calculated after the calculation of contact forces. This is discussed in the next section (Section 5.7).

5.7 Implementing liquid bridge forces

5.7.1 Introducing liquid bridges

Pendular liquid bridges may be introduced or removed at any stage of the cyclic calculations. Liquid bridges are introduced by the command **'LIQUID'**, which specifies the liquid volume, surface tension, contact angle and viscosity of the liquid bridges. The same command may also be used to remove previously introduced liquid bridges if the liquid volume is set to zero. When the command **LIQUID** is issued, the contact arrays are searched. For a contact array, if the contact is a solid contact, a liquid bridge is formed. Otherwise, a quantity of liquid is still assigned, but the liquid bridge will not be formed until the potential contact becomes a solid contact.

The rupture distance of each newly introduced liquid bridge is calculated. For a liquid bridge between two unequal sized spheres of radius R_1, R_2, the rupture distance $S_c = S_{c1} + S_{c2}$ may be related to the liquid volume by,

$$S_{ci} = \frac{1}{2}(1 + 0.5\theta)\sqrt[3]{2V_i} \tag{5.31}$$

where $i = 1$ or 2 and V_1, V_2 are the half liquid volumes that the liquid bridge is fictitiously divided into.

From the relation $V = V_1 + V_2$, it follows that

$$V = \frac{1}{2}[(\frac{2S_{c1}}{1 + 0.5\theta})^3 + (\frac{2S_{c2}}{1 + 0.5\theta})^3] \tag{5.32}$$

However, for a given quantity of liquid, this equation is not sufficient to evaluate S_{c1}, S_{c2}. Another relationship between S_{c1} and S_{c2} is required. This relationship is obtained through the following procedures.

For a given set of the sphere radii R_1, R_2, half liquid volume V_1, the half rupture distance S_{c1} was evaluated using the relationship 5.31 and the half-filling angle was determined using an iteration scheme based on the toroidal approximation. From geometrical considerations, the half rupture distance S_{c2} and hence half liquid volume V_2 were accordingly determined. This procedure was repeated for different sphere radii R_1, R_2 and half liquid volume V_2 to obtain a set of half rupture distances S_{c1}, S_{c2}.

Figure 5.8 shows the dependence of the ratio of half rupture distances S_{c2}/S_{c1} on the dimensionless liquid volume V/R_1^3 for different values of the ratio of sphere radii. It can be seen that the relationship between the ratio of half rupture distances and the dimensionless liquid volume can be best fitted by a family of curves in the form of

$$\ln(\frac{S_{c2}}{S_{c1}}) = c_0 + c_1 \ln(\frac{V}{R_1^3}) + c_2 \ln^2(\frac{V}{R_1^3}) \tag{5.33}$$

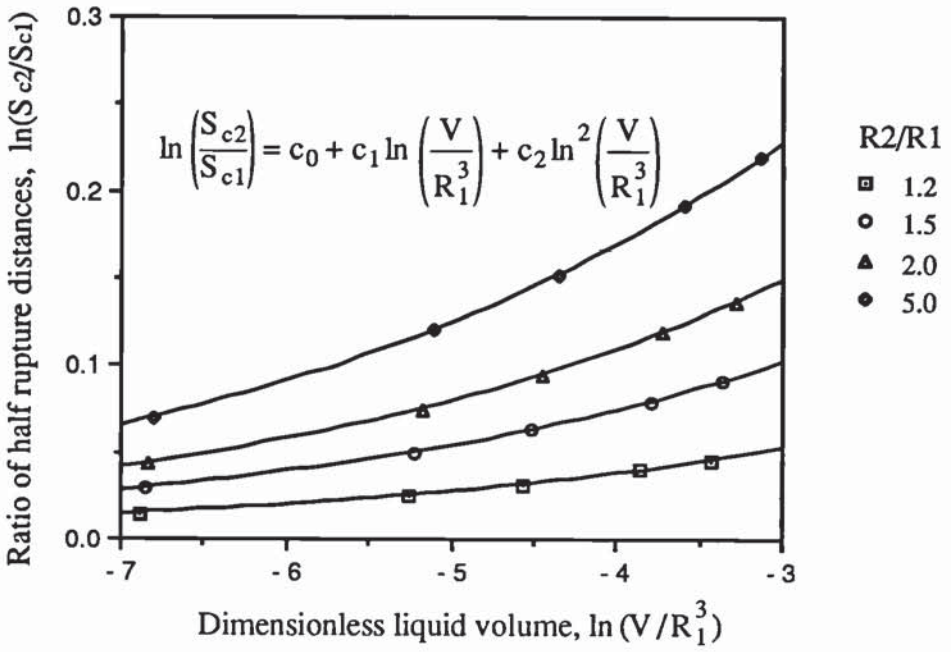

Figure 5.8: The ratio of half rupture distances as a function of the dimensionless liquid volume for different values of the ratio of sphere radii.

R_2/R_1	c_0	c_1	c_2
1.2	0.11051	0.02401	0.00146
1.5	0.21350	0.04588	0.00277
2.0	0.30951	0.06583	0.00395
5.0	0.46645	0.09722	0.00573

Table 5.1: Fitting coefficients of c_0, c_1, c_2.

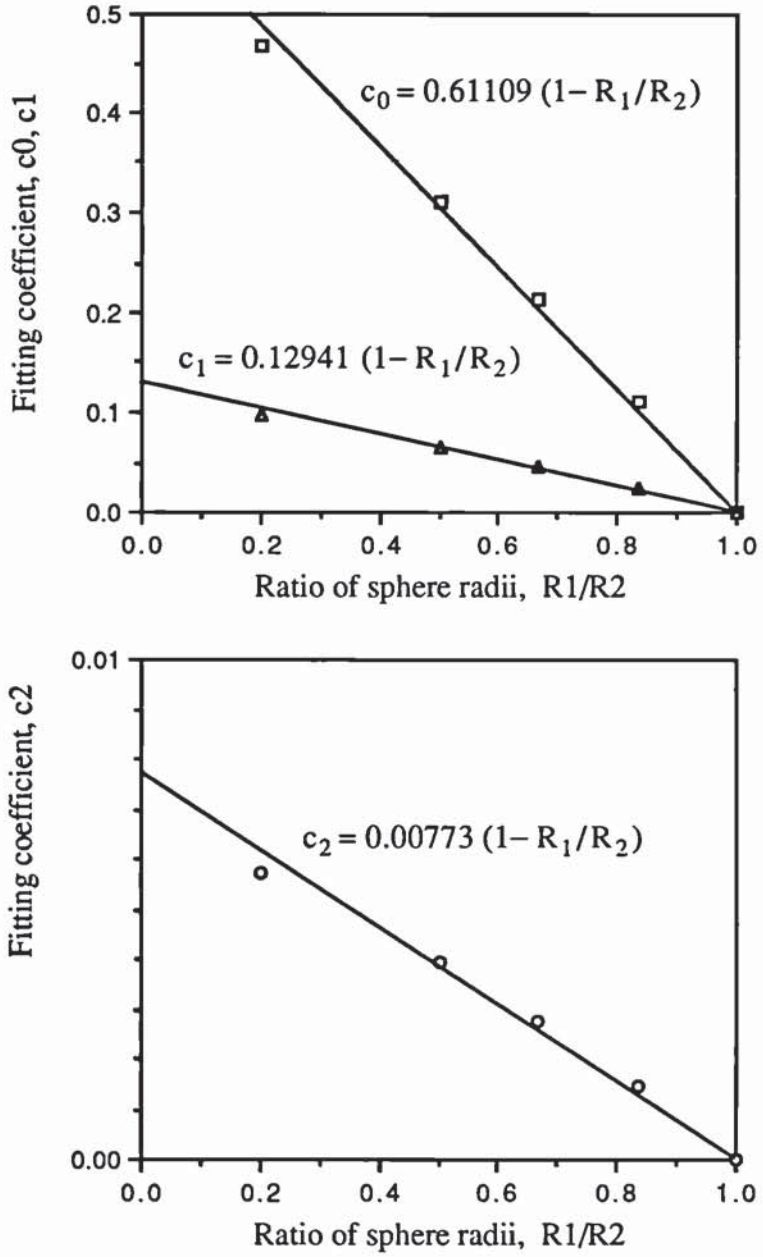

Figure 5.9: Effect of the ratio of sphere radii on the fitting coefficients c_0, c_1, c_2

The three fitting coefficients c_0, c_1, c_2 are only dependent on the the ratio of sphere radii. For different values of the ratio of sphere radii, the corresponding fitting coefficients are given in table 5.1.

It was found that the three coefficients could be further expressed as simple functions of the ratio of sphere radii. This is shown in figure 5.9 which shows that the three coefficients were linearly related to the ratio of sphere radii R_1/R_2 and are best fitted by

$$c_0 = 0.61109(1 - \frac{R_1}{R_2}) \tag{5.34}$$

$$c_1 = 0.12941(1 - \frac{R_1}{R_2}) \tag{5.35}$$

$$c_2 = 0.00773(1 - \frac{R_1}{R_2}) \tag{5.36}$$

Thus, for a liquid bridge with a given quantity of liquid volume and given sphere radii, the rupture distances are uniquely determined using equations 5.32 and 5.33

5.7.2 Computing liquid bridge forces

During the cyclic calculations, liquid bridge forces are calculated after the computation of solid contact forces. Instead of using the incremental method, both the static and viscous forces are calculated directly by using integral equations. The static liquid bridge forces are calculated according to Fisher's toroidal approximation using the 'gorge' method of equation (4.46). As it has been demonstrated in Chapter 4, the gorge method gives the best estimate of the total static forces. In equation 4.46, the static force that a liquid bridge exerts on the spheres is given in terms of ρ_1 and ρ_2, which are expressed in terms of the separation distance and half-filling angle. Since the half-filling angle varies with separation for given liquid bridge volumes, the main

problem is how to determine the half-filling angle. It is known that for a given volume of liquid held between two spheres, the relationship between the half-filling angles and the separation distance is given by equation (4.55) where for two spheres of radii R_i ($i = 1, 2$) the half-filling angle ϕ_2 may be expressed in terms of ϕ_1 as indicated by equation (4.61). Thus for a liquid bridge between two unequal sized spheres with a given set of parameters of sphere radii R_1, R_2, separation distance S and liquid volume V, the half-filling angle ϕ_1 and hence ϕ_2 are uniquely determined.

However, the equations (4.55) and (4.61) do not permit an explicit expression for the half-filling angle ϕ_1 or ϕ_2 in terms of the separation distance, liquid bridge volume and sphere radii. Numerical solution for the half-filling angle can be achieved although it requires iterative calculations and costs much more in computer time. In TRUBAL, an approximate relationship between the half-filling angle and separation distance is used. This relationship is obtained by fitting the numerical results with a third order polynomial function.

Figure 5.10 shows the relationship between the half-filling angle ϕ_1 and separation distance at different liquid bridge volumes and different sphere radius ratios R_2/R_1. The half filling angle is plotted against the relative separation distance $S_r = S/S_c$ where $S_c = S_{c1} + S_{c2}$ is the maximum separation distance of rupture and the liquid volume is made dimensionless to R_1^3. It can be seen that for a constant dimensionless liquid volume, the dependence of the half-filling angle ϕ_1 on the relative separation distance S/S_c can be best fitted by a third order polynomial function given as

$$\phi_1 = C_0 + C_1\frac{S}{S_c} + C_2(\frac{S}{S_c})^2 + C_3(\frac{S}{S_c})^3 \tag{5.37}$$

where C_0, C_1, C_2 and C_3 are four fitting coefficients.

It has been found that the four fitting coefficients are only dependent on the dimensionless volume of liquid bridges and the ratio of sphere radii. For different sets

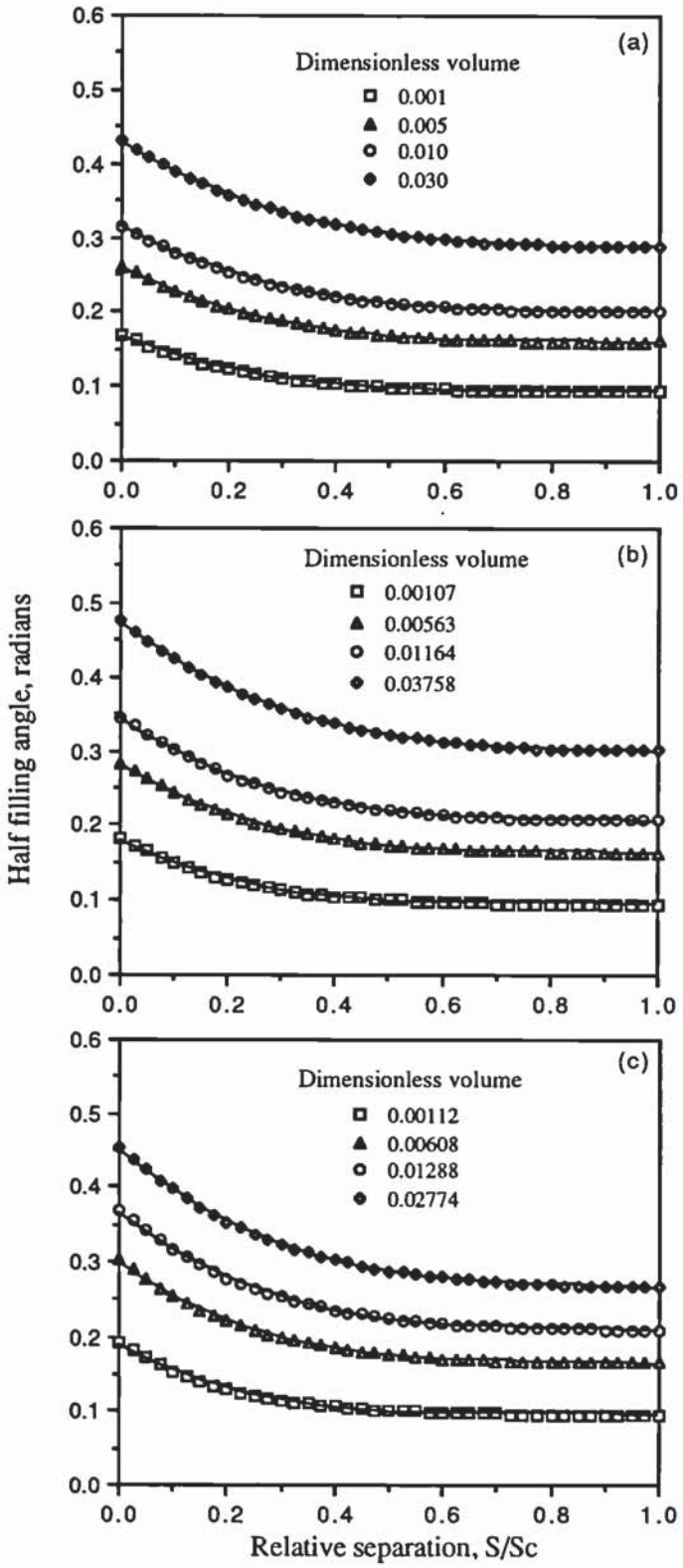

Figure 5.10: Dependence of the half-filling angle ϕ_1 on the relative separation S/S_c as fitted by third order polynominals for different dimensionless liquid volumes and different ratios of sphere radii: (a) $\frac{R_2}{R_1} = 1.0$, (b) $\frac{R_2}{R_1} = 2.0$ and (c) $\frac{R_2}{R_1} = 5.0$.

R_2/R_1	V/R_1^3	C_0	C_1	C_2	C_3
	0.00100	0.16702	-0.28582	0.37579	-0.16440
	0.00500	0.25947	-0.35601	0.43167	-0.17593
1.0	0.01000	0.31461	-0.38911	0.45302	-0.17792
	0.02000	0.38246	-0.42474	0.47284	-0.17819
	0.03000	0.42938	-0.44723	0.48390	-0.17763
	0.00102	0.17069	-0.30147	0.40023	-0.17671
	0.00519	0.26593	-0.37800	0.46296	-0.19087
1.2	0.01049	0.32299	-0.41431	0.48704	-0.19368
	0.02126	0.39351	-0.45349	0.50925	-0.19445
	0.03219	0.44248	-0.47824	0.52151	-0.19400
	0.00105	0.17477	-0.31925	0.42825	-0.19090
	0.00540	0.27313	-0.40321	0.49922	-0.20831
1.5	0.01104	0.33238	-0.44330	0.52656	-0.21213
	0.02268	0.40597	-0.48667	0.55157	-0.21348
	0.03470	0.45733	-0.51410	0.56514	-0.21312
	0.00107	0.17933	-0.33966	0.46078	-0.20749
	0.00563	0.28125	-0.43246	0.54180	-0.22896
2.0	0.01164	0.34301	-0.47710	0.57317	-0.23407
	0.02429	0.42015	-0.52553	0.60160	-0.23617
	0.03758	0.47431	-0.55620	0.61670	-0.23588
	0.00112	0.18917	-0.38552	0.53511	-0.24577
	0.00608	0.29893	-0.49937	0.64127	-0.27783
5.0	0.01288	0.36628	-0.55504	0.68297	-0.28650
	0.02774	0.45145	-0.61588	0.72017	-0.29073
	0.04394	0.51199	-0.65454	0.73914	-0.29069

Table 5.2: Fitting coefficients C_0, C_1, C_2, C_3 for the half-filling angle.

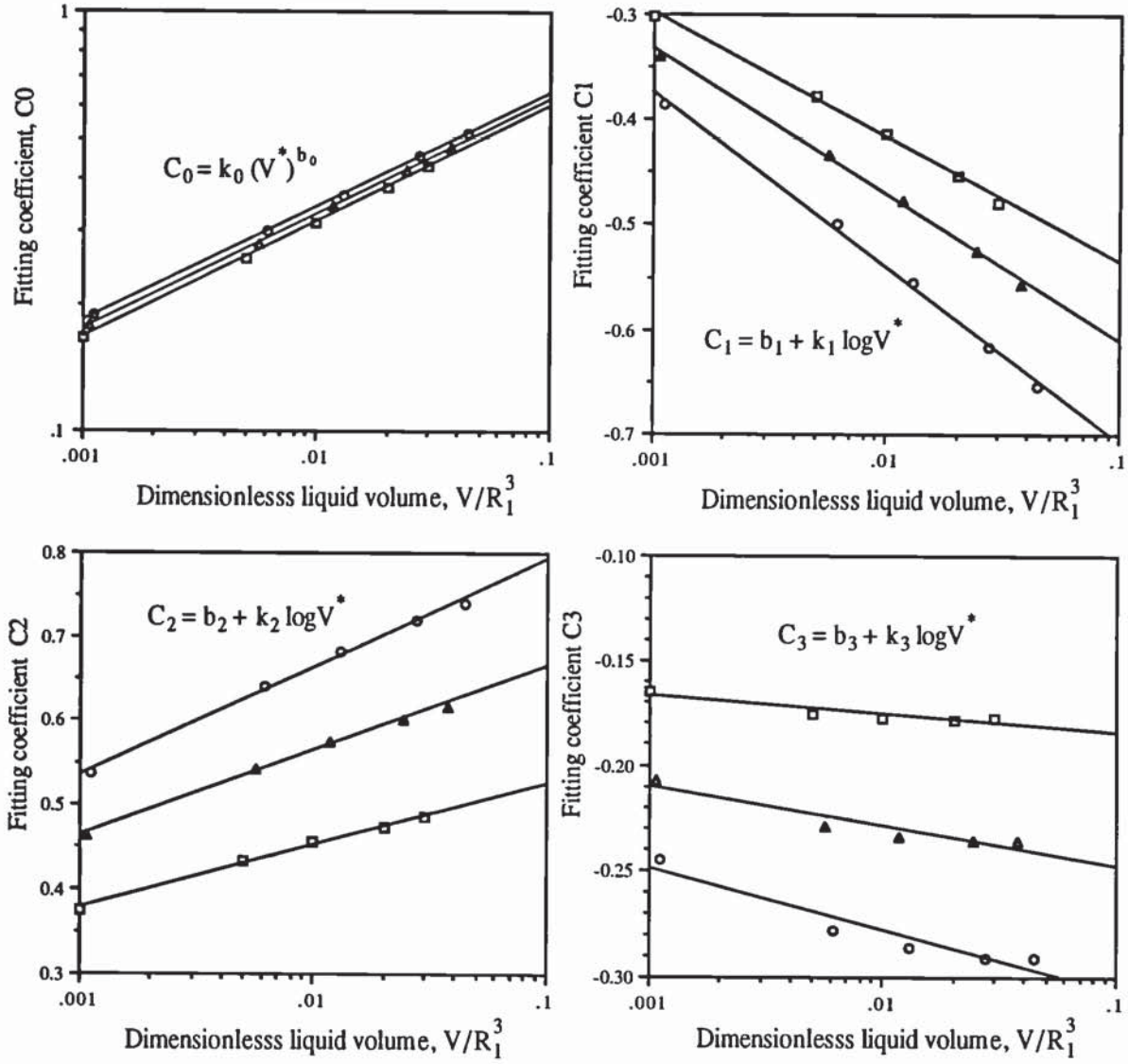

Figure 5.11: The fitting coefficients C_0, C_1, C_2, C_3 as functions of the dimensionless liquid volume at different ratios of sphere radii, $R_2/R_1 = 1.0$ (□), $R_2/R_1 = 2.0$ (△), and $R_2/R_1 = 5.0$ (○).

R_2/R_1	b_0	k_0	b_1	k_1	b_2	k_2	b_3	k_3
1.0	0.2774	1.1319	-0.6094	-0.1087	0.5978	0.0734	-0.1941	-0.0092
1.2	0.2758	1.1379	-0.6497	-0.1174	0.6453	0.0812	-0.2146	-0.0118
1.5	0.2748	1.1492	-0.6966	-0.1277	0.7007	0.0905	-0.2385	-0.0150
2.0	0.2732	1.1600	-0.7507	-0.1395	0.7656	0.1014	-0.2669	-0.0188
5.0	0.2712	1.1938	-0.8776	-0.1682	0.9209	0.1290	-0.3359	-0.0289

Table 5.3: Fitting coefficients of b_j, k_j, $(j = 0, 1, 2, 3)$.

of dimensionless liquid volumes and sphere radii, the four fitting coefficients obtained are given in table 5.2. In figure 5.11, the four fitting coefficients were plotted as functions of the dimensionless liquid volume for a range of ratios of sphere radii. It can be seen that the four fitting coefficients can be further expressed in terms of the dimensionless liquid volume by functions in the following forms,

$$C_0 = k_0(\frac{V}{R_1^3})^{b_0} \tag{5.38}$$

$$C_1 = b_1 + k_1 \log(\frac{V}{R_1^3}) \tag{5.39}$$

$$C_2 = b_2 + k_2 \log(\frac{V}{R_1^3}) \tag{5.40}$$

$$C_3 = b_3 + k_3 \log(\frac{V}{R_1^3}) \tag{5.41}$$

where b_j, k_j, $(j = 0, 1, 2, 3)$ are fitting coefficients that depend on the ratio of sphere radii only. For a range of the ratios of sphere radii, these fitting coefficients were obtained and are given in table 5.3. Figure 5.12 shows that when plotted against the ratio of sphere radii R_1/R_2, all sets of the fitting coefficients b_j, k_j, $(j = 0, 1, 2, 3)$ produce straight lines and can be represented by the following simple fitting equations,

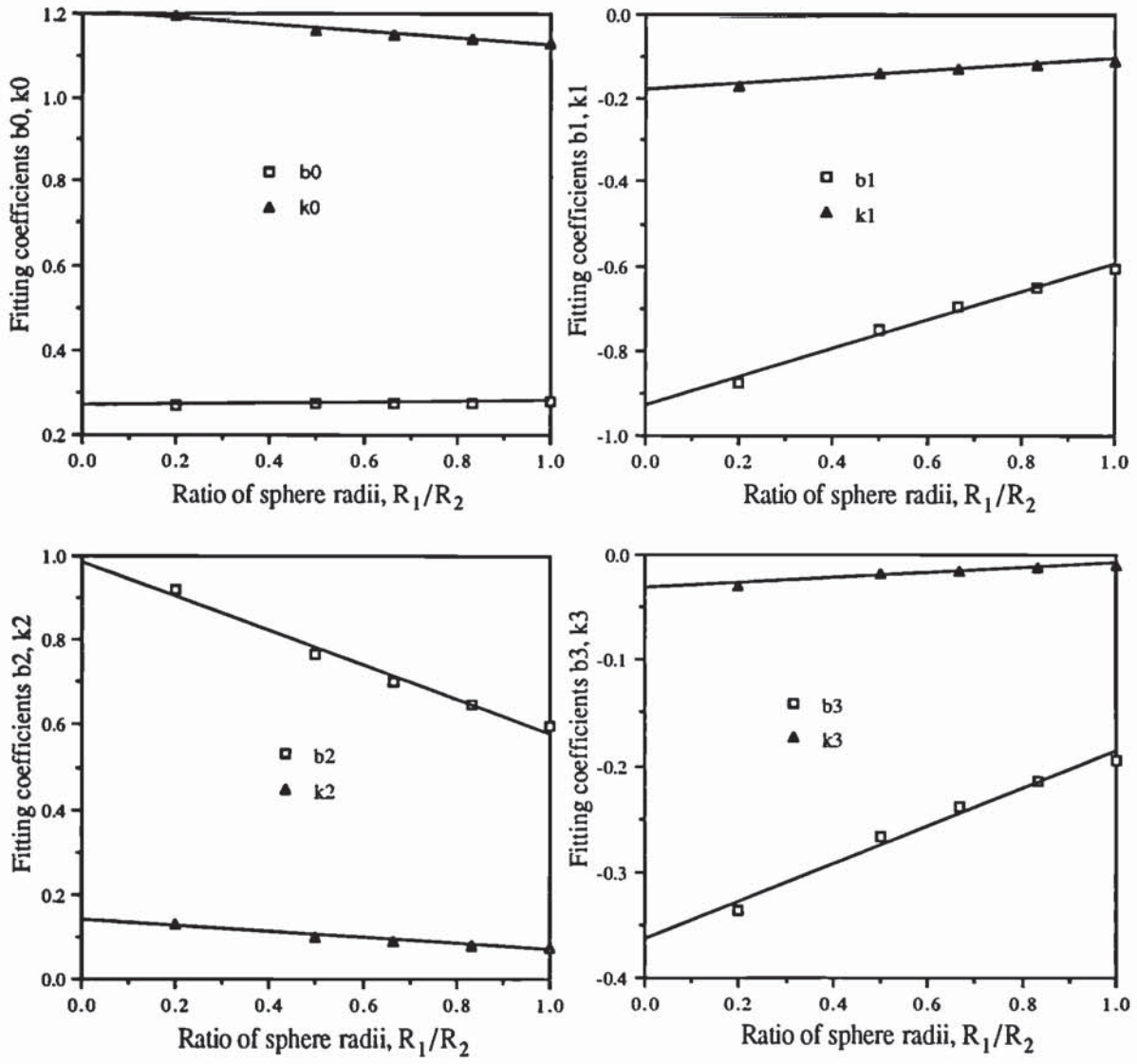

Figure 5.12: The fitting coefficients b_j, k_j $(j = 0, 1, 2, 3)$ as functions of the ratio of sphere radii.

$$b_0 = 0.26958 - 0.00766\frac{R_1}{R_2} \tag{5.42}$$

$$k_0 = 1.20420 + 0.07753\frac{R_1}{R_2} \tag{5.43}$$

$$b_1 = -0.93128 + 0.33513\frac{R_1}{R_2} \tag{5.44}$$

$$k_1 = -0.17990 + 0.07435\frac{R_1}{R_2} \tag{5.45}$$

$$b_2 = 0.98431 - 0.40353\frac{R_1}{R_2} \tag{5.46}$$

$$k_2 = 0.13948 - 0.06938\frac{R_1}{R_2} \tag{5.47}$$

$$b_3 = -0.36328 + 0.17703\frac{R_1}{R_2} \tag{5.48}$$

$$k_3 = -0.03245 + 0.02456\frac{R_1}{R_2} \tag{5.49}$$

In summary, the procedures for calculating the static force of liquid bridges are described as follows. For each liquid bridge, the fitting coefficients b_j, k_j $(j = 0, 1, 2, 3)$ are evaluated by equations (5.42)-(5.49) respectively with the given sizes of the two spheres. These parameters are then substituted into equations (5.38)-(5.41) accordingly to determine the coefficients C_j $(j = 0, 1, 2, 3)$ for a given quantity of liquid. Thus, the half-fitting angle ϕ_1 may be obtained from equation (5.37) for a given separation distance. Finally, the calculation of the principal radii ρ_1, ρ_2 of the toroidal curvature and hence the force is straightforward using equations (4.39), (4.40), (4.43) and (4.46) which are given in chapter 4.

For the calculation of viscous force of a liquid bridge, the relative normal and tangential velocities between two spheres are given as,

$$v_n = (v_i^B - v_i^A)n_i \tag{5.50}$$

$$v^t i_i = (v_i^B - v_i^A) - v_n n_i \tag{5.51}$$

Equation 4.73 from Adams and Perchard (1985) is applied for the computation of viscous force due to normal velocity and equations 4.76 and 4.77 for the tangential velocity. However, these equations predict an infinite force when the separation distance approaches zero. This is because the models are based on the assumption that the spheres are rigid with perfect smooth surfaces. For real particles, however, the separation gap can not reach zero due to both the roughness of the surfaces and elastic-plastic deformation of the spheres. Elastic and plastic deformation of the sphere may occur when the viscous hydraulic pressure is high. Considering the full elasto-plasto-hydro-dynamics of particles with surface roughness is too complicated. In the current version of TRUBAL the problem is eliminated by setting the separation gap to some limiting value. In the work reported in Chapter 6 and Chapter 7 the limiting separation gap has been related to the sphere diameter using values in the range $R/1000 < S_{min} < R/100$. For micron sized particles this corresponds to a minimum separation gap of $0.001 \sim 0.01 \mu m$. Also in the work reported in Chapter 6 and Chapter 7 the viscous force of liquid bridges due to the tangential velocity is not included.

5.8 Energy dissipation

Particulate systems are not energy conserving. With strain rate controlled periodic cells or wall controlled boundaries, the particle system gains energy from the external applied field. This causes problems for the simulation of quasi-static systems, e.g. agglomerate preparation, shear testing, where energy has to be dissipated in order to reach quasi-equilibrium. TRUBAL provides two forms of viscous damping: contact

damping and global damping. The contact damping considers the energy losses during the force transmission through the solid particles. This type of damping is modelled by a dashpot. The damping force is calculated to be proportional to the the relative velocity and the normal and tangential contact force increments. Having calculated the contact forces between spheres, damping forces are calculated and added to the contact forces to give the total contributions to the out-of-balance forces of each sphere.

The global damping is a type of mass proportional damping. It operates in the form of classical Rayleigh damping and is handled in the subroutine which calculates the motion of each sphere. The mass proportional damping can be envisaged as dashpots that connect all constituent particles to the reference axes of the simulated system. For each sphere, the resistance force of global damping that is exerted on the sphere is opposite to its velocity vector (both translational and rotational) of the sphere. The magnitude of the resistance force is proportional to the absolute velocity of the particle. The effect of global damping is like immersing the constituent particles in a viscous fluid. It is useful to dissipate kinetic energy during the preparation of a simulated system in order to avoid excessive computer time. Before the system is subjected to the desired computer simulated experiment, the global damping should be switched off.

In addition to the two damping mechanisms, energy is naturally dissipated by interparticle friction, adhesive peeling, and viscous resistance of liquid bridges.

5.9 Results output

In the current version of TRUBAL, the results of a computer simulated experiment can be either printed and/or plotted. With the printout option, one can obtain the results of sphere data, wall data, contact data, energy terms, stress tensor and

other general information. All such data can be printed out at any stage during the simulation. With the graphics plotting option, one can obtain 3-D colour pictures of spheres, walls, contact forces, contact connection diagram, particle velocities, particle displacements and particle clusters. The contact forces are plotted by lines passing through the contact point. The magnitude of the force is scaled to the thickness of the line. The contact connection diagram provides information about the evolution of contacts, i.e. the contacts still existing, deleted, or newly made, in reference to a previously saved state. Different coloured lines joining the centres of spheres represent the different types of contact. Particle velocities and displacements are illustrated by vectors originating from the centre of each sphere. For the plot of particle clusters, the individual particles are colour coded according to the size of the cluster to which they belong.

The current version of TRUBAL also provides a screen monitoring facility which permits the evolution of the energy partitions, stress tensor, contact number, porosity and other general information to be monitored on the screen during the simulation.

The graphic package of the current version of TRUBAL is written in FORTRAN using graPHIGS API for IBM RS6000 workstations.

Chapter 6

Computer simulation of a moist agglomerate impact with a wall

In this chapter, the results of computer simulations of a moist agglomerate impacting with a wall are presented and discussed. A body-centred cubic moist agglomerate consisting of 4062 primary particles was prepared for the computer simulation. The visco-plastic deformation and interstitial liquid bridge rupture of the impacted agglomerate have been examined and the effects of the cohesive liquid bridges have been investigated. Some of the work in this chapter has been also reported by Thornton, Lian and Adams (1993).

6.1 Introduction

Agglomerate properties, particularly strength and deformability, are clearly of relevance to granule coalescence, attrition and breakage. Although many different types of tests have been described for assessing agglomerate strength and attrition tendency, the impact test is the most simple and direct method to quantify and measure the deformation and breakage of particulate solids. The impact test falls into two categories, namely single particle impact tests and multi-particle (agglomerate) impact tests. The single particle impact test is mainly used to enhance the understanding of the mechanisms of particle breakage but the results are difficult to compare with real agglomerate breakage observed in process engineering. The agglomerate impact test is more closely related to the granulation, attrition and breakage processes but, with real experiments, it is primarily empirical. This is because with real experiments it is difficulty to obtain the internal parameters describing the packing structure of the agglomerates, such as particle shapes, sizes and interparticle contact forces. Also with real experiments, only a limited number of variables can be considered.

Computer simulated 2D and 3D dry agglomerate impact tests were recently reported by Yin (1992), Thornton and Kafui (1992), Thornton, Kafui and Yin (1993) and Kafui and Thornton (1993). Adapted from the 2D program BALL and 3D program TRUBAL, these authors incorporated surface adhesion forces between particles. It is clear from the computer graphics provided that the computer simulated agglomerate impact tests provide micro-level scrutiny of the crack initiation and propagation within the agglomerate during impaction. In this chapter, 3D computer simulated impact tests on a body-centred cubic moist agglomerate consisting of 4062 primary particles are reported. The mechanical behaviour of the moist agglomerate-wall collisions has been examined and information has been obtained concerning visco-plastic deformation and internal damage in terms of the interparticle liquid bridge forces and packing structures.

6.2 Computer simulation procedures

6.2.1 Agglomerate preparation

For the computer simulated moist agglomerate impact with a wall, a 3D body-centred cubic agglomerate consisting of 4062 primary particles was prepared. The primary particles of radius $R = 30\mu m$ were attributed with the following properties: density $\rho = 2.65Mg\,m^{-3}$, Young's modulus $E = 70Gpa$, Poisson's ratio $\nu = 0.3$ and friction coefficient $\mu = 0.3$. To prepare the agglomerate, primary particles were generated inside a circumscribing spherical region of radius $R_c = 575\mu m$. The structure of the generated particles is body-centred cubic with point contacts between the particles. Pendular liquid bridges were then specified for each contact and the quantity of liquid assigned to each contact was 0.1% of the particle volume, which, in the case of the body-centred cubic arrangement, corresponds to a degree of saturation of 0.85%. The liquid modelled was silicone fluid with the following properties: surface tension $\gamma_{lv} = 0.025Nm^{-1}$, solid-liquid contact angle $\theta = 0^0$ and viscosity $\eta = 0.00 \sim 0.10Pa\,s$.

After the creation of the particles with liquid bridges, cyclic calculations were performed to allow the agglomerate to reach a state of equilibrium. During this stage, high viscosity ($0.1\ Pa\,s$) of the liquid bridges was used to damp out the kinetic energy which was produced when the attractive forces of the liquid bridges pulled the primary particles closer together. After 450,000 time steps, the total contact force (i.e. the combination of the attractive liquid bridge force and the repulsive Hertzian contact force) at each contact was less than $1.0\mu N$ and the global rectilinear velocity of each particle was around $10\mu m/s$. This stage of the agglomerate was assumed as the quasi-equilibrium state and was used as the initial state for all subsequent simulations of agglomerate impact. Figure 6.1 shows the agglomerate at the quasi-equilibrium state together with the distributions of the residual total contact forces (figure 6.1b) and the residual rectilinear velocities (figure 6.1c). At this stage, there were 14906 interstitial

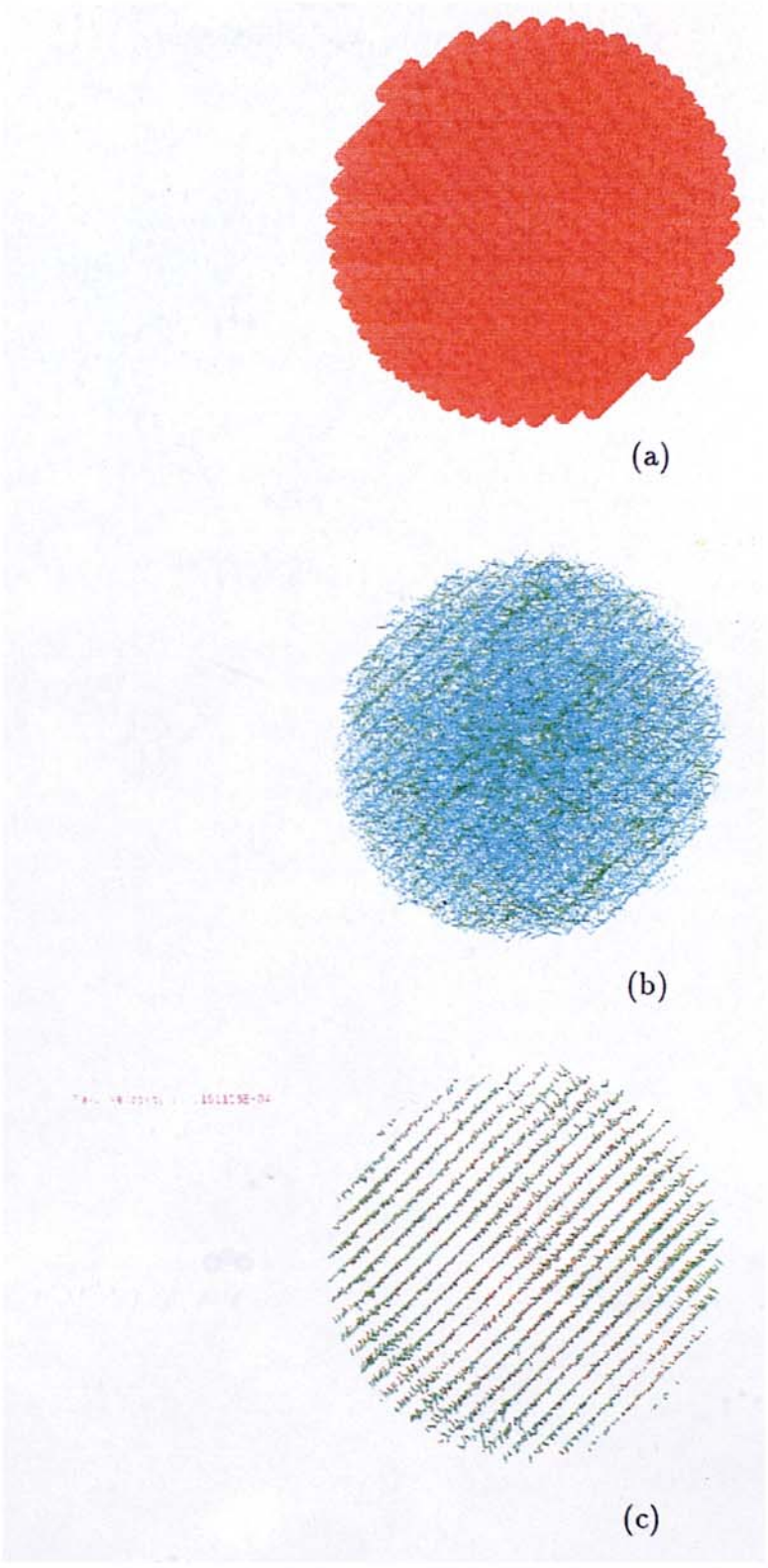

Figure 6.1: The initial state of the prepared moist agglomerate with a body-centred cubic arrangement: (a) the agglomerate, (b) total contact force distribution and (c) rectilinear velocity field.

liquid bridges which corresponds to a measured average coordination number of 7.339. Theoretically, the coordination number of a body-centred cubic packing should be 8, but this only applies to an infinite structure. For the body-centred cubic agglomerate of 4062 particles, the particles on the periphery have less than 8 contacts.

In figure 6.1b, contact forces (the overall force of liquid bridges and Hertzian contact) between particles are represented by lines joining the centroid of particles with the compressive forces represented by green lines and the tensile forces by blue ones. Of the 14906 contacts, there are 7391 compressive and 7515 tensile. The magnitude of the contact forces is indicated by the thickness of the lines which are scaled to the current maximum force ($1.3 \times 10^{-6}N$). In figure 6.1c the rectilinear velocities of each particle are represented by lines each with a red dot to indicate the forward direction. The length of each line is scaled to the magnitude of the velocity. The maximum speed of the constitutent particles at this stage is $1.9 \times 10^{-5}m/s$. It can be seen that the residual velocities and contact forces are very small and are all randomly distributed. Due to the numerical truncation of the computer calculations, it is impossible to reach the absolute equilibrium state with uniform or zero particle velocities.

6.2.2 Test procedures

For each impact test, a smooth and continuous 'massive' elastic plane wall was created. This wall was generated at a position below the agglomerate. The properties of the wall were considered to be the same as the primary particles and the thickness of the wall was simulated as a semi-infinite half-space. Each impact test was performed by setting an appropriate colliding velocity to all the primary particles of the agglomerate and the wall was stationary. In total, three series of agglomerate-wall impact tests were performed with each series considering different viscosities of

Liquid viscosity $Pa.s$	Impact velocity (ms^{-1})
0.00	0.2, 0.3, 0.4, 0.5, 1.0, 2.0
0.01	0.2, 0.3, 0.44, 0.6, 1.0, 2.0, 3.0
0.10	0.3, 0.4, 0.6, 1.0, 2.0, 4.0, 8.0

Table 6.1: Series of the moist agglomerate-wall impact tests

0.00, 0.01 and $0.10 Pa.s$ respectively for the interstitial liquid bridges. The series of the agglomerate-wall impact tests is described in table 6.1.

6.3 Results and discussion

6.3.1 Visual observations

Computer graphics visualisation of all the simulations, showing the agglomerates after impact, are provided in Appendix C.1.

Computer simulated 2D and 3D dry agglomerate-wall impact tests were reported by Yin (1992), Thornton and Kafui (1992), Thornton, Kafui and Yin (1993) and Kafui and Thornton (1993). For all their simulations reported, the properties of both the particles and the wall were: density $\rho = 2.65 Mg\, m^{-3}$, Young's modulus $E = 70 Gpa$, Poisson's ratio $\nu = 0.3$ and friction $\mu = 0.35$. The primary particles adhered together as a result of van der Waals' forces (auto-adhesion). The 2D simulations were carried out on a 1000 primary particle monodisperse agglomerate in order to provide clear

visual evidence of the internal agglomerate damage processes. The radius of the primary particles was $R = 100\mu m$. The 1000 primary particles were initially randomly generated within a prescribed circular region and then a centripetal gravity field was imposed to bring the particles together. For the 3D simulations, Thornton, Kafui and Yin (1993) reported a dry agglomerate which consisted of 7912 primary particles arranged in a face-centred cubic packing to form a spherical agglomerate. They used a primary particle size $R = 100\mu m$.

In the 2D dry agglomerate-wall impact simulation, it was found that when the agglomerates were impacted at a relatively high velocity, they were effectively shattered with more than 80% of the interparticle bonds being broken. Many singlets and very small clusters were produced in the region nearest to the wall and at the rear of the agglomerates. When impacted at moderate velocities, it was observed that the agglomerates failed in a very different way. Only a very small portion of the primary particles were broken away as small clusters (i.e fine debris). As a result of the impact, fracture occurred which roughly divided the agglomerates into two parts.

Thornton and Kafui (1992) and Thornton, Kafui and Yin (1993) reported that, in the case of the 3D agglomerates, moderate impact velocities resulted in a main fracture along a meridian plane and the two divided hemispheres were themselves fractured by small cracks. It was clear from the computer graphics provided that at moderate impact velocities, the dry agglomerates appear to fail by brittle fracture. It was also shown that at low impact velocities, the dry agglomerates bounced off the wall after the impact and there were few bonds broken. However, Kafui and Thornton (1993) reported that in their subsequent 3D agglomerate wall impact tests fracture along a meridian plane was not observed.

For the computer simulated moist agglomerate impact test, however, it was found that the agglomerate behaved in a very different way. Figure 6.2–6.4 shows some pictures of the side and top views of a moist agglomerate with zero liquid viscosity

after impact with a wall at different velocities of 0.2, 0.5 and $2.0m/s$ respectively. For all the pictures shown here and the following pictures, the size of the clusters is represented by different colours. Particles belong to a cluster if they are all held together by the pendular liquid bridges. The colour code of the cluster sizes is as follows,

Green	Singlets
Cyan	Clusters with 2-10 primary particles
Black	Clusters with 11-50 primary particles
Blue	Clusters with 51-200 primary particles
Yellow	Clusters with 201-600 primary particles
Red	Clusters with more than 600 primary particles

It can be seen from figure 6.2 that when the moist agglomerate with inviscid liquid bridges was impacted on to the wall at a low velocity of $0.2m/s$, it remained adhered to the wall. There were no particles broken away from the parent cluster and the agglomerate deformed slightly in the region near to the wall. Figure 6.3 shows that when the impact velocity was increased to $0.5m/s$, no debris of small clusters was produced but the plastic deformation of the whole agglomerate was increased significantly. Figure 6.4 indicates that with further increase in the impact velocity to $2.0m/s$, the moist agglomerate flattened and spread over the wall due to the collision. Quite a number of singlets and small clusters were produced by either the dislodgement from the agglomerate surfaces or from local shattering in the zone near to the wall. However, although a significant number of primary particles were broken away and many internal bonds of liquid bridges were broken, it can be seen that the moist agglomerate is not fractured in a brittle manner. The agglomerate is neither extensively shattered nor fractured as in the case of the dry agglomerates.

The top view of figure 6.2–6.4 indicates that due to the impact strain along the direction of the collision, the moist agglomerate dilated horizontally and the maximum

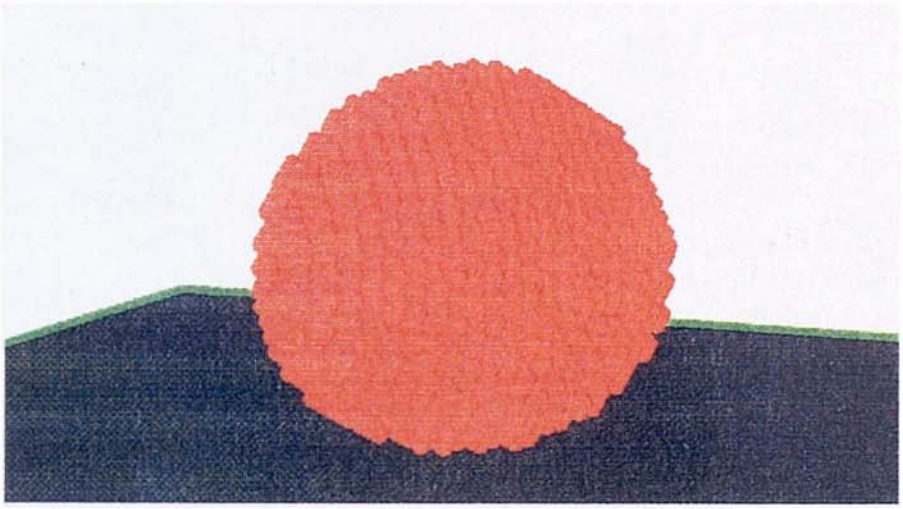

(a)

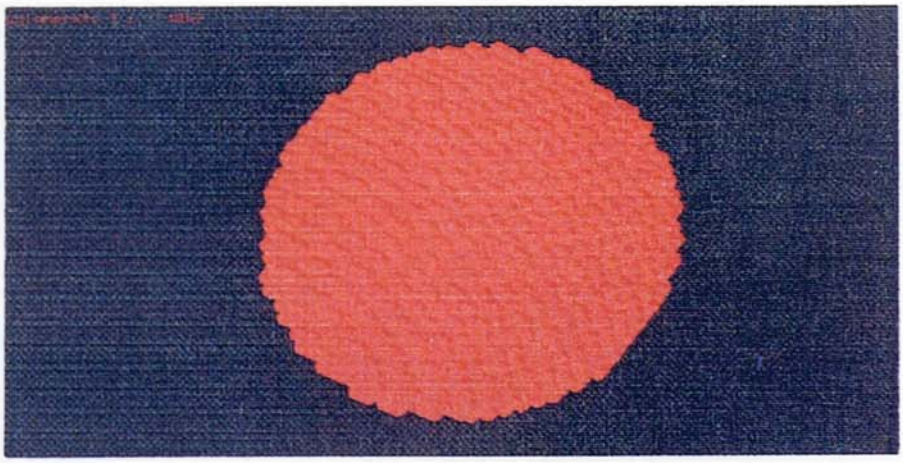

(b)

Figure 6.2: Side (above) and top (below) views of a moist agglomerate with a zero liquid viscosity after impact with a wall at a velocity of $0.2m/s$.

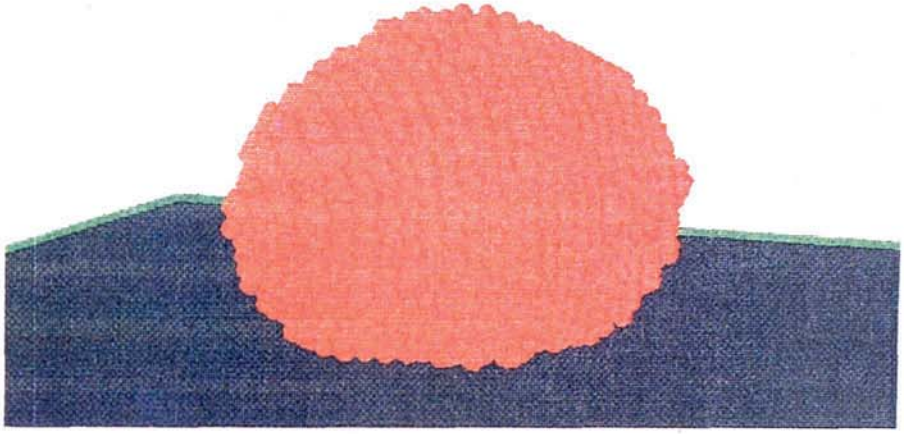

(a)

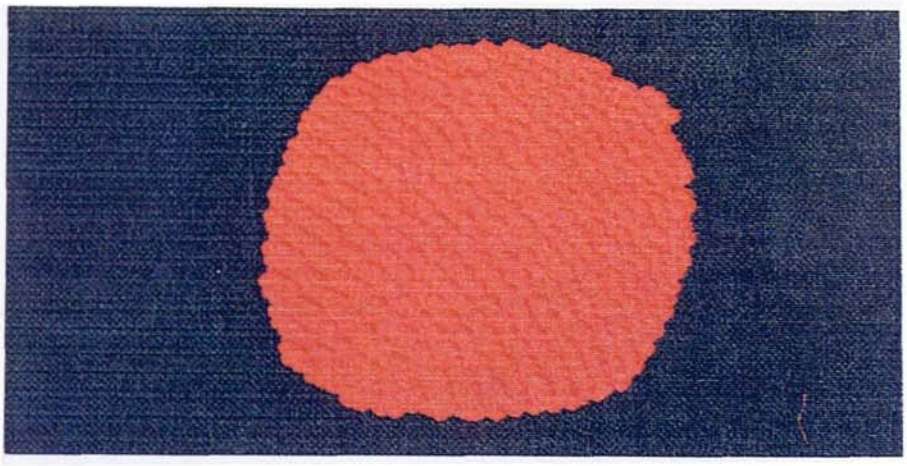

(b)

Figure 6.3: Side (above) and top (below) views of a moist agglomerate with a zero liquid viscosity after impact with a wall at a velocity of $0.5m/s$.

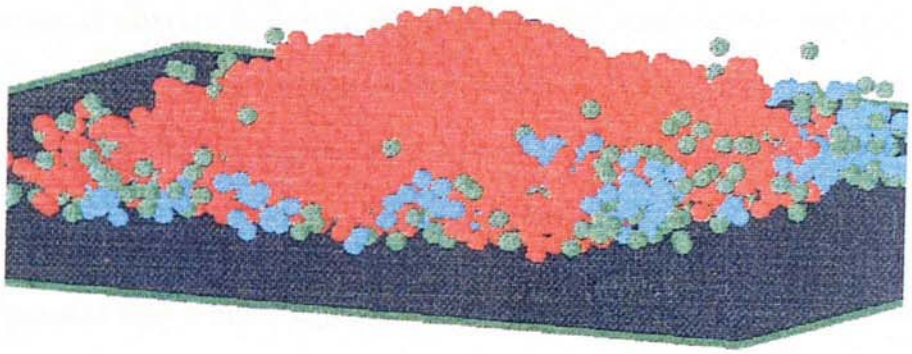

(a)

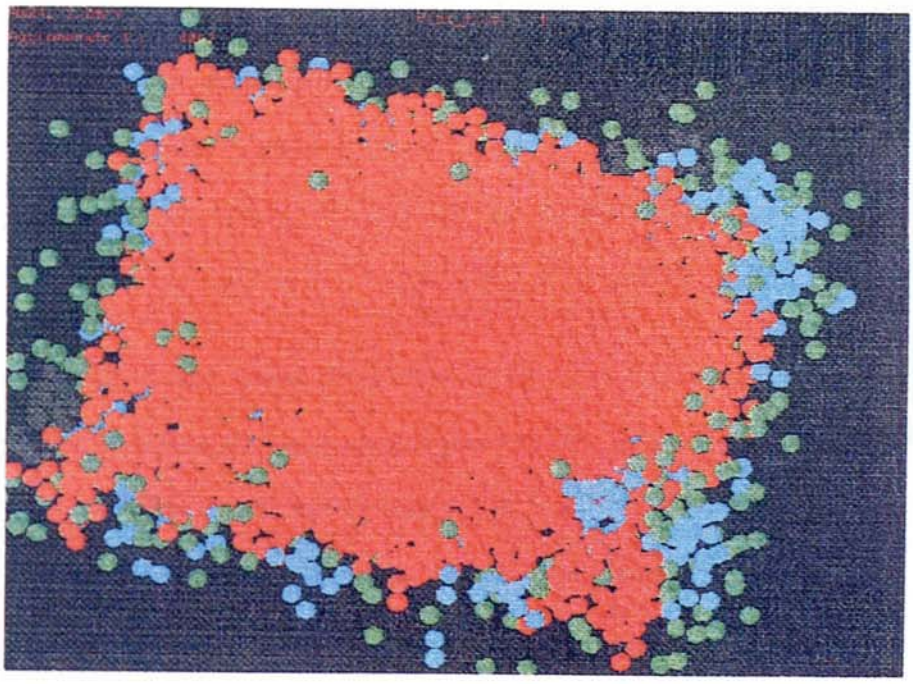

(b)

Figure 6.4: Side (above) and top (below) views of a moist agglomerate with a zero liquid viscosity after impact with a wall at a velocity of $2.0m/s$.

extension was along the four diagonal directions normal to the impact direction. In figures 6.2b, 6.3b, 6.4b the agglomerate is viewed in a direction slightly inclined to the vertical and hence the agglomerate appears to be "rectangular" rather than square. The preferential dilation is due to the fact that the agglomerate was impacted in a direction orthogonal to the square-packed planes of the body-centred cubic arrangement. Thus, when the the agglomerate was more strained at high impact velocities, its preferential extension became more significant.

It is apparent that a moist agglomerate is more resistant to fracture/fragmentation and can sustain a much larger amount of plastic deformation in comparison to a dry agglomerate. This is because in comparison with the auto-adhesion of van der Waals' forces, the liquid bridge bonds are much more extendible and provide more energy accommodation. Lian et al (1993) indicated that, if, for example, the degree of liquid saturation of a monodisperse particle system is 1%, the critical extension at which the liquid bridge bonds rupture is about 15% of the particle radius . For a dry agglomerate, according to JKR theory, rupture of contact bonds occurs at a separation distance of only $\sim 10^3 \mathring{A}$ (assuming $E \sim 10^{10} Pa$ and $\gamma \sim 10^{-1} J/m^2$).

The strength of the moist agglomerate to resist fracture/fragmentation and to sustain plastic deformation is greatly increased by increasing the viscosity of liquid bridges. This is illustrated by figures 6.5–6.7 which show the side and top views respectively for the wet agglomerate with $0.1 Pa.s$ liquid viscosity after impact at different velocities of 1.0, 2.0 and $8.0 m/s$. It can be seen that when a higher viscosity was assigned to the liquid bridges of the agglomerate, a much higher impact velocity was required to deform the agglomerate to a similar extent. Increasing the viscosity also decreases the number of fine particles broken away. With a viscosity of $0.1\ Pa\,s$ attributed to the liquid bridges, it is apparent from figures 6.5 and 6.6 that, at the impact velocities of 1.0 and $2.0 m/s$, the agglomerate remains completely intact but deforms as though it was a visco-plastic ball. At a high impact velocity of $8.0 m/s$,

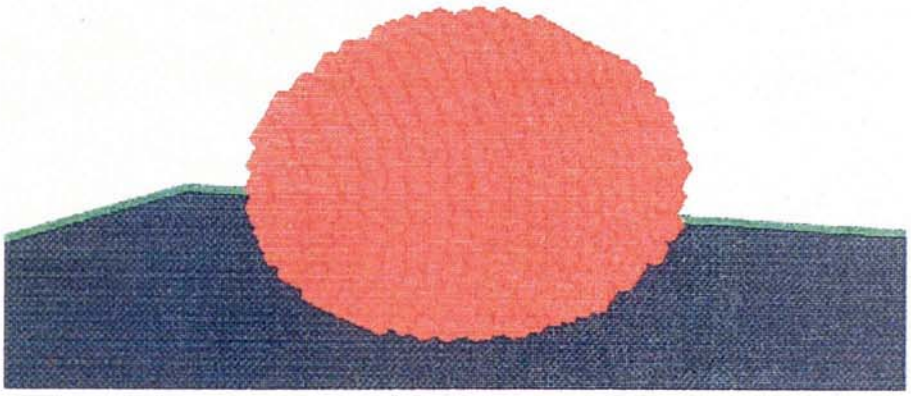

(a)

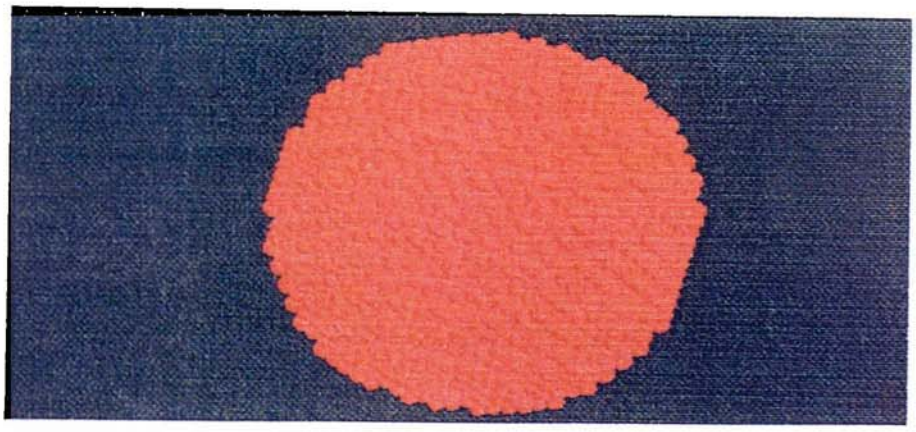

(b)

Figure 6.5: Side (above) and top (below) views of a moist agglomerate with a liquid viscosity of $0.1 Pa.s$ after impact with a wall at a velocity of $1.0 m/s$.

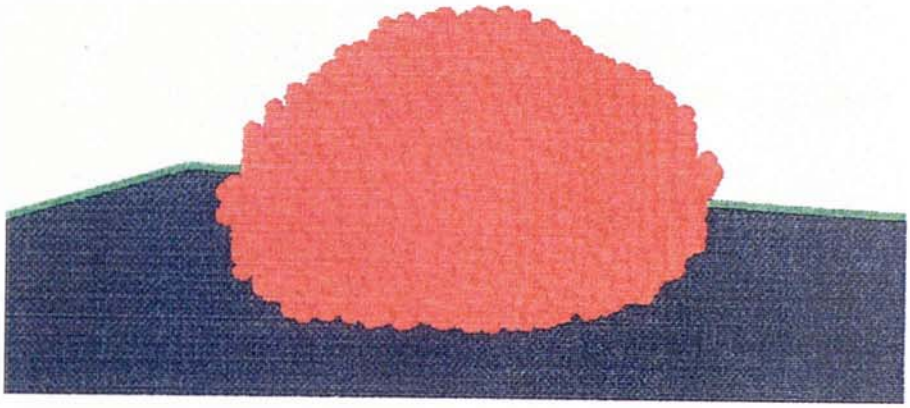

(a)

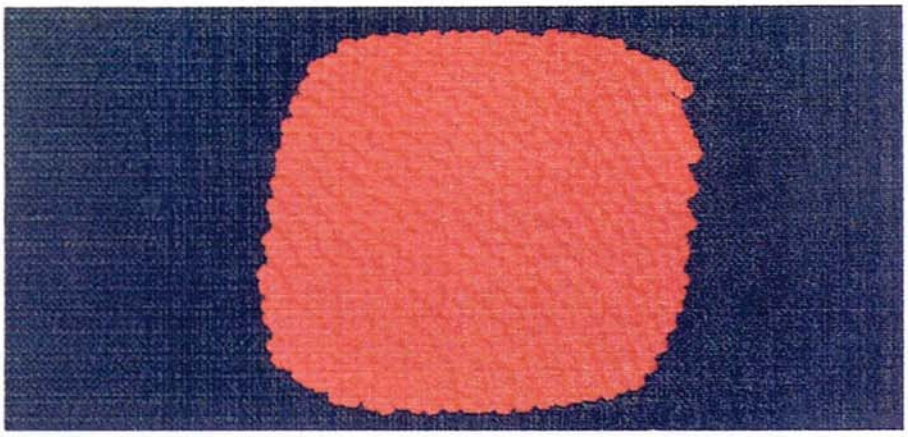

(b)

Figure 6.6: Side (above) and top (below) views of a moist agglomerate with a liquid viscosity of $0.1 Pa.s$ after impact with a wall at a velocity of $2.0 m/s$.

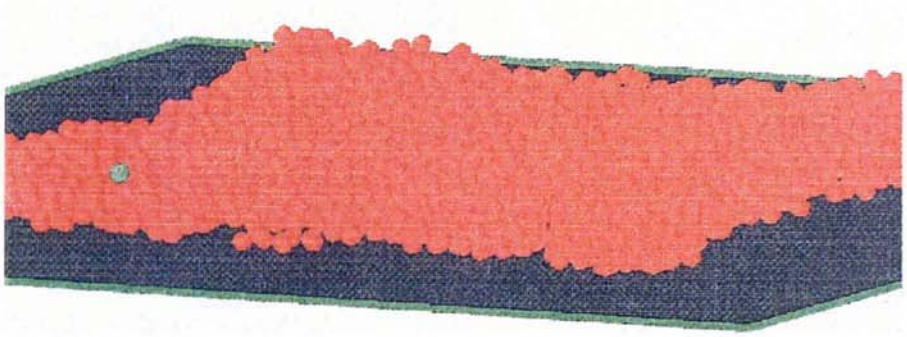

(a)

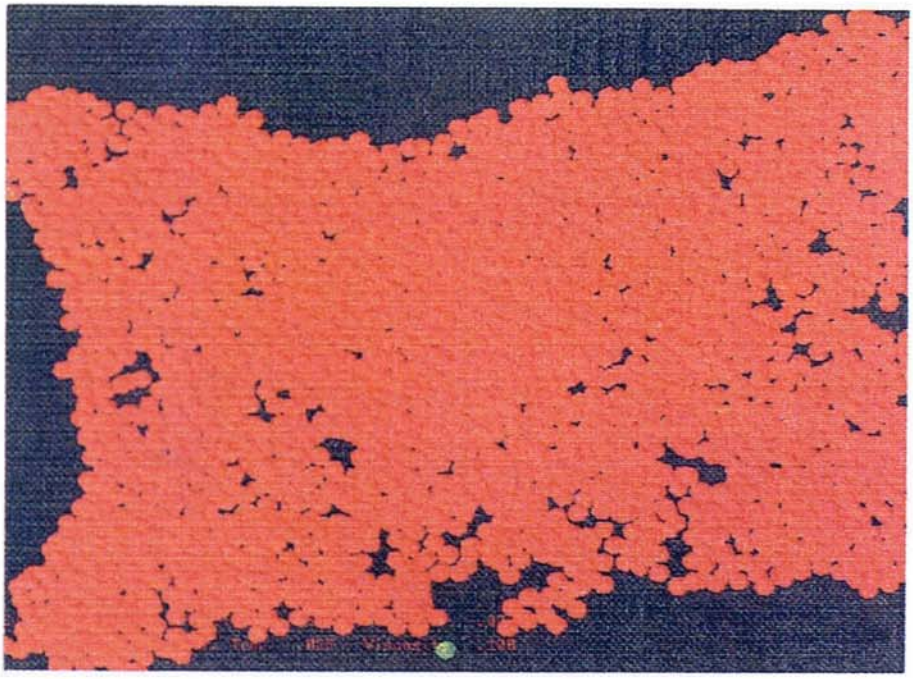

(b)

Figure 6.7: Side (above) and top (below) views of a moist agglomerate with a liquid viscosity of $0.1 Pa.s$ after impact with a wall at a velocity of $8.0 m/s$.

figure 6.7 indicates that the agglomerate was so severely deformed that it was planar shaped. However, attrition still did not occur.

The rheological behaviour of the computer simulated moist agglomerate may be explained in terms of the interaction forces between particles. Since deforming the agglomerate requires external applied forces to overcome the interparticle friction and liquid bridge forces, the bulk behaviour of the agglomerate is dominated by the contact interactions. As the viscosity of the liquid bridges increases, the force and energy required to break the liquid bridge bonds also increase. Mazzone et al (1987) demonstrated that the force and energy required to break a viscous liquid bridge is sometimes orders of magnitude higher than that required in geometrically identical non-viscous systems. As a result, the visco-plastic deformation (rheological flow) behaviour of the moist agglomerate is more obvious when the viscosity of interparticle liquid bridges increases. From this point of view, the computer simulated results of the moist agglomerate impacts qualitatively demonstrate the effectiveness of adding viscous binders to prevent agglomerate attrition and promote powder granulation, a common practice in process engineering.

6.3.2 Agglomerate deformation

At the macroscopic level, the visco-plastic deformation of the agglomerate can be quantified by the diametrical compression induced orthogonal to the wall surface and the lateral spreading of the agglomerate over the wall surface. The relative height $(h/2R_c)$ of the impacted agglomerate as a function of the impact velocity and the viscosity of the liquid binder is shown in figure 6.8a, where h is the measured height of the impacted agglomerate and R_c is the radius of the initial agglomerate before impact. It can be seen that, as the impact velocity increases, the relative height of the impacted agglomerate decreases. At very low impact velocities, changing the

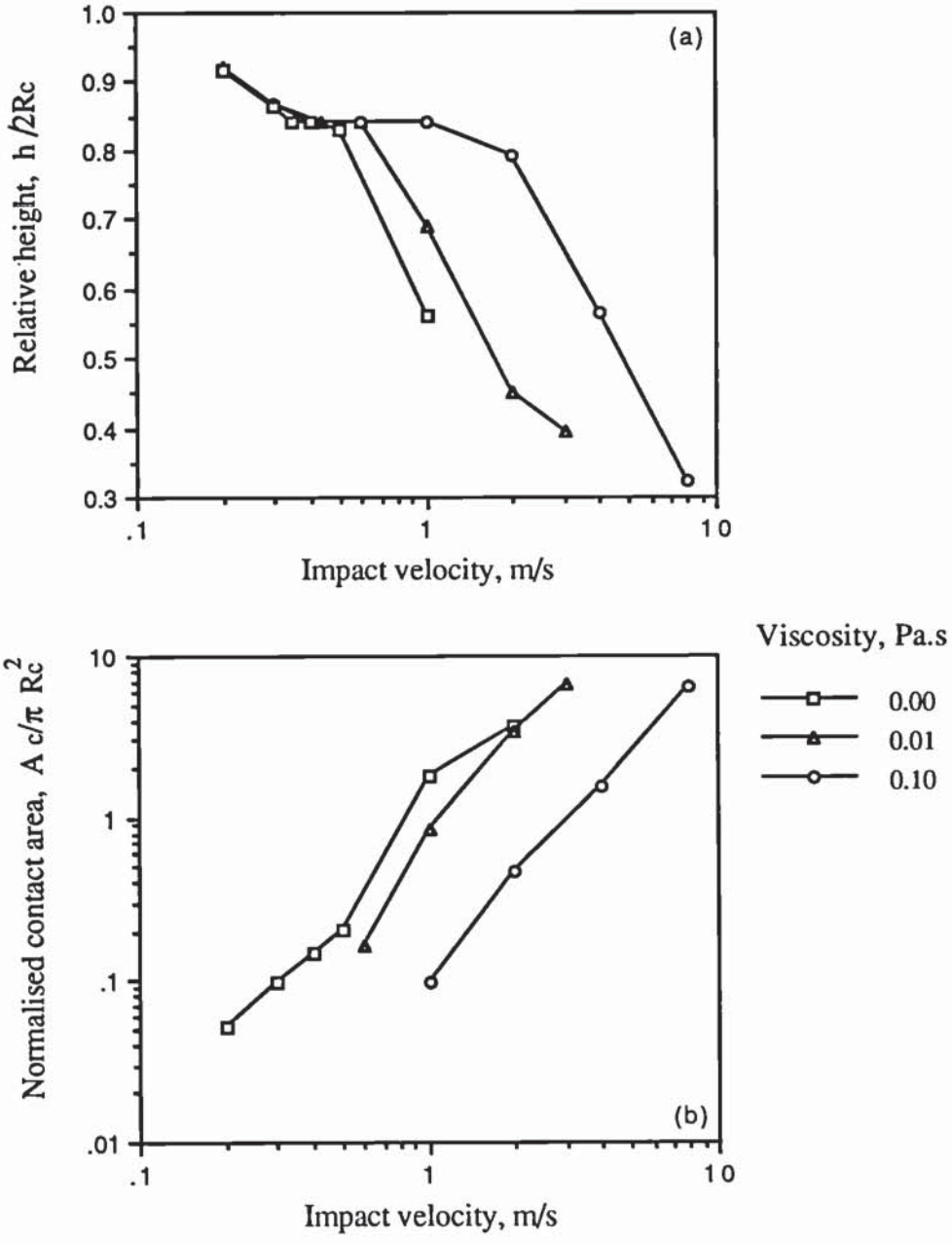

Figure 6.8: Relative height and dimensionless contact area of moist agglomerates after colliding with a wall.

viscosity of the interstitial liquid binder has no significant effect. At higher impact velocities, however, the relative height reduces with reduction in the viscosity of the liquid bridges. This indicates that at low impact velocities, interparticle friction and static liquid bridge forces are more significant and the viscous effect becomes dominant when the impact velocity is relatively high.

In figure 6.8b the dimensionless contact area of the agglomerate with the wall ($A_c/\pi R_c^2$) is plotted against impact velocity in a log-log scale. It can be seen that, for each value of viscosity, the relationship almost follows a straight line with a slope of 2. This implies that the contact area is almost a linear function of the initial kinetic energy of the agglomerate. Comparing the results shown for liquid viscosities of $0.01Pa.s$ and $0.10Pa.s$, it is observed that the normalised contact area scales inversely with the viscosity. This may suggests that,

$$A_c \propto \frac{v^2}{\eta} \tag{6.1}$$

where v is the impact velocity and η is the viscosity of liquid bridges. However, this does not apply to the agglomerate with inviscid liquid bridges because its bulk behaviour is dominated by interparticle friction and static liquid bridge forces.

6.3.3 Damage assessment

Visual observation of the computer simulated moist agglomerate impact tests indicated that attrition only occurred when agglomerates with low viscosities were impacted at high velocities. Neither shattering nor semi-brittle fracture were observed. Instead, for the most severe damage case of the inviscid agglomerate impacted at a speed of $2.0m/s$, a large cluster consisting of 3501 primary particles survived, in spite of being subjected to severe plastic deformation. This cluster accounts for 86.2% in mass of the original agglomerate. The other 13.8% corresponds to the debris which

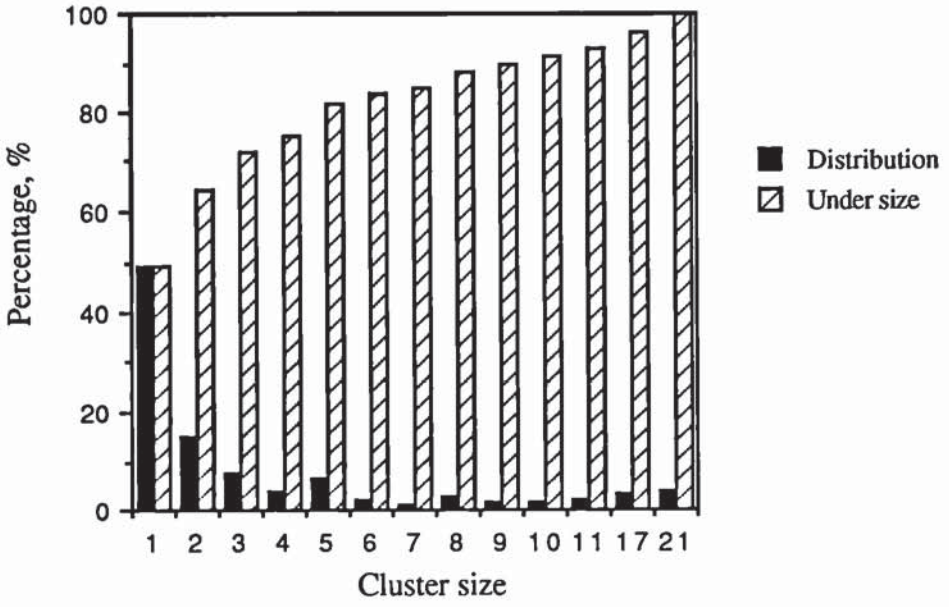

Figure 6.9: Size distribution of the debris produced by a body-centred cubic agglomerate with inviscid liquid bridges impacting normal to a wall at a velocity of $2.0m/s$.

mainly consisted of singlets, doublets and triplets. The size distribution of the debris is shown in figure 6.9. It can be seen that of the 13.8% debris, there are 49.02% singlets, 15.33% doublets and 7.49% triplets. The clusters with more than 10 primary particles only account for 8.73% of the debris with the largest cluster consisting of 21 primary particles.

The number of particles and small clusters that break away from the moist agglomerate is greatly reduced when the viscosity of the interparticle liquid bridges increases. This is indicated in figures 6.5–6.7. When the viscosity of the liquid bridges of the agglomerate was increased to $0.1Pa\,s$, no particles were broken away even when the impact velocity was very high and the agglomerate was severely flattened.

Although collisions do not produce significant attrition and fracture, especially for very viscous agglomerates, significant internal damage may occur if the impact velocity is relatively high. This is shown by figure 6.10a where the damage ratio of

the moist agglomerate is plotted as a function of the impact velocity for different liquid bridge viscosities. The damage ratio is defined as,

$$D_r = \frac{N_d}{N_o} \tag{6.2}$$

where N_d is the number of the ruptured liquid bridges and N_o is the number of initial liquid bridges in the agglomerate before impact.

It can be seen from figure 6.10a that there is a distinct threshold velocity below which the impact causes no internal liquid bridge rupture. Above the threshold velocity, the damage ratio increases as the impact velocity increases. In the semi-logarithmic plot, each set of damage ratio data produces a straight line with a slope of 1. Consequently, the dependence of the damage ratio on the impact velocity can be represented by a logarithm function of the following form,

$$D_r = \log \frac{v}{v_o} \tag{6.3}$$

where v_o is the threshold impact velocity below which the impact causes almost no internal damage to the agglomerate. This relationship is similar to that obtained for dry agglomerate impacts as reported by Yin (1992). Figure 6.10a shows that the threshold velocity increases with the bond strength of the liquid bridges. For the three liquid viscosities of 0.0, 0.01 and $0.10 Pa.s$, the best fit of data gives the threshold velocities as 0.35, 0.44 and $0.98 m/s$ respectively.

During the impact process, whenever a collision between the primary particles occurred, a new liquid bridge was formed if there was no liquid bridge before. Figure 6.10b shows that, in addition to liquid bridge rupture, there were also quite a number of new liquid bridges formed. The ratio of newly made bridges also increases as the impact velocity increases. Newly made liquid bridges occurred at much lower impact velocities than the threshold velocity to cause damage. As a result, the overall bridge

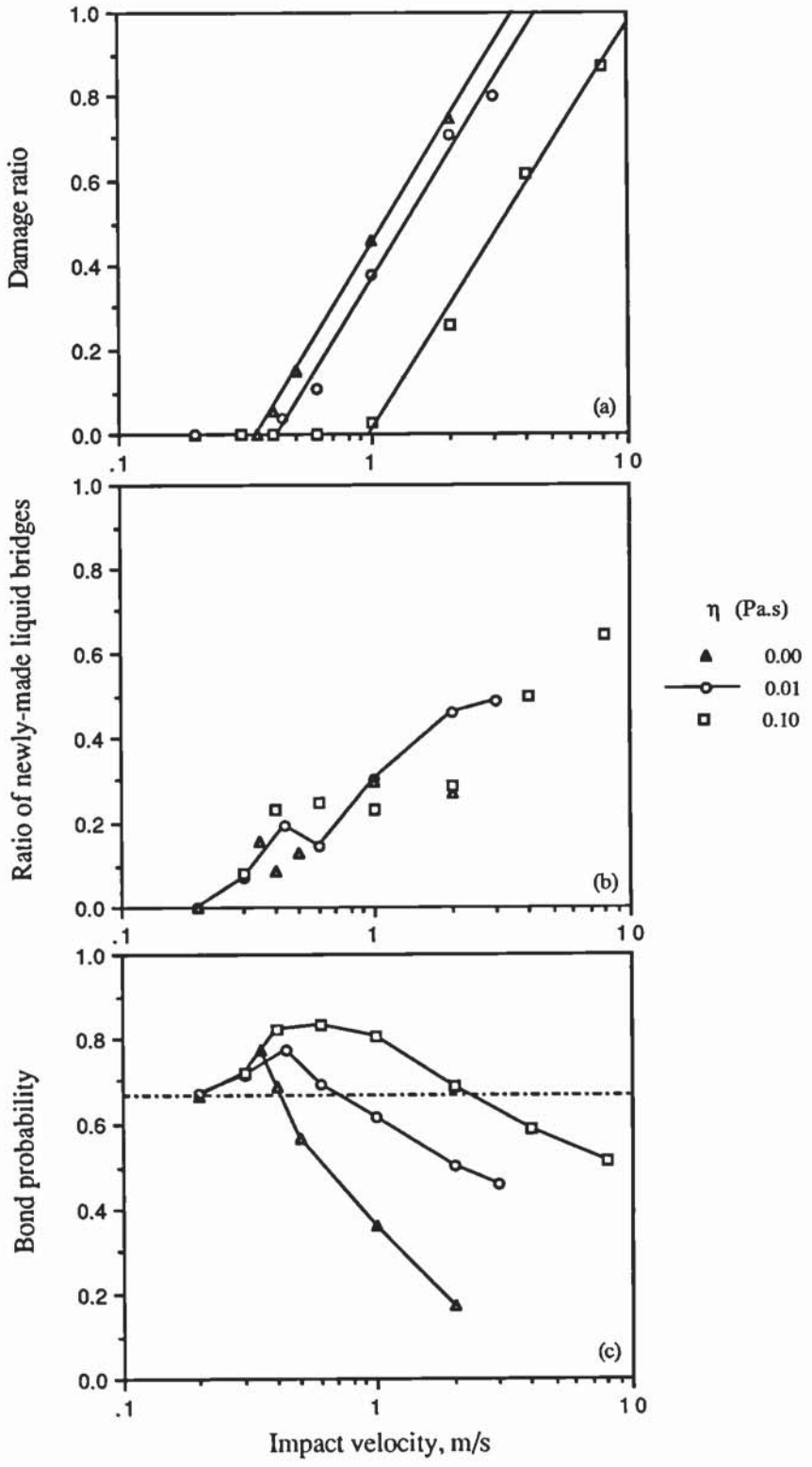

Figure 6.10: The dependence of (a) the damage ratio, (b) the newly-made liquid bridge bonds and (c) the overall bond probability of the moist agglomerate on the impact velocity.

number increased if the impact velocity was below the threshold velocity. However, when the impact velocity was above the threshold velocity, the rate of increase in the number of ruptured bridges with impact velocity was much higher than that of the newly made liquid bridges. Consequently, the overall number of liquid bridges in the agglomerate after impact decreased at high impact velocities. It is also observed from figure 6.10b that as the impact velocity reaches the threshold velocity for damage the number of newly-made liquid bridges decreases slightly.

The overall contact number due to the balance between the broken liquid bridges and newly made ones can be described by the bond probability which is defined as the ratio of the final to initial number of liquid bridges,

$$p_b = \frac{Z}{12}\frac{N_o - N_d + N_n}{N_o} = \frac{8}{12}(1 - \frac{N_d - N_n}{N_o}) \tag{6.4}$$

where N_n is the number of the newly made liquid bridges and Z is the coordination number. The coefficient $Z/12$ is introduced because, for regular packings, the densest packing is face-centred cubic (FCC) which has a coordination number of 12. Thus, the coefficient $Z/12$ scales the bond probability of the face-centred cubic arrangement to the highest bond probability 1. According to this definition, the coordination number of the body-centred cubic (BCC) is $Z = 8$ and the bond probability is 2/3. Strictly speaking, 8 and 12 are the coordination numbers for BCC and FCC but not when there are finite boundaries. For agglomerates of BCC and FCC the coordination numbers are less than 8 and 12 respectively. For simplicity, we use 8/12 to scale the bond probability of the body-centred cubic agglomerate.

Figure 6.10c shows that in terms of bond probability, there are two distinct regions of moist agglomerate-wall impact. In the low impact velocity region, the bond probability first increases and then decreases as the impact velocity increases, but the bond probability is above the initial value of 2/3. Thus, the agglomerate may be considered to be stronger after the impact because there were more interparticle

liquid bridges. In this sense, the strongest agglomerate is obtained by impacting at the damage threshold velocity which also corresponds to the maximum bond probability of the agglomerate after impact. In the high impact velocity region the bond probability is reduced to less than the initial value of 2/3 and the agglomerate may be considered to have been weakened by the impact. This is due to there being more broken bridges than newly-made ones.

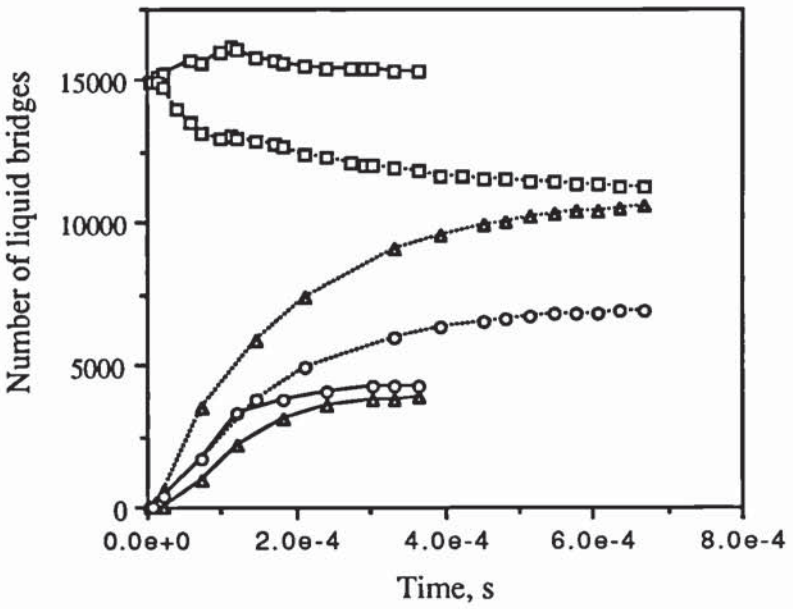

Figure 6.11: The evolution of broken contacts (△), newly-made contacts (o) and overall remaining contacts (□) of liquid bridges of a low viscosity ($0.01 Pa.s$) agglomerate (broken lines) and a high viscosity ($0.1 Pa.s$) agglomerate (solid lines) impacting at a speed of $2.0 m/s$.

In order to illustrate further the apparent strengthening/weakening process, the evolution of broken bridges, newly-made bridges and overall remaining bridges are plotted in figure 6.11 for two typical cases. It shows clearly that when the agglomerate with a lower viscosity of $0.01 Pa.s$ was impacted at a velocity of $2.0 m/s$, the rate of bridge rupture exceeded the rate at which newly-made liquid bridges were formed.

Consequently, the overall number of liquid bridges continuously reduced until a constant value was reached when the kinetic energy of the collision had been almost fully dissipated. When the viscosity of the binding liquid was $0.1 Pa.s$, the rate of liquid bridge rupture was initially less than the rate at which new liquid bridges were formed and during this stage the overall number of the bridges, therefore, increased. Subsequently, the overall number of liquid bridges decreased due to the rate of bridge rupture exceeding the rate of forming new contacts. However, at the equilibrium state, the final number of liquid bridges was still larger than the initial number prior to impact.

6.4 Summary

Results have been presented from computer simulations of a moist agglomerate impacting with a wall. The agglomerate consisted of 4062 primary particles with a body-centred cubic arrangement. It has been shown that when the agglomerate was impacted, it remained adhered to the wall and deformed visco-plastically. Only at high impact velocities did any attrition occur with the agglomerate being greatly deformed into a planar shape. The maximum amount of attrition was observed when the inviscid agglomerate was impacted at a velocity of 2.0m/s. However, the debris produced consisted of only a small portion of the agglomerate mass. Semi-brittle fracture/fragmentation and shattering behaviour observed for dry agglomerates were not observed in the moist agglomerate simulations. When the viscosity of the binding liquid increases, attrition due to the break up of single particles or small clusters decreases and so does the visco-plastic deformation of the agglomerate. This indicates that the resistance of the agglomerate to attrition and deformation increases with the increase in the liquid bridges viscosity.

At moderate impact velocities, attrition did not occur. Internal damage to the

agglomerate was produced due to the rupture of interparticle liquid bridges. There is a distinct threshold velocity above which the ratio of ruptured liquid bridges increases logarithmically as the impact velocity increases. At low impact velocities, below the threshold velocity, the impact did not cause any internal bridge rupture. The threshold velocity was found to increase as the viscosity of the liquid bridges and hence the strength of the agglomerate was increased.

It has been shown by the computer simulations that new liquid bridges were also formed between the primary particles of the agglomerate during the impacts. The creation of new liquid bridges can occur at impact velocities much below the threshold velocity of bridge rupture. The number of newly-made liquid bridges increases with the impact velocity and is dependent on the viscosity of the binding liquid. The total number of liquid bridges, as represented by the bond probability of the agglomerate, reflects the balance between ruptured and newly-made liquid bridges. It was found that at low impact velocities, the bond probability of the impacted agglomerate increased because more liquid bridges were created than were ruptured. This may be interpreted as a strengthening (or hardening) of the agglomerate during impact. In this sense, the strongest agglomerate, having the highest bond probability, is obtained at the threshold velocity for damage. At high impact velocities, the bond probability is reduced during impact, implying a weakened agglomerate due to more liquid bridges being broken than new bridges being created. The transition from the "strengthening" to "weakening" depends on the viscosity of the liquid bridges. When the viscosity of the liquid is increased, the transition occurs at a higher impact velocity and the maximum bond probability also increases.

Chapter 7

Computer simulation of agglomerate-agglomerate collisions

This chapter is concerned with the computer simulation of agglomerate-agglomerate collisions using TRUBAL. Two moist agglomerates each consisting of 1000 randomly generated particles were prepared. Results of normal and oblique collisions of the two moist agglomerates are reported. The coalescence and attrition mechanisms of the agglomerate collisions have been examined in terms of the energy dissipation and visco-plastic deformation. The effect of interstitial liquid bridge properties has also been investigated. Some results presented in this chapter have been reported by Lian, Thornton and Adams (1993a).

7.1 Introduction

For powder granulation, moist particles or granules are agitated to move about and collide with each other. As a result of a collision, the granules may stick, break-up or rebound. Whether the collision of moist granules or agglomerates leads to size enlargement or reduction, the review in chapter 2 indicates that the underlying mechanism is not clear. The study by Nienow and Rowe (1985) stressed the importance of the balance of interparticle binding forces and collisional break up forces. They argued that if the binding forces dominate over the break-up forces, agglomerates continue to grow in size. If the break-up forces are greater than the binding forces, agglomerates will break up. However, binding forces and break-up forces in agglomerates are not well understood, and are rarely quantified (Adams, Mullier and Seville 1987).

At the microscopic level, studies reported by Davis (1987), Ennis et al (1991) and others (Barnocky and Davis 1988a, 1988b; Davis et al 1986; and Serayssol and Davis 1986) indicated that for single pairs of elastic or rigid particles, successful coalescence may occur only if they have insufficient relative kinetic energy to overcome the retarding force of the binding liquid. However, it has been demonstrated by the computer simulated agglomerate impact tests in chapter 6 that moist agglomerates differ from single rigid or elastic particles in that they behave visco-plastically. In comparison with dry agglomerates, moist agglomerates are also more resistant to attrition and fracture-fragmentation because the interparticle bonds of liquid bridges are more extendible and provide more energy accommodation. At the microscopic level, it has also been demonstrated that the strength and deformability of moist agglomerates are mainly dependent on the viscosity of the interparticle liquid bridges.

In order to examine the mechanisms that control the coalescence and break up of moist agglomerates, the computer program TRUBAL has been applied to simulate

collisions between two moist agglomerates. The two agglomerates, each consisting of 1000 randomly packed particles, were prepared and a series of normal and oblique collisions were performed. Pictures of the two agglomerates after collisions are presented and their coalescence and attrition mechanisms are discussed in terms of the energy dissipation and visco-plastic deformation. At the microscopic level, the effect of the liquid bridge properties is also examined.

7.2 Computer simulation procedures

7.2.1 Agglomerate preparation

For the computer simulated moist agglomerate-agglomerate collisions, two agglomerates each consisting of 1000 randomly packed particles were prepared by the following procedures. First, one thousand particles were randomly generated in each of two spherical regions. The radius of the generated primary particles was $R = 30\mu m$ with a normally distributed deviation of $\pm 3\mu m$. This deviation of the particle size is used to ensure random packing of the agglomerates. The properties of the primary particles were: density $\rho = 2.65 Mg\, m^{-3}$, Young's modulus $E = 70 Gpa$, Poisson's ratio $\nu = 0.3$ and friction coefficient $\mu = 0.3$.

When the particles were first generated, there were no initial inter-particle contacts. Centripetal gravity fields were then applied to the particles in each region to bring them together. During this process, whenever a collision between the primary particles occurred, a quantity of liquid (0.1% of the particle volume) was assigned to the contact between the particles to form a liquid bridge. The liquid bridges were modelled with the following properties: surface tension $\gamma_{lv} = 0.025 \sim 0.050 N\, m^{-1}$, viscosity $\eta = 0.001 \sim 0.1 Pa\, s$ and solid-liquid contact angle $\theta = 0°$.

Because of the viscous resistance of the liquid bridges, all particles gradually coalesced under the centripetal gravity fields and two agglomerates were formed. However, the coalescence of the particles under the centripetal gravity field requires very long computer time because, with the normal density of the particles, the time step is very small. Thus, during the agglomerate preparation process, a high density of $\rho = 2.65 \times 10^3 Mg\,m^{-3}$ for the particles was specified so that a much larger time step could be used. When the kinetic energy of the two coalesced particle systems was satisfactorily dissipated by the viscous damping of the liquid bridges the centripetal gravity fields were then slowly removed so that the two agglomerates were not disturbed due to the sudden removal of the applied gravity field. After the removal of the centripetal gravity field, normal density was assigned to all the particles and further cyclic calculations were carried out to ensure that the systems of the two moist agglomerates attained a state of quasi-equilibrium. The two agglomerates were then moved close to each other prior to specifying the desired impact velocities.

The two wet agglomerates formed by the above process are shown in figure 7.1 where the distributions of the overall contact forces and residual rectilinear velocities of the constituent particles are also presented. In figure 7.1b contact forces are represented by lines joining the centroids of the primary particles that are in contact. A green line indicates a compressive force and a blue line indicates a tensile force. The magnitude of the contact forces is indicated by the thickness of the lines. In figure 7.1c, the rectilinear velocity of each particle is represented by a line that starts from the particle center and ends at a red dot. The magnitude of the velocities is indicated by the length of the line.

For the two agglomerates shown in figure 7.1a, the measured radii of the circumscribing spheres are $384\mu m$ and $383\mu m$ respectively. Altogether there were 7183 interstitial liquid bridges which corresponds to a degree of average saturation of 0.71% and an average coordination number of 7.183. The coordination number is very close

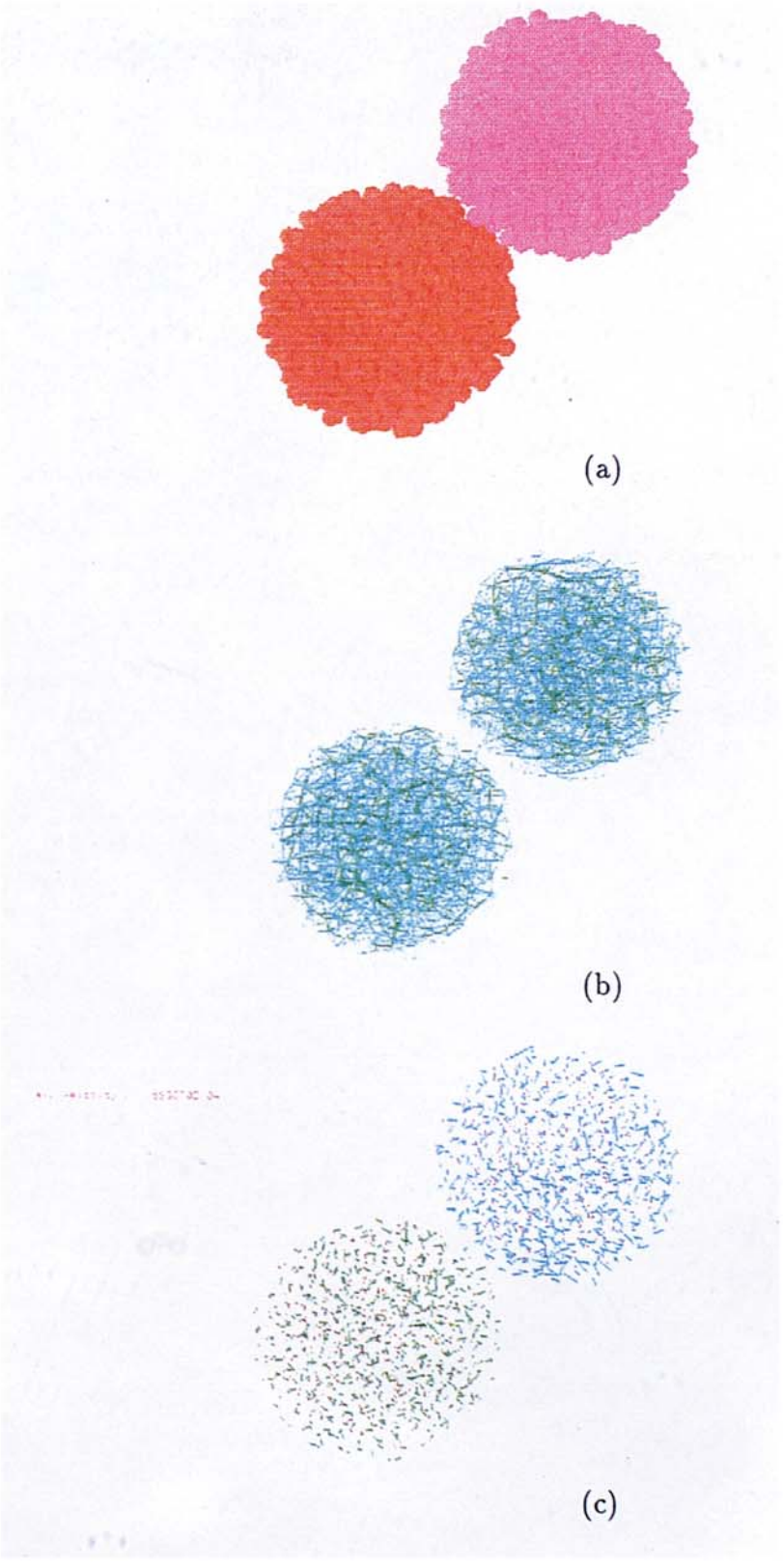

Figure 7.1: The initial state of the two prepared moist agglomerates: (a) the agglomerates, (b) total contact force distribution and (c) rectilinear velocity field.

to that measured for the body-centred cubic agglomerate of 4062 particles reported in the previous chapter. Theoretically, the coordination number of a body-centred cubic packing should be 8, but for the agglomerate of 4062 particles the measured average coordination number was 7.339. This is because for the reported body-centred cubic agglomerate, the particles on the periphery have less than 8 contacts. Thus, the measured average coordination number is less than 8.

Of the 7183 interstitial liquid bridges, the overall forces are either compressive (3263 in total) or tensile (3920 in total). The magnitude of the maximum force is $1.5 \times 10^{-5} N$. It can be seen from 7.1b that the tensile and compressive forces are randomly distributed within the two agglomerates. The translational velocities of the constituent particles are shown by figure 7.1c. It can be seen that they are also randomly distributed. The maximum rectilinear velocity is around $1.0e{-}5m\,s^{-1}$. The kinetic energy of the two agglomerates is $9.21 \times 10^{-17} J$. Further cyclic calculations to reduce the kinetic energy was not attempted because it was observed that the local oscillations of the primary particles were more dominant and it needs a lot more cyclic calculations to further reduce the translational velocities. The stage of the agglomerates shown in figure 7.1 was achieved after about 340,000 calculation cycles (time steps) from the very beginning when the primary particles were first generated.

7.2.2 Impact simulations

All successive computer simulated collisions were started with the same agglomerates from the same stage. Two series of agglomerate-agglomerate collision tests were performed. The first series of tests involved the normal collisions of the two agglomerates. The effects of impact velocity, liquid viscosity and surface tension were examined. The second test series was concerned with oblique collisions of the two agglomerates in order to investigate the influence of different incident angles on the

agglomerate coalescence and attrition. Both series of impact tests are described in table 7.1.

Normal impact			
Liquid viscosity $(Pa.s)$	Surface tension (N/m)	Incident angle (deg)	Impact velocity (m/s)
0.001	0.025	0	0.2, 0.5, 1.0, 1.2, 1.5, 2.0
0.010	0.025	0	0.5, 1.0, 1.5, 2.0, 2.5, 3.0, 4.0, 5.0
0.010	0.050	0	0.5, 1.0, 2.0, 3.0, 4.0, 5.0
0.100	0.025	0	2.0, 5.0, 6.0, 7.0, 10.0, 15.0
Oblique impact			
Liquid viscosity $(Pa.s)$	Surface tension (N/m)	Impact velocity (m/s)	Incident angle (deg)
0.010	0.025	2.0	15, 30, 45, 60, 75, 85
0.010	0.025	5.0	15, 30, 45, 60, 75, 85
0.001	0.025	2.0	15, 30, 45, 60, 75, 85

Table 7.1: Agglomerate-agglomerate impact tests performed.

7.3 Normal collisions

7.3.1 General observation

All pictures of the computer simulated normal collisions of the two moist agglomerates are shown in appendix C.2. Figure 7.2 illustrates three typical cases where the

two agglomerates are shown after they had collided at relative velocities of 1.0, 2.0, and $5.0\,m\,s^{-1}$ respectively; the properties of the interstitial binding liquid for all three cases were: viscosity $0.01\,Pa\,s$ and surface tension $0.025\,N\,m^{-1}$. It can be seen from figure 7.2 that, in all cases, the two moist agglomerates coalesced. When the relative colliding velocity was $1.0\,m\,s^{-1}$, the two agglomerates coalesced but were only slightly deformed near the local region of impact. The shape of the two moist agglomerates remained essentially unchanged. When the relative velocity was increased to $2.0\,m\,s^{-1}$, the two moist agglomerates also coalesced but their deformation was increased to such an extent that they were almost deformed to hemispheres as a result of the collision. When the relative impact velocity was further increased to $5.0\,m\,s^{-1}$, however, attrition occurred due to the removal of single particles and the two agglomerates were so greatly deformed that the resultant coalesced agglomerate was disc-shaped and would probably be prone to significant attrition in any subsequent collision.

The effect of binder viscosity is illustrated in figure 7.3 which shows the two moist agglomerates after colliding at the same relative velocity of $2.0m/s$. It can be seen that the stronger agglomerates, with a liquid viscosity of $0.100Pa.s$, coalesced and were only slightly deformed after the collision. When the viscosity of the binding liquid was reduced to $0.010Pa.s$, the two collided agglomerates coalesced but were deformed to almost hemi-spheres. For the weakest agglomerates with a liquid viscosity of $0.001Pa.s$ a small amount of agglomerate attrition occurred and the two original agglomerates were also greatly deformed.

For all cases of the two moist agglomerates subjected to normal collisions at different impact velocities and with different properties of liquid bridges, pictures shown in appendix C.2 indicate that they all coalesced. Only when the two agglomerates with low liquid viscosities were impacted at relatively high impact velocities, did any attrition occur, with just a few particles broken away. When the viscosity of the binding liquid increases, the impact velocity to produce attrition also increases. But with

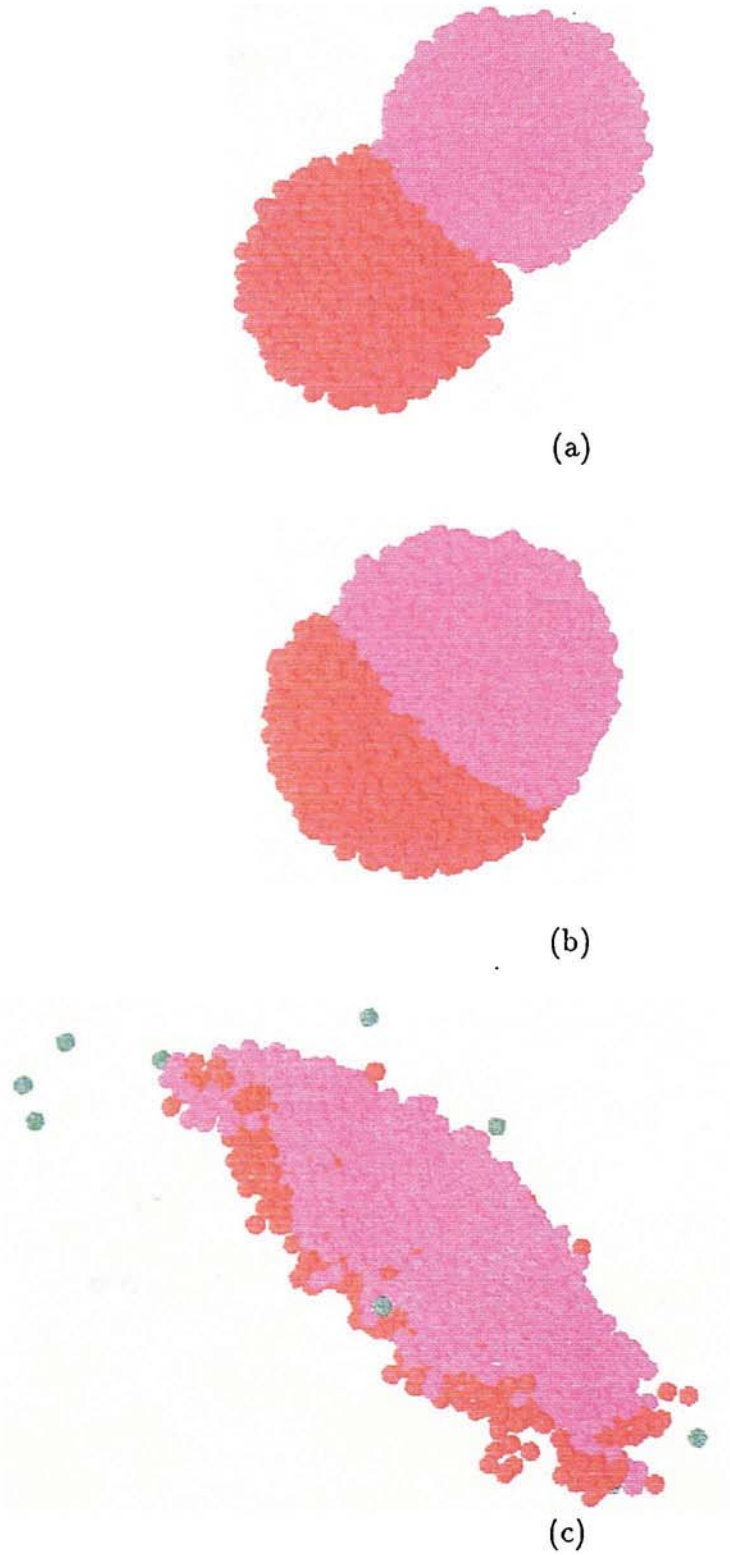

Figure 7.2: Two moist agglomerates with 0.01 $Pa\,s$ viscosity and 0.025 $N\,m^{-1}$ surface tension of liquid bridges after colliding at velocities of (a) $1.0\,m\,s^{-1}$, (b) $2.0\,m\,s^{-1}$ and (c) $5.0\,m\,s^{-1}$.

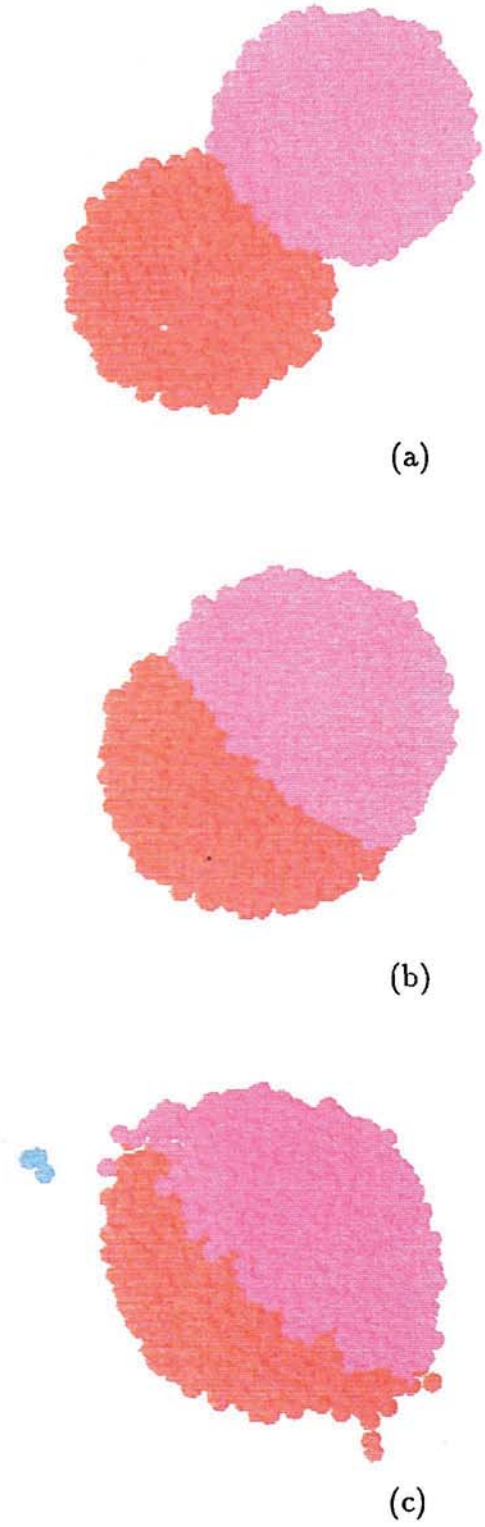

Figure 7.3: Two moist agglomerates after colliding at a relative speed of $2.0m/s$ but with different liquid viscosities of (a) $0.100Pa.s$, (b) $0.010Pa.s$ and (c) $0.001Pa.s$

higher viscosities of liquid bridges, fewer primary particles were broken away even if the two agglomerates were greatly deformed. The impact velocity for producing attrition also increases if the surface tension of the binding liquid is increased.

The observed damage behaviour of the moist agglomerates is much different from that observed for dry agglomerates impacted at corresponding velocities (Yin 1992; Thornton and Kafui 1992; and Thornton, Kafui and Yin 1993; and Kafui and Thornton 1993). In the computer simulated collisions of the moist agglomerates, neither shattering nor semi-brittle fracture was observed. Break-up of single particles or small clusters was observed only at high impact velocities. At low collision velocities the wet agglomerates coalesced and deformed. An increase in the impact velocity leads to an increase in the plastic deformation of the agglomerates and consequently affects the size and shape of the resulting coalesced agglomerate.

A simple way of characterising the shape and size of an agglomerate is provided by fractal geometry. According to Mandlebrot (1983), for an agglomerate with the number of primary particles, N_p, the fractal dimension, D_f, is related to the radius of the smallest sphere that circumscribes the agglomerate, R_c, by the equation

$$N_p = \phi_s (R_c/R)^{D_f} \tag{7.1}$$

where R is the radius of the primary particles and the parameter ϕ_s is often taken to be unity but, if known, is the solid fraction of the agglomerate, Feder (1988). For simplicity we will assume $\phi_s = 1.0$.

The fractal dimension is also a measure of the agglomerate structure. Using equation 7.1, the size and shape of the BCC agglomerate (4062 primary particles, $R = 30\mu m$) reported in chapter 6 may be defined by a circumscribing sphere radius $R_c = 572\mu m$ and fractal dimension $D_f = 2.82$. Kafui and Thornton (1993) reported a face-centred cubic agglomerate consisting of 7912 primary particles of radius $R =$

$10\mu m$. The measured radius of the circumscribing sphere is $R_c = 230.5\mu m$ which corresponds to a measured fractal dimension of $D_f = 2.86$. For the two randomly generated agglomerates reported in this chapter, the size and shape of each of the initial agglomerates before impact may be defined by $R_c = 0.3835mm$ and $D_f = 2.71$. Considering the two agglomerates together when they are just touching each other, the fractal dimension is $D_f = 2.345$.

Figure 7.4 illustrates how the radius of the circumscribing spheres and the fractal dimension of the resultant coalesced agglomerate are dependent on the relative impact velocity, surface tension and viscosity of the liquid bridges. As the velocity increases the size of the coalesced agglomerate decreases and the fractal dimension increases. There is an optimum velocity above which the size increases due to the extensive flattening in the plane orthogonal to the impact direction, with a corresponding decrease in the fractal dimension due to the increased tendency to produce a flat "two-dimensional" agglomerate.

Figure 7.4 also shows the effects of different binding liquid properties on the size and shape of the coalesced agglomerate. When the viscosity of the liquid bridges increases, the fractal dimension increases with impact velocity at a slower rate and the maximum fractal dimension is obtained at a higher optimum impact velocity. Correspondingly, the circumscribing sphere radius decreases with impact velocity at a reduced rate due to the increase in viscosity. The effect of the surface tension of the liquid is similar to that of the liquid viscosity.

In terms of granulation and attrition, it is generally believed by experimentalists that the effect of increasing the impact velocity (by increasing the gas velocity of a fluidised bed for instance) is to decrease particle agglomeration and increase attrition. It is argued that, as the gas velocity increases, the particles will have greater impact velocities and hence the break-up forces will be increased (Smith and Nienow 1983a; Mullier 1991). In the computer simulated agglomerate collisions, however, it was

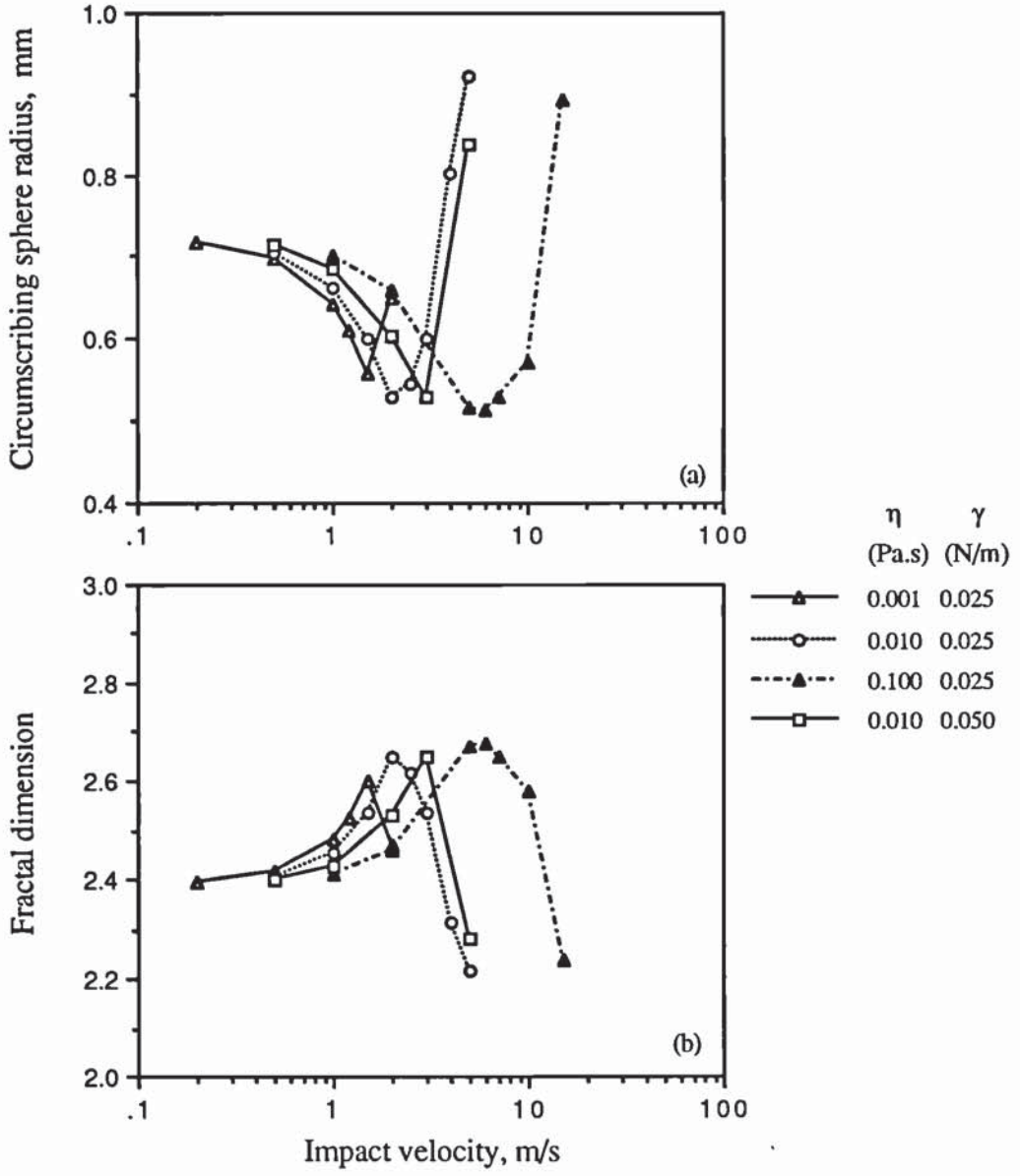

Figure 7.4: The size and shape of the resultant coalesced agglomerate as a function of impact velocity: (a) Radius of circumscribing sphere and (b) fractal dimension.

observed that, below the optimum impact velocity, an increase in impact velocity enhances the coalescence of the two agglomerates. This is because of the fact that in this region of impact velocities, the number of newly-made liquid bridges between the two agglomerates increases as the impact velocity increases and attrition does not occur. Apart from that, the size of the coalesced agglomerate also decreases with the impact velocity. At the optimum impact velocity, the collision produced a near spherical shaped agglomerate which should minimize attrition due to subsequent collisions. Only at high impact velocities beyond the maximum impact velocity did any attrition occur, with some particles or small clusters broken away. However, the two agglomerates were also severely flattened. It is only in this region, where the impact velocity is above the maximum impact velocity, that the increase of the impact velocity will increase the attrition of the agglomerates and hence decreases granulation.

7.3.2 Energy dissipation

Generally speaking, for the size enlargement process of moist agglomerates, energy dissipation and visco-plastic deformation are essential for their successful coalescence. At the micro-level, Davis (1987) and others (Barnocky and Davis 1988a, 1988b; Davis et al 1986; Serayssol and Davis 1986) studied the elasto-hydro-dynamic collision of elastic solid spheres. A similar theory was also presented by Ennis et al (1991) for moist granules, where the granules were considered to be rigid spheres covered by thin liquid layers. For either rigid or elastic spheres, the successful coalescence was shown to be due to the complete dissipation of the kinetic energy only by the thin layers of the liquid that covered the spheres. From the computer simulated moist agglomerate collisions, however, the coalescence mechanism was seen to be quite different. Dissipation of the kinetic energy for the moist agglomerates was not solely due to the viscous resistance of the binding liquid, but also due to the rearrangement

(visco-plastic deformation) of the particle structure which involved energy dissipation due to interparticle friction, viscous resistance and liquid bridge rupture.

Figure 7.5a shows the initial kinetic energy and the energy dissipated by viscous resistance, interparticle friction and liquid bridge rupture as a result of the two agglomerates colliding at different velocities, where the properties of the binding liquid were: viscosity $\eta = 0.01 Pa.s$ and surface tension $\gamma_{lv} = 0.025 N/m$. In figure 7.5b the energy dissipated is expressed as a ratio of the initial kinetic energy. It can be seen that when the viscosity of the liquid is $0.01 Pa\,s$, the energy dissipated by the viscous liquid accounts for about 60% of the initial kinetic energy and the energy dissipated due to interparticle friction accounts for more than 30%. The energy dissipated as a result of rupturing the internal liquid bridges is a very small proportion of about 5% of the initial kinetic energy. The impact velocity does not significantly affect the relative ratios of energy dissipation except for very low impact velocities. At low impact velocities, it can be seen from figure 7.5b that the energy ratio dissipated by viscous resistance increases and the energy ratio dissipated by friction decreases as the impact velocity decreases.

The ratios of kinetic energy dissipated by viscous resistance, interparticle friction and liquid bridge rupture are dependent on the viscosity and surface tension of the binding liquid bridges. This is shown in figure 7.6. It can be seen from figure 7.6a that when the viscosity of the liquid was increased to $0.100 Pa.s$, the ratio of the kinetic energy dissipated by viscous resistance correspondingly increased to about 80% and that by interparticle friction decreased to about 20%. The energy dissipated by the rupture of liquid bridge bonds slightly decreased when the viscosity increases.

Figure 7.6a also indicates that the surface tension of the liquid bridges also affects the ratios of the initial kinetic energy dissipated. By increasing the surface tension from $0.025 N/m$ to $0.50 N/m$, the energy dissipated by interparticle friction increased by more than 5% and the energy dissipated by viscous resistance decreased by more

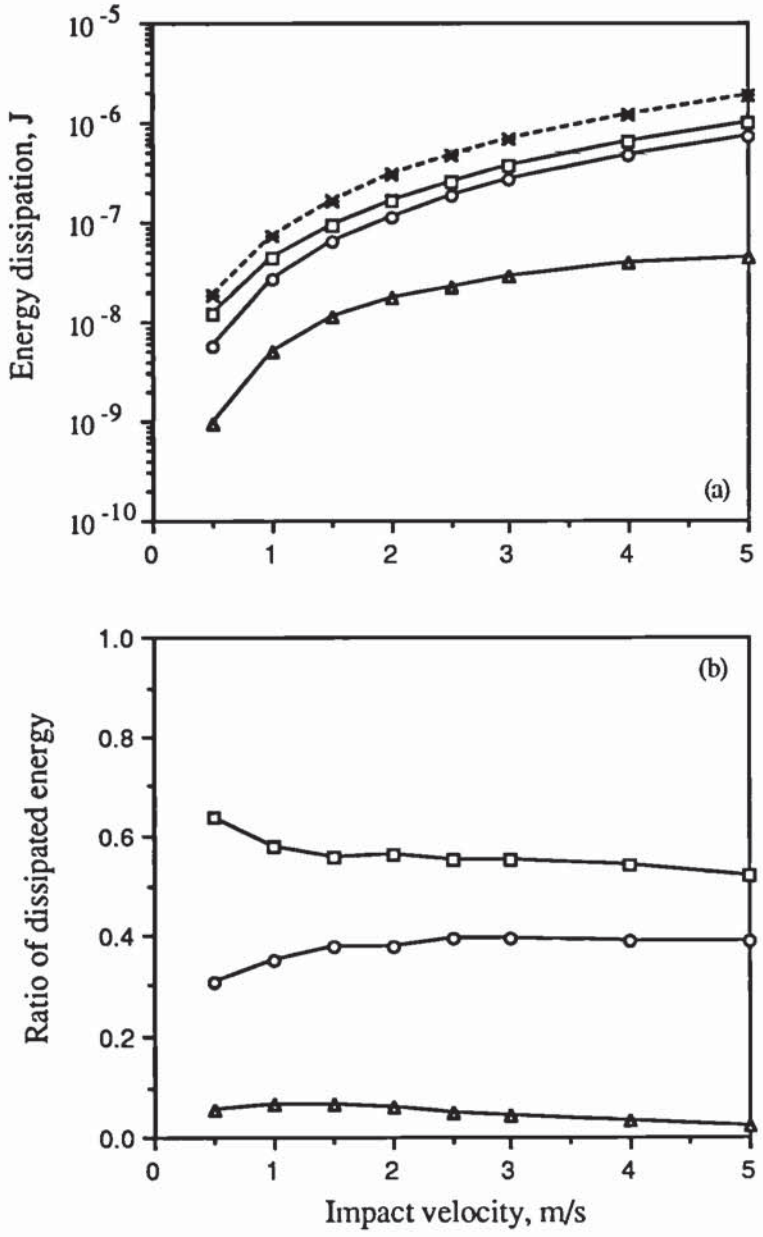

Figure 7.5: Ratio of initial kinetic energy (*) dissipated by viscous resistance (□), interparticle friction (o) and liquid bridge rupture (△) for two collided moist agglomerates with a liquid viscosity of $0.01 Pa.s$ and a surface tension of $0.025 N/m$.

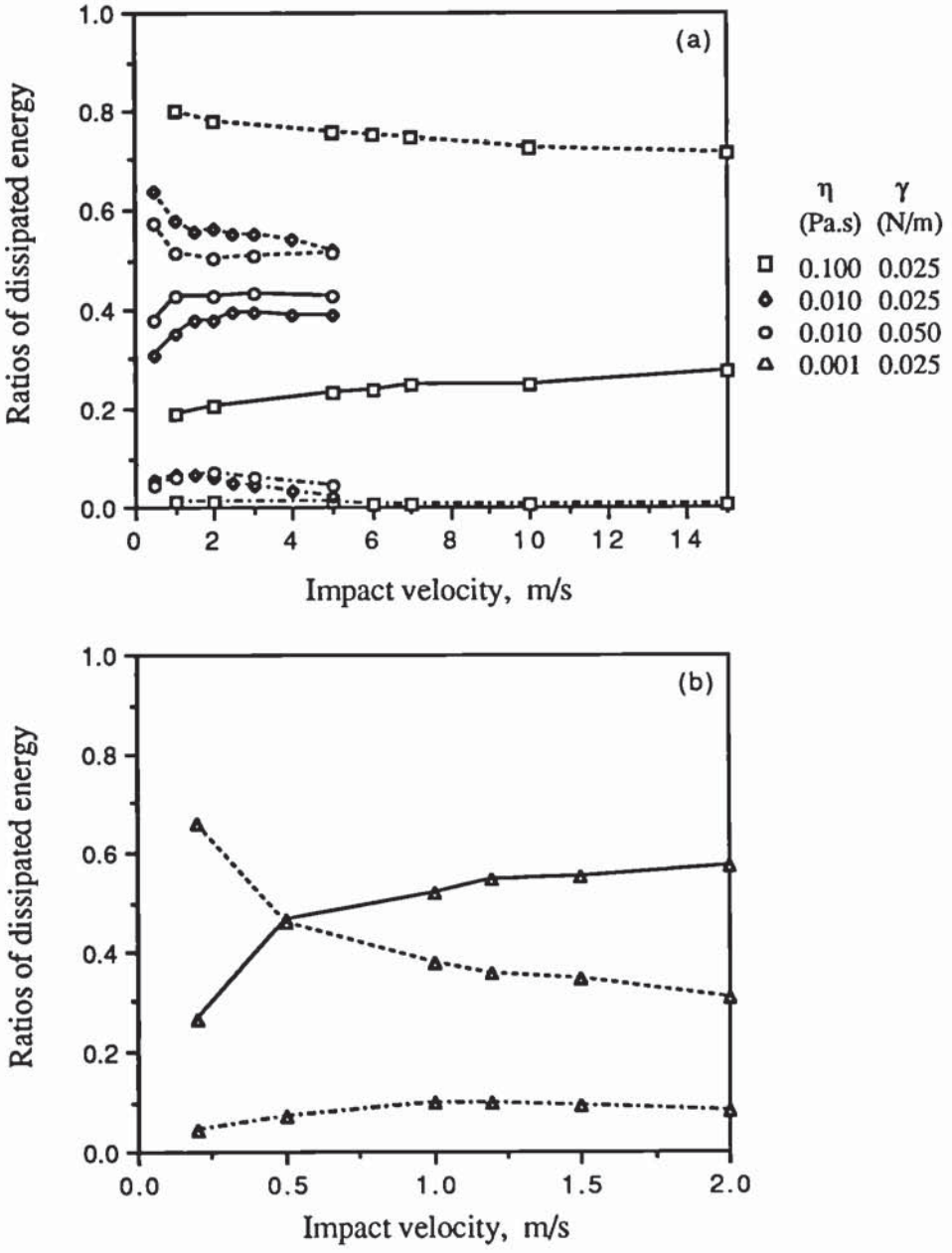

Figure 7.6: Effects of the viscosity and surface tension of liquid bridges on the ratios of initial kinetic energy dissipated by viscous resistance (dashed lines), interparticle friction (solid lines) and liquid bridge rupture (dot dashed lines).

than 5%. The energy dissipated by the rupture of interstitial liquid bridges also slightly increased.

For all the cases shown in figure 7.6a, the relative ratios of energy dissipation remained almost constant at high impact velocities. At low impact velocities, the energy ratio dissipated by viscous resistance increases and the energy ratio dissipated by interparticle friction decreases as the impact velocity decreases. In addition, the energy ratio dissipated by viscous resistance always exceeded the energy ratio dissipated by interparticle friction regardless of impact velocity. However, figure 7.6b indicates that when the viscosity of the liquid is very low, the distribution of energy dissipation is different from the above cases. It can be seen from 7.6b that, with a liquid viscosity of $0.001 Pa.s$, the energy dissipated by viscous resistance decreased from 70% to 30% as the impact velocity increases. On the other hand, the energy dissipated by interparticle friction correspondingly increased from 25% to 60% of the initial kinetic energy. Therefore, at low impact velocities, the energy ratio dissipated by viscous resistance is dominant, but, when the relative impact velocity is higher than $0.5 m/s$, frictional dissipation dominates.

During the course of a collision, there are only relatively few new contacts and liquid bridges formed between the particles of one agglomerate and the other. As a result, most of the energy dissipated by interparticle friction and viscous resistance is accommodated by the internal contacts and liquid bridges where the relative movement between particles is propagated by the deformation of the agglomerates themselves. Consequently, the theory of single elastic or rigid particle models must underestimate the energy dissipation of moist agglomerates significantly since they do not account for the most significant microscopic energy dissipation mechanisms of internal viscous and frictional damping.

7.3.3 Damage assessment

Of the three contributions to the energy dissipation, the viscous and frictional energy dissipation components are associated with the overall visco-plastic deformation of the granules and favour agglomerate coalescence. However, the rupture of the liquid bridges between the particles constitutes internal damage to the agglomerates. Although the energy dissipated due to liquid bridge rupture is only a small percentage, which decreases when the impact velocity is increased, the damage to the agglomerate is, however, increased since the number of the broken liquid bridges increases with impact velocity. It was observed that for the computer simulated moist agglomerate collisions, a certain number of new contacts of liquid bridges were also made due to the collisions of the primary particles. Thus, some of the broken liquid bridges were compensated for by the newly made ones. The number of broken liquid bridges and the number of newly made ones are illustrated by figure 7.7a for different interparticle liquid bridge strengths and different impact velocities. It can be seen that both the ratios of ruptured liquid bridges and newly-made ones are logarithmically dependent on the impact velocities but, when a higher velocity is used, the increase in newly-made liquid bridges is less than the increase in ruptured liquid bridges. There are no distinct threshold velocities. It was found that, even at low impact velocities, a small number of liquid bridges were ruptured and new bridges were formed. At high impact velocities, however, the damage ratio of liquid bridge rupture can be fitted by,

$$D_r = \log \frac{v}{v_o} \tag{7.2}$$

and the ratio of newly-made liquid bridges can be fitted by,

$$n_r = 0.62 \log \frac{v}{v_o'} \tag{7.3}$$

where v is the relative impact velocity and v_o is the fitted threshold velocity of liquid bridge rupture and v_o' is the fitted threshold velocity of newly-made liquid bridges.

For the agglomerates with liquid bridges of a surface tension of $\gamma_{lv} = 0.025N/m$ and viscosities of $\eta = 0.001$, 0.010, and $0.100Pa.s$, the fitted threshold velocities of liquid bridge rupture are 0.73, 0.91, and $2.29m/s$ and the fitted threshold velocities for the newly-made liquid bridges are 0.87, 1.02 and $2.15m/s$ respectively. When the liquid viscosity is $0.010Pa.s$ and the surface tension is $0.050N/m$, the fitted threshold velocities are $v_o = 1.19m/s$ and $v_o' = 1.35m/s$.

Overall, the total number of liquid bridges did not change significantly at low impact velocities. Only when the impact velocity was high did the overall number of liquid bridges decrease. In figure 7.7c the overall bond probability of the coalesced agglomerate is plotted as a function of the impact velocity for different liquid bridge viscosities and surface tensions. Equation 6.4 is used to calculate the bond probability. The measured initial coordination number and hence the initial bond probability of the two agglomerates before collision are very close to that of the body-centred cubic agglomerate with 4062 particles. It can be seen from figure 7.7 that, for the normal collision of two agglomerates, the relationship between the bond probability and the impact velocity is slightly different from that of the agglomerate-wall collisions. At relatively low impact velocities, the bond probability did not change much after the collision, suggesting that there is no significant increase nor decrease in the "strength" of the coalesced agglomerates. At relatively high impact velocities, the bond probability of the coalesced agglomerate decreased. It is also noted that there is a significant reduction in the bond probability at the optimum impact velocities which produced near spherical coalesced agglomerates.

For all the simulated two agglomerate collisions reported herein, the damage behaviour of the coalesced agglomerate is very similar to that of the agglomerate-wall impacts. The damage was mainly in the form of the internal breakdown of the liquid bridges. Agglomerate attrition was only observed at high impact velocities, with only a few individual particles separated from the parent cluster. However, for the colli-

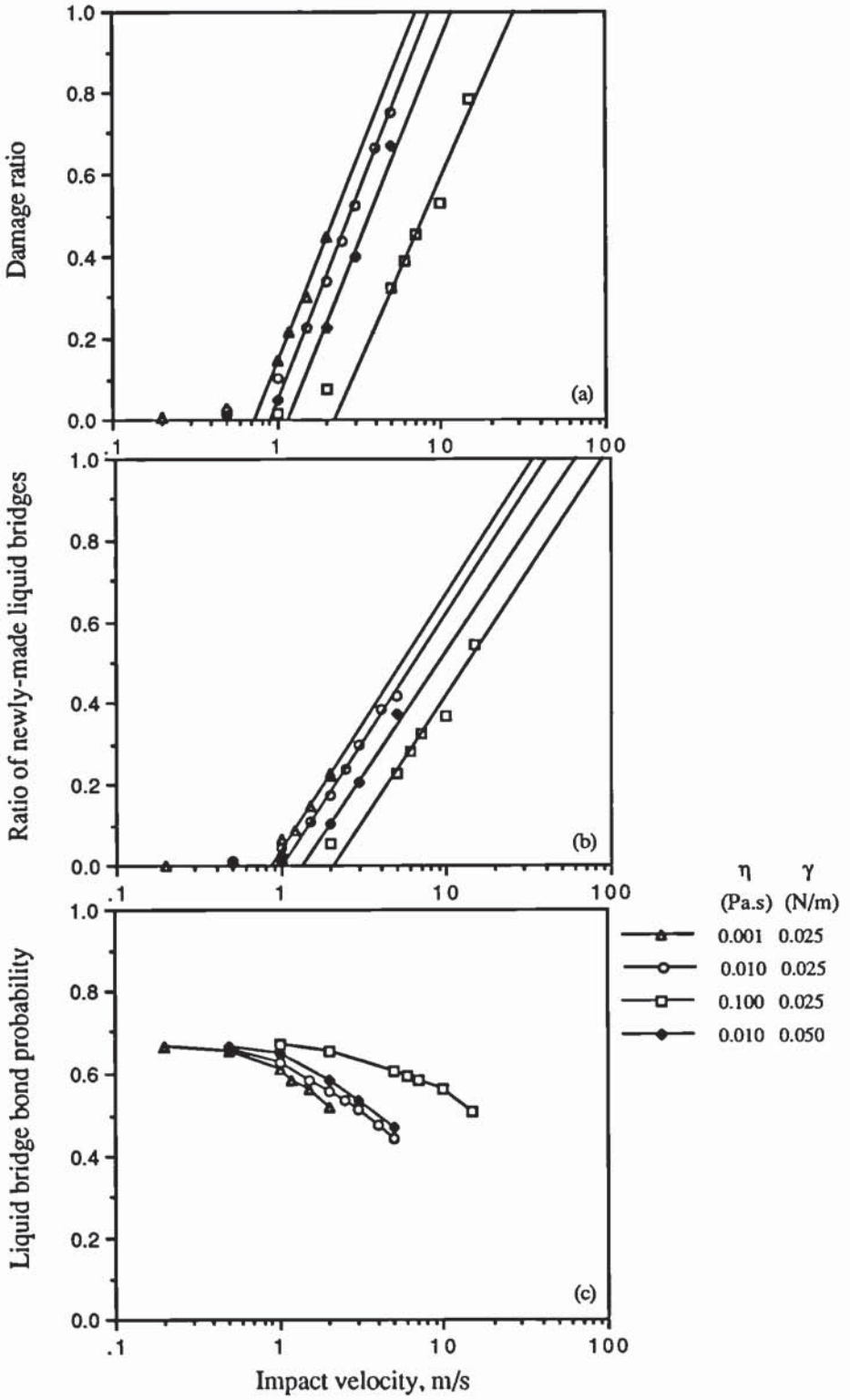

Figure 7.7: The effect of impact velocity on (a) the damage ratio, (b) the ratio of newly made liquid bridges and (c) the bond probability of the collided agglomerates.

sions at velocities above the optimum impact velocity, the internal damage of liquid bridge contacts breakdown is significant. Thus attrition may be produced when the coalesced agglomerate is subjected to future collisions.

The internal damage caused to the moist agglomerates was much lower than that previously observed for dry agglomerates by Thornton and Kafui (1992), Thornton, Kafui and Yin (1993) and Yin (1992), but was comparable to that observed in the moist agglomerate-wall impact tests reported in chapter 6. For the computer simulated normal collisions of the two moist agglomerates, it was observed that the kinetic energy and force transmission propagated from the contact region to the rear end of the agglomerates. Due to the viscous and frictional damping, the kinetic energy is significantly dissipated within a region close to the interface between the two original agglomerates. The remaining energy then further propagates. This is illustrated by figures 7.8 and 7.9.

Figure 7.8 shows the spatial distribution of liquid bridges that have been broken (red lines), newly made (blue lines) and survived (light lines) during a collision between the two agglomerates at a relative velocity of 2.0m/s. Here the liquid bridges are represented by lines connecting the centroids of the particles. The liquid bridge properties of the two agglomerates were: surface tension $\gamma_{lv} = 0.025N/m$ and viscosity $\eta = 0.01\,Pa\,s$. It can be seen from figure 7.8 that the ruptured liquid bridges are oriented mainly in the direction of extensional agglomerate strain and the newly made liquid bridges are oriented mainly in the direction of compressional strain.

Figure 7.8a corresponds to an elapsed time of $61\mu s$. At this stage, most of the liquid bridges that have been broken and newly made have occurred near the contact region. Slightly away from the contact region, there are very few liquid bridges broken or newly made. After $194\mu s$, however, figure 7.8b indicates that the region of the ruptured liquid bridges produced by the collision penetrated further into each agglomerate and so did the newly-made liquid bridges. The final pattern of the

liquid bridges that have been ruptured and newly-made is shown by figure 7.8c which corresponds to an elapsed time of $437\mu s$. About 98% of initial kinetic energy of the two agglomerates was dissipated at this stage. It can be seen that by the end of the collision, the region of the ruptured liquid bridges and newly-made liquid bridges is still contained within the two hemi-spheres adjacent to the agglomerate-agglomerate interface.

The final spatial distribution of ruptured and newly-made liquid bridges is dependent on both the impact velocity and the the liquid bridge viscosity. This is illustrated in figure 7.9. Figure 7.9a corresponds to a collision at a relative velocity of $2.0m/s$ with a liquid viscosity of $0.10Pa.s$. It can be seen that both the broken and newly made liquid bridges mainly occurred in a small region around the interface between the two agglomerates. Slightly away from the contact region, the liquid bridges bonds were not affected. Figure 7.9b shows the contact diagram of the two agglomerates with the same viscosity of $0.10Pa.s$ but after a collision at an increased relative impact velocity of $6.0m/s$. It can be seen that, due to the increase in impact velocity, the distribution of both the broken and newly made liquid bridges extended over a much larger domain.

Figure 7.9c show the liquid bridge distribution after a collision at a relative velocity of $2.0m/s$ with the liquid bridge viscosity reduced to $0.01Pa.s$. It can be seen that, in comparison with figure 7.9a, the number of the broken liquid bridges was greatly increased and so was the number of newly-made liquid bridges due to the decrease in the viscosity of the binding liquid. The broken and newly made liquid bridges extended over a much larger region. This indicates that the collisional energy can be more easily propagated through agglomerates with less viscous liquid bridges.

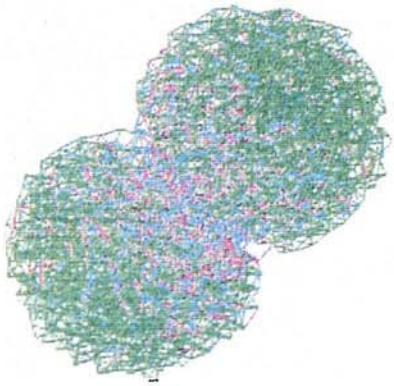

(a) $t = 61\mu s$

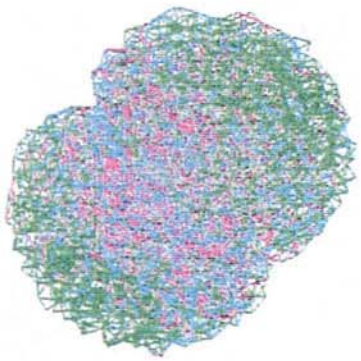

(b) $t = 194\mu s$

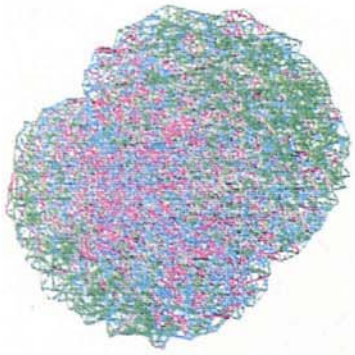

(c) $t = 437\mu s$

Figure 7.8: Distribution of broken (red lines), newly made (blue lines) and existing (cyan lines) liquid bridges of two moist agglomerates during a collision at a speed of 2.0m/s and with the liquid bridge properties of surface tension $\gamma_{lv} = 0.025N/m$ and viscosity $\eta = 0.01Pa.s$.

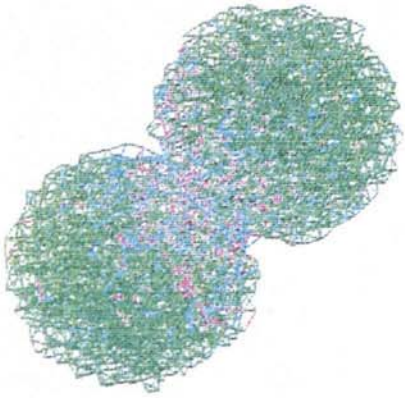

(a) $\gamma_{lv} = 0.025N/m$, $\eta = 0.10Pa.s$, $v = 2.0m/s$

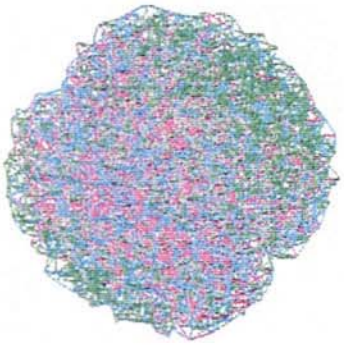

(b) $\gamma_{lv} = 0.025N/m$, $\eta = 0.10Pa.s$, $v = 5.0m/s$

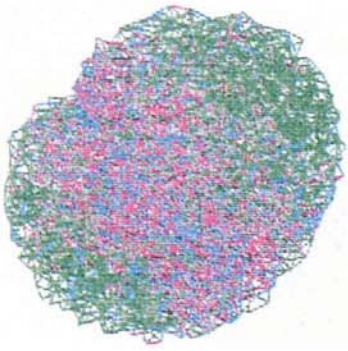

(c) $\gamma_{lv} = 0.025N/m$, $\eta = 0.01Pa.s$, $v = 2.0m/s$

Figure 7.9: Effects of impact velocity and liquid viscosity on the final distribution of broken (red lines), newly made (blue lines) and existing (cyan lines) liquid bridges of the coalesced agglomerate.

7.4 Oblique collisions

Oblique collisions of the two agglomerates were also simulated in order to investigate the effect of different incident angles. Appendix C.2 illustrates all the computer graphic pictures of the oblique impacts. For oblique impacts between the two agglomerates, the incident angle Θ is defined as shown by figure 7.10.

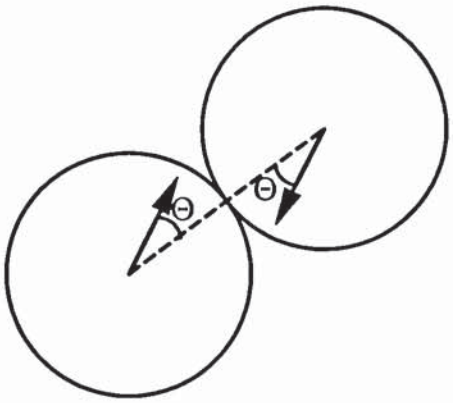

Figure 7.10: Schematic representation of the oblique impact of two agglomerates

Figure 7.11 shows the two agglomerates after impact at different incident angles of 30°, 45° and 60° respectively. The relative impact speed was $2.0m/s$ and the properties of the liquid bridges were: surface tension $\gamma_{lv} = 0.025N/m$ and viscosity $\eta = 0.01Pa.s$. It can be seen that at a low incident angle of 30°, the two agglomerates coalesced and deformed during the collision. However, in comparison with the corresponding normal impact shown by figure 7.2b, the coalesced agglomerate was significantly distorted due to the oblique impact effect. When the two agglomerates collided at an incident angle of 45°, they still coalesced but there were far fewer interparticle contacts between the two agglomerates. As a result, the coalesced agglomerate will be prone to attrition or break-up in any subsequent collision.

The deformation of the two agglomerates was also decreased to such an extent that although abrasion occurred near the interface the two agglomerates remained essentially undeformed. Figure 7.11c illustrates that at an incident angle of 60°, the two agglomerates bounced off each other and their shape remained essentially unchanged. However, attrition also occurred with a few primary particles produced by abrasion.

Typical results obtained for the same agglomerates impacted at a relative speed of $5.0m/s$ are shown in figure 7.12. It can be seen that, due to the higher impact speed, attrition occurred for all incident angles. The debris produced was only a very small mass fraction of the two agglomerates and consisted of single particles or small clusters. Fracture or fragmentation of large clusters did not occur. Figure 7.12a shows that when the two agglomerates collided at an incident angle of 30°, they coalesced and were also greatly deformed. The debris of primary particles produced appears to be ejected as a result of the arrival of the compression wave at the agglomerate surface. Figure 7.12b indicates that when the incident angle was increased to 45°, the two agglomerates still coalesced but their deformation was decreased. The attrition mechanism was also different. Debris of primary particles was produced not only by the compression wave but also by abrasion at the rough interface between the two agglomerates. The agglomerate attrition by surface abrasion appears to be more significant when the incident angle of the impact was increased to 60° as shown by figure 7.12c. Here the debris of primary particles was mainly removed by the sliding between the rough surfaces of the two agglomerates. The agglomerates did not coalesce and their deformation was so decreased that they were only abraded near to the colliding surfaces.

The effect of the viscosity of the liquid bridges, and hence the strength of the agglomerates, on the oblique impact behaviour was also investigated. This is illustrated by figure 7.13 for the same agglomerate impacted at a relative speed of $2.0m/s$ but with a lower liquid viscosity of $0.001Pa.s$. When compared with the stronger

agglomerates ($\eta = 0.01 Pa.s$), figure 7.11, it was found that due to the decrease in the agglomerate strength, attrition always occurred. At an incident angle of 30°, the debris produced was mainly due to the ejection caused by the compression wave. At an incident angle of 45°, attrition of the weaker agglomerates occurred as a result of both particle ejection and interface abrasion. When the incident angle was increased to 60°, however, the two agglomerates were mainly abraded and did not coalesce.

In terms of coalescence, the incident angle has an important effect on the shape and size of the agglomerates subjected to oblique impacts. This is shown in figure 7.14 where the circumscribing sphere radius and fractal dimension of the coalesced agglomerates due to oblique impact are plotted as a function of incident angle. It can be seen that, for all the cases of the oblique impacts, the agglomerates coalesced only when the incident angle was not greater than 45°. For the oblique impacts at a relative speed of $5.0 m/s$ and with a liquid viscosity of $0.01 Pa.s$, the circumscribing sphere radius was increased and the fractal dimension decreased as the impact angle was slightly increased to 15°. This is because, with a small incident angle, the normal flattening of the two coalesced agglomerates remained almost the same as the normal impact but the shearing between the two agglomerates in the tangential direction of the collision became very significant and the tangential shearing increased the circumscribing sphere radius and, hence, decreased the fractal dimension. As the incident angle was further increased from 15° to 45°, however, the normal flattening was significantly reduced although the tangential shearing was increased. As the decrease of normal flattening is to decrease the size of the resultant agglomerates, the circumscribing sphere radius was decreased and the fractal dimension increased.

For the same agglomerates impacted at a lower relative speed of $2.0 m/s$, however, when the incident angle was increased, the normal deformation was also decreased, but the reduction of the normal deformation is to increase the size of the resultant coalesced agglomerates because the normal impact produced an almost spherical shaped

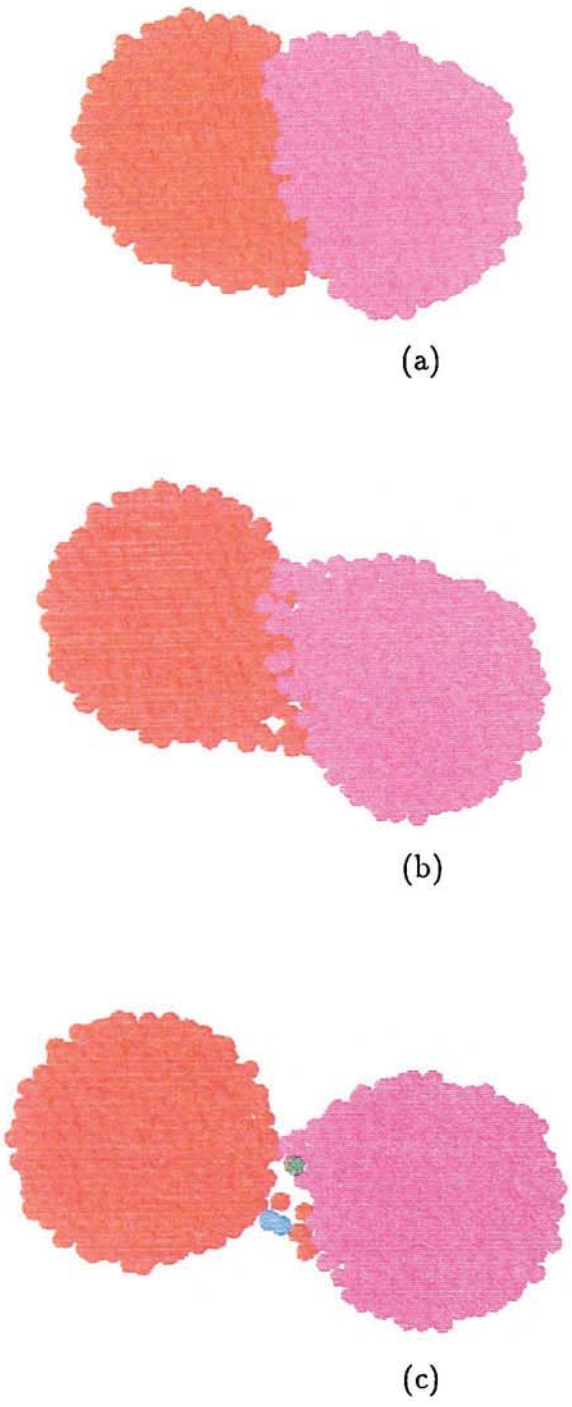

Figure 7.11: Two moist agglomerates after oblique collisions at a velocity of $2.0m/s$ and different incident angles of (a) 30°, (b) 45° and (c) 60°. The properties of the binding liquid were: surface tension $\gamma_{lv} = 0.025N/m$ and viscosity $\eta = 0.01Pa.s$.

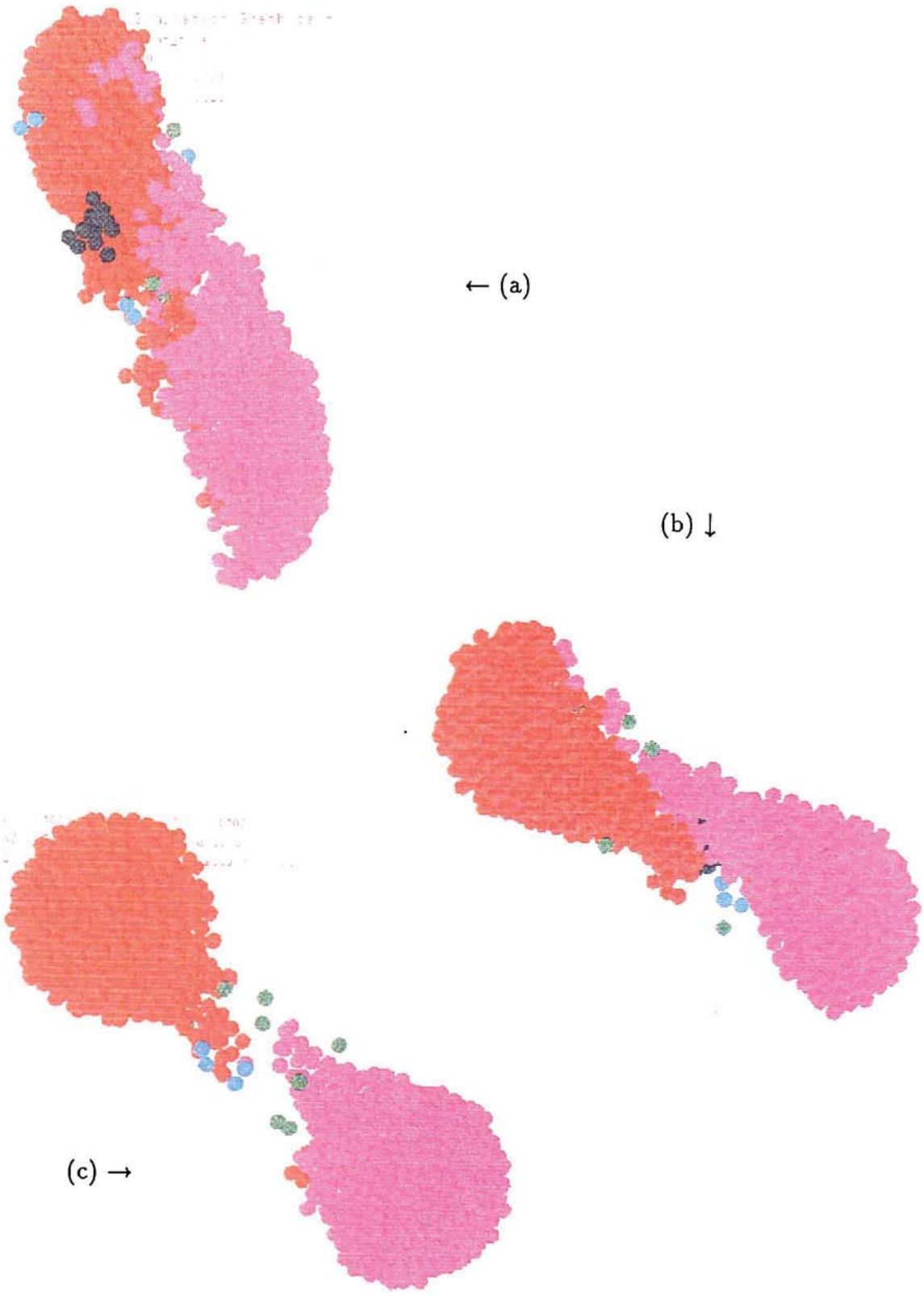

Figure 7.12: Two moist agglomerates after oblique collisions at a velocity of $5.0m/s$ and different incident angles of (a) 30°, (b) 45° and (c) 60°. The properties of the binding liquid were: surface tension $\gamma_{lv} = 0.025N/m$ and viscosity $\eta = 0.01Pa.s$.

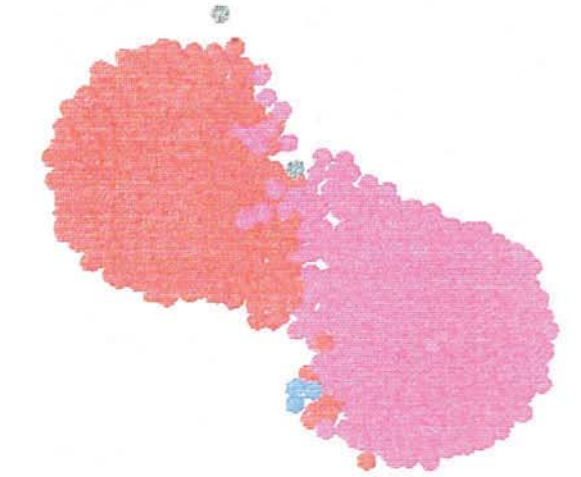

(a)

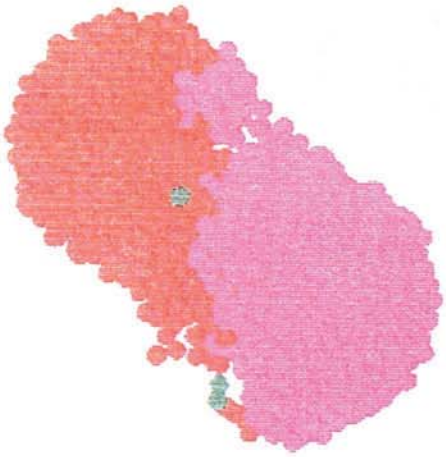

(b)

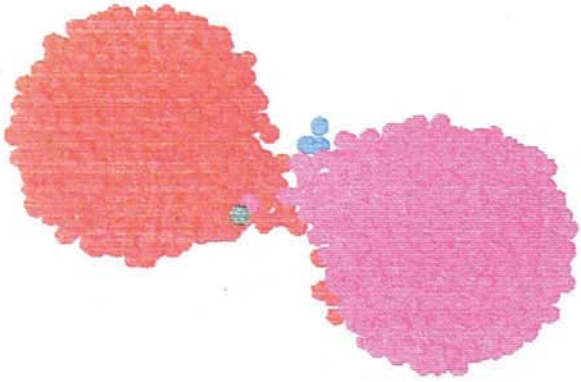

(c)

Figure 7.13: Two moist agglomerates after oblique collisions at a velocity of $2.0m/s$ and different incident angles of (a) 30°, (b) 45° and (c) 60°. The properties of the binding liquid were: surface tension $\gamma_{lv} = 0.025N/m$ and viscosity $\eta = 0.001Pa.s$.

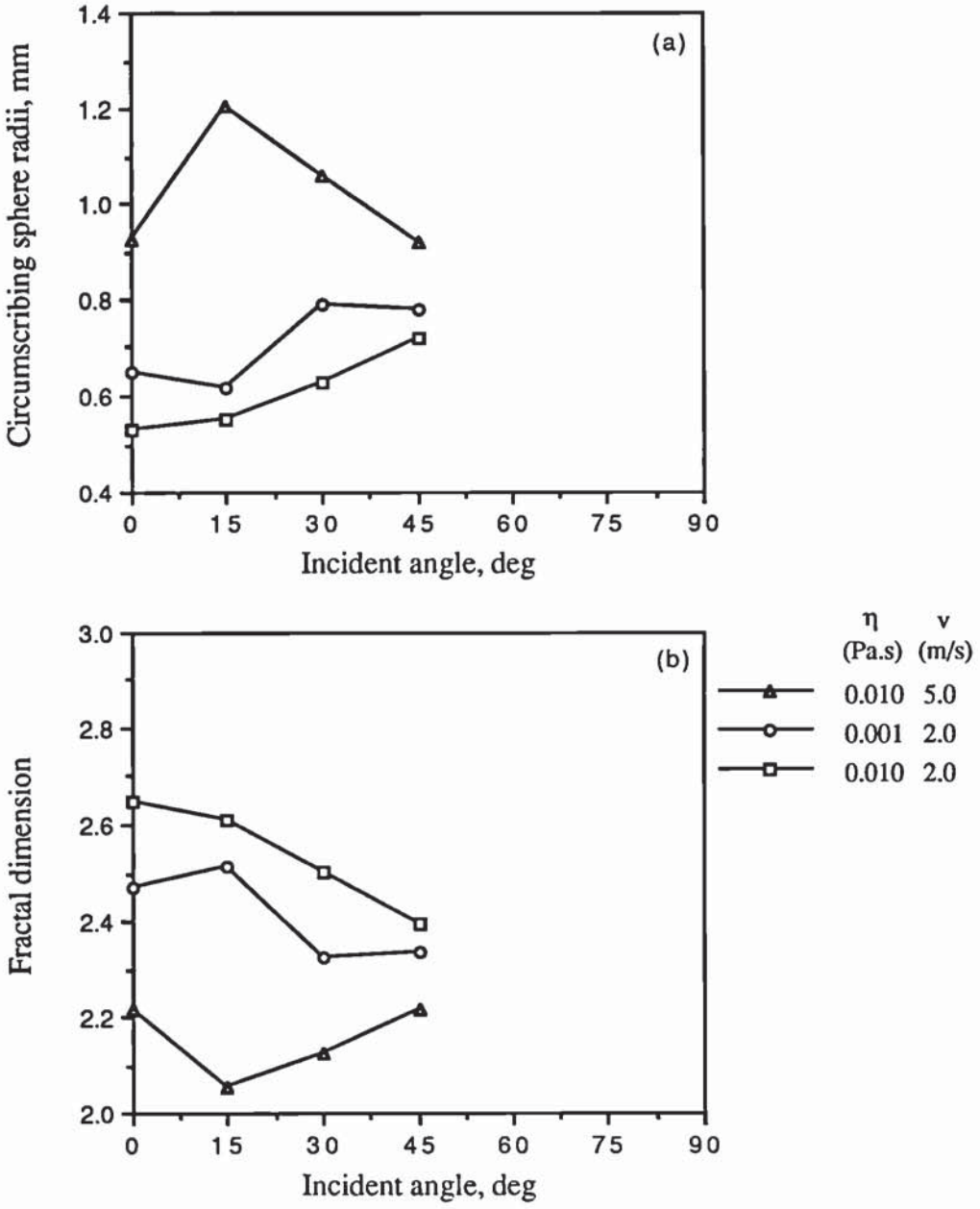

Figure 7.14: Circumscribing sphere radius and fractal dimension of the coalesced agglomerates as a function of the incident angle of oblique impacts.

resultant agglomerate. Thus, as it is shown in figure 7.14, the increase of the incident angle always resulted in the increase of the circumscribing sphere radius and the decrease of the fractal dimension.

For the less viscous agglomerates ($0.001 Pa.s$) agglomerate impacted at a relative speed of $2.0 m/s$, the effect of the incident angle on the size and shape of the coalesced agglomerate is also shown in figure 7.14. It can be seen that, except for the normal impact, when the incident angle was increased, below 30^o, the circumscribing sphere radius was also increased due to the increase of tangential shearing. The fractal dimension was correspondingly decreased. Further increase in the incident angle from 30^o to 45^o resulted in a slight reduction in the circumscribing sphere radius and an increase in the fractal dimension due to the reduction in the normal strain. For the normal impact, the size of the coalesced agglomerates was higher than that of the 15^o impact. The picture of figure 7.3a indicates that, for the normal impact, there are two particles which remain attached to the bottom of the resultant coalesced agglomerate and, hence, the circumscribing sphere radius is significantly increased and the fractal dimension is decreased.

For the oblique impacts, the debris expressed in mass percentage of the original agglomerates is plotted in figure 7.15 as a function of the incident angle. It can be seen that there is a general trend that suggests that the maximum amount of debris is produced at relatively low incident angles in the range of 15^o – 45^o. However, the evidence in support of this suggestion is based on the results of only a few simulations in which the debris consisted of a very small number of primary particles. More simulations are necessary to be confident that the data are statistically representative.

In figure 7.16, the damage ratio (ratio of ruptured liquid bridges), the ratio of newly-made liquid bridges and the overall bond probability resulting from the oblique collisions are plotted as functions of the incident angle. It is clear that both liquid bridge rupture and new bridge formation decreased as the incident angle increased.

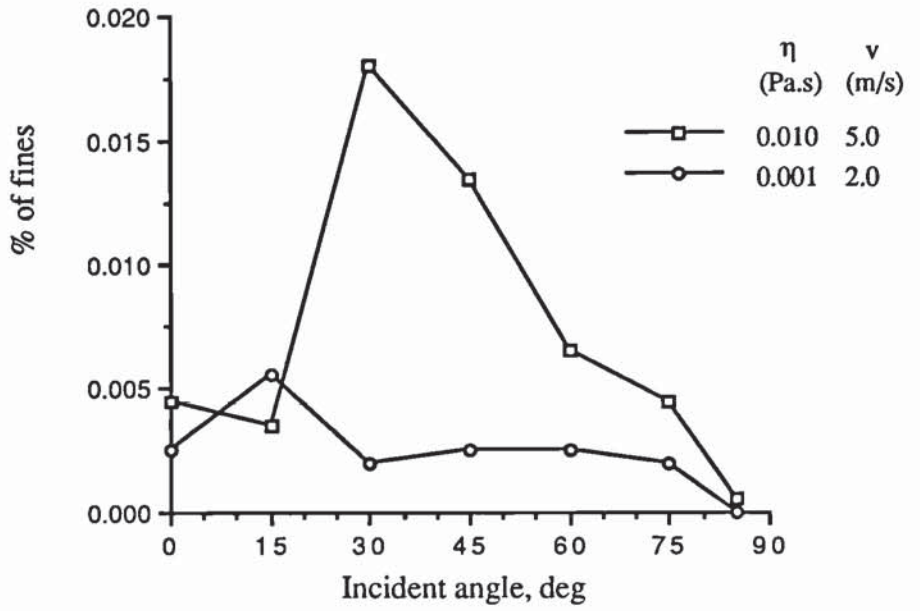

Figure 7.15: Mass percentage debris produced by oblique impacts of two moist agglomerates.

For all cases, except when $\Theta \rightarrow 90°$, the number of ruptured bridges exceeded the number of newly made ones and, hence, the bond probability of the two agglomerates decreased as a result of the impact. At very high incident angles, $\Theta \rightarrow 90°$, the resultant bond probability of the two agglomerates remained almost unchanged after collision.

Figure 7.16 also indicates that both the damage ratio and the ratio of newly-made liquid bridges can be best fitted by the following cosine functions,

$$D_r = D_o \cos^2 \Theta \tag{7.4}$$

$$n_r = n_o \cos^3 \Theta \tag{7.5}$$

from which we can, using equation 6.4, derive the expression for the bond probability as follows,

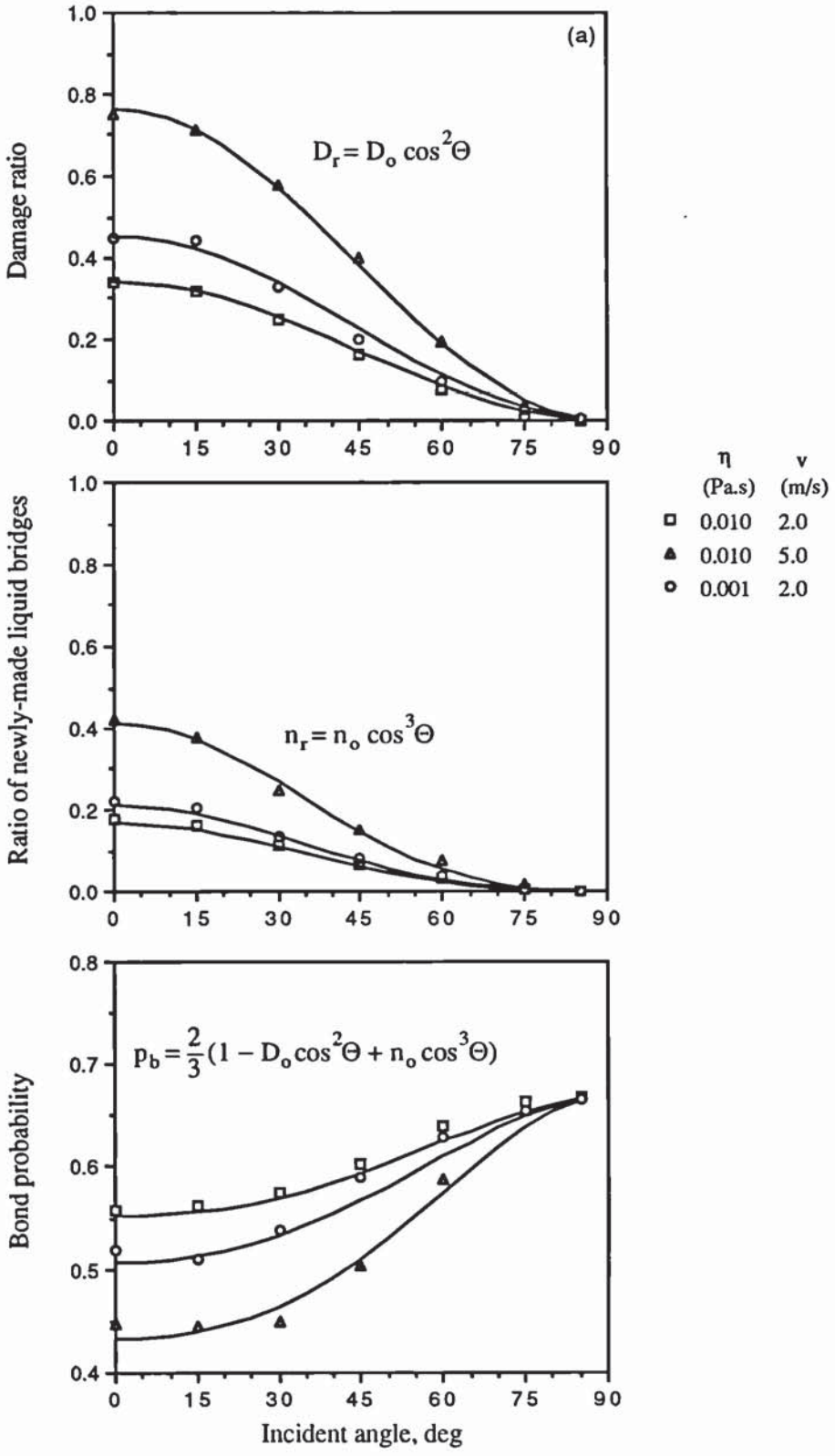

Figure 7.16: The dependence of (a) the damage ratio, (b) the newly-made liquid bridge bonds and (c) the overall bond probability of the moist agglomerate on the incident angle.

$$p_b = \frac{2}{3}(1 - D_r + n_r) = \frac{2}{3}(1 - D_o cos^2\Theta + n_o \cos^3\Theta) \tag{7.6}$$

where D_o and n_o are the damage ratio and newly-made liquid bridge ratio of the agglomerates produced by normal impact, which may be defined by equations 7.2 and 7.3. Hence, for the general case,

$$D_r = \cos^2\Theta \log\frac{v}{v_o} \tag{7.7}$$

$$n_r = 0.62\cos^3\Theta \log\frac{v}{v_o'} \tag{7.8}$$

which can be further rearranged as,

$$D_r = \left(\frac{v_n}{v}\right)^2 \log\frac{v}{v_o} \tag{7.9}$$

$$n_r = 0.62\left(\frac{v_n}{v}\right)^3 \log\frac{v}{v_o'} \tag{7.10}$$

where v_n is the relative normal velocity component and v, v_o and v_o' have been defined previously.

Recalling equation 7.6, it follows that,

$$p_b = \frac{2}{3}[1 - \left(\frac{v_n}{v}\right)^2 \log\frac{v}{v_o} + 0.62\left(\frac{v_n}{v}\right)^3 \log\frac{v}{v_o'}] \tag{7.11}$$

7.5 Summary

The significance of interstitial liquid bridges on moist agglomerate coalescence and attrition has been investigated by computer simulated normal collisions of two moist agglomerates. It has been demonstrated that at relatively low impact velocities the

two moist agglomerates deformed and coalesced after collision. As the impact velocity increases, the deformation of each agglomerate increases and the size of the coalesced agglomerate decreases. There is an optimum impact velocity that minimises the size of the coalesced agglomerate. In terms of attrition, the optimum velocity produces a near spherical shape which should minimize any breakage due to subsequent collisions. Below the optimum impact velocity, an increase in velocity enhances granulation. At high impact velocities, above the optimum velocity, the size of the coalesced agglomerate increases as the velocity increases due to the increasing tendency to flatten the agglomerates in the direction orthogonal to the impact direction. The resultant disc-shaped coalesced agglomerates should probably experience significant attrition, and possibly fragmentation, as a result of subsequent collisions.

In the computer simulated normal collisions of the two agglomerates, debris consisting of single particles or small clusters was produced due to extensive flattening at very high impact velocities. Semi-brittle fracture and shattering were not observed. At moderate impact velocities, it has been found that collisions cause internal bridge rupture. Generally speaking, the damage ratio is logarithmically dependent on the impact velocity, but there is no distinct threshold velocity. A small number of liquid bridges were ruptured even at very low impact velocities. Agglomerate collisions also produced new liquid bridges between particles. The bond probability of the resultant coalesced agglomerates remained almost unchanged if the impact velocity was below the optimum velocity that produced a spherically shaped coalesced agglomerate. At high impact velocities, above the optimum velocity, the overall bond probability of the coalesced agglomerate decreased significantly. Thus, in terms of coalescence and attrition, there are two distinct regions for agglomerate collisions. Below the optimum velocity, the collision produced a coalesced agglomerate with a bond probability similar to that of the initial agglomerates. In this region collisions enhance agglomerate coalescence. Above the optimum impact velocity, the collision produces a significant amount of internal bridge rupture and may result in attrition of fine particles.

The viscosity of the interstitial liquid has significant effects on the coalescence propensity and attrition resistance of moist granules. It has been found that, as the liquid viscosity is increased, the optimum impact velocity to produce a spherically shaped coalesced agglomerate increases.

From the oblique collision simulation, it was found that the agglomerates coalesced only if the incident angle is not greater than 45°. At low incident angles, the increase of the incident angle resulted in the increase of the circumscribing sphere radius and the reduction of the fractal dimension of the coalesced agglomerates. For low speed oblique impacts, where the normal collision produced a spherical shaped resultant agglomerate, the increase in the size of the coalesced agglomerates continued. However, for high speed oblique impacts or less viscous agglomerate impacts, where the normal collisions produced intensive normal flattening, the size of the coalesced agglomerates reaches a maximum at a small incident angle and further increase in incident angle resulted in a reduction of the size of the coalesced agglomerates due to the the significant reduction in the normal flattening. The incident angle at which the size of the coalesced agglomerates reaches a maximum increases if the initial flattening of normal impacts decreases.

When the incident angle of the impact increases, the number of internal liquid bridge rupture decreases and so does the newly made liquid bridges. It has been found that, to a good approximation, the ratio of ruptured liquid bridges is a cosine squared function of the incident angle, suggesting that the liquid bridge rupture is mainly controlled by the normal component of the impact kinetic energy. It has been also found that the ratio of newly-made liquid bridges is best fitted by a third order cosine function of the incident angle.

Attrition also occurred for oblique impacts. However, depending on the angle of impact, attrition occurred due to different mechanisms. At low incident angles, it was found that attrition occurred by the ejection of particles due to propagation of the

compression wave. At high incident angles, attrition was mainly produced by surface abrasion. The simulation also suggests that the maximum amount of attrition occurs at small impact angles in the range of $15^o < \Theta < 45^o$.

Chapter 8

Conclusions

This chapter summarises the main findings and achievements of this research programme together with some comments and suggestions about possible future work.

8.1 Cohesive force of moist particles

Powder granulation with a liquid binder is heavily utilized in process industries. At the microscopic level, the fundamental mechanism of particle enlargement by granulation is based on the competing interparticle forces. In the pendular state, where the liquid is present as either adsorbed immobile films or discrete liquid bridges, the cohesive force between particles mainly arises from two different mechanisms, the van der Waals' intermolecular adhesive force and liquid bridge binding force. Theories for the van der Waals' adhesive force between elastic spherical particles have been reviewed and discussed. It has been shown that both the theories of JKR (Johnson et al 1971) and DMT (Derjaguin et al 1975) are approximations. A major difference between the two theories is that the former predicts a pull-off force of $\frac{3}{2}\pi\Gamma R^*$ and the later of $2\pi\Gamma R^*$. The more recent theory of Maugis (1992) represents the more general situations between the two extremes of JKR and DMT models. The effects of van der Waals' adhesive force on the tangential interactive force between spherical particles have also been discussed by reviewing the theories of Savkoor and Briggs (1977) and Thornton (1991).

For the binding liquid bridges, the interactive force between particles arises from the capillary pressure deficiency, surface tension and viscous resistance of the liquid. For static liquid bridges between two spherical rigid bodies of equal radii under conditions when the effects of gravity are negligible, the geometry is governed by the Laplace-Young equation which relates the liquid bridge pressure deficiency to the mean curvature. Since the Laplace-Young equation cannot be solved analytically except for a few special cases, a numerical scheme has been developed. Numerical solutions have been obtained for a dimensionless liquid bridge between two spheres in close proximity. For the Laplace-Young equation of liquid bridges, there are two solutions that satisfy. As the separation distance between the spheres increases, the two solutions converge to a unique solution at a critical separation. At greater separa-

tions, no solutions exist. Previous workers have conjectured that, when the solutions are expressed in terms of the liquid bridge diameter or filling angle, the critical separation corresponds to the rupture of the liquid bridge. The current work shows that the more explicit criterion for specifying the stable solution and critical separation is provided by the total free energy of the liquid bridge system. The formulation of the minimum free energy is shown to be equivalent to previous conjectures. It has been further observed that the critical separation for rupture is given by the cube root of the liquid bridge volume to a good approximation and this relationship is in good agreement with the experimental data of Mason and Clark (1965).

For a liquid bridge between two spheres, Fisher (1926) proposed a much simpler approach for estimating the static liquid bridge forces. It was based on a toroidal approximation, which involved treating the meridional profile of the liquid-air interface as an arc of a circle, and leads to a range of values since this approximation results in a liquid bridge geometry of varying mean curvature which is inconsistent with the Laplace-Young equation. Consequently, there is no physically correct solution for the toroidal approximation, only one that leads to an optimal simple procedure in terms of the accuracy of calculating the forces. The uncertainty of the accuracy of the toroidal approximation has been checked against the numerical solution. It has been found that the best estimate of the total liquid bridge force was obtained using the 'gorge method' in which the area and mean curvature at the neck is used in the calculation of the force. For a wide range of liquid bridge volumes and all stable separation distances, this method of evaluation produces errors in the static liquid bridge force that are less than 10% of those obtained using an exact numerical technique and the accuracy is independent of the contact angle.

The 'gorge method' based on the toroidal approximation coupled in combination with the simple relationship that specifies the critical separation distance of rupture provides a closed-form solution for the static liquid bridge forces. It has been shown

that this simple closed-form expression can be also extended to the liquid bridges between unequal sized spheres from geometrical considerations. The only limitation of the toroidal approximation is that for a given volume of the liquid, the filling angle cannot be expressed explicitly. This problem has been solved in this work by showing that, for a constant liquid volume, the relationship between the half-filling angle and relative separation distance can be fitted by a third order polynomial relationship in which the fitting coefficients can be further expressed in terms of sphere radii and liquid volume.

8.2 Moist agglomerate collisions

Based on the closed-form solution of 'the gorge method', a third order polynomial relationship between the half-filling and separation distance has been observed for liquid bridges between unequal sized spheres with given quantities of liquid volume. Simple algorithms to calculate the static liquid bridges forces have been developed and implemented into the Aston version of TRUBAL. For the computation of viscous liquid bridge forces, the equation proposed by Adams and Perchard (1985) was used for the normal component and the equations by Goldman et al (1967a, 1967b) were applied for the tangential component.

Using the modified DEM computer program TRUBAL, the normal impact tests of a 3-D body-centred cubic agglomerate with a wall have been performed and the effects of the interstitial liquid bridge forces have been examined. The agglomerate consisted of 4062 mono-disperse particles. It has been shown by the computer simulation that, for the inviscid agglomerates with a zero liquid viscosity, high impact velocity produced significant attrition. The attrition was produced by the break-up of singlets and small clusters of primary particles. Semi-brittle fracture and shattering behaviour previously reported for dry agglomerate impact simulations was not observed for the

moist agglomerate. At relatively low impact velocities, the agglomerate deformed and remained adhered to the wall after the impact. Attrition did not occur. However, internal damage did occur due to the rupture of some liquid bridges between particles. There is a distinct threshold velocity for the agglomerate below which the impact cause no internal damage. Above the threshold impact velocity, the damage ratio of ruptured liquid bridges is logarithmically dependent on the impact velocity.

During the agglomerate-wall impact, it has been found that new liquid bridges were also formed between the primary particles. The ratio of newly-made liquid bridges is also dependent on the impact velocity. The creation of newly made liquid bridges can occur at velocities below the threshold velocity of liquid bridge rupture. In terms of the overall bond probability of the agglomerate after impact, there are two distinct regions. At low impact velocities, the bond probability of the agglomerate after impact increased because there were more newly-made liquid bridges and none or few broken ones. This may be interpreted as a strengthening (or hardening) of the agglomerate during impact. In this sense the strongest resultant agglomerate, having the highest bond probability, is obtained at the threshold velocity of liquid bridge rupture. At high impact velocities, the overall bond probability of the agglomerate was decreased during impact, implying a deteriorated agglomerate due to the internal liquid bridge rupture.

The effects of the interstitial liquid bridge viscosity on the agglomerate-wall impact were examined. It has been found that when the liquid viscosity was increased, the strength of the moist agglomerate to resist attrition and break-up also increased and the agglomerate deformed more visco-plastically. For a liquid viscosity of $0.1 Pa.s$, attrition did not occur even when the agglomerate was impacted at a high velocity of $8.0 m/s$ and deformed to a planar shape. It has been also observed that an increase in the liquid viscosity resulted in the reduction in the agglomerate deformation, as quantified by the relative height and normalised contact area, if the impact velocity

is the same. For the interstitial liquid bridges, an increase in the liquid viscosity resulted in the increase of the threshold velocity of internal liquid bridge rupture. The ratio of newly made liquid bridges, however, is not significantly affected by the change of liquid viscosity. In terms of the overall bond probability of liquid bridges, it has been found that, due to the increase in the the liquid viscosity, the transition from "strengthening" to "weakening" occurs at a higher impact velocity and the maximum bond probability increases.

Computer simulated agglomerate-agglomerate collisions have been also performed. Each agglomerate consisted of 1000 randomly packed primary particles and had a co-ordination number of 7.183 of liquid bridges, corresponding to a degree of saturation of 0.71%. For all the computer simulated normal collisions, the two agglomerates coalesced. At low impact velocities, the two agglomerates were slightly deformed. At high impact velocities, the two agglomerates were greatly deformed and the resultant coalesced agglomerate was disc-shaped. Debris of primary particles and small clusters was also produced at very high impact velocities. There is an optimum impact velocity where the circumscribing sphere radius of the resultant coalesced agglomerate is minimised and the fractal dimension is maximized. This optimum impact velocity produces a near spherical shaped resultant agglomerate which should minimize attrition due to subsequent collisions.

For the normal collisions of the two moist agglomerates, it has been shown that before any attrition occurred, internal damage of interstitial liquid bridge rupture was produced. The damage ratio of the liquid bridge rupture is almost logarithmically dependent on the impact velocity, but there is no distinct threshold velocity of liquid bridge rupture. Even at very low velocities, it was observed that a small number of liquid bridges of the agglomerates were ruptured during impact. It was also found that new contacts of liquid bridges were formed during agglomerate-agglomerate collisions. Overall, at low impact velocities, below the optimum impact velocity, the

bond probability of the resultant coalesced agglomerate remained almost unchanged. At high impact velocities, above the optimum impact velocity, however, the ruptured liquid bridges exceeded the newly-made ones and, hence, the bond probability decreased significantly. The resultant coalesced agglomerate is disc shaped and would be probably prone to attrition and fragmentation in any subsequent collisions.

Although the ratio of internal liquid bridge rupture is relatively high at high impact velocities, the energy dissipation due to it is only a small percentage of about 5%. It has been found that over 90% of the initial kinetic energy of collision was dissipated by the viscous resistance of interstitial liquid bridges and tangential friction between primary particles. Since viscous resistance and interparticle friction arise from the visco-plastic deformation of the agglomerates, the visco-plastic deformation and the associated energy dissipation are essential for the successful coalescence of moist granules. This implies that the simple theories of granule coalescence based on single pairs of elastic or rigid spheres cannot be applied to agglomerate-agglomerate aggregation.

The viscosity and surface tension of the interstitial liquid bridges have a significant effect on the coalescence and breakage of agglomerate-agglomerate collisions. When the liquid viscosities or surface tension were decreased, attrition of primary particle breakage was increased and the optimum impact velocity to produce a near spherical shape of the resultant coalesced agglomerate decreased. The bond probability was also decreased due to more liquid bridges being ruptured and fewer newly-made. This indicates that both the coalescence propensity and attrition resistance of moist granules were decreased as the cohesive force of interstitial liquid bridges was decreased. The decrease of liquid viscosity also resulted in the decrease of the energy ratio dissipated by viscous resistance and the increase of the energy ratio dissipated by interparticle friction. As a whole, however, the energy dissipation by viscous resistance and interparticle friction still dominates and the energy dissipated by liquid

bridge rupture dissipated only about 5% of the total kinetic energy of collision.

Oblique collisions of the two moist agglomerates were also performed. It has been observed that varying the incident angle of impact has a remarkable effect on the coalescence and attrition of moist granules. Coalescence occurred only if the incident angle was not greater than 45°. For low speed oblique impacts, where the normal impact produced a spherical shaped coalesced agglomerate, an increase in the incident angle resulted in an increase in the circumscribing sphere radius and a decrease in the fractal dimension of the coalesced agglomerate. For high speed oblique impacts, where the normal impact produced a disc shaped coalesced agglomerate, the circumscribing sphere radius first increases and then decreases as the incident angle increases. The incident angle that maximizes the size of the coalesced agglomerate was increased if the disc shaped flattening produced by normal impacts was decreased.

For oblique impacts, attrition mainly occurred at high impact velocities and with low liquid viscosity agglomerates. The agglomerates were also severely deformed if any attrition occurred. It was noticed that, depending on the incident angle of impact, attrition occurred due to different mechanisms. At low incident angles, attrition occurred by the ejection of particles due to propagation of the compression wave. At high incident angles, attrition was mainly produced by surface abrasion. Agglomerates did not coalesce and their shape remained essentially unchanged after collisions. In terms of mass percentage of debris, the oblique impact simulation suggested that the maximum amount of attrition occurs at small impact angles in the range of 15°–45°.

Both the ratio of ruptured liquid bridges and the ratio of new liquid bridges were reduced when the incident angle was increased. To a good approximation, the ratio of ruptured bridges is a cosine squared function of the incident angle. This suggests that, for oblique impacts, liquid bridge rupture is mainly controlled by the normal component of kinetic energy. However, the ratio of newly-made liquid bridges was

best fitted by a third order cosine function of the incident angle.

8.3 Limitations and future work

It has been shown that the computer program TRUBAL using the Discrete Element Method (DEM) is capable of modelling moist agglomerate collisions. The advantage of the DEM simulation is that it provides scrutiny of the microlevel mechanisms of agglomerate coalescence and breakage. The current version of TRUBAL simulates a moist granule as an assembly of spherical particles held together by interstitial liquid bridges. For the interaction force between particles, the force exerted by particle deformation, surface adhesion, tangential friction and interstitial liquid bridges have been considered.

In terms of the future work, the present computer program TRUBAL at Aston has two major limitations. Firstly, the current research centres on the modelling of moist agglomerates with immobile fluid which is present as pendular liquid bridges. There is a need to develop new algorithms to model mobile fluid, funicular state fluid and capillary state fluid of particle assemblies. Secondly, the constituent particles are spherical. It is desirable to develop algorithms to model non-spherical particles and, through computer simulation, to examine the effects of particle shape and size.

The coalescence propensity and attrition resistance of moist granules are greatly influenced by their internal packing structures such as particle size, shape and distribution. This research has only simulated a body-centred cubic agglomerate impacting with a wall and two randomly packed agglomerates colliding with each other. For the interaction force between particles, the surface adhesion was set to zero (which corresponds to perfect wetting) and only liquid bridge forces in association with elastic deformation and tangential friction forces between particles were considered. It is therefore believed that more computer simulations of agglomerates with different

packings, sizes and different interstitial liquid cohesivenesses should be performed before any firm conclusions of moist granule coalescence and breakage can be reached.

The DEM computer program has found a wide range of applications in the simulation of particle systems. There are more potential applications. More powerful computer facilities are also required if the DEM is to be extended to simulate larger scale particle assemblies. The current version of TRUBAL is only capable of effectively simulating assemblies up to 10,000 particles on the 320 and 320H models of IBM RISC 6000 workstations. An alternative to combat the limited computer power is to develop more efficient algorithms for the implementation of other interaction forces in the future.

References

[1] Adams, M. J. 1985. The strength of particulate solids. *Journal of Powder & Bulk Solids Technology*, 9:15–20.

[2] Adams, M. J. and Edmondson, B. 1987. Forces between particles in continuous and discrete liquid media. In B. J. Briscoe and M. J. Adams, editors, *Tribology in Particulate Technology*, pages 154–172.

[3] Adams, M. J., Mullier, M. A. and Seville, J. P. K. 1987. Agglomeration. In B. J. Briscoe and M. J. Adams, editors, *Tribology in Particulate Technology*, pages 375–389.

[4] Adams, M. J., Mullier, M. A., Seville, J. P. K. and Williams, W. 1989. A fracture mechanics approach to the breakage of agglomerated particulate solids. In J. Biarez and R. Gourves, editors, *Powders and Grains*, pages 105–110.

[5] Adams, M. J. and Perchard, V. 1985. The cohesive forces between particles with interstitial liquid. In *I. Chem. E. Symposium Series No. 91*, pages 147–160.

[6] Adams, M. J., Williams, D. and Williams, J. G. 1989. The use of linear elastic fracture mechanics for particulate solids. *Journal of Materials Science*, 24:1772–1776.

[7] Arbiter, N., Harris, C. C. and Stamboltzis, G. A. 1969. Single fracture of brittle spheres. *Trans. AIME*, 244:118–133.

[8] Austin, L. G. 1987. Approximate calculation of specific fracture energies for grinding. *Powder Technology*, 53:145–150.

[9] Austin, L. G., Barahona, C. A. and Menacho, J. M. 1986. Fast and slow chipping fracture and abrasion in autogenous grinding. *Powder Technology*, 46:81–87.

[10] Austin, L. G. and Brame, K. 1983. A comparison of the bond method for sizing wet tumbling ball mill with a size–mass balance simulation model. *Powder Technology*, 34:261–274.

[11] Austin, L. G., Jindal, V. K. and Gotsis, C. 1979. A model for continuous grinding in a laboratory hammer mill. *Powder Technology*, 22:199–204.

[12] Austin, L. G. and Klimpel, R. C. 1989. An investigation of wet grinding in a laboratory overflow ball mill. *Mineral & Metallurgical Processing*, 6:7–14.

[13] Ayala, R. E., Hartley, P. A. and Parfitt, G. D. 1986. The relevance of powder/liquid wettability to the cohesiveness of carbon black agglomerates. *Particle Characterization*, 3:26–31.

[14] Ayala, R. E. and Parfitt, G. D. 1984. Wetting of powder agglomerates. In *Proc. of the Tech. Prog. – 10th Annual Powder & Bulk Solid Conference*, pages 328–334.

[15] Badrick, A. S. T. and Puttick, K. E. 1986. Surface tensile stresses around indentations in NaCl. *J. Phys. D: Appl. Phys.*, 19:51–56.

[16] Barnocky, G. and Davis, R. H. 1988a. The effect of maxwell slip on the aerodynamic collision and rebound of spherical particles. *Journal of Colloid and Interface Science*, 121:226–239.

[17] Barnocky, G. and Davis, R. H. 1988b. Elastohydrodynamic collision and rebound of spheres: Experimental verification. *Phys. Fluids*, 31:1324–1329.

[18] Barquins, M., Maugis, D. and Courtel, R. 1977. Rôle de l'adhésion dans le frottement du caoutchouc. Nouvell définition du coefficient de frottement. *C. R. Acad. Sci. Paris*, 284:127–130.

[19] Bathurst, R. J. and Rothenburg, L. 1988. Micromechanical aspects of isotropic granular assemblies with linear contact interactions. *Journal of Applied Mechanics*, 55:17–23.

[20] Bayramli, E., Abou-obeid, A. and van de Ven, T. G. M. 1987. Liquid bridges between spheres in a gravitational field. *Journal of Colloid and Interface Science*, 116:490–502.

[21] Bayramli, E. and van de Ven, T. G. M. 1987. An experimental study of liquid bridges between spheres in a gravitational field. *Journal of Colloid and Interface Science*, 116:502–510.

[22] Bier, H. P., Leuenberger, H. and Sucker, H. 1979. Determination of the uncritical quantity of granulating liquid by powder measurements on planetary mixers. *Pharm. Ind.*, 41:375–380.

[23] British Materials Handling Board. 1987. *Particle Attrition.* Trans Tech Publications.

[24] Bradley, R. S. 1932. Cohesion between solid surfaces, and surface energy of solids. *Phil. Mag.*, 13:853–862.

[25] Brenner, H. 1961. The slow motion of a sphere through a viscous fluid towards a plane surface. *Chemical Engineering Science*, 16:242–251.

[26] Briscoe, B. J. and Kremnitzer, S. L. 1979. A study of the friction and adhesion of polyethylene-terephthalate monofilaments. *J. Phys. D: Appl. Phys.*, 12:505–516.

[27] Campbell, C. S. and Brennen, C. E. 1985a. Chute flows of granular materials: Some computer simulations. *Transactions of the ASME*, 52:172–178.

[28] Campbell, C. S. and Brennen, C. E. 1985b. Computer simulation of granular shear flow. *J. Fluid Mech.*, 151:167–188.

[29] Campbell, C. S. and Gong, A. 1986. The stress tensor in a two-dimensional granular shear flow. *J. Fluid Mech.*, 164:107–125.

[30] Chan, D. Y. C. and Horn, R. G. 1985. The drainage of thin liquid films between solid surfaces. *J. Chem. Phys.*, 83:5311–5324.

[31] Chan, S. Y., Pilpel, N. and Cheng, D. C.-H. 1983. The tensile strengths of single powders and binary mixtures. *Powder Technology*, 34:173–189.

[32] Cheng, D. C.-H. 1968. The tensile strength of powders. *Chemical Engineering Science*, 23:1405–1420.

[33] Clark, W. C., Haynes, J. M. and Mason, G. 1968. Liquid bridges between a sphere and a plane. *Chemical Engineering Science*, 23:810–812.

[34] Cox, R. G. and Brenner, H. 1967. The slow motion of a sphere through a viscous fluid towards a plane surface–ii small gap widths, including inertial effects. *Chemical Engineering Science*, 22:1753–1777.

[35] Cross, N. L. and Picknett, R. G. 1963. The liquid layer between a sphere and a plane surface. *Trans. Faraday Soc.*, 59:864–855.

[36] Cundall, P. A. 1971. A computer model for simulating progressive, large scale movements in blocky rock systems. In *Proceedings of the Symposium of International Society of Rock Mechanics*, Nancy.

[37] Cundall, P. A. 1978. Ball–a program to model granular media using the distinct element method. Technical report, Advanced Technology Group, Dames and Moore, London.

[38] Cundall, P. A. 1983. Modelling of microscopic mechanisms in granular material. In J. T. Jenkins and M. Satake, editors, *Mechanics of Granular Materials: New Models and Constitutive Relations.* Elsevier, Amsterdam.

[39] Cundall, P. A. 1988. Computer simulations of dense sphere assemblies. In M. Satake and J. T. Jenkins, editors, *Micromechanics of Granular Materials*, pages 113–123.

[40] Cundall, P. A., Jenkins, J. T. and Ishibashi, I. 1989. Evolution of elastic moduli in a granular assembly. In J. Biarez and R. Gourves, editors, *Powders and Grains*, pages 319–322.

[41] Cundall, P. A. and Strack, O. D. L. 1979a The dintinct element method as a tool for research in granular media, Part II. Report to NSF, Grant ENG76-20771, University of Minnesota.

[42] Cundall, P. A. and Strack, O. D. L. 1979b A discrete numerical model for granular assemblies. *Geotechnique*, 29:47–65.

[43] Davis, R. H. 1987. Elastohydrodynamic collisions of particles. *PhysicoChemical Hydrodynamics*, 9:41–52.

[44] Davis, R. H., Serayssol, J-M. and Hinch, E. J. 1986. The elastohydrodynamic collision of two spheres. *J. Fluid Mech.*, 163:479–497.

[45] De Josselin de Jong, G. and Verruijt, A. 1969. Etude photo-élastique d'un empilement de disques. *Cah. Grpe fr. Etud. Rhéol.*, 2:73–86.

[46] DeBisschop, F. R. E. and Rigole, W. J. L. 1982. A physical model for liquid capillary bridges between adsorptive solid spheres: The nodoid of Plateau. *Journal of Colloid and Interface Science*, 88:117–128.

[47] Derjaguin, B. V. 1940. Repulsive forces between charged colloid particles, and theory of slow coagulation and stability of lyophobesols. *Trans. Faraday Soc.*, 36:203–215.

[48] Derjaguin, B. V., Muller, V. M. and Toporov, Y. P. 1975. Effect of contact deformations on the adhesion of particles. *Journal of Colloid and Interface Science*, 53:314–326.

[49] Derjaguin, B. V., Muller, V. M. and Toporov, Y. P. 1978. On the role of molecular forces in contact deformations (critical remarks concerning Dr. Tabor's report). *Journal of Colloid and Interface Science*, 67:378–379.

[50] Drescher, A. and de Josselin de Jong, G. 1972. Photoelastic verification of a mechanical model for the flow of a granular material. *J. Mech. Phys. Solids*, 20:337–351.

[51] Dugdale, D. S. 1960. Yielding of steel sheets containing slits. *J. Mech. Phys. Solids*, 8:100–104.

[52] Ennis, B. J., Li, J., Tardos, G. I. and Pfeffer, R. 1990. Influence of viscosity on an axially strained pendular liquid bridge. *Chemical Engineering Science*, 45:3071–3088.

[53] Ennis, B. J., Tardos, G. I. and Pfeffer, R. 1991. A microlevel-based characterization of granulation phenomena. *Powder Technology*, 65:257–272.

[54] Erle, M. A., Dyson, D. C. and Morrow, N. R. 1971. Liquid bridges between cylinders, in a torus, and between spheres. *AIChE Journal*, 17:115–121.

[55] Feder, J. 1988. *Fractals.* Plenum, New York.

[56] Fisher, R. A. 1926. On the capillary forces in an ideal soil; correction of formulae given by W. B. Haines. *Journal of Agricultural Science*, 16:492–505.

[57] Ghadiri, M. and Yuregir, K. R. 1987. Impact attrition of NaCl particles. In B. J. Briscoe and M. J. Adams, editors, *Tribology in Particulate Technology*, pages 439–452.

[58] Ghadiri, M., Yuregir, K. R. Pollock, H. M., Ross, J. D. J. and Rolfe, N. 1991. Influence of processing conditions on attrition of NaCl crystals. *Powder Technology*, 65:311–320.

[59] Goldman, A. J., Cox, R. G. and Brenner, H. 1967a. Slow viscous motion of a sphere parallel to a plane wall–I Motion through a quiescent fluid. *Chemical Engineering Science*, 22:637–651.

[60] Goldman, A. J., Cox, R. G. and Brenner, H. 1967b. Slow viscous motion of a sphere parallel to a plane wall–II Couette flow. *Chemical Engineering Science*, 22:653–660.

[61] Hamaker, H. C. 1937. The London-van der Waals attraction between spherical particles. *Physica*, 4:1058–1072.

[62] Hartley, P. A. and Parfitt, G. D. 1985a. Analysis of liquid bonding forces in agglomerates of fine particle powders. In *Particulate and Multiphase Processes*, volume 1, pages 525–537.

[63] Hartley, P. A. and Parfitt, G. D. 1985b. Dispersion of powders in liquid. 1. The contribution of the van der Waals force to the cohesiveness of carbon black powders. *Langmuir*, 1:651–657.

[64] Hocking, L. M. 1973. The effect of slip on the motion of a sphere close to a wall and of two adjacent spheres. *J. Engng. Maths*, 7:207–221.

[65] Holm, P., Schaefer, T. and Kristensen, H. G. 1985a. Granulation in high-speed mixers. Part V. Power consumption and temperature changes during granulation. *Powder Technology*, 43:213–224.

[66] Holm, P., Schaefer, T. and Kristensen, H. G. 1985b. Granulation in high-speed mixers. Part VI. Effects of process conditions on power consumption and granule growth. *Powder Technology*, 43:225–233.

[67] Horn, R. G., Israelachvili, J. N. and Pribac, F. 1987. Measurement of the deformation and adhesion of solids in contact. *Journal of Colloid and Interface Science*, 115:480–492.

[68] Horwatt, S. W., Rwei, S-P and Manas-Zloczower, I. 1989. The influence of interstitial liquids on the cohesive strength of carbon-black agglomerates. *Rubber Chemistry and Technology*, 62:928–938.

[69] Hotta, K., Takeda, K. and Iinoya, K. 1974. The capillary force of a liquid bridge. *Powder Technology*, 10:231–242.

[70] Hunter, B. M. and Ganderton, D. 1972. The effect of particle size on the granulation of lactose by massing and screening. *J. Pharm. Pharmacol.*, 24:17P–24P.

[71] Israelachvili, J. N. and Tabor, D. 1972. The measurement of van der Waals dispersion force in the range 1.5 to 130 nm. *Proc. Roy. Soc. Lond. Ser. A*, 331:19–38.

[72] Jaiyeoba, K. T. and Spring, M. S. 1979. The granulation of ternary mixtures containing lactose and boric acid with different starches. *J. Pharm. Pharmacol.*, 31:197–200.

[73] Jenkins, J. T., Cundall, P. A. and Ishibashi, I. 1989. Micromechanical modeling of granular materials with the assistance of experiments and numerical simulations. In J. Biarez and R. Gourves, editors, *Powders and Grains*, pages 1818–1820.

[74] Johnson, K. L. 1976. Adhesion at the contact of solids. In W. T. Koiter, editor, *Theoretical and Applied Mechanics*, pages 133–143.

[75] Johnson, K. L. 1985. *Contact Mechanics.* Cambridge University Press, Cambridge.

[76] Johnson, K. L., Kendall, K. and Roberts, A. D. 1971. Surface energy and the contact of elastic solids. *Proc. R. Soc. Lond. A.*, 324:301–313.

[77] Kafui, K. D. and Thornton, C. 1993. Computer simulated impact of agglomerates. In C. Thornton, editor, *Powders & Grains*, pages 401–406.

[78] Kapur, P. C. 1978. Balling and granulation. *Advances in Chemical Engineering*, 10:55–123.

[79] Kendall, K. 1986. Inadequacy of Coulomb's friction law for particle assemblies. *Nature*, 319:203–205.

[80] Kendall, K. 1987. Relevance of contact mechanics to powders – elasticity, friction and agglomerate strength. In B. Briscoe and M. J. Adams, editors, *Tribology in Particulate Technology*, pages 110–122.

[81] Kendall, K. 1988. Agglomerate strength. *Powder Metallurgy*, 31:28–31.

[82] Kendall, K., Alford, N. McN. and Birchall, J. D. 1987. A new method for measuring the surface energy of solids. *Nature*, 325:794–796.

[83] Klimpel, R. R. and Austin, L. G. 1983. A preliminary model of liberation of binary system. *Powder Technology*, 34:121–130.

[84] Knight, P. C. and Bridgwater, J. 1985. Comparison of methods for assessing powder attrition. *Powder Technology*, 44:99–102.

[85] Koka, V. R. and Trass, O. 1987. Determination of breakage parameters and modelling of coal breakage in the szego mill. *Powder Technology*, 51:201–214.

[86] Kristensen, H. G., Holm, P. and Schaefer, T. 1985a. Mechanical properties of moist agglomerates in relation to granulation mechanisms. part ii. effect of particle size distribution. *Powder Technology*, 44:239–247.

[87] Kristensen, H. G., Holm, P. and Schaefer, T. 1985b. Mechanical properties of moist agglomerates in relation to granulation mechanisms. part i. deformability of moist, densified agglomerates. *Powder Technology*, 44:227–237.

[88] Kristensen, H. G. and Schaefer, T. 1987. Granulation: A review on pharmaceutical wet-granulation. *Drug Dev. & Ind. Pharm.*, 13:803–872.

[89] Lian, G., Thornton, C. and Adams, M. J. 1993a. Effect of liquid bridge forces on agglomerate collisions. In C. Thornton, editor, *Powders and Grains*, pages 59–64.

[90] Lian, G., Thornton, C. and Adams, M. J. 1993b. A theoretical study of the liquid bridge forces between two rigid spherical bodies. *Journal of Colloid and Interface Science*, 161:138–147.

[91] Lindberg, N. O. 1977. Studies on granulation in a small planetary mixer. *Acta Pharm. Suecica*, 14:197–204.

[92] MacFarlane, J. S. and Tabor, D. 1950. Adhesion of solids and the effect of surface films. *Proc. R. Soc., Lond. Ser. A*, 202:224.

[93] Mandelbrot, B. B. 1983. *The Fractal Geometry of Nature*. Freeman, San Francisco.

[94] Mason, G. and Clark, W. C. 1965. Liquid bridges between spheres. *Chemical Engineering Science*, 20:859–866.

[95] Matthewson, M. J. 1988. Adhesion of spheres by thin liquid films. *Philosophical Magazine A*, 57:207–261.

[96] Maugis, D. 1992. Adhesion of spheres: The JKR-DMT transition using a Dugdale model. *Journal of Colloid and Interface Science*, 150:243–269.

[97] Mazzone, D. N., Tardos, G. I. and Pfeffer, R. 1986. The effect of gravity on the shape and strength of a liquid bridge between two spheres. *Journal of Colloid and Interface Science*, 113:544–556.

[98] Mazzone, D. N., Tardos, G. I. and Pfeffer, R. 1987. The behavior of liquid bridges between two relatively moving particles. *Powder Technology*, 51:71–83.

[99] McGrady, E. D. and Ziff, R. M. 1987. Shattering transition in fragmentation. *Physical Review Letters*, 58:892–895.

[100] Mehrotra, V. P. and Sastry, K. V. S. 1980. Pendular bond strength between unequal-sized spherical particles. *Powder Technology*, 25:203–214.

[101] Mindlin, R. D. 1949. Compliance of elastic bodies in contact. *Journal of Applied Mechanics*, 16:259–268.

[102] Mindlin, R. D. and Deresiewicz, H. 1953. Elastic spheres in contact under varying oblique forces. *Journal of Applied Mechanics*, 20:327–344.

[103] Mindlin, R. D., Mason, W. P., Osmer, T. F. and Deresiewicz, H. 1951. Effects of an oscillating tangential force on the contact surfaces of elastic spheres. In *Proc. First U.S. National Cong. Applied Mechanics*, pages 203–208.

[104] Muller, V. M., Yushchenko, V. S. and Derjaguin, B. V. 1980. On the influence of molecular forces on the deformation of an elastic sphere and its sticking to a rigid plane. *Journal of Colloid and Interface Science*, 77:91–101.

[105] Muller, V. M., Yushchenko, V. S. and Derjaguin, B. V. 1983. General theoretical consideration of the influence of surface forces on contact deformations and the reciprocal adhesion of elastic spherical particles. *Journal of Colloid and Interface Science*, 92:92–101.

[106] Mullier, M. A. 1991. *The strength of agglomerates and their breakage during fluidization.* PhD thesis, University Surrey.

[107] Mullier, M. A., Seville, J. P. and Adams, M. J. 1987. A fracture approach to the breakage of particle agglomerates. *Chemical Engineering Science*, 42:667–677.

[108] Mullier, M. A., Seville, J. P. and Adams, M. J. 1991. The effect of agglomerate strength on attrition during processing. *Powder Technology*, 65:321–333.

[109] Nienow, A. W. and Rowe, P. N. 1985. Particle growth and coating in gas-fluidized beds. In J. F. Davidson, R. Clift, and D. Harrison, editors, *Fluidization*, pages 563–594.

[110] Orr, F. M., Scriven, L. E. and Rivas, A. P. 1975. Pendular rings between solids: meniscus properties and capillary force. *J. Fluid Mech.*, 67:732–742.

[111] Paramanathan, B. K. and Bridgwater, J. 1983a. Attrition of soilids–I Cell development. *Chemical Engineering Science*, 38:197–206.

[112] Paramanathan, B. K. and Bridgwater, J. 1983b. Attrition of soilids–II Material behaviour and kinetics of attrition. *Chemical Engineering Science*, 38:207–224.

[113] Parker, M. D. and Rowe, R. C. 1991. Source variation in the wet massing (granulation) of some microcrystalline celluses. *Powder Technology*, 65:273–281.

[114] Princen, H. M. 1968. Comments on the effect of capillary liquid on the force between two spherical solid particles. *Journal of Colloid and Interface Science*, 26:249–253.

[115] Randall, C. W. 1989. *The application of contact mechanics to the numerical simulation of particulate materials.* PhD thesis, The University of Aston in Birmingham.

[116] Ray, D. T. and Hogg, R. 1987. Agglomerate breakage in polymer-flocculated suspensions. *Journal of Colloid and Interface Science*, 116:256–268.

[117] Rowe, P. W. 1962. The stress-dilatancy relation for static equilibrium of an assembly of particles in contact. *Proc. Roy. Soc. London A.*, 269:500–527.

[118] Rumpf, H. 1962. The strength of granules and agglomerates. In W. A. Knepper, editor, *Agglomeration*, pages 379–418.

[119] Rumpf, H. 1977. Particle adhesion. In K. V. S. Sastry, editor, *Agglomeration 77*, pages 97–129.

[120] Savkoor, A. R. and Briggs, G. A. D. 1977. The effect of tangential force on the contact of elastic solids in adhesion. *Proc. R. Soc. Lond. A.*, 356:103–114.

[121] Schubert, H. 1975. Tensile strength of agglomerate. *Powder Technology*, 11:107–119.

[122] Schubert, H. 1977. Tensile strength and capillary pressure of moist agglomerates. In K. V. S. Sastry, editor, *Agglomeration 77*, pages 144–155.

[123] Schubert, H., Herrmann, W. and Rumpf, H. 1975. Deformation behaviour of agglomerates under tensile stress. *Powder Technology*, 11:121–131.

[124] Serayssol, J-M. and Davis, R. H. 1986. The influence of surface interactions on the elastohydrodynamic collision of two spheres. *Journal of Colloid and Interface Science*, 114:54–66.

[125] Sherrington, P. J. and Oliver, R. 1981. *Granulation.* Heyden.

[126] Shoji, K., Lohrasb, S. and Austin, L. G. 1980. The variation of breakage parameters with ball and powder loading in dry ball milling. *Powder Technology*, 25:109–114.

[127] Smith, P. G. and Nienow, A. W. 1983. *Chemical Engineering Science*, 38:1223–1231.

[128] Strack, O. D. L. and Cundall, P. A. 1978. The distinct element method as a tool for research in granular media, Part I. Report to NSF, Grant ENG76-20771, University of Minnesota.

[129] Tabor, D. 1977. Surface forces and surface interactions. *Journal of Colloid and Interface Science*, 58:2–13.

[130] Tabor, D. 1978. On the role of molecular forces in contact deformations (critical remarks concerning Dr. Tabor's report). *Journal of Colloid and Interface Science*, 67:380.

[131] Tabor, D and Winterton, R. H. S.1969. The direct measurement of normal and retarded van der Waals forces. *Proc. Roy. Soc. Lond. Ser. A*, 312:435–450.

[132] Thornton, C. 1977. Deformation of a simple particulate model. In *Proc. Special Session 9, IX ICSMFE*, Tokyo, pages

[133] Thornton, C. 1987a. Computer simulated experiments on particulate material. In B. J. Briscoe and M. J. Adams, editors, *Tribology in Particulate Technology*, pages 292–302.

[134] Thornton, C. 1987b. Induced anisotropy and energy dissipation in particulate material–results from computer simulated experiments. In J. P. Boehler, editor, *Yielding, Damage, and Failure of Anisotropic Solids*, Mech. Eng., pages 113–130.

[135] Thornton, C. 1989. A direct approach to micromechanically based continuum models for granular material. In M. Satake, editor, *Mechanics of Granular Materials*, Japanese SMFE Society, pages 145–150.

[136] Thornton, C. 1992a. Applications of DEM to process engineering problems. *Engineering Computations*, 9:289–297.

[137] Thornton, C. 1992b. Interparticle sliding in the presence of adhesion. *J. Phys. D: Appl. Phys.*, 24:1942–1946.

[138] Thornton, C. 1993. On the relationship between the modulus of particulate media and the surface energy of the constituent particles. *J. Phys. D: Appl. Phys.*, 26:1587–1591.

[139] Thornton, C. and Barnes, D. J. 1986. Computer simulated deformation of compact granular assemblies. *Acta Mechanica*, 64:45–61.

[140] Thornton, C., Kafui, D. and Yin, K. K. 1993. Applications of DEM to impact fracture/fragmentation. In J. R. Williams and G. W. Mustoe, editors, *Proc. of the 2nd Int. Conf. on Discrete Element Methods (DEM)*, pages 265–273.

[141] Thornton, C. and Kafui, D. 1992. Computer simulated agglomerate fracture/ fragmentation. In *Symposium Attrition and Wear in Powder Technology*, pages 19–28, Utrecht, the Netherlands.

[142] Thornton, C., Lian, G. and Adams, M. J. 1993. Modelling of liquid bridges between particles in DEM simulations of particle systems. In J. R. Williams and G. W. Mustoe, editors, *Proc. of the 2nd Int. Conf. on Discrete Element Methods (DEM)*, pages 177–187.

[143] Thornton, C. and Randall, C. W. 1988. Applications of theoretical contact mechanics to solid particle system simulation. In M. Satake and J. T. Jenkins, editors, *Micromechanics of Granular Materials*, pages 133–142.

[144] Thornton, C. and Yin, K. K. 1991. Impact of elastic spheres with and without adhesion. *Powder Technology*, 65:153–166.

[145] Ting, J. M., Corkum, B. T., Kauffman, C. R. and Greco, C. 1989. Discrete numerical model for soil mechanics. *Journal of Geotechnical Engineering*, 115:379–398.

[146] Vervoorn, P. M. M. and Austin, L. G. 1990. The analysis of repeated breakge events as an equivalent rate process. *Powder Technology*, 63:141–147.

[147] Walton, O. R. 1983. Particle dynamics calculations of shear flows. In J. T. Jenkins and M. Satake, editors, *Mechanics of Granular Materials: New Models and Constitutive Relations*, pages 327–338. Elsevier, Amsterdam.

[148] Walton, O. R. 1984. Application of molecular dynamics to macroscopic particles. *Int. J. Engng. Sci.*, 22:1097–1107.

[149] Walton, O. R. and Braun, R. L. 1985. Viscosity, granular temperature and stress calculations for shearing assemblies of inelastic, frictional disks. *Journal of Rheology*, 30:949.

[150] Yin, K. K. 1992. *Numerical modelling of agglomerate degradation.* PhD thesis, The University of Aston in Birmingham.

[151] Yuregir, K. R., Ghadiri, M. and Clift, R. 1987. Impact attrition of sodium chloride crystals. *Chemical Engineering Science*, 42:843–853.

[152] Zhang, Y. and Cundall, P. A. 1986. Numerical simulation of slow deformations. In *Proc. Symp. on the Mech. of Particulate Media*, pages 347–349.

[153] Ziff, R. M. and McGrady, E. D. 1985. The kinetics of cluster fragmentation and depolymerisation. *J. Phys. A: Math. Gen.*, 18:3027–3037.

Appendix A

Frictional energy loss of elastic spheres under oblique forces

A.1 Introduction

For two elastic spheres in contact under an oblique force, Mindlin (1949) demonstrated that the effect of the tangential force is to cause relative slip over an annular region of the contact area. The slip annulus is initiated at the perimeter of the contact area and progresses inward as the tangential force increases. As a result of the relative slip and sliding frictional energy dissipation occurs. For the special case of two spheres in contact under a constant normal force P but an oscillating tangential force between $-T$ and T ($T < \mu P$), Mindlin et al (1951) derived the energy dissipation for one cycle loop as,

$$A_{slip} = \frac{9\mu^2 P^2}{10 G^* a}\left\{1 - (1 - \frac{T}{\mu P})^{5/3} - \frac{5T}{6\mu P}[1 + (1 - \frac{T}{\mu P})^{2/3}]\right\} \tag{A.1}$$

where μ is the coefficient of friction and a is the radius of the contact area, which, according to the Hertzian theory, is given as,

$$a^3 = \frac{3PR^*}{4E^*} \tag{A.2}$$

For two spheres of radii R_1, R_2 and elastic properties E_1, G_1, ν_1 and E_2, G_2, ν_2, R^*, E^* and G^* are defined as,

$$\frac{1}{R^*} = \frac{1}{R_1} + \frac{1}{R_2} \tag{A.3}$$

$$\frac{1}{E^*} = \frac{1 - \nu_1^2}{E_1} + \frac{1 - \nu_1^2}{E_2} \tag{A.4}$$

$$\frac{1}{G^*} = \frac{2 - \nu_1}{G_1} + \frac{2 - \nu_2}{G_2} \tag{A.5}$$

However, for other more general cases, the expression for frictional energy dissipation has not been obtained yet. Here, based on the partial-slip solution of Mindlin

(1949) and Mindlin and Deresiewicz (1953), an analysis is made of the frictional energy dissipation of elastic spheres due to slip and slide.

A.2 Normal force constant

Consider two spheres in contact under a constant normal force P which produces a contact area of radius a as given by equation A.2. Mindlin (1949) showed that the application of a tangential force is to cause relative slip over an annulus of the contact area. The slip annulus spreads radially inwards until sliding occurs. The precise tangential traction varies depending on the loading path and was given as a sequential superimposition of several terms in the following form,

$$q(r) = q_0(1 - \frac{r^2}{\rho^2})^{1/2} \qquad r \leq \rho \tag{A.6}$$

Correspondingly the elastic displacement on the surface of each sphere is,

$$u_i = \begin{cases} \frac{\pi q_o}{32 G_i \rho}[4(2-\nu_i)\rho^2 + 2(2-\nu_i)r^2 + \nu_i r^2 cos 2\psi] & r \leq \rho \\ \frac{q_o}{16 G_i \rho}\{2(2-\nu_i)[(2\rho^2 - r^2)\arcsin\frac{\rho}{r} + \rho\sqrt{r^2-\rho^2}] & \\ \quad + \nu_i[r^2 \arcsin\frac{\rho}{r} + (\frac{2\rho^2}{r^2} - 1)\rho\sqrt{r^2-\rho^2}]\cos 2\psi\} & r > \rho \end{cases} \tag{A.7}$$

where $i = 1$ or 2.

A.2.1 Energy dissipation during loading

If the tangential force is monotonically increased from zero to $T \leq \mu P$, slip is initiated at the edge and progresses inward to a radius c_0. The distribution of the tangential traction is given as $q = q^{(1)} + q^{(2)}$ where the two additive terms are defined as follows,

$$q^{(1)} = \frac{3\mu P}{2\pi a^3}(a^2 - r^2)^{1/2} \qquad r \leq a \tag{A.8}$$

$$q^{(2)} = -\frac{3\mu P}{2\pi a^3}(c_0^2 - r^2)^{1/2} \qquad r \leq c_0 \tag{A.9}$$

The overall tangential force and relative displacement between the two spheres are accordingly obtained as,

$$T = \mu P(1 - \frac{c_0^3}{a^3}) \tag{A.10}$$

$$\delta = \frac{3\mu P}{16G^* a}(1 - \frac{c_0^2}{a^2}) \tag{A.11}$$

Considering the two traction distribution given by equations A.8 and A.9 and applying equation A.7 over the range $c_o < r < a$ provides the elastic displacement over the slip annulus as,

$$u_i = \frac{3\mu P}{16G_i a}(2 - \nu_i)\left\{1 - \frac{c_0^2}{a^2} - \frac{1}{\pi a^2}[g_1(c_o, r) - \frac{\nu_i}{4 - 2\nu_i} g_2(c_o, r)\cos 2\psi]\right\} \tag{A.12}$$

where $i = 1$ or 2. From this expression, the relative slip can be derived as,

$$s = \delta - (u_1 + u_2) = \frac{3\mu P}{16\pi G^* a^3}\left[g_1(c_0, r) - \frac{G^*}{2}(\frac{\nu_1}{G_1} + \frac{\nu_2}{G_2}) g_2(c_o, r)\cos 2\psi\right] \tag{A.13}$$

where the g_1 and g_2 are two functions denoted as,

$$g_1(c, r) = (r^2 - 2c^2)\arccos\frac{c}{r} + c\sqrt{r^2 - c^2} \tag{A.14}$$

$$g_2(c, r) = r^2 \arccos\frac{c}{r} - (\frac{2c^2}{r^2} - 1)\, c\sqrt{r^2 - c^2} \tag{A.15}$$

If the tangential force further increases by an amount of ΔT, the relative displacement and slip will correspondingly increase. From equations A.10, A.11 and A.13 it follows that,

$$\Delta T = -3\mu P \frac{c_0^2}{a^3} \Delta c_0 \tag{A.16}$$

$$\Delta \delta = -\frac{3\mu P c_0}{8 G^* a^3} \Delta c_0 \tag{A.17}$$

$$\Delta s = -\frac{3\mu P}{16\pi G^* a^3} \left[4c_0 \arccos \frac{c_0}{r} + G^* \left(\frac{\nu_1}{G_1} + \frac{\nu_2}{G_2} \right) \frac{4c_0^4 - 4c_0^2 r^2}{r^2 \sqrt{r^2 - c_0^2}} \cos 2\psi \right] \Delta c_0 \tag{A.18}$$

Substituting equation A.17 into A.18 we obtain,

$$\Delta s = \frac{1}{2\pi c_0} \left[4c_0 \arccos \frac{c_0}{r} + G^* \left(\frac{\nu_1}{G_1} + \frac{\nu_2}{G_2} \right) \frac{4c_0^4 - 4c_0^2 r^2}{r^2 \sqrt{r^2 - c_0^2}} \cos 2\psi \right] \Delta \delta \tag{A.19}$$

Due to the increase of the relative slip, energy is dissipated by friction. The dissipated energy can be derived as

$$\Delta A_{slip} = \int_{c_0}^{a} \int_0^{2\pi} q \, \Delta s \, r dr d\psi = \frac{\mu P}{2} \left(2 - \frac{3c_0}{a} + \frac{c_0^3}{a^3} \right) \Delta \delta \tag{A.20}$$

Subtracting this energy from the work done by the incremental tangential force we further derive the elastic energy stored as follows

$$\Delta A_{elas} = T \Delta \delta - \Delta A_{slip} = \frac{3\mu P}{2} \left(\frac{c_0}{a} - \frac{c_0^3}{a^3} \right) \Delta \delta \tag{A.21}$$

A.2.2 Energy dissipation during unloading

If the applied tangential force is, after it is monotonically loaded to T_1 ($< \mu N$), unloaded to T ($-T_1 < T < T_1$), Mindlin (1949) suggested that the slip produced by loading is frozen and reverse slip is to start at the perimeter of the contact area and propagate inward to a radius c_1 ($c_0 < c_1 < a$). The distribution of the tangential traction consists of three terms $q = q^{(1)} + q^{(2)} + q^{(3)}$ which are given as follows

$$q^{(1)} = -\frac{3\mu P}{2\pi a^3}(a^2 - r^2)^{1/2} \qquad r \leq a \tag{A.22}$$

$$q^{(2)} = -\frac{3\mu P}{2\pi a^3}(c_0^2 - r^2)^{1/2} \qquad r \leq c_0 \tag{A.23}$$

$$q^{(3)} = \frac{3\mu P}{\pi a^3}(c_1^2 - r^2)^{1/2} \qquad r \leq c_1 \tag{A.24}$$

The overall tangential force and relative displacement are

$$T = \mu P\left(2\frac{c_1^3}{a^3} - \frac{c_0^3}{a^3} - 1\right) = T_1 - 2\mu P\left(1 - \frac{c_1^3}{a^3}\right) \tag{A.25}$$

$$\delta = \frac{3\mu P}{16G^* a}\left(2\frac{c_1^2}{a^2} - \frac{c_0^2}{a^2} - 1\right) = \delta_1 - \frac{3\mu P}{8G^* a}\left(1 - \frac{c_1^2}{a^2}\right) \tag{A.26}$$

where T_1 and δ_1 are the tangential force and relative displacement from which unloading commenced. Over the slip annulus $c_1 \leq r \leq a$, we can, using equations A.7, A.22, A.23 and A.24, derive the elastic displacement of each sphere as

$$u_i = \frac{3\mu P(2 - v_i)}{16G_i a}\left\{2\frac{c_1^2}{a^2} - \frac{c_0^2}{a^2} - 1\right.$$

$$\left. -\frac{1}{\pi a^2}\{g_1(c_0, r) - 2g_1(c_1, r) - [g_2(c_0, r) - 2g_2(c_1, r)]\frac{\nu_i \cos 2\psi}{4 - 2\nu_i}\}\right\} \tag{A.27}$$

where $i = 1$ or 2. This leads to the relative slip expressed as,

$$s = \frac{3\mu P}{16G^* a^3}\left\{ g_1(c_0, r) - 2g_1(c_1, r)\right.$$

$$\left. -\frac{G^*}{2}(\frac{\nu_1}{G_1} + \frac{\nu_2}{G_2})[g_2(c_0, r) - 2g_2(c_1, r)]\cos 2\psi\right\} \tag{A.28}$$

If the unloading tangential force further changes by an amount of ΔT, it follows from A.25, A.26 and A.28 that

$$\Delta T = 6\mu P \frac{c_1^2}{a^3} \Delta c_1 \tag{A.29}$$

$$\Delta \delta = \frac{6\mu P c_1}{8 G^* a^3} \Delta c_1 \tag{A.30}$$

$$\Delta s = \frac{3\mu P}{8\pi G^* a^3} \left[4c_1 \arccos \frac{c_1}{r} + G^* \left(\frac{\nu_1}{G_1} + \frac{\nu_2}{G_2} \right) \frac{4c_1^4 - 4c_1^2 r^2}{r^2 \sqrt{r^2 - c_1^2}} \cos 2\psi \right] \Delta c_1$$

$$= \frac{1}{2\pi c_1} \left[4c_1 \arccos \frac{c_1}{r} + G^* \left(\frac{\nu_1}{G_1} + \frac{\nu_2}{G_2} \right) \frac{4c_1^4 - 4c_1^2 r^2}{r^2 \sqrt{r^2 - c_1^2}} \cos 2\psi \right] \Delta \delta \tag{A.31}$$

From the distribution of the tangential traction and relative slip the energy loss during unloading is obtained as follows,

$$\Delta A_{slip} = \int_{c_1}^{a} \int_{0}^{2\pi} q \, \Delta s \, r dr d\psi = -\frac{\mu P}{2} \left(2 - \frac{3c_1}{a} + \frac{c_1^3}{a^3} \right) \Delta \delta \tag{A.32}$$

A.2.3 Energy dissipation during reloading

If the tangential force, after it has been unloaded to T_2, is reloaded again, the slip caused by loading and unloading becomes fixed and a new slip annulus is developed at the contact area perimeter and spreads radially inwards to a radius c_2 ($c_0 < c_1 < c_2 < a$). The distribution of the tangential traction is due to the contribution of four terms $q = q^{(1)} + q^{(2)} + q^{(3)} + q^{(4)}$ where

$$\tau^{(1)} = \frac{3\mu P}{2\pi a^3} (a^2 - r^2)^{1/2} \qquad r \le a \tag{A.33}$$

$$\tau^{(2)} = -\frac{3\mu P}{2\pi a^3} (c_0^2 - r^2)^{1/2} \qquad r \le c_0 \tag{A.34}$$

$$\tau^{(3)} = \frac{3\mu P}{\pi a^3} (c_1^2 - r^2)^{1/2} \qquad r \le c_1 \tag{A.35}$$

$$\tau^{(4)} = -\frac{3\mu P}{\pi a^3} (c_2^2 - r^2)^{1/2} \qquad r \le c_2 \tag{A.36}$$

From these terms, the tangential force and displacement are accordingly given as,

$$T = \mu P \left(1 - \frac{c_0^3}{a^3} + 2\frac{c_1^3}{a^3} - 2\frac{c_2^3}{a^3}\right) = T_2 + 2\mu P \left(1 - \frac{c_2^3}{a^3}\right) \tag{A.37}$$

$$\delta = \frac{3\mu P}{16 G^* a} \left(1 - \frac{c_0^2}{a^2} + 2\frac{c_1^2}{a^2} - 2\frac{c_2^2}{a^2}\right) = \delta_2 + \frac{3\mu P}{8 G^* a} \left(1 - \frac{c_2^2}{a^2}\right) \tag{A.38}$$

where T_2 and δ_2 are the tangential force and relative displacement from which reloading commenced.

By analogy, it can be derived that, during the tangential reloading, the relative slip and energy dissipation are correspondingly expressed as,

$$\Delta s = \frac{1}{2\pi c_2} \left[4c_2 \arccos\frac{c_2}{r} + G^*\left(\frac{\nu_1}{G_1} + \frac{\nu_2}{G_2}\right)\frac{4c_2^4 - 4c_2^2 r'^2}{r'^2\sqrt{r'^2 - c_2^2}} \cos 2\psi\right] \Delta\delta \tag{A.39}$$

$$\Delta A_{slip} = \int_{c_2}^{a}\int_0^{2\pi} q\,\Delta s\, r dr d\psi = \frac{\mu P}{2}\left(2 - \frac{3c_2}{a} + \frac{c_2^3}{a^3}\right)\Delta\delta \tag{A.40}$$

A.3 Normal force changing

The tangential compliance of elastic spheres under varying oblique forces was studied by Mindlin and Deresiewicz (1953). Suppose that an initial state has been obtained by applying a normal force P and followed by a tangential force T ($< \mu P$). A change of the normal force by an amount ΔP results in a change of the contact area with the radius of the new contact area given as

$$a_1^3 = \frac{3(P + \Delta P)R^*}{4E^*} \tag{A.41}$$

However, if the tangential force changes by an amount of ΔT, Mindlin and Deresiewicz argued that the tangential displacement not only depends on the past history

of the tangential force but also the relative rates of change for the tangential force and normal force. Generally speaking, there are four different cases for the instantaneous relative rates of change of normal and tangential forces. These includes (a) normal force increasing, tangential force increasing, (b) normal force increasing, tangential force decreasing, (c) normal force decreasing, tangential force increasing, (d) normal force decreasing, tangential force decreasing. Of the four cases, (a) and (c) applies to the path of tangential force loading or reloading and the other two applies to unloading.

For the loading and reloading cases ($\Delta T > 0$) if the normal force is also increasing ($\Delta P > 0$) then the contact area is increasing. Mindlin and Deresiewicz (1953) suggested that, during the process of increasing the contact area, the initial tangential traction is frozen over the initial contact area $r \leq a$. The increase of the tangential force generates slip which originates at $r = a_1$ ($a_1 > a$) and spreads inwards to $r = c_j'$ ($j = 0$ for loading, $j = 2$ for reloading). There is a jump discontinuity in the inward propagation of the slip annulus when $\Delta T = \mu \Delta P$. For $\Delta T < \mu \Delta P$, the inner radius of the slip annulus is greater than the initial contact radius, i.e. $c_j' > a$. For $\Delta T > \mu \Delta P$, the inner radius of the slip annulus is less than the inner radius of the initial slip annulus which was frozen prior to the increment in normal force, i.e. $c_j' < c_j$.

If $\Delta T \leq \mu \Delta P$, since $c_j' \geq a$, the area of the slip annulus $c_j' < r < a_1$ is negligible in comparison to the overall contact area and hence the energy dissipated may be neglected. Consequently, for $\Delta T > \mu P$, only the excess increment $\Delta T' = \Delta T - \mu \Delta P$ is considered to produce displacements which involve the dissipation of energy. The general expression for the total displacement increment, see chapter 3 section 3.3.2, may be written as

$$\Delta \delta = \frac{1}{8G^* a} \left[\pm \mu \Delta P + \frac{\Delta T \mp \mu \Delta P}{c_j / a} \right] \tag{A.42}$$

For loading or reloading with $\Delta P > 0$ this reduces to

$$\Delta\delta = \frac{\mu\Delta P}{8G^*a} + \frac{\Delta T'}{8G^*c_j} \tag{A.43}$$

Hence, the displacement increment corresponding to $\Delta T'$, defined as $\Delta\delta'$, takes the form

$$\Delta\delta' = \Delta\delta - \frac{\mu\Delta P}{8G^*a} \tag{A.44}$$

and

$$c_0 = a\left[1 - \frac{T + \mu\Delta P}{\mu(P + \Delta P)}\right]^{1/3} \tag{A.45}$$

$$c_2 = a\left[1 - \frac{T - T_2 + 2\mu\Delta P}{2\mu(P + \Delta P)}\right]^{1/3} \tag{A.46}$$

Recalling equation A.20 or A.40 we obtain, by analogy, the energy loss due to frictional slip as

$$\Delta A_{slip} = \frac{\mu(P + \Delta P)}{2}\left(2 - \frac{3c_j}{a} + \frac{c_j^3}{a^3}\right)\left(\Delta\delta - \frac{\mu\Delta P}{8G^*a}\right) \tag{A.47}$$

If the normal force is decreasing ($\Delta P < 0$) the contact area is decreasing and the annulus $a_1 < r < a$ is no longer in contact. Consequently, before a reduction of the normal force may be considered, it is necessary to remove the initial tangential traction from the annulus $a_1 < r < a$. Mindlin and Deresiewicz suggested that this could be accomplished by the application of a distribution of tangential traction which allows no slip on the contact area $r < a_1$. This corresponds to a reduction of the tangential force by an amount $\mu\Delta P$ and a decrease in tangential displacement by an amount $\mu\Delta P/8G^*a$ without any loss of energy. Therefore, when considering the

energy dissipation due to the subsequent increment in tangential force, it is necessary to consider the increment $\Delta T' = \Delta T - \mu\Delta P$ in which ΔP is negative and hence $\Delta T' > \Delta T$. The corresponding displacement increment $\Delta\delta'$ is given by equation A.44 and the energy loss due to frictional slip is provided by equation A.47 using equations A.45 and A.46 provided that, in each of these equations, ΔP is taken to be negative.

Mindlin and Deresiewicz (1953) demonstrated that similar arguments to those presented above also apply to the unloading case ($\Delta T < 0$). For the unloading case, equation A.42 takes the form

$$\Delta\delta = \frac{1}{8G^*a}\left[-\mu\Delta P + \frac{\Delta T + \mu\Delta P}{c_1/a}\right] \tag{A.48}$$

in which ΔT is always negative and ΔP may be positive or negative depending on whther the normal force is increasing or dcreasing. When examining the energy dissipation it is necessary to consider the increment $\Delta T' = \Delta T + \mu\Delta P$ and, hence, equation A.48 may be rewritten as,

$$\Delta\delta = -\frac{\mu\delta P}{8G^*a} + \frac{\Delta T'}{8G^*c_1} \tag{A.49}$$

and the effective displacement increment

$$\Delta\delta' = \Delta\delta + \frac{\mu\Delta P}{8G^*a} \tag{A.50}$$

remembering that $\Delta\delta$ is negative. Consequently, the energy dissipation due to slip, for the unloading case, is given as

$$\Delta A_{slip} = -\frac{\mu(P + \Delta P)}{2}\left(2 - \frac{3c_1}{a} + \frac{c_1^3}{a^3}\right)\left(\Delta\delta + \frac{\mu\Delta P}{8G^*a}\right) \tag{A.51}$$

where

$$c_1 = a\left[1 + \frac{T - T_1 - 2\mu\Delta P}{2\mu(P + \Delta P)}\right]^{1/3} \tag{A.52}$$

Re-examining the equations developed in this appendix, it is concluded that, for all cases, the energy dissipation due to slip may be defined by the general expression

$$\Delta A_{slip} = (-1)^j \frac{\mu(P + \Delta P)}{2}\left(2 - \frac{3c_j}{a} + \frac{c_j^3}{a^3}\right)\left(\Delta\delta - (-1)^j \frac{\mu\Delta P}{8G^* a}\right) \tag{A.53}$$

where $j = 0$ for loading, $j = 1$ for unloading, $j = 2$ for reloading and the algebraic (not the absolute) values of ΔP and $\Delta\delta$ are used.

A.4 Sliding

The partial-slip solution of Mindlin and Deresiewicz (1953) implies that once the slip annulus has reached the centre of the contact area, sliding all over the contact area occurs. During sliding, the distribution of the tangential traction is in the form

$$q = \pm\frac{3\mu P}{2\pi a^3}(a^2 - r^2)^{1/2} \qquad r \leq a \tag{A.54}$$

and the overall tangential force is accordingly given as,

$$T = \pm\mu P \tag{A.55}$$

This distribution of tangential traction produces the following elastic deformations over the contact area of the two spheres,

$$u_i = \pm\frac{3\mu P}{64 G_i a^3}[2(2 - \nu_i)(2a^2 - r^2) + \nu_i r^2 \cos 2\psi] \tag{A.56}$$

where $i = 1$ or 2 indicating the two spheres respectively.

If, during sliding, the normal force changes by an amount of ΔP, then the elastic deformation of each sphere also changes by an amount of,

$$\Delta u_i = \pm \frac{3\mu \Delta P}{64 G_i a^3}[2(2-\nu_i)(2a^2 - r^2) + \nu_i r^2 \cos 2\psi] \tag{A.57}$$

From the tangential traction and elastic deformation, we may obtain the corresponding energy stored in the elastic deformation as given below

$$\Delta A_{elas} = \int_0^a \int_0^{2\pi} q(\Delta u_1 + \Delta u_2) r dr d\psi = \frac{3\mu \Delta P T}{20 G^* a} \tag{A.58}$$

As a result, the frictional energy loss due to sliding is expressed as,

$$\Delta A_{slide} = T\Delta\delta - \Delta A_{elas} = T(\Delta\delta - \frac{3\mu\Delta P}{20 G^* a}) \tag{A.59}$$

A.5 With adhesion

For the tangential interaction between two adhering elastic spheres, Thornton (1991) suggested that the partial-slip solution of Mindlin and Deresiewicz (1953) could be applied after the adhesive peeling and until, when $T = \mu P_e$, sliding occurs. Here $P_e = P + 2P_c$ or $P_e = P_1(1 - (P_1 - P)/3P_1)^{3/2}$, as suggested by Thornton (1991), is the effective normal force and $P_c = 3\pi\gamma R^*$ is the pull-off force, P_1 is the equivalent Hertzian force, see chapter 3 section 3.3. Hence, it follows that the energy dissipation of the tangential force can be obtained using the foregoing analysis with the substitution of P_e for P. This is summarised as follows

$$\Delta A_{slip} = \frac{\mu(P_e + \Delta P_e)[(-1)^j \Delta T - \mu \Delta P_e]}{16 G^* c_j} \left(2 - \frac{3c_j}{a} + \frac{c_j^3}{a^3}\right) \tag{A.60}$$

if $(-1)^j \Delta T > \mu \Delta P_e$. The radius of the slip annulus c_j is given as,

$$c_j = \begin{cases} a\sqrt[3]{1 - \frac{T+\mu\Delta P_e}{\mu(P_e+\Delta P_e)}} & j = 0 \\ a\sqrt[3]{1 - \frac{(-1)^j(T-T_j)+2\mu\Delta P_e}{2\mu(P_e+\Delta P_e)}} & j = 1,2 \end{cases} \tag{A.61}$$

where $j = 0, 1, 2$ denotes the path of loading, unloading and reloading.

Otherwise, if $(-1)^j \Delta T \leq \mu \Delta P_e$, the energy dissipation is negligible. When sliding occurs, the frictional energy loss may be still calculated by the expression A.59, with the substitution of P_e for P.

During the peeling process before the following critical value of T is reached,

$$T_c = 4\sqrt{\frac{G^*}{E^*}(PP_c + P_c^2)} \tag{A.62}$$

the tangential force is described by Mindlin's no-slip solution as suggested by Savkoor and Briggs (1977). If this is the case, there is no frictional energy dissipation before peeling is completed.

Appendix B

Command list of TRUBAL

B.1 Introduction

The commands listed here apply to the current version of **TRUBAL** (1st May 1992) resident on IBM RS6000 workstations. Commands may be given in any order that is physically meaningful except for the **Start** and **Restart** commands which must be given as the first command in any command file. Most commands require parameters. When parameters are arranged horizontally, they must all be given, except for optional parameters, denoted by brackets [ ]. Parameters arranged vertically after a command denote the selection of options that may be given: any or all of these parameters may be given in any order. For example **Print G C I** will print the grid-size, contacts and general information respectively. Parameters that start with a lower-case stand for numbers: e.g. **nball** may be given as 100 and **ed22** may be given as 1.2e-7. Parameters and commands that start with an upper-case letter are typed literally – either in upper- or lower-case. These commands and keywords may be typed in full, or truncated to just those letters in upper-case. For example, the command **Print Contacts** may be given as **p c, Pr cO** or any other variation. Parameters may be separated by any number of spaces, commas, brackets () or slashes. For clarity it is helpful to give a minimum of three letters.

When starting **TRUBAL**, a file called *TRUBAL.DIR* should exist in your current working directory. If this file contains the word BATCH, the program will operate in batch mode and take its input from file *TRUBAL.DAT* and place its output in *TRUBAL.OUT*. If *TRUBAL.DIR* contains the word *TERM*, the program will expect input from the keyboard and send its output to the display. Input and output redirection can however be used in this case to take input from and send output to specified files.

B.2 Command list

AGGlomerate nagg x_c y_c z_c R_A

Define a spherical region of radius $\mathbf{R_A}$ centred at $(\mathbf{x_c}, \mathbf{y_c}, \mathbf{z_c})$ for the agglomerate **nagg**, where particles belong to the agglomerate are to be generated (refer to the commands **AGEnerate** and **RGEnerate**). **nagg** should be given as either 1 or 2 because only up to 2 agglomerates can be handled by the computer program.

AGEnerate isize imat iagg x_o y_o z_o **dx dy dz**

Particles of **isize** radius and **imat** material type are automatically generated in a way that the lowest left particle is at $\mathbf{x_o}, \mathbf{y_o}, \mathbf{z_o}$ and others are placed at the specified incremental distance of **dx**, **dy**, **dz** in each direction from one each other. **iagg** is the agglomerate number the generated particles belong to. If a spherical region is specified for the agglomerate (refer to the command **AGGlomerate**), only those particles fall inside the spherical region are accepted and others fall outside are rejected. Otherwise, particles are to be generated to fill the whole cubic cell. This command is useful to generate regular packings.

AWAll n [P d a b c] [V vx vy vz] [M mtyp] [SE F vmax g]
n [SP d a b c] [V vx vy vz vr] [M mtyp] [SE F vmax g]

This command alters the position (**P/SP**) or velocity (**V**) or material-type (**M**) of a wall. **S** selection sets servo control for the wall. See **DWAll** for definition of parameters. **P/SP, V, M** and **SE** are all selectable but the wall number **n** must be logically specified. The first form is used for a plane wall and the second form applies to a hollow sphere wall. With **AWAll** command, one can change a plane wall to a sphere wall or vice versa.

COHesion γ mtyp

γ is taken as the surface energy for particles of material type **mtyp**.

CReate x y z v_x v_y v_z θ_x θ_y θ_z isize mtyp

A particle is created at location (**x, y, z**) with size type **isize** and material type **mtyp**. The x, y and z linear and angular velocity components for the sphere are given as v_x, v_y, v_z, θ_x, θ_y, θ_z respectively. Currently, **TRUBAL** allows 10 size-types and 5 material-types. If the created particle overlaps existing particle or particles it is then rejected.

Cycle n [S0 v]
[S1MS2 v]
[S11 v]
[S22 v]
[S33 v]
[RING v]

The program executes **n** calculation cycles, and returns control to the user when they are complete. The optional keywords denote that the servo-control will attempt to hold the specified variable constant at the value **v**. Keyword **S0** corresponds to mean stress σ_0 where $\sigma_0 = (\sigma_{11}+\sigma_{22}+\sigma_{33})/3$. Keyword **S1MS2** is similar, but corresponds to the "two-dimensional mean stress" : $(\sigma_{11}+\sigma_{22})/2$. Individual stresses, σ_{11}, σ_{22} and σ_{33} are controlled by the keywords **S11**, **S22** and **S33**, respectively. **RING** controls the angle of major principal stress in a ring shear test. Combinations of control keywords may be used when this is physically reasonable. See related commands **Gain** and **Mode**.

DAmping frac freq imass istiff iswitch

Damping is specified in terms of the Rayleigh damping parameters: **frac** is the fraction of critical damping at the modal frequency **freq**. Rayleigh damping involves mass-proportional (global) damping and stiffness-proportional (contact) damping : the former may be switched off by giving **imass** as 1, and the latter by giving **istiff** as 1. Otherwise these parameters should be set to zero for full Rayleigh damping. Note that contact damping may require a reduction in time step for numerical stability. If in doubt give **istiff** as 1. The damping parameters are specified for ball-to-ball contact if **iswitch** is given as 1 and for ball-to-wall contact if **iswitch** is given as 0.

Density d mtyp

d is taken as the mass density of all particles of material type **mtyp**.

DWAll P d a b c V vx vy vz M mtyp SE F vmax g
SP d a b c [V vx vy vz vr M mtyp SE F vmax g

This command creates a wall. In the first form, a plane wall is created. **P** defines the plane wall as **ax+by+cz=d**. Only walls parallel to one of the three planes x-y, y-z and x-z are handled in 3-d at the moment. This means that only one of the parameters **a, b** or **c** is non-zero for any wall. For a non-zero **a** for example, the ratio **d/a** then gives the x-intercept of a 'y-z' plane wall. In the 2-d case which handles only walls parallel to either the x- or y-axis, the equation reduces to **ax+by=d**, but a value of zero must still be specified for **c**. **V** gives the translational velocity of the wall (**vx, vy, vz**) and **M** indicates the material-type of the wall (given by **mtyp**). The selection **SE** introduces servo control to the wall. **F** is the desired normal force to be reached by the wall. **vmax** is the maximum normal velocity allowed for the wall, **g** is the servo gain.

In the second form, an hollow sphere wall is created. The sphere wall is defined by **SP** as $d^2 = (x-a)^2 + (y-b)^2 + (z-c)^2$. **V** sets the translational velocity of the wall to (**vx, vy, vz**) and the radial velocity to **vr**. **SE** sets the radial force **F**, maximum radial velocity **vmax** and gain **g** for the servo control mechanism of the wall. For both forms, the order of the last three items can be given in any order. The first three items must be specified.

Fix ix iy iz irx iry irz iadd

All

The translational or angular velocity of any particle may be held constant by setting the appropriate parameter equal to 1 : **ix, iy** and **iz** control the x, y and z velocities, and **irx, iry** and **irz** the angular velocities about the x, y and z axes, respectively. The constraints may be removed by setting the parameters to zero. The final parameter, **iadd**, is the address of the particle to be fixed. If the word **All** is substituted, then all particles are affected. Note that the **Fix** command does *not* set velocities to zero — see the **Zero** command.

FMM r

All applied particle forces are multiplied by **r**. This command has no effect on particle-particle forces and force-sums of fixed particles.

FRO

Sets angular velocities of all particles to zero.

FRAction f

The time step is set to a fraction of the critical time-step $\Delta t = f\Delta t_{crit}$. The critical time step (Δt_{crit}) is based on the Rayleigh wave speed. The default value of **f** is 1.

FRiction amu mtyp

The friction coefficient is set to **amu** for particles or walls of material type **mtyp.** For two different material types in contact, the smaller of the two coefficients is used in the program.

GAIN g edmax

The servo gain, **g,** and the maximum allowed strain-rate, **edmax,** are set. In mode 0 (see **Mode** command), the parameter **g** represents $\triangle\dot{e}/\sigma_{error}$, where $\triangle\dot{e}$ is the change in grid strain-rate that occurs for an error in the controlled stress σ_{error}. The "controlled stress" is the one given on the **Cycle** command, and the "error" is the difference between the given value and the measured value for the assembly of particles. For mode 1 operation, the parameter **g** is $\dot{e}/\sigma_{error}$. The optimum value of **g** is, to some extent, a matter of trial and error. If it is too high, the servo will "hunt" or will be unstable; if **g** is too low, the servo will be sluggish and the error may be too large.

GRAvity gx gy gz

Gravitational accelerations are prescribed for each of the coordinate directions. Note that gravity is not meaningful when full periodic boundaries are in effect.

GRID ed11 ed22 ed33 ed12 ed23 ed31

The strain-rates $\dot{e}_{11}, \dot{e}_{22}, \dot{e}_{33}, \dot{e}_{12}, \dot{e}_{23}, \dot{e}_{31}$, of periodic space are set. Note that the strain rates $\dot{e}_{23}$ and $\dot{e}_{31}$ are not used although they should be entered on the **Grid** command as zero. The components $\dot{e}_{11}$, $\dot{e}_{22}$ and $\dot{e}_{33}$ cause the periodic volume to change shape. However the component $\dot{e}_{12}$ does not distort the periodic volume in shear; rather there is a step in x or z displacement between the bottom y-boundary and the top y-boundary. This step in shear is printed out when the **Print Grid** command is given.

Iset k iadd

The integer **k** is inserted into the main memory array IA() at address **iadd.** Great caution is needed when using this command.

LIQuid pvol gsurf gcon gvis

By using the command, liquid is distributed to all contacts (including those not taking load). Liquid bridges are immediately formed for all contacts which are taking load. For those that are not taking load, liquid bridges are formed when they start to take load. The volume of the liquid bridge at each contact is set to be **pvol%** of the volume of the two spheres. The other three parameters are surface tension (**gsurf**, in N/m, not to be zero if **pvol** is not given as zero), solid-liquid contact angle (**gcon**, in degree) and viscosity (**gvis**, in pa.s) respectively. To change the liquid volume or any one of the other parameters, simply use the command again. If **pvol** is set to be zero, all liquid bridges formed before are removed.

Log ON

OFF

The command **Log ON** causes all commands, comments, error messages, etc., to be reproduced on a file *TRUBAL.OUT*. The command **Log OFF** suppresses this echo function, except for output from the **Print** command.

Mode n

This selects the type of servo control. **Mode 0,** which is the default, selects "velocity increment control", in which the *increment* in grid velocity is proportional to the error (difference between measured value and desired value). **Mode 1** selects "velocity control", whereby the grid velocity is set directly by the servo.

New

The program returns to the point at which it expects a **Start** or **Restart** command. The data for the current problem is lost from memory.

Plot **BALl** or **DISks**

BOU (for 3-d) or **GRId** (for 2-d)

CLUster or **LCLuster**

CND or **LCNd**

COUple

FORces or **LFOrces** or **MFOrces**

RDIsp

ROTation

SAVe

VELocity

WALl

The **Plot** command produces either 2-d $x-y$ plots or 3-d $x-y-z$ plots. The different options are explained below.

Ball or **DISks** produces a plot of the constituent particles. For the option **BALl**, particles are plotted as spheres (3-d) or shaded circles (2-d). **Disks** is an option used only in the 3-d mode to plot the particles as shaded circles as seen from one viewpoint.

BOu plots an $x-y-z$ box of the simulation volume or the x, y and z axes (3-d mode only). The corresponding 2-d parameter **Grid** gives an $x-y$ grid of the simulated area.

CLUster plots clusters (or fragments) of the agglomerate(s) in different colours according to the numbers of particles of the clusters. The option **LCLuster**, plots the clusters connected by liquid bridges.

Cnd plots the contact connection diagram, which compares the current state of the simulated agglomerate(s) with a previously saved state and identifies the contacts which are still present (*existing contacts*), newly made (*new contacts*) and broken (*deleted contacts*). The option **Lcnd** is to plot the connection diagram of liquid bridge contacts.

COuple produces a plot of couple stresses as vectors (never been used at Aston).

Forces plots the contact forces as lines oriented in the direction of the force. In 2-d, the thickness of the line is proportional to the magnitude of the force (scaled to the current maximum force). The options **LFOrces** and **MFOrces** are used to plot the contact forces of liquid bridges and body contacts respectively.

Save does not produce a plot, but causes the current state to be saved in a memory buffer : this state is necessary before using the parameters **Rdisp** and **Rotation**, which produce plots of relative displacement and relative rotation respectively. Typical usage is:

```
plot save
cycle 200
plot bou rdisp
```

In this example, the incremental displacement vectors corresponding to a 200-cycle interval will be plotted.

Vel causes velocity vectors to be plotted.

Wall causes all walls to be plotted.

PRA v mtyp

Specifies the Poisson ratio value **v** for material-type **mtyp**.

PRint **Balls**

CHist

Contacts [All or Gap]

Energy

Entries

Grid

Info

Map

Partitions

Stress

A printout is made of various quantities. The above parameters correspond, respectively, to: *balls, contact histogram, contacts, energy terms, box entries, grid size, general information, memory map, stress partitions and stress tensor.* The optional keyword **All** requests that all contacts are printed, rather than just those taking load, which is the default. The optional keyword **Gap** causes only contact overlaps and normal forces to be printed. To reduce the amount of output, the **Window** command may be given prior to the **Print** command.

PRObe **E11**

E22

E33

E12

E23

E31

E1M2

E2M3

E3M1

The command causes a strain increment to be made at the current state. The

resulting modulus (stress/strain) is printed out. Only one of the above keywords may be given per **Probe** command : they correspond, respectively, to probes of Δe_{11}, Δe_{22}, Δe_{33}, Δe_{12}, Δe_{23}, Δe_{31}, $\Delta e_{11} - \Delta e_{22}$, $\Delta e_{22} - \Delta e_{33}$, $\Delta e_{33} - \Delta e_{11}$. The current state is saved before the probe is done and is restored afterwards. During the probe, 500 cycles are done at zero strain, to get the "baseline" state; then 250 cycles of probe are done, and finally 500 cycles of zero strain are done. So a probe takes quite some time to execute.

RAdius r isize

r is taken as the radius of particles of size type **isize**.

RESet

Accumulated rotations are set to zero. This has no effect on the mechanical behaviour, since only incremental rotations are used in the calculation. These rotations are simply the summations, over time, of the incremental rotations.

Restart [filename]

A previously-saved problem is restored from the file **filename**. If a file name is not given, a default file name of **save.old** is assumed. The command **Restart** may only be given as the first command of a run or as the first command after a **New** command.

RGEnerate n isize mtyp naggm
Seed n

In the first form of the command, **n** particles of size type **isize** and material type **mtyp** are randomly generated over a spherical region (defined by the command **AGGlomerate**) for agglomerate **naggm** or over the cubic cell (otherwise). No effort is made to fit particles into gaps between other particles. If a candidate

particle overlaps an existing particle, it is rejected and another one is tried. Before giving this command, a radius must already have been defined for the size type **isize**. If several sizes of particles are to be combined in an assembly, the larger ones should be generated first since it is easier to fit small particles. **naggm** (1 0r 2) indicates the number of agglomerates that the generated particles belong to. In the second form of the command **RGE Seed n**, no particles are generated, but the random number generator produces **n** numbers that are discarded. This is useful when generating different distributions of the same particles.

Rset r iadd

The real number **r** is inserted into the main memory array IA() at the address **iadd**. Great caution is needed when using this command.

SAve [filename]

The current problem state is saved on the file **filename**. If a file name is not given, a default file name **save.new** is assumed. If a file name is specified that already exists, the existing data is over-written. The saved state records all positions, velocities, forces, options and so on, at a given stage in a run; it corresponds to a "snapshot" at a single point in time. The **Save** command does *not* record a sequence of commands.

Start xmax ymax zmax nbox nball nwall [Log]

This command (or the **Restart** command) must be the first one to run **TRUBAL**. The parameters **xmax, ymax** and **zmax** are the total widths of the box volume (also the periodic volume) in the x, y and z directions, respectively. **nbox** is the number of boxes requested, and **nball** is the maximum number of spheres that may be needed — there is no problem if fewer spheres

are subsequently generated: the purpose of the **Start** command is to allocate enough memory to hold all the required boxes and particles. The parameter **nwall** indicates the maximum number of walls that may be needed. The optional keyword **Log** turns the "log" facility on immediately: i.e. output is echoed to the output file *TRUBAL.OUT* unless redirected.

Stop

Stops the program. The current state of the problem is not saved automatically. Use the **Save** command to do that before issuing the **stop** command.

VELocity v1x v1y v1z ivd

v1x v1y v1z v2x v2y v2z ivd

This command is used to specify the velocity of a particle or particles in an agglomerate. The parameters **v1x, v1y, v1z** specify the x, y and z components of the desired velocity for particles in the first agglomerate, and where there are two agglomerates, **v2x, v2y, v2z** specify the velocity components for the second agglomerate particles. The parameter **ivd** is used to indicate whether the agglomerate(s) is (are) being impacted (**ivd**=1) or not (**ivd**=0). In the former case, a flag is set in the program which ensures that any secondary contacts formed after impact use a base value of surface energy corresponding to van der Waal's forces of attraction only.

VMU r

The velocities of all fixed degrees-of-freedom are multiplied by **r**. See the **FIX** command.

Window x1 x2 y1 y2 z1 z2

This command limits the volume (or area) space that is addressed by the **Print** command, when it is printing out information on spheres, contacts, etc. The volume is:

$$\mathbf{x1} < x < \mathbf{x2}$$

$$\mathbf{y1} < y < \mathbf{y2}$$

$$\mathbf{z1} < z < \mathbf{z2}$$

YMD ymod mtyp

Specifies a Young's modulus value of **ymod** for all particles of material-type **mtyp**.

Zero izf

Sets the particle velocities (translational and rotational) to zero. If **izf** is given as 1, in all subsequent cycles, the particle velocities are set to zero after *each* cycle. Use **izf**=0 to over-ride this.

2-D

This command causes **TRUBAL** to operate in two-dimensional mode. The particles are still regarded as spheres, but they are constrained to move in the $x-y$ plane only. Although the equations of motion are truncated to two dimensions, the force-displacement calculation (subroutine HFORD) still operates in three dimensions. This could be modified to improve running speed. In 2-d mode, the generation routine sets the z coordinate of all particles to the same value — corresponding to the centre of the box volume in the z direction. Only one box should be specified in the z direction, although **TRUBAL** will not complain if more are requested.

Appendix C

Graphics printings of computer simulated wet agglomerate impact

This appendix presents the graphics printings of the series of computer simulated moist agglomerate collision tests described in Chapter 6 and 7. All the graphics printings are colour copies of the screen visualisation of a IBM RS 6000 workstation (340 model) provided by a GAMMACOLOR System 400.

C.1 Agglomerate-wall impact

Computer simulated agglomerate-wall impacts were performed of a body-centred cubic moist agglomerate consisting of 4062 particles of radius $R = 30\mu$. The properties of the constitutive particles were: density $\rho = 2.65 Mg\,m^{-3}$, Young's modulus $E = 70 Gpa$, Poisson's ratio $\nu = 0.3$ and friction coefficient $\mu = 0.3$. At each contact, a quantity of liquid of 0.1% of the particle volume was assigned to form a liquid bridge. This corresponds degree of saturation was 0.85% for the body-centred cubic arrangement. The liquid modelled was silicon fluid with the following properties: surface tension $\gamma_{lv} = 0.025$, solid-liquid contact angle $\theta = 0^0$ and viscosity $\eta = 0.00 \sim 0.1 Pa\,s$.

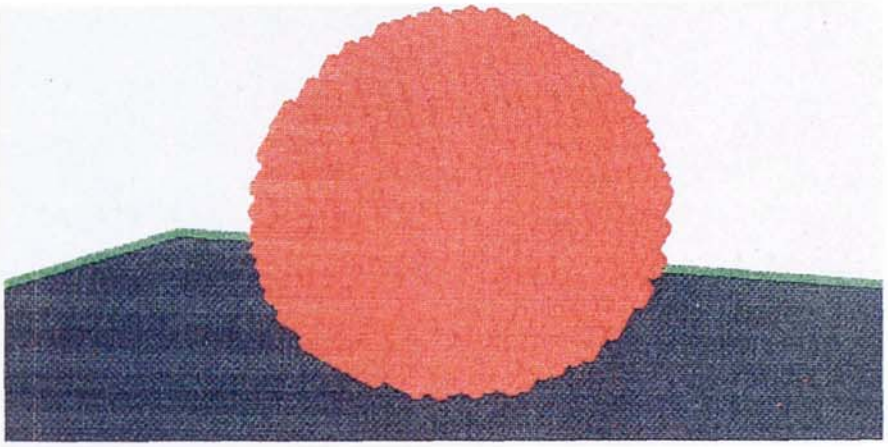

Impact velocity $v = 0.2m/s$, viscosity $\eta = 0.0$, surface tension $\gamma_{lv} = 0.025N/m$.

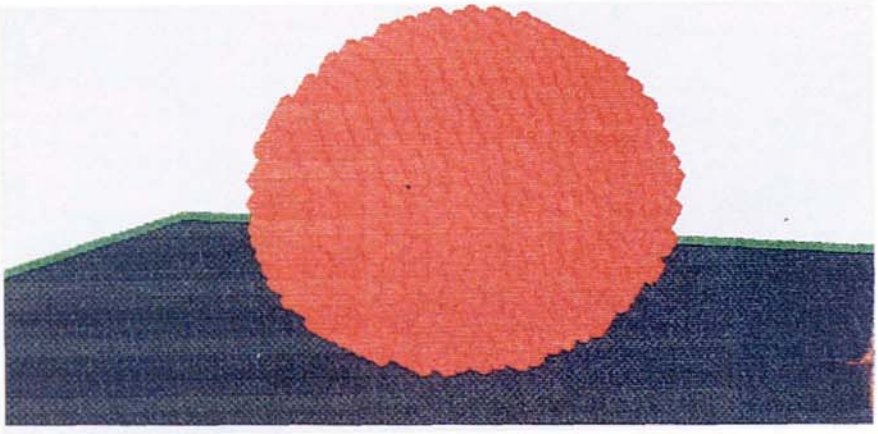

Impact velocity $v = 0.3m/s$, viscosity $\eta = 0.0$, surface tension $\gamma_{lv} = 0.025N/m$.

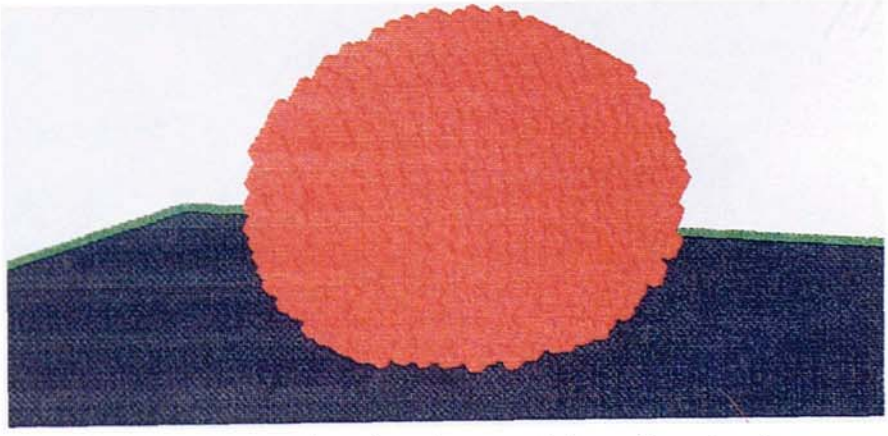

Impact velocity $v = 0.4m/s$, viscosity $\eta = 0.0$, surface tension $\gamma_{lv} = 0.025N/m$.

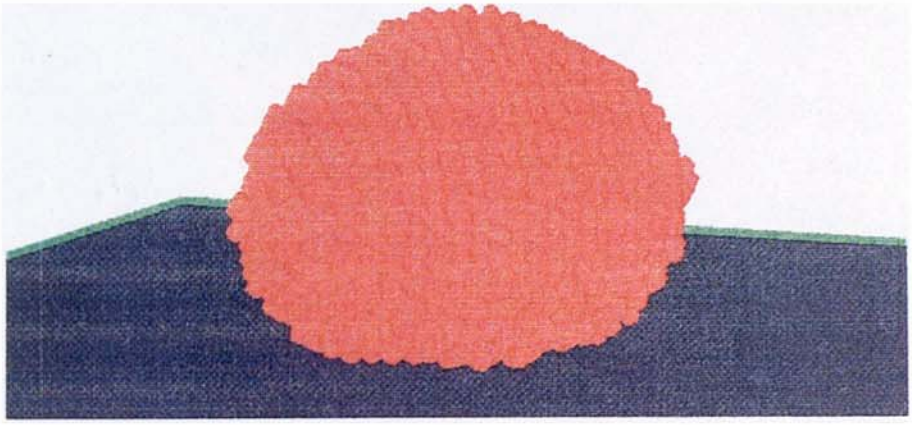

Impact velocity $v = 0.5m/s$, viscosity $\eta = 0.0$, surface tension $\gamma_{lv} = 0.025N/m$.

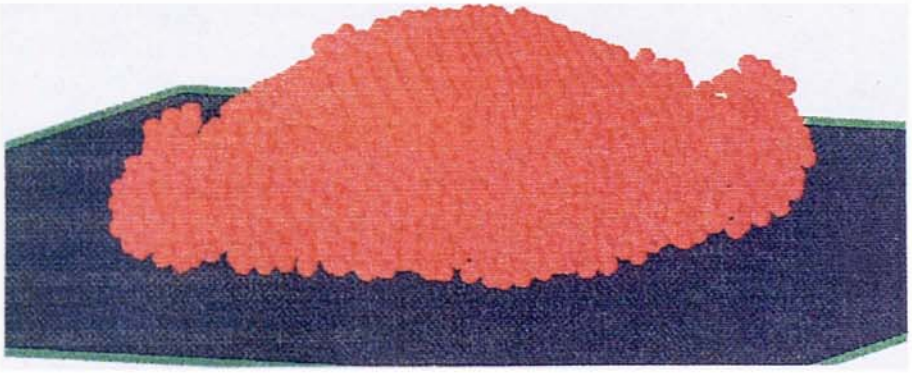

Impact velocity $v = 1.0m/s$, viscosity $\eta = 0.0$, surface tension $\gamma_{lv} = 0.025N/m$.

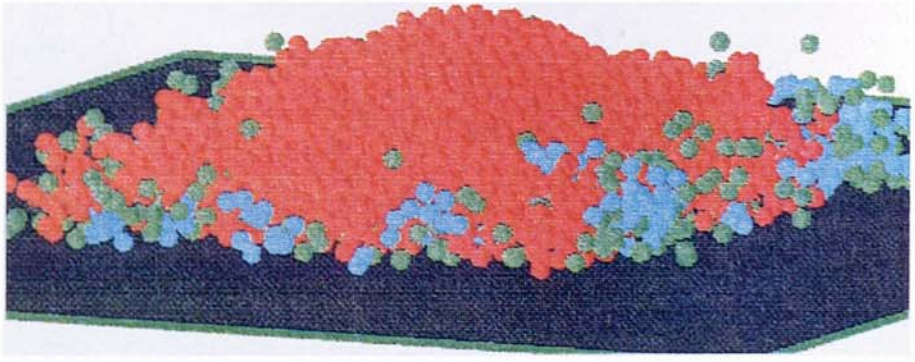

Impact velocity $v = 2.0m/s$, viscosity $\eta = 0.0$, surface tension $\gamma_{lv} = 0.025N/m$.

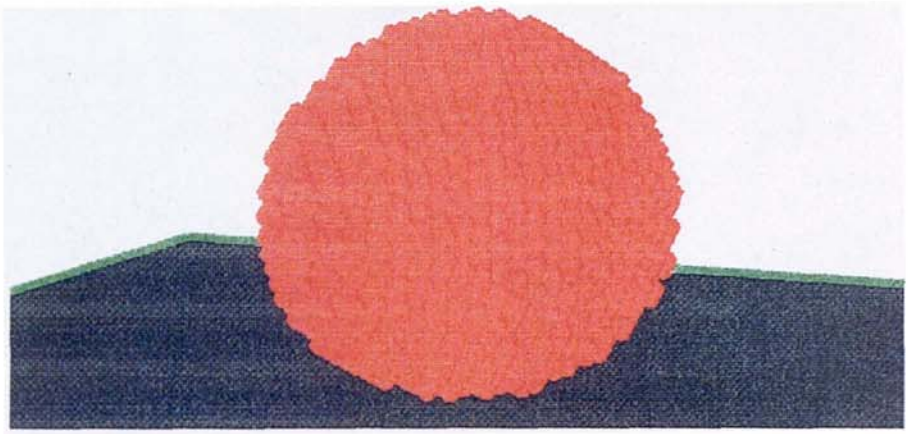

Impact velocity $v = 0.2m/s$, viscosity $\eta = 0.01Pa.s$, surface tension $\gamma_{lv} = 0.025N/m$.

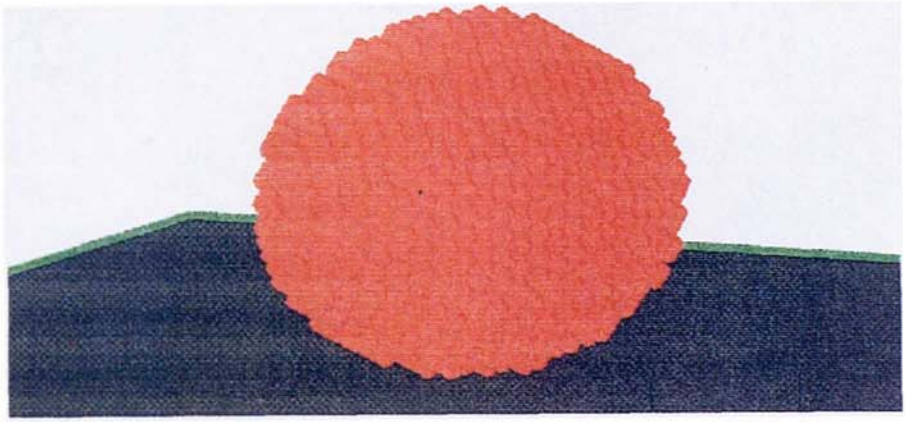

Impact velocity $v = 0.3m/s$, viscosity $\eta = 0.01Pa.s$, surface tension $\gamma_{lv} = 0.025N/m$.

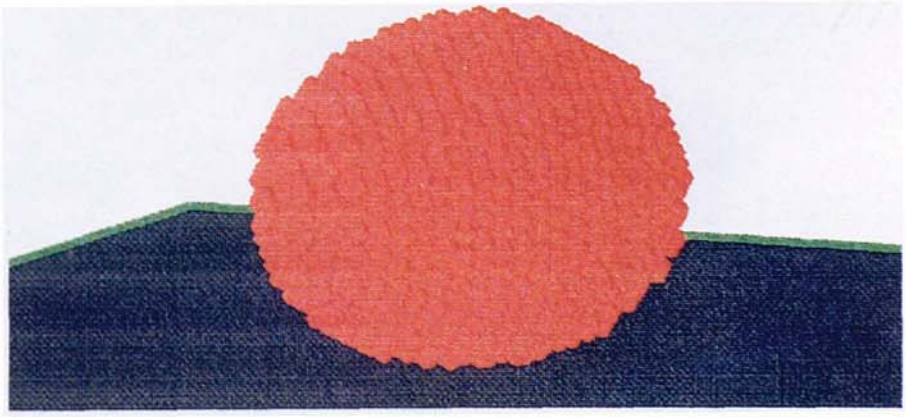

Impact velocity $v = 0.44m/s$, viscosity $\eta = 0.01Pa.s$, surface tension $\gamma_{lv} = 0.025N/m$.

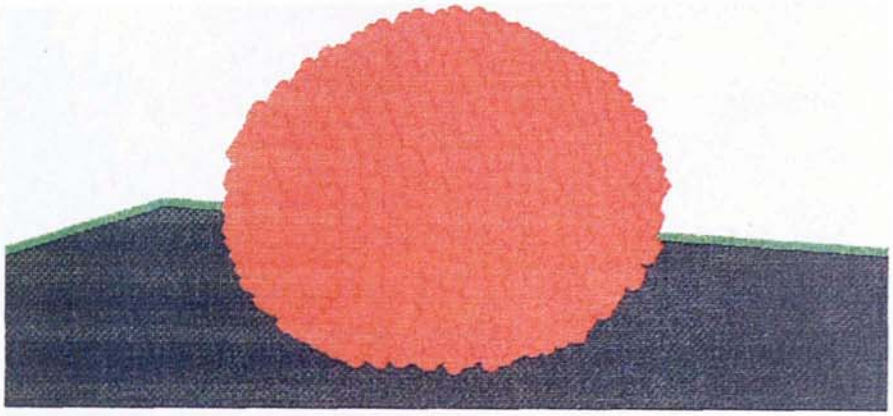

Impact velocity $v = 0.6m/s$, viscosity $\eta = 0.01 Pa.s$, surface tension $\gamma_{lv} = 0.025N/m$.

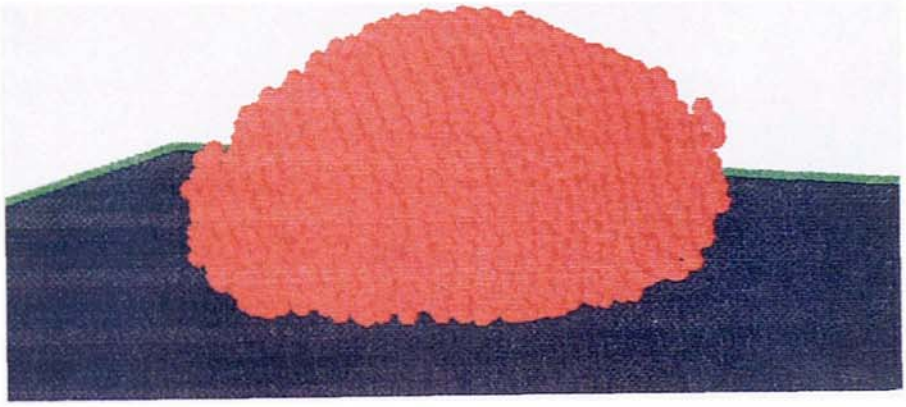

Impact velocity $v = 1.0m/s$, viscosity $\eta = 0.01 Pa.s$, surface tension $\gamma_{lv} = 0.025N/m$.

Impact velocity $v = 2.0m/s$, viscosity $\eta = 0.01 Pa.s$, surface tension $\gamma_{lv} = 0.025N/m$.

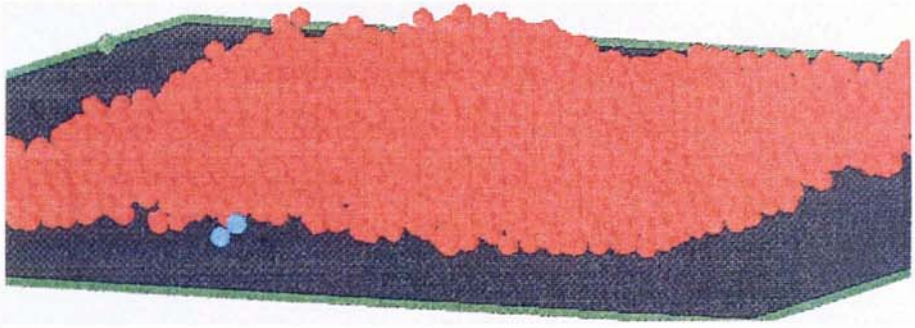

Impact velocity $v = 3.0m/s$, viscosity $\eta = 0.01Pa.s$, surface tension $\gamma_{lv} = 0.025N/m$.

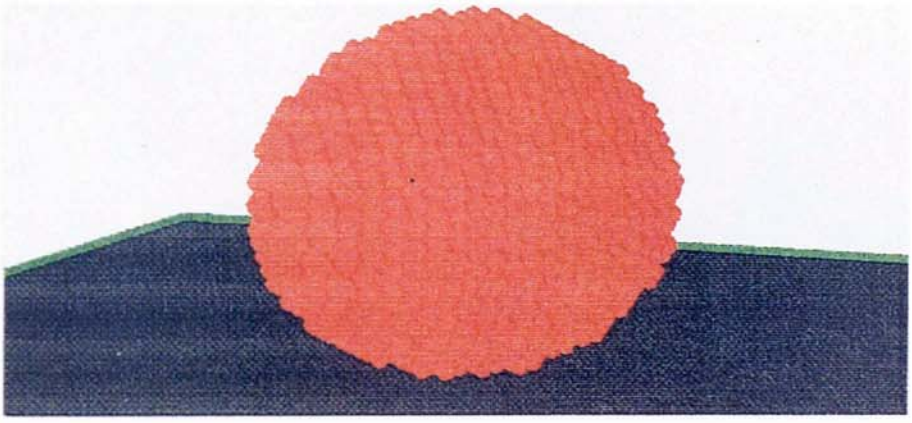

Impact velocity $v = 0.3m/s$, viscosity $\eta = 0.10Pa.s$, surface tension $\gamma_{lv} = 0.025N/m$.

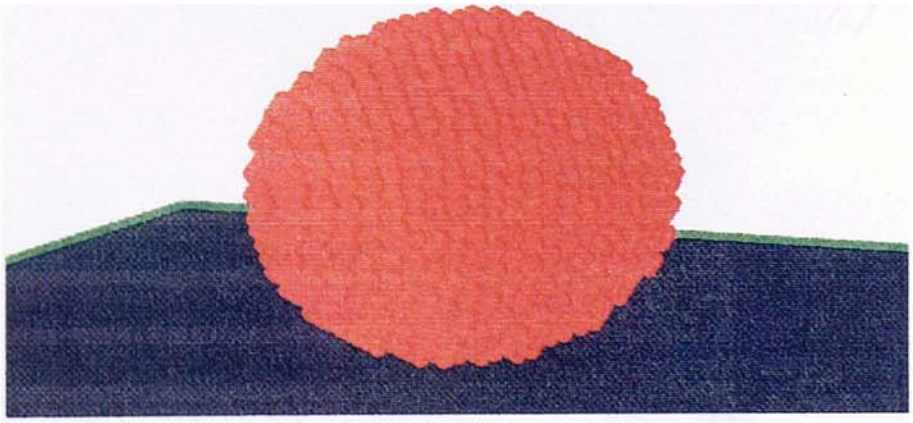

Impact velocity $v = 0.4m/s$, viscosity $\eta = 0.10Pa.s$, surface tension $\gamma_{lv} = 0.025N/m$.

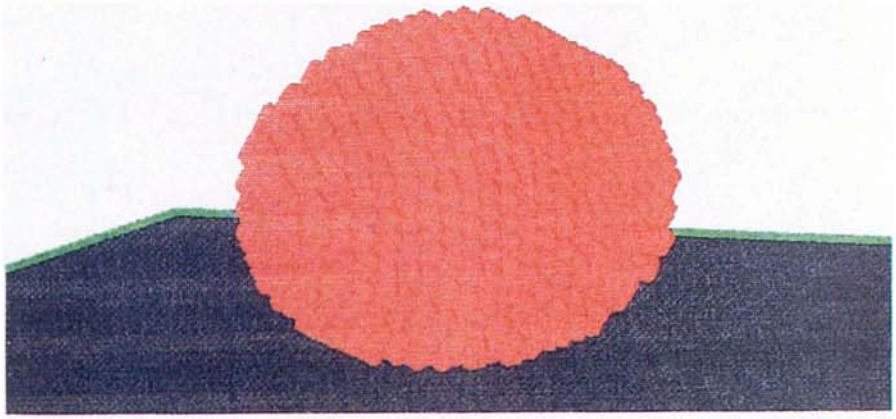

Impact velocity $v = 0.6m/s$, viscosity $\eta = 0.10Pa.s$, surface tension $\gamma_{lv} = 0.025N/m$.

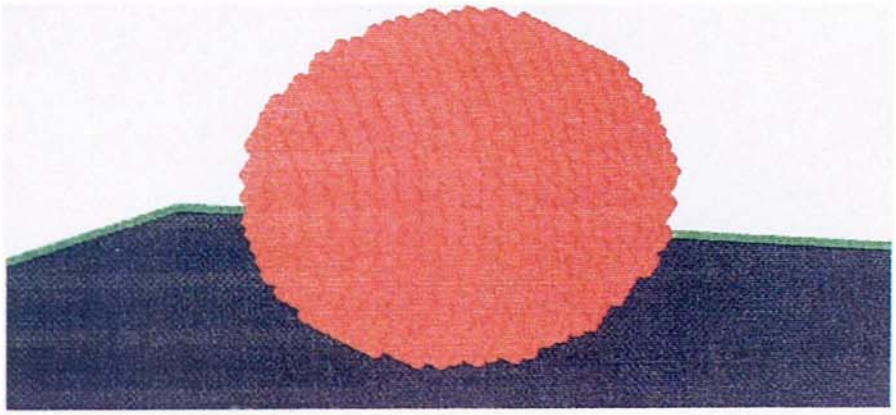

Impact velocity $v = 1.0m/s$, viscosity $\eta = 0.10Pa.s$, surface tension $\gamma_{lv} = 0.025N/m$.

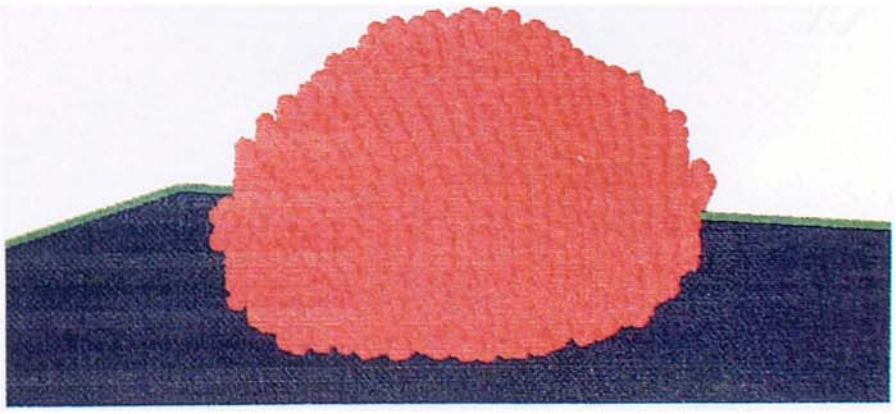

Impact velocity $v = 2.0m/s$, viscosity $\eta = 0.10Pa.s$, surface tension $\gamma_{lv} = 0.025N/m$.

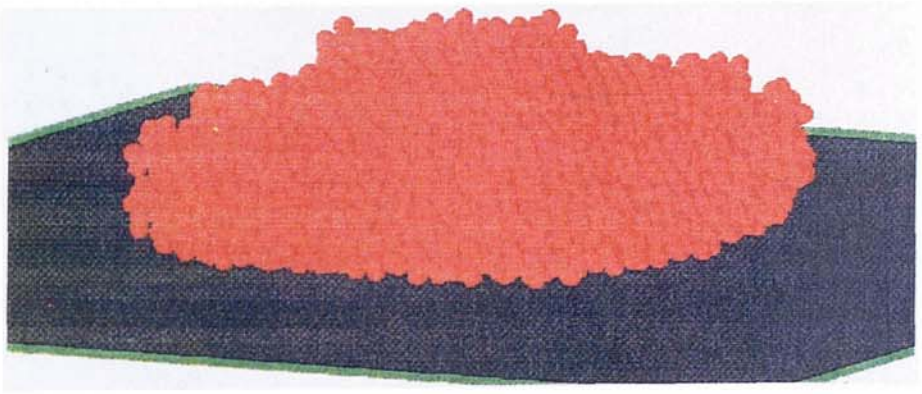

Impact velocity $v = 4.0m/s$, viscosity $\eta = 0.10Pa.s$, surface tension $\gamma_{lv} = 0.025N/m$.

Impact velocity $v = 8.0m/s$, viscosity $\eta = 0.10Pa.s$, surface tension $\gamma_{lv} = 0.025N/m$.

C.2 Agglomerate-agglomerate collisions

Appendix C.2 presents graphics printings of the computer simulated agglomerate-agglomerate collisions reported in Chapter 7. Each agglomerate consisted of 1000 randomly packed particles of radius $R = 30\mu m$ with a normally distributed deviation of $\pm 3\mu m$. The properties of the constitutive particles were: density $\rho = 2.65 Mg\, m^{-3}$, Young's modulus $E = 70 Gpa$, Poisson's ratio $\nu = 0.3$ and friction coefficient $\mu = 0.3$. At each contact, a quantity of liquid of 0.1% of the particle volume was assigned to form a liquid bridge and the corresponding degree of saturation was 0.71%. The liquid modelled was silicon fluid with the following properties: surface tension $\gamma_{lv} = 0.025 \sim 0.050 Nm^{-1}$, solid-liquid contact angle $\theta = 0^0$ and viscosity $\eta = 0.001 \sim 0.10 Pa\, s$.

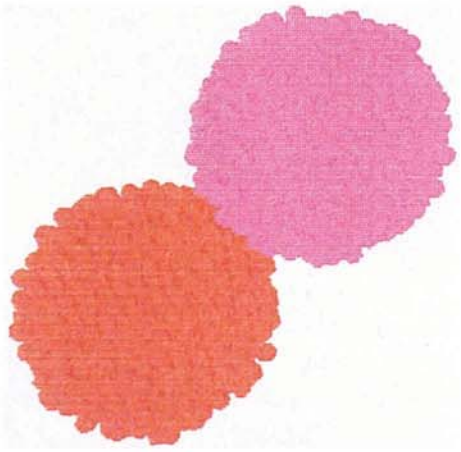

Impact velocity $v = 0.2m/s$, incident angle $\Theta = 0°$,
viscosity $\eta = 0.001Pa.s$, surface tension $\gamma_{lv} = 0.025N/m$.

..

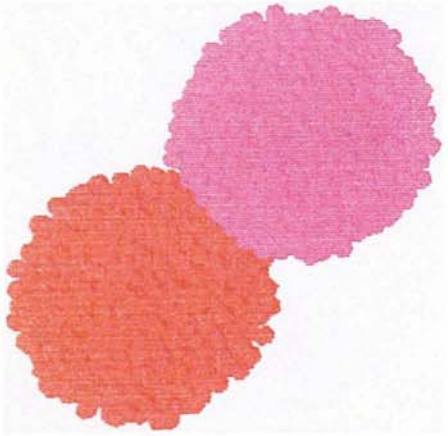

Impact velocity $v = 0.5m/s$, incident angle $\Theta = 0°$,
viscosity $\eta = 0.001Pa.s$, surface tension $\gamma_{lv} = 0.025N/m$.

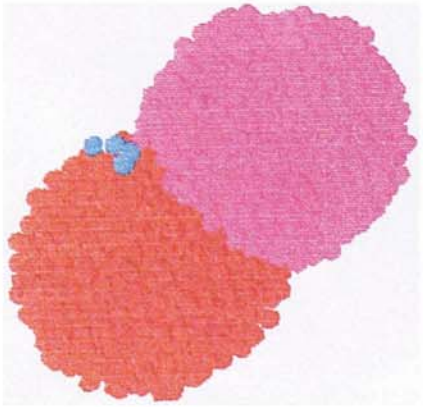

Impact velocity $v = 1.0m/s$, incident angle $\Theta = 0°$,
viscosity $\eta = 0.001Pa.s$, surface tension $\gamma_{lv} = 0.025N/m$.

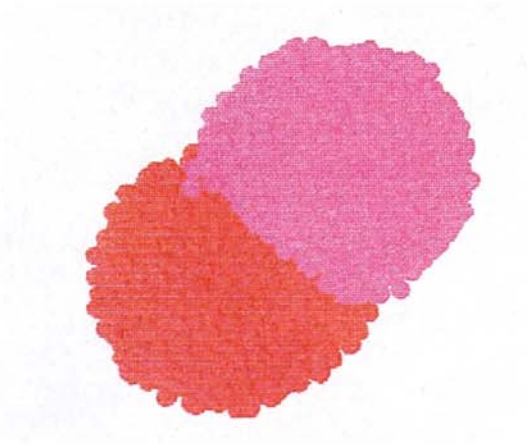

Impact velocity $v = 1.2m/s$, incident angle $\Theta = 0°$,
viscosity $\eta = 0.001Pa.s$, surface tension $\gamma_{lv} = 0.025N/m$.

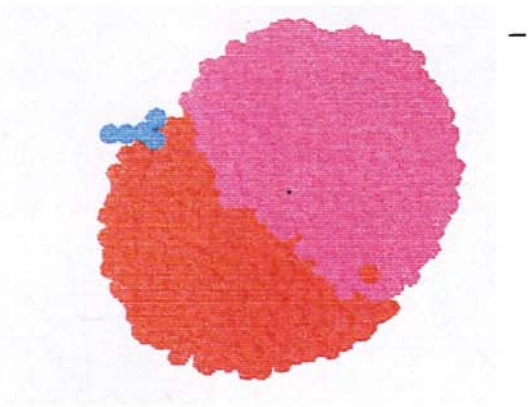

Impact velocity $v = 1.5m/s$, incident angle $\Theta = 0°$,
viscosity $\eta = 0.001Pa.s$, surface tension $\gamma_{lv} = 0.025N/m$.

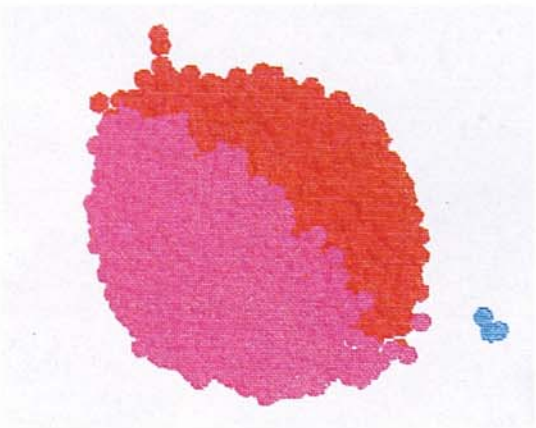

Impact velocity $v = 2.0m/s$, incident angle $\Theta = 0°$,
viscosity $\eta = 0.001Pa.s$, surface tension $\gamma_{lv} = 0.025N/m$.

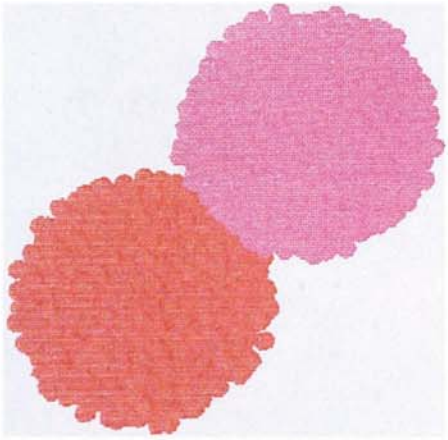

Impact velocity $v = 0.5m/s$, incident angle $\Theta = 0^o$,
viscosity $\eta = 0.01 Pa.s$, surface tension $\gamma_{lv} = 0.025 N/m$.

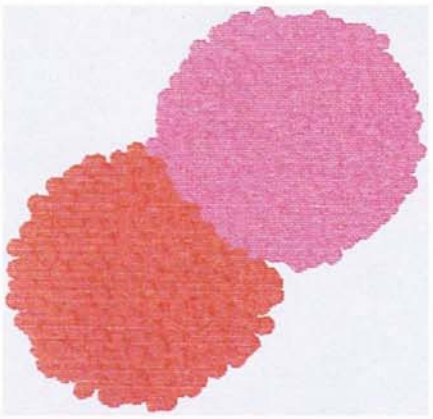

Impact velocity $v = 1.0m/s$, incident angle $\Theta = 0^o$,
viscosity $\eta = 0.01 Pa.s$, surface tension $\gamma_{lv} = 0.025 N/m$.

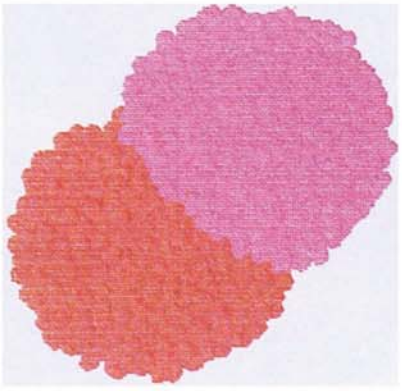

Impact velocity $v = 1.5m/s$, incident angle $\Theta = 0^o$,
viscosity $\eta = 0.01 Pa.s$, surface tension $\gamma_{lv} = 0.025 N/m$.

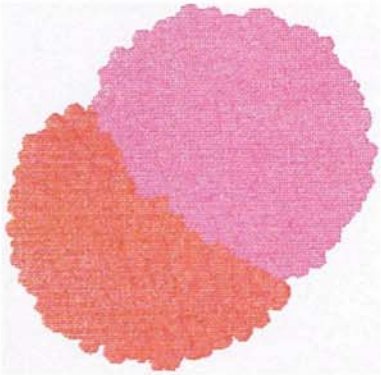

Impact velocity $v = 2.0m/s$, incident angle $\Theta = 0°$,
viscosity $\eta = 0.01Pa.s$, surface tension $\gamma_{lv} = 0.025N/m$.

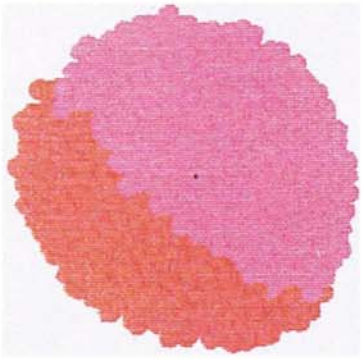

Impact velocity $v = 2.5m/s$, incident angle $\Theta = 0°$,
viscosity $\eta = 0.01Pa.s$, surface tension $\gamma_{lv} = 0.025N/m$.

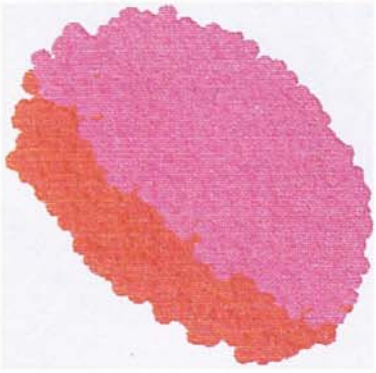

Impact velocity $v = 3.0m/s$, incident angle $\Theta = 0°$,
viscosity $\eta = 0.01Pa.s$, surface tension $\gamma_{lv} = 0.025N/m$.

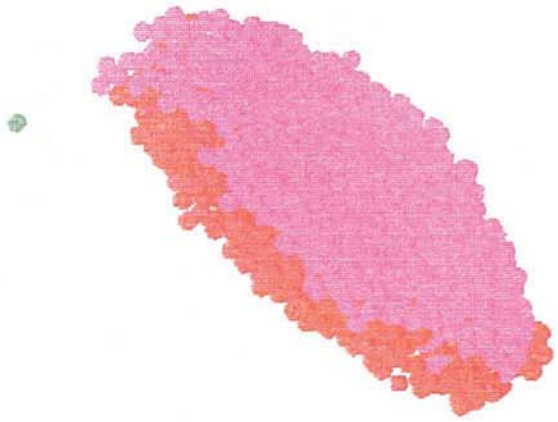

Impact velocity $v = 4.0m/s$, incident angle $\Theta = 0°$,
viscosity $\eta = 0.01 Pa.s$, surface tension $\gamma_{lv} = 0.025 N/m$.

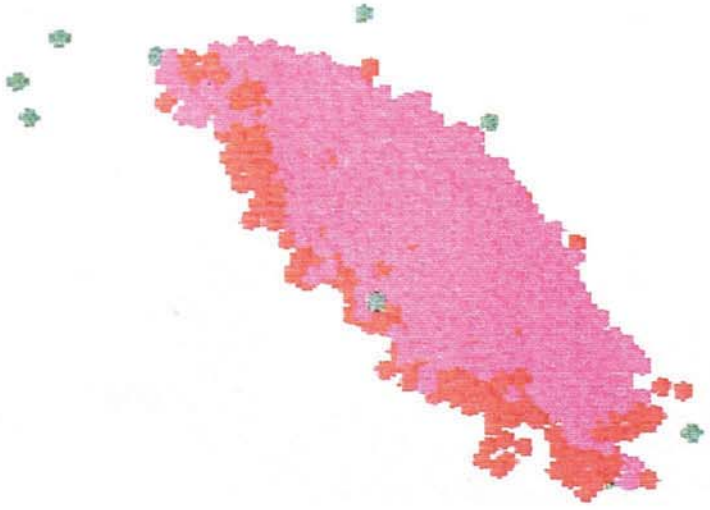

Impact velocity $v = 5.0m/s$, incident angle $\Theta = 0°$,
viscosity $\eta = 0.01 Pa.s$, surface tension $\gamma_{lv} = 0.025 N/m$.

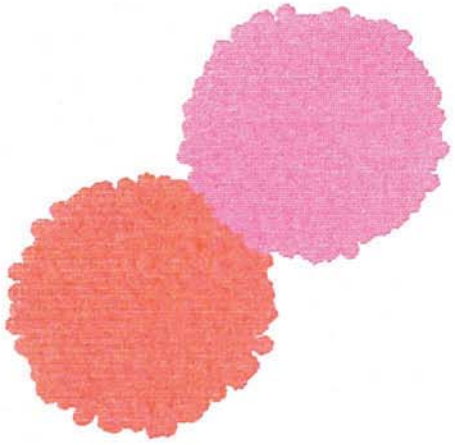

Impact velocity $v = 0.5m/s$, incident angle $\Theta = 0^o$,
viscosity $\eta = 0.01Pa.s$, surface tension $\gamma_{lv} = 0.05N/m$.

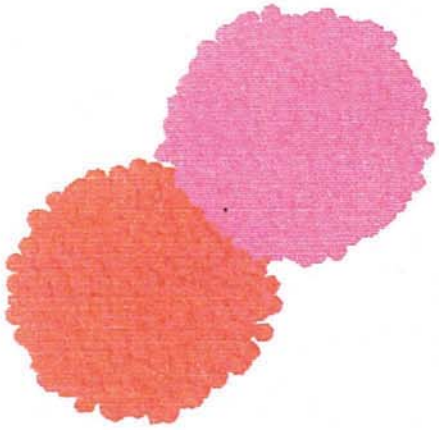

Impact velocity $v = 1.0m/s$, incident angle $\Theta = 0^o$,
viscosity $\eta = 0.01Pa.s$, surface tension $\gamma_{lv} = 0.05N/m$.

Impact velocity $v = 2.0m/s$, incident angle $\Theta = 0^o$,
viscosity $\eta = 0.01Pa.s$, surface tension $\gamma_{lv} = 0.05N/m$.

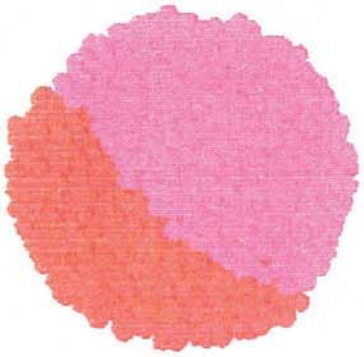

Impact velocity $v = 3.0m/s$, incident angle $\Theta = 0°$,
viscosity $\eta = 0.01Pa.s$, surface tension $\gamma_{lv} = 0.05N/m$.

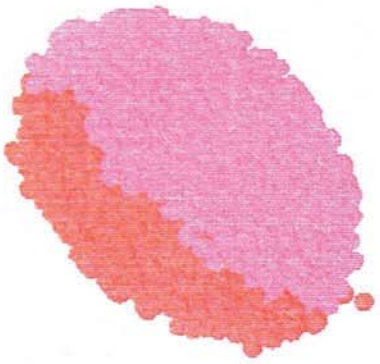

Impact velocity $v = 4.0m/s$, incident angle $\Theta = 0°$,
viscosity $\eta = 0.01Pa.s$, surface tension $\gamma_{lv} = 0.05N/m$.

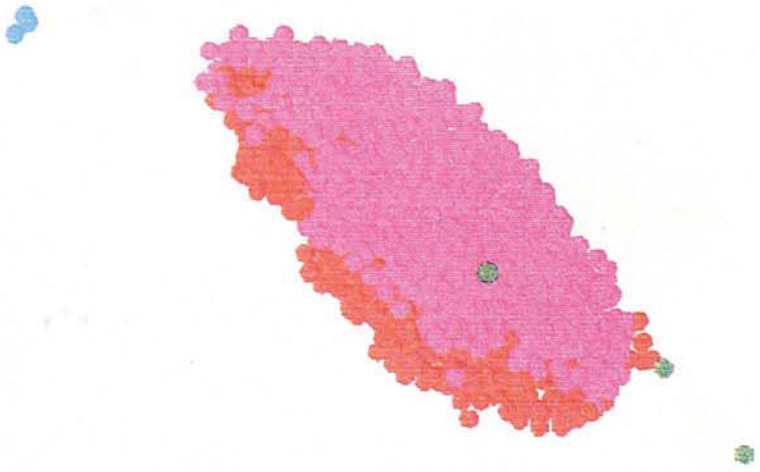

Impact velocity $v = 5.0m/s$, incident angle $\Theta = 0°$,
viscosity $\eta = 0.01Pa.s$, surface tension $\gamma_{lv} = 0.05N/m$.

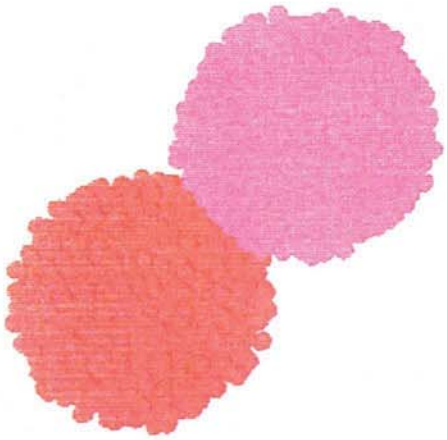

Impact velocity $v = 2.0m/s$, incident angle $\Theta = 0°$,
viscosity $\eta = 0.1Pa.s$, surface tension $\gamma_{lv} = 0.025N/m$.

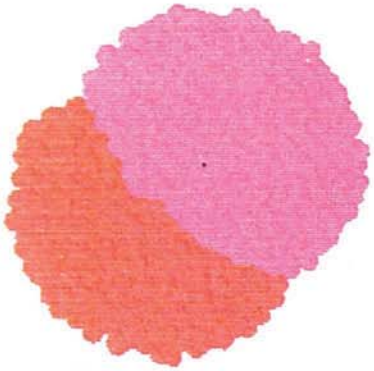

Impact velocity $v = 5.0m/s$, incident angle $\Theta = 0°$,
viscosity $\eta = 0.1Pa.s$, surface tension $\gamma_{lv} = 0.025N/m$.

Impact velocity $v = 6.0m/s$, incident angle $\Theta = 0°$,
viscosity $\eta = 0.1Pa.s$, surface tension $\gamma_{lv} = 0.025N/m$.

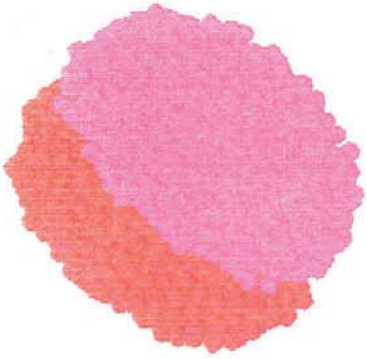

Impact velocity $v = 7.0m/s$, incident angle $\Theta = 0^o$,
viscosity $\eta = 0.1Pa.s$, surface tension $\gamma_{lv} = 0.025N/m$.

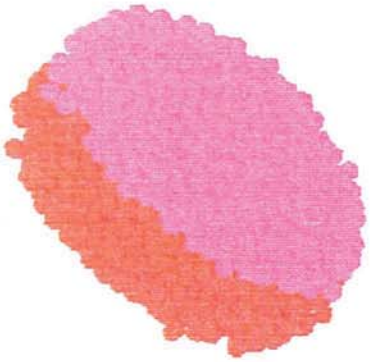

Impact velocity $v = 10.0m/s$, incident angle $\Theta = 0^o$,
viscosity $\eta = 0.1Pa.s$, surface tension $\gamma_{lv} = 0.025N/m$.

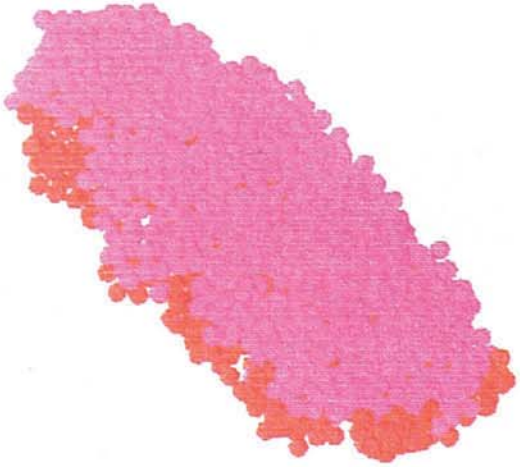

Impact velocity $v = 15.0m/s$, incident angle $\Theta = 0^o$,
viscosity $\eta = 0.1Pa.s$, surface tension $\gamma_{lv} = 0.025N/m$.

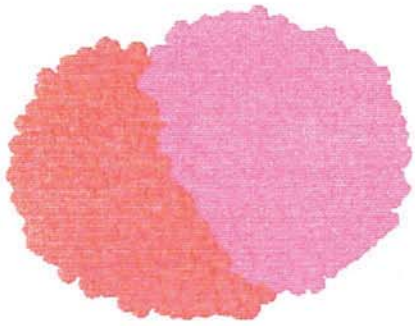

Impact velocity $v = 2.0m/s$, incident angle $\Theta = 15°$,
viscosity $\eta = 0.01 Pa.s$, surface tension $\gamma_{lv} = 0.025 N/m$.

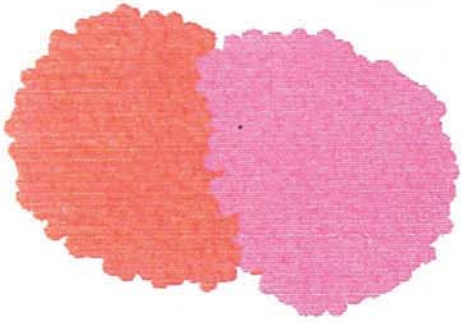

Impact velocity $v = 2.0m/s$, incident angle $\Theta = 30°$,
viscosity $\eta = 0.01 Pa.s$, surface tension $\gamma_{lv} = 0.025 N/m$.

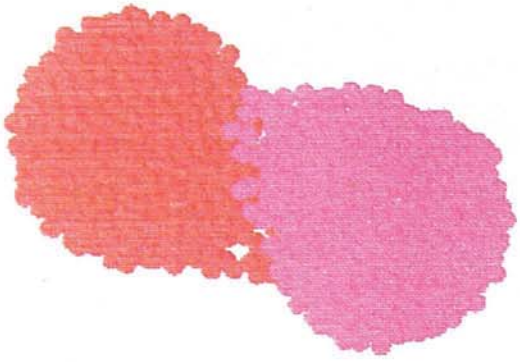

Impact velocity $v = 2.0m/s$, incident angle $\Theta = 45°$,
viscosity $\eta = 0.01 Pa.s$, surface tension $\gamma_{lv} = 0.025 N/m$.

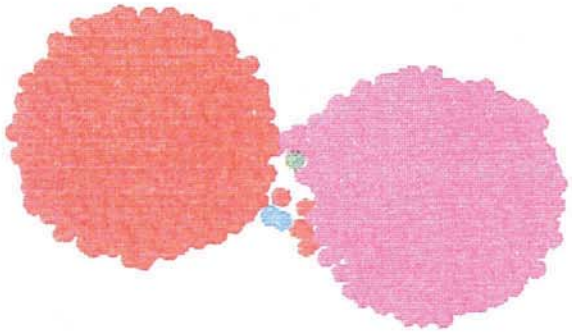

Impact velocity $v = 2.0m/s$, incident angle $\Theta = 60°$,
viscosity $\eta = 0.01 Pa.s$, surface tension $\gamma_{lv} = 0.025 N/m$.

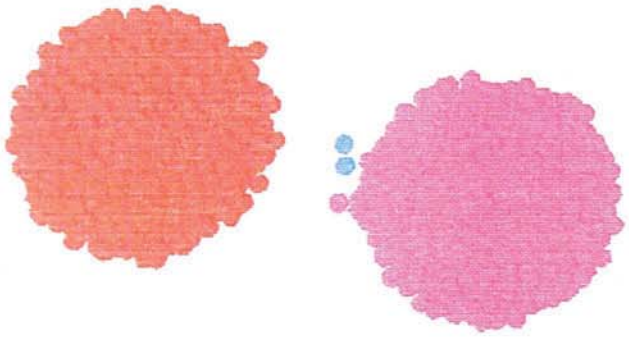

Impact velocity $v = 2.0m/s$, incident angle $\Theta = 75°$,
viscosity $\eta = 0.01 Pa.s$, surface tension $\gamma_{lv} = 0.025 N/m$.

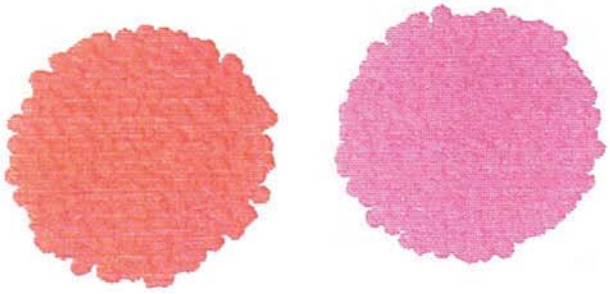

Impact velocity $v = 2.0m/s$, incident angle $\Theta = 85°$,
viscosity $\eta = 0.01 Pa.s$, surface tension $\gamma_{lv} = 0.025 N/m$.

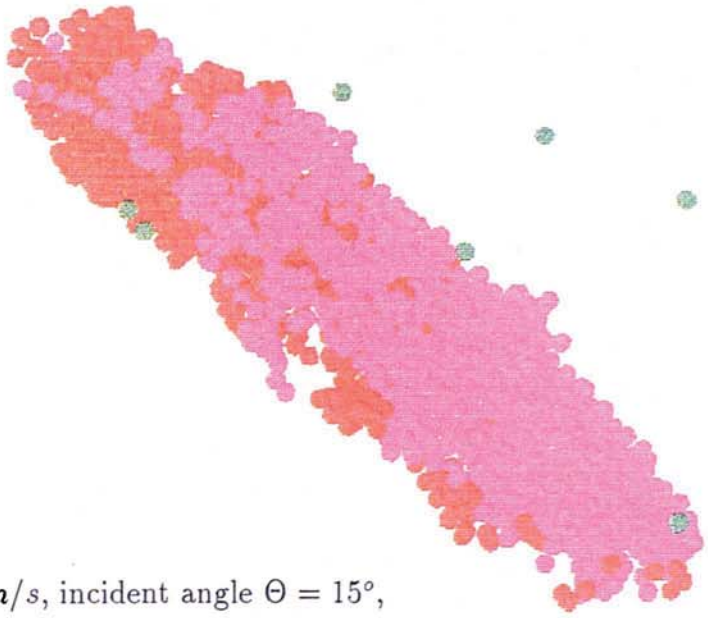

Impact velocity $v = 5.0m/s$, incident angle $\Theta = 15°$,
viscosity $\eta = 0.01 Pa.s$, surface tension $\gamma_{lv} = 0.025 N/m$.

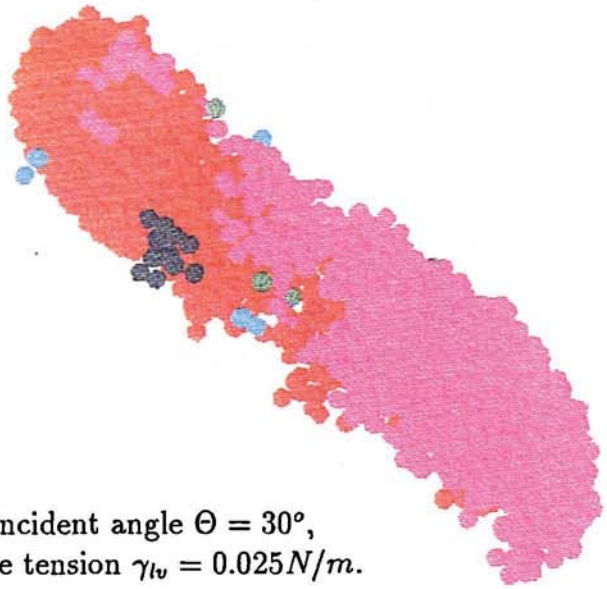

Impact velocity $v = 5.0m/s$, incident angle $\Theta = 30°$,
viscosity $\eta = 0.01 Pa.s$, surface tension $\gamma_{lv} = 0.025 N/m$.

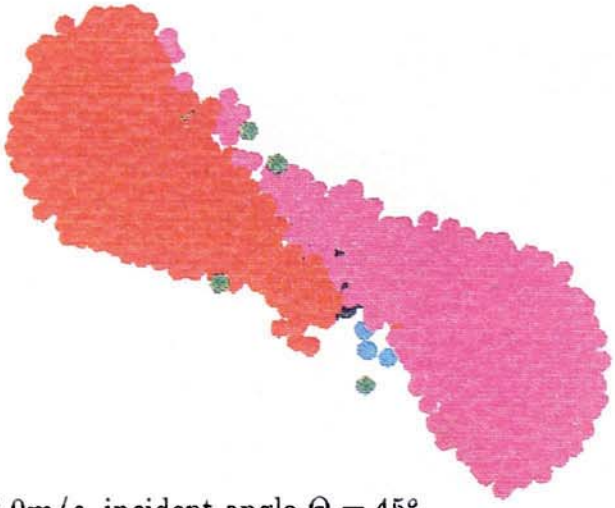

Impact velocity $v = 5.0m/s$, incident angle $\Theta = 45°$,
viscosity $\eta = 0.01 Pa.s$, surface tension $\gamma_{lv} = 0.025 N/m$.

Impact velocity $v = 5.0m/s$, incident angle $\Theta = 60^o$,
viscosity $\eta = 0.01 Pa.s$, surface tension $\gamma_{lv} = 0.025 N/m$.

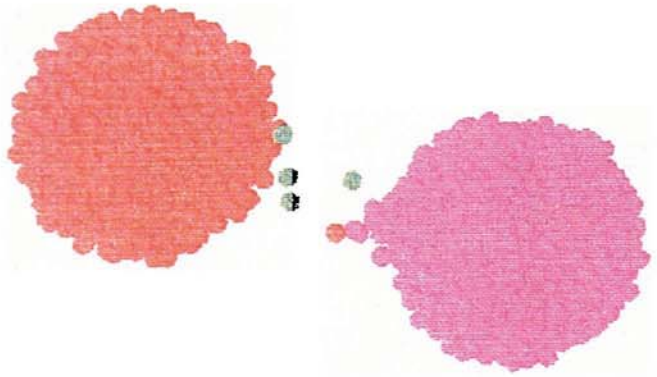

Impact velocity $v = 5.0m/s$, incident angle $\Theta = 75^o$,
viscosity $\eta = 0.01 Pa.s$, surface tension $\gamma_{lv} = 0.025 N/m$.

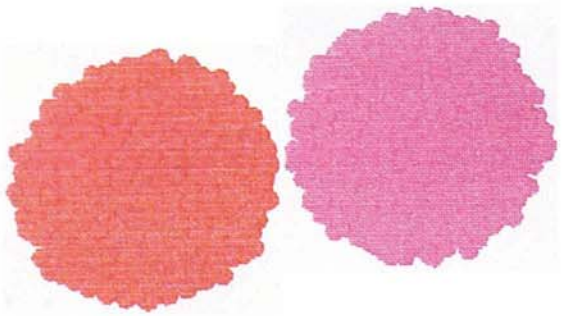

Impact velocity $v = 5.0m/s$, incident angle $\Theta = 85^o$,
viscosity $\eta = 0.01 Pa.s$, surface tension $\gamma_{lv} = 0.025 N/m$.

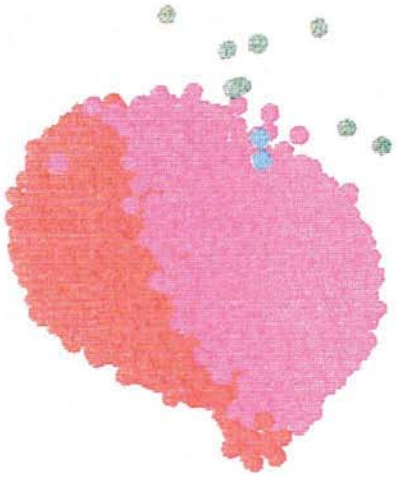

Impact velocity $v = 2.0m/s$, incident angle $\Theta = 15°$,
viscosity $\eta = 0.001Pa.s$, surface tension $\gamma_{lv} = 0.025N/m$.

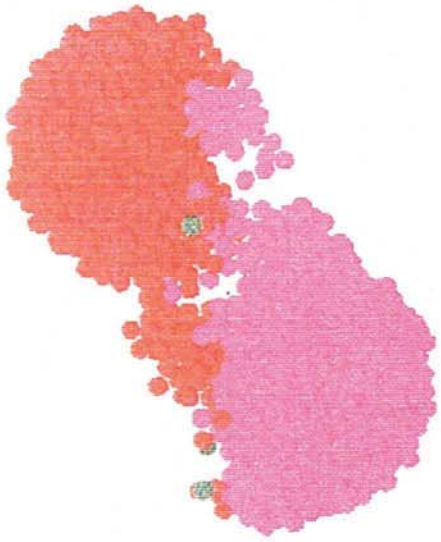

Impact velocity $v = 2.0m/s$, incident angle $\Theta = 30°$,
viscosity $\eta = 0.001Pa.s$, surface tension $\gamma_{lv} = 0.025N/m$.

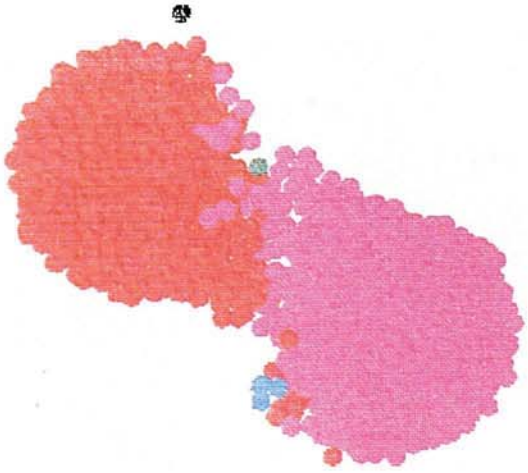

Impact velocity $v = 2.0m/s$, incident angle $\Theta = 45°$,
viscosity $\eta = 0.001Pa.s$, surface tension $\gamma_{lv} = 0.025N/m$.

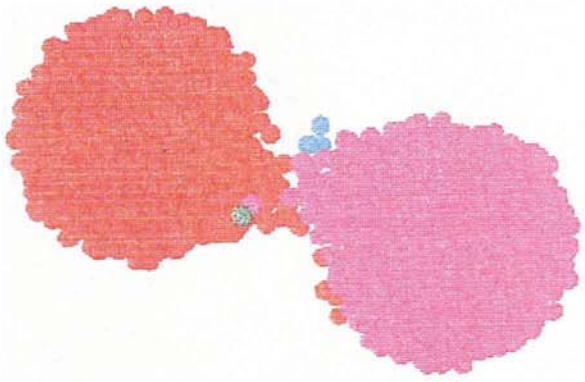

Impact velocity $v = 2.0m/s$, incident angle $\Theta = 60^o$,
viscosity $\eta = 0.001Pa.s$, surface tension $\gamma_{lv} = 0.025N/m$.

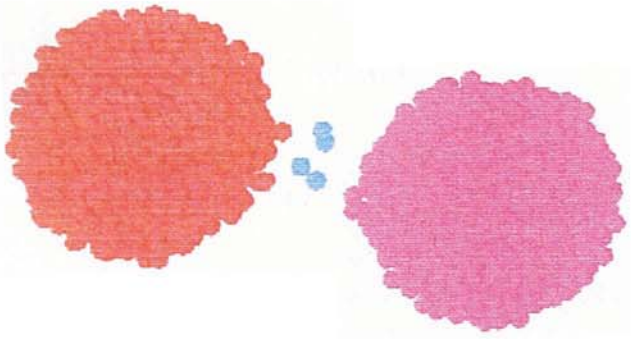

Impact velocity $v = 2.0m/s$, incident angle $\Theta = 75^o$,
viscosity $\eta = 0.001Pa.s$, surface tension $\gamma_{lv} = 0.025N/m$.

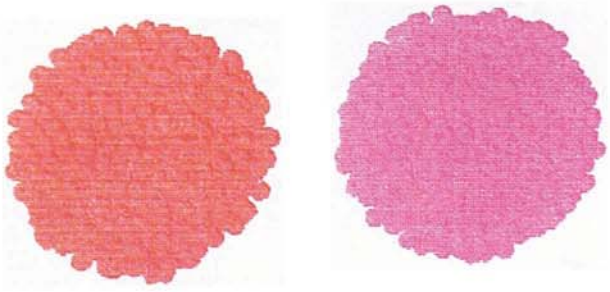

Impact velocity $v = 2.0m/s$, incident angle $\Theta = 85^o$,
viscosity $\eta = 0.001Pa.s$, surface tension $\gamma_{lv} = 0.025N/m$.